NOVEL MISFIT LAYER SYSTEMS:
SYNTHESIS AND CHARACTERIZATION

by

MICHAEL D. ANDERSON

A DISSERTATION

Presented to the Department of Chemistry
and the Graduate School of the University of Oregon
in partial fulfillment of the requirements
for the degree of
Doctor of Philosophy

September 2011

DISSERTATION APPROVAL PAGE

Student: Michael D. Anderson

Title: Novel Misfit Layer Systems: Synthesis and Characterization

This dissertation has been accepted and approved in partial fulfillment of the requirements for the Doctor of Philosophy degree in the Department of Chemistry by:

Dr. Mark C. Lonergan	Chair
Dr. David C. Johnson	Advisor
Dr. James Hutchison	Member
Dr. Catherine Page	Member
Dr. Stephen Gregory	Outside Member
Dr. Ian M. Anderson	Honorary Member

and

Kimberly Andrews Espy	Vice President for Research & Innovation/ Dean of the Graduate School

Original approval signatures are on file with the University of Oregon Graduate School.

Degree awarded September 2011

DISSERTATION ABSTRACT

Michael D. Anderson

Doctor of Philosophy

Department of Chemistry

September 2011

Title: Novel Misfit Layer Systems: Synthesis and Characterization

Approved: _____
Dr. David C. Johnson

Stabilizing mechanisms and design considerations for generating misfit layer compounds with a variety of different structural motifs were explored using designed precursors consisting of elemental layers. Layer order in the precursor film and the behavior of binary reaction couples was used to avoid undesirable reaction intermediates.

Electron diffraction patterns of $CuCr_2Se_4$were inconsistent with prior reports that this compound has the spinel structure and were more consistent with a hexagonal $R\bar{3}$ structure. STEM imaging also suggests $CuCr_2Se_4$prepared using the compositionally modulated kinetic trapping approach is a new polymorph of the spinel structure. Electrical and magnetic properties were consistent with prior literature reports. Magnetic susceptibility measurements show pronounced hard and easy axes of magnetization not previously documented, which are consistent with a hexagonal crystal symmetry.

The $[\{(PbSe)_m\}_{0.99}(WSe_2)_n]_r$ and $[\{(PbSe)_m\}_{1.00}(MoSe_2)_n]_r$ systems were investigated by STEM, XRD and density functional theory (DFT) modeling. No crystallographic registration between MSe and TSe_2 layers was observed and the

diffraction observed in the $hk0$ and hkl directions, where $h = k = 0$, can be described by diffraction from discrete layers of finite thickness. A distortion of the MX structure for $m > 4$ was documented. The distortion in MSe layers was largest for $m = 2$ and independent of TSe_2 thickness.

A novel family of compounds, $[\{(FeSe)_m\}_{1+y}(NbSe_2)_n]_r$, were synthesized inspired by a geological precedent. Single FeSe and $NbSe_2$ layer thicknesses ((0.571 ± 0.005) nm and (0.653 ± 0.002) nm respectively) are consistent with literature values for the binary compounds. STEM-HAADF images of the $[\{(FeSe)_5\}_{1+y}(NbSe_2)_5]_r$ revealed a multilayer structure with two distinct structural subunits. STEM-EELS analysis of the film showed no intermixing between the Nb and Fe regions within the limit of the measurement.

Another family of misfit layer compounds, $[\{(NbSe_2)_m\}_{1+y}(CuCr_2Se_4)_n]_r$, designed to test requirements for a stable misfit layer compound, were successfully synthesized. STEM analysis of the $[\{(NbSe_2)_5\}_{1+y}(CuCr_2Se_4)_1]_r$ compound showed a well segregated film with two distinct subunit structures. Thicknesses for individual layers of $NbSe_2$ or $CuCr_2Se_4$ ((0.648 ± 0.004) nm and (1.76 ± 0.01) nm respectively) are consistent with prior literature reports of the individual binary compounds.

This dissertation includes previously published and unpublished co-authored material.

CURRICULUM VITAE

NAME OF AUTHOR: Michael D. Anderson

GRADUATE AND UNDERGRADUATE SCHOOLS ATTENDED:

University of Oregon, Eugene, Oregon
Washington State University, Richland, Washington
Columbia Basin College, Pasco, Washington

DEGREES AWARDED:

Doctor of Philosophy in Materials Chemistry, 2011, University of Oregon
Master of Science in Materials Chemistry, 2007, University of Oregon
Bachelor of Science in Chemistry, 2006, Washington State University
Associate of Science, 2002, Columbia Basin College

AREAS OF SPECIAL INTEREST:

Solid State Chemistry, Materials Science, Electron Microscopy

PROFESSIONAL EXPERIENCE:

Sr. Process Engineeer, Advanced Module Technology Development Group, GlobalFoundries, 2011-Present

Graduate Intern, Surface & Microanalysis Sciences Division, National Institute of Standards and Technology, 2008-2011

Graduate Research Assistant, Department of Chemistry, University of Oregon, Eugene, Oregon, 2007-2008

Graduate Teaching Fellow, Department of Chemistry, University of Oregon, Eugene, Oregon, 2006-2007

Research Assistant, Energy Materials Directorate, Pacific Northwest National Laboratory, Richland, Washington, 2002-2006

GRANTS, AWARDS AND HONORS:

National Science Foundation IGERT Fellow, University of Oregon Department of Chemistry, 2008-2011

Cum laude, Washington State University, 2006

Bernard S. Baker Award for Student Fuel Cell Research, 3^{rd} Place, SOFC Magazine, 2006

Outstanding Performance Award, Pacific Northwest National Laboratory, 2004 and 2006

PUBLICATIONS:

Bailey, M. M.; Kline, S. R.; Anderson, M. D.; Staymates, J.; Berkland, C. *Langmuir* **2011** (Submitted),

Thompson, J. O.; Anderson, M. D.; Ngai, T.; Allen, T.; Johnson, D. C. *J. Alloys Compd.* **2011** (Accepted),

Beekman, M.; Heideman, C.; Anderson, M. D.; Smeller, M.; Atkins, R.; Lin, Q.; Nguyen, N.; Johnson, D. In *Design and realization of nanostructured inorganic intergrowths*, 2nd ed.; Rowe, D. M., Ed.; CRC Handbook of Thermoelectrics; CRC Press, **2011** (Accepted)

Richart, J. W.; Anderson, M. D.; Johnson, D. C. *Z. Anorg. Allg. Chem.* **2011** (Accepted), Translation of Hahn, H.; de Lorent, C.; Harder, B. *Z. Anorg. Allg. Chem.* **1956**, *283*, 138–42.

Nguyen, N. T.; Berseth, P. A.; Lin, Q.; Chiritescu, C.; Cahill, D. G.; Mavrokefalos, A.; Shi, L.; Zschack, P.; Anderson, M. D.; Anderson, I. M.; Johnson, D. C. *Chemistry of Materials* **2010**, *22*, 2750–2756

Heideman, C.; Rostek, R.; Anderson, M.; Herzing, A.; Anderson, I.; Johnson, D. *J. Elec. Mater.* **2010**, *39*, 1–6

Lin, Q.; Smeller, M.; Heideman, C.; Zschack, P.; Koyano, M.; Anderson, M.; Kykyneshi, R.; Keszler, D.; Anderson, I.; Johnson, D. *Chem. Mater.* **2010**, *22*, 1002–1009

Jiang, K.; Zakutayev, A.; Stowers, J.; Anderson, M.; Tate, J.; McIntyre, D.; Johnson, D.; Keszler, D. *Solid State Sci.* **2009**, *11*, 1692–1699

ACKNOWLEDGEMENTS

There are a number of people and organizations that deserve my thanks and acknowledgment for their contribution to and the success of this work. I hope the future readers of this document will excuse my momentarily breaking with the tradition of scientific and technical brevity for the sake of heart felt gratitude.

I came to the University of Oregon to work with Dave Johnson. I had the pleasure of a lengthy correspondence with him during my undergraduate studies. At the time I observed his great passion for his work, and almost palpable vested interest in the success of his students. I am grateful that he was willing to invest the time and effort in mentoring me and give me the freedom to take a considerable risk with this new research direction.

One of the keys to the success of this project has been the people that I have had the opportunity to collaborate with at NIST. I am grateful to Ian Anderson, Keana Scott, Andrew Herzing, and Jeff Davis of the Surface and Microanalysis Sciences Division for their tutelage and expertise. I am also grateful to Cindi Dennis of the Metallurgy Division for her assistance with the magnetic characterization without which chapter 5 would not have been possible.

Most people thank their parents in acknowledgements and I'm no exception. That said, I for one know full well how much I have to be grateful to my parents for. My father has been my model for so much in my life and I don't feel that I could have a better example to learn from. My mother has spent years of her life fostering in equal parts my creativity, inquisitive nature, and love of a good pen.

This all would not have been possible with out my wife, Andra. Your patience through all the moving, the long hours, and stress have been amazing. I don't deserve

you, and I am more grateful than you will ever know that I have had you with me through the past 7 years.

I would like to acknowledge the agencies that funded this research. This material is based, in part, upon work supported by the University of Oregons National Science Foundation IGERT Fellowship Program under Grant No. DGE-0549503. This work has had the support of, through an extended internship with Surface and Microanalysis Sciences Division, the National Institute of Standards and Technology operated by the United States Department of Commerce.

The alchemists spent years in their laboratories, observing the fire that purified the metals. They spent so much time close to the fire that they gradually gave up the vanities of the world. They discovered that the purification of the metals had led to a purification of themselves.

The Alchemist by Paulo Coelho

TABLE OF CONTENTS

Chapter Page

I. INTRODUCTION 1

1.1. Incommensurate Crystal Systems 1
1.2. Overview of Misfit Layer Compounds 3
1.3. Current Misfit Layer Compounds and Composite Systems . . . 9
1.4. Iron (II) Selenide 11
1.5. Niobium (IV) Selenide 21
1.6. Copper Selenochromite 25
1.7. Solid State Synthesis and Deposition Methodologies 32
1.8. Statement of Problem and Project Overview 45

II. EXPERIMENTAL THEORY AND PROCEDURES 50

2.1. Synthesis and Compositionally Modulated Kinetic Trapping 50
2.2. Structural Characterization and Diffraction Theory 60
2.3. Electron Probe Microanalysis 71
2.4. Analytical Electron Microscopy 75
2.5. Magnetic Characterization 84

Chapter Page

III. NUCLEATION AND GROWTH KINETICS OF CO-DEPOSITED Cu AND Se PRECURSORS TO FORM METASTABLE COPPER SELENIDES 86

3.1. Co-authorship Statement 86

3.2. Introduction 86

3.3. Experimental 89

3.4. Results and Discussion 91

3.5. Conclusions 104

3.6. Bridge 104

IV. COMPOSITIONALLY MODULATED KINETIC TRAPPING: THE IMPLICATIONS OF CONTROLLED INTERMIXING ON SYNTHETIC PATHWAY CONTROL 106

4.1. Co-authorship Statement 106

4.2. Introduction 106

4.3. Experimental 110

4.4. Results and Discussion 112

4.5. Conclusions 128

4.6. Bridge 128

V. MAGNETIC AND ELECTRICAL PROPERTIES OF THIN $CuCr_2Se_4$ FILMS SYNTHESIZED BY COMPOSITIONALLY MODULATED KINETIC TRAPPING 130

5.1. Co-authorship Statement 130

Chapter Page

5.2. Introduction 130
5.3. Experimental 132
5.4. Discussion 135
5.5. Conclusion 150
5.6. Bridge 151

VI. STRUCTURAL ANALYSIS OF NOVEL $MoSe_2$ AND WSe_2 BASED MISFIT LAYER COMPOUNDS 153

6.1. Co-authorship Statement 153
6.2. Introduction 153
6.3. Experimental 155
6.4. Results and Discussion 159
6.5. Conclusions 163
6.6. Bridge 166

VII. SIZE DEPENDENT STRUCTURAL DISTORTIONS IN ONE DIMENSIONAL NANOSTRUCTURES 172

7.1. Co-authorship Statement 172
7.2. Discussion 172
7.3. Bridge 180

Chapter Page

VIII. DEVELOPMENT OF $[\{(FeSe)_M\}_{1+Y}(NbSe_2)_N]_R$: AN ARTIFICIAL TOCHILINITE ANALOG 182

8.1. Co-authorship Statement 182

8.2. Introduction 182

8.3. Experimental 185

8.4. Results and Discussion 187

8.5. Conclusions 194

8.6. Bridge 197

IX. SYNTHESIS OF $[\{(NbSe_2)_M\}_{1+Y}(CuCr_2Se_4)_N]_R$: A DESIGNED LAYERED INTERGROWTH COMPOUND 199

9.1. Co-authorship Statement 199

9.2. Introduction 199

9.3. Experiemental 204

9.4. Results and Discussion 206

9.5. Conclusion 217

X. CONCLUSIONS 218

APPENDICES

A. NOMENCLATURE AND NOTATIONS 222

A.1. Nomenclature 222

Chapter Page

A.2. Notation 223

B. RIETVELD REFINEMENTS FOR THE $[\{(PbSe)_M\}_{0.99}(WSe_2)_N]_R$ FAMILY OF COMPOUNDS 228

C. SOLID STATE PHASE DIAGRAMS 235

C.1. FeSe 235

C.2. $NbSe_2$ 236

C.3. $CuCr_2Se_4$ 236

D. CRYSTAL STRUCTURES 239

D.1. FeSe 239

D.2. $NbSe_2$ 240

D.3. $CuCr_2Se_4$(Cubic) 240

D.4. $CuCr_2Se_4$(Hexagonal) 241

E. BRAGG'S LAW 242

E.1. High Angle Approximation 242

E.2. Low Angle Correction 243

F. THE ISSUE OF NOMENCLATURE IN TETRAGONAL FeSe 246

Chapter Page

G. LIST OF ACRONYMS AND ABBREVIATIONS 249

REFERENCES CITED 252

LIST OF FIGURES

Figure Page

1.1. Geological examples of the MLC structural motif. 2

1.2. Schematic representation of the classic MLC. 8

1.3. The periodic table showing elements that have been incorporated into MLCs. 12

1.4. The crystal structure of the $(Pb_2FeS_3)_{0.58}NbS_2$ MLC. 13

1.5. The α-FeSe and β-FeSe crystal structures. 15

1.6. The aggregate and spin polarized density of states for α-FeSe. 19

1.7. Structure of the transition metal dichalcogenide $NbSe_2$. 22

1.8. Density of states for $NbSe_2$. 24

1.9. A cross section of known compounds AB_2X_4. 26

1.10. The literature structure for $CuCr_2Se_4$. 28

1.11. The spin polarized density of states for $CuCr_2Se_4$. 30

1.12. The general reaction pathways possible with solid state synthetic methods. 36

1.13. Schematic representation of the CMKT method. 44

2.1. Schematic representation of CMKT used for generating a kinetically stable ternary structure in thin film form. 51

2.2. Annealing and nucleation in the CMM precursor. 52

2.3. Example Calibration Curve for Nb-Se CMM precursor. 55

2.4. Example of a plot of the supercell c-parameter versus the number of layers of the variable subunit. 57

2.5. Example of analysis for compositional ratios as determined by EPMA. 59

2.6. Image of the deposition system interior during operation. 61

2.7. Scale schematic diagrams of the evaporative deposition chamber. 61

Figure Page

2.8. Interference model of crystal diffraction. 62

2.9. Example of experimental XRR data 67

2.10. Simulations of XRR data showing the effects of various sample structures on the XRR pattern 68

2.11. Schematic of the X-ray crystallography experimental set-up used for structural characterization. 72

2.12. Summary of possible outcomes of the interaction between an incident beam of electrons and a thin, electron transparent specimen. 76

2.13. Schematic representation of a transimission electron microscope and ray trace diagrams. 79

2.14. Schematic representation of a scanning transmission electron microscope with a ray trace diagram. 82

3.1. Schematic diagram of the reaction path for formation of metastable intermediate phases from an amorphous precursor. 88

3.2. Reproduction of the copper-selenium binary phase diagram for compositions between 48% and 85% selenium. 92

3.3. DSC scans of co-deposited Cu-Se samples with compositions between 51% and 81% selenium performed at a heating rate of $4\,^{\circ}\mathrm{C\,min^{-1}}$. . 94

3.4. XRD data for the sample containing 51% selenium annealed to indicated temperatures in a DSC at a rate of $4\,^{\circ}\mathrm{C\,min^{-1}}$ and cooled. 96

3.5. XRD data for a sample containing 64% selenium and annealed in a DSC at a rate of $4\,^{\circ}\mathrm{C\,min^{-1}}$ to the indicated temperatures and cooled. . 97

3.6. XRD data for a sample containing 68% selenium and annealed to various temperatures in a DSC to the indicated temperatures and cooled. . 99

3.7. DSC scans for 67% selenium samples at heating rates of $4\,^{\circ}\mathrm{C\,min^{-1}}$ and $10\,^{\circ}\mathrm{C\,min^{-1}}$. 101

3.8. XRD patterns of 67% selenium samples heated at $4\,^{\circ}\mathrm{C\,min^{-1}}$ and $10\,^{\circ}\mathrm{C\,min^{-1}}$. 101

3.9. XRD data for a sample containing 66% selenium annealed to various temperatures at a DSC at a rate of $4\,^{\circ}\mathrm{C\,min^{-1}}$. 102

Figure Page

3.10. Kissinger plot used to derive the activation energy for nucleation of cubic $CuSe_2$. 103

4.1. The variation of the composition ratio and modulation wavelength of Cr-Se, and Cu-Cr binary films. 113

4.2. XRD data collected from Cu-Se films of various composition and modulation wavelength. 114

4.3. A summary of diffraction data on Cu-Se binary compositionally modulated multilayers. 115

4.4. Schematic representations of the three repeat layering schemes used to investigate the effect of layer repeat thickness and order on reaction pathway. 117

4.5. Representative XRD patterns for as-deposited films with waveform 3. . 118

4.6. Representative XRD patterns collected as a function of annealing temperature for films with waveform 3. 119

4.7. Schematic representations of the Cu-Cr-Se compositional waveforms used to study the formation of $CuCr_2Se_4$. 121

4.8. Powder diffraction pattern for representative Cu-Cr-Se samples using the $\varpi_{c,4}$ and $\varpi_{c,5}$ waveforms. 122

4.9. XRD and XRR patterns for a representative Cu-Cr-Se film with waveform 5 collected at different annealing temperatures. 124

4.10. XRD pattern for a representative Cu-Cr-Se film with waveform 5 annealed at 375 °C for 48 h and 600 °C for 1 h. 125

4.11. Rocking curves from the 222 reflection of $CuCr_2Se_4$ collected as a function of annealing temperature. 127

5.1. The variation of the composition ratio and modulation wavelength (λ_c) of Cr-Se, and Cu-Cr binary films. 136

5.2. The calibrated compositional waveform (ϖ_c) for $CuCr_2Se_4$. Layer thicknesses reported reflect the product of shutter time and deposition rates. 137

5.3. XRD and XRR data for the annealing of an ≈ 50 nm film of $CuCr_2Se_4$ between 30 °C and 600 °C. 138

5.4. XRD of a powder produced from an ≈ 200 nm thick film of $CuCr_2Se_4$. . 139

Figure Page

5.5. Aberration-corrected STEM-HAADF images and CBED pattern for a CMKT generated $CuCr_2Se_4$ film. 140

5.6. Temperature dependent resistivity data for a quartz supported $CuCr_2Se_4$ film. 142

5.7. Temperature dependent magnetization measurements for a supported $CuCr_2Se_4$ film. 143

5.8. Hysteresis loops for a supported $CuCr_2Se_4$ film at 5 K, 30 K, 60 K, 125 K and 175 K. 144

5.9. Temperature dependent coercivity and saturation magnetization a supported $CuCr_2Se_4$ film. 145

5.10. Hysteresis loops for a supported $CuCr_2Se_4$ film at 5 K collected perpendicular and parallel the plane of the substrate. 147

5.11. The E_{cryst} surfaces for the hexagonal, $R\bar{3}$, and cubic, $Fd\bar{3}m$ structures as functions of θ and ϕ using calculated anisotropy constants from the hysteresis curves. 151

6.1. High resolution STEM-HAADF image of $[\{(PbSe)_1\}_{1.00}(MoSe_2)_1]_r$ with aggregate intensity plot. 160

6.2. A schematic representation of the refined positions of the atomic planes along the c-axis of $[\{(PbSe)_1\}_{0.99}(WSe_2)_1]_r$. 161

6.3. High resolution STEM-HAADF image of $[\{(PbSe)_2\}_{1.00}(MoSe_2)_2]_r$ with aggregate intensity plot. 162

6.4. High resolution STEM-HAADF image of $[\{(PbSe)_2\}_{0.99}(WSe_2)_1]_r$ with aggregate intensity plot. 163

6.5. A schematic representation of the refined positions of the atomic planes along the c axis of $[\{(PbSe)_2\}_{0.99}(WSe_2)_2]_r$. 164

6.6. High resolution STEM-HAADF image of $[\{(PbSe)_3\}_{1.00}(MoSe_2)_3]_r$ with aggregate intensity plot. 166

6.7. A schematic representation of the refined position of the atomic planes along the c axis of $[\{(PbSe)_3\}_{0.99}(WSe_2)_3]_r$. 167

6.8. High resolution STEM-HAADF image of $[\{(PbSe)_4\}_{1.00}(MoSe_2)_4]_r$ with aggregate intensity plot. 168

6.9. A schematic representation of the refined position of the atomic planes along the c axis of $[\{(PbSe)_4\}_{0.99}(WSe_2)_4]_r$. 169

6.10. High resolution STEM-HAADF image of $[\{(PbSe)_5\}_{1.00}(MoSe_2)_5]_r$ with aggregate intensity plot. 170

6.11. A schematic representation of the refined position of the atomic planes along the c axis of $[\{(PbSe)_5\}_{0.99}(WSe_2)_5]_r$. 171

7.1. High resolution STEM-HAADF images of $[\{(PbSe)_m\}_{1.00}(MoSe_2)_n]_r$ compounds in the family $m = n$. 175

7.2. High resolution STEM-HAADF images of structural variants $(m, n) = (2, 2)$, $(3, 3)$, and $(3, 1)$ of $[\{(PbSe)_m\}_{1.00}(MoSe_2)_n]_r$. 176

7.3. XRD patterns acquired from structural variants $(m, n) = (3, 3)$, and $(3, 1)$ of $[\{(PbSe)_m\}_{1.00}(MoSe_2)_n]_r$. 178

7.4. The change in the magnitude of the PbSe lattice distortion with increasing layer thickness. 181

8.1. The proposed $[\{(FeSe)_1\}_{1+y}(NbSe_2)_1]_r$ structure. 184

8.2. Temperature dependent X-ray diffraction (XRD) study of the $[\{(FeSe)_1\}_{1+y}(NbSe_2)_1]_r$ compound. 188

8.3. Compositional waveforms (ϖ_c) for the (m, n)=$(1, 1)$, $(m, 1)$, $(1, n)$, and $(m = n)$ parameters of the $[\{(FeSe)_m\}_{1+y}(NbSe_2)_n]_r$ system. 190

8.4. XRD data for the for the $(m, 1)$, $(1, n)$ and $(m = n)$ families of the $[\{(FeSe)_m\}_{1+y}(NbSe_2)_n]_r$ compounds annealed at 200 °C. 191

8.5. Analysis of the dependance of m and n on the measured c-lattice parameter for the $(m, 1)$ and $(1, n)$ families of the $[\{(FeSe)_m\}_{1+y}(NbSe_2)_n]_r$ system. 192

8.6. XRR and XRD data collected normal to the substrate for the $(5, 1)$ member of the $[\{(FeSe)_m\}_{1+y}(NbSe_2)_n]_r$ family. 193

8.7. In-plane XRD for the $[\{(FeSe)_5\}_{1+y}(NbSe_2)_5]_r$ compound. 194

8.8. STEM-HAADF image of the $[\{(FeSe)_5\}_{1+y}(NbSe_2)_5]_r$ film. 195

8.9. STEM-EELS image of $[\{(FeSe)_5\}_{1+y}(NbSe_2)_5]_r$ film. 196

8.10. Schematic representation of the energy surface and reaction progress in a the precursor for a compositionally modulated kinetic trapping reaction. 197

9.1. Structural model of the proposed $[\{(NbSe_2)_3\}_{1+y}(CuCr_2Se_4)_1]_r$ layered intergrowth compound. 202

9.2. Possible variations to the base CMM used for the $(1,1)$ member of the $[\{(NbSe_2)_m\}_{1+y}(CuCr_2Se_4)_n]_r$ family of compounds 203

9.3. XRR data for the as deposited films in the $m = 1, 2, \ldots, 5$ members of the $[\{(NbSe_2)_m\}_{1+y}(CuCr_2Se_4)_1]_r$ family of compounds. 207

9.4. Regression analysis of the change in λ_c for the $m = 1, 2, \ldots, 5$ members of the $[\{(NbSe_2)_m\}_{1+y}(CuCr_2Se_4)_1]_r$ family of compounds. 208

9.5. Temperature dependent XRD study conducted on the $(1,1)$ member of the $[\{(NbSe_2)_m\}_{1+y}(CuCr_2Se_4)_1]_r$ family of compounds. 209

9.6. XRD pattern for the $(5,1)$ member of the $[\{(NbSe_2)_m\}_{1+y}(CuCr_2Se_4)_1]_r$ family of compounds. 211

9.7. In-plane XRD for the $[\{(NbSe_2)_5\}_{1+y}(CuCr_2Se_4)_1]_r$ compound. 212

9.8. XRD patterns for the $m = 1, 2, \ldots, 5$ members of the optimized $[\{(NbSe_2)_m\}_{1+y}(CuCr_2Se_4)_1]_r$ system. 213

9.9. Regression analysis of the change in c for the $m = 2, 3, 4, 5$ members of the $[\{(NbSe_2)_m\}_{1+y}(CuCr_2Se_4)_1]_r$ family of compounds. 214

9.10. STEM-HAADF image of the $m = 1, 2, 3, 4$ members of the $[\{(NbSe_2)_m\}_{1+y}(CuCr_2Se_4)_1]_r$ family of compounds. 215

9.11. STEM-HAADF image of the $[\{(NbSe_2)_5\}_{1+y}(CuCr_2Se_4)_1]_r$ compound showing segregated regions of $NbSe_2$ and $CuCr_2Se_4$. 216

B.1. Diffraction data and calculated diffraction profile for the $(1,1)$ compound of the $[\{(PbSe)_m\}_{0.99}(WSe_2)_n]_r$ family. 228

B.2. Diffraction data and calculated diffraction profile for the $(2,2)$ compound of the $[\{(PbSe)_m\}_{0.99}(WSe_2)_n]_r$ family. 229

B.3. Diffraction data and calculated diffraction profile for the $(3,3)$ compound of the $[\{(PbSe)_m\}_{0.99}(WSe_2)_n]_r$ family. 229

B.4. Diffraction data and calculated diffraction profile for the $(4,4)$ compound of the $[\{(PbSe)_m\}_{0.99}(WSe_2)_n]_r$ family. 230

Figure Page

B.5. Diffraction data and calculated diffraction profile for the $(5, 5)$ compound of the $[\{(PbSe)_m\}_{0.99}(WSe_2)_n]_r$ family. 230

E.1. Geometric derivation of Bragg's Law 243

E.2. Geometric derivation of Bragg's Law corrected for refraction 244

LIST OF TABLES

Table Page

1.1. Common substructures found in MLCs 12

1.2. Properties and Data for $CuCr_2Se_4$. 30

2.1. Relevant physical data for evaporative deposition of the elements in this work. 60

2.2. Summary of X-ray experimental parameters. 73

2.3. Summary of Electron Microprobe Analytical Parameters. 75

2.4. Mean atomic number for compounds considered in this work. 83

A.1. Notation for crystallographic planes and reflections in real and reciprocal space. 227

B.1. The refined lattice parameter and the fractional position of atomic planes along the c-axis for the compound $[\{(PbSe)_1\}_{0.99}(WSe_2)_1]_r$. 231

B.2. The refined lattice parameter and the fractional position of atomic planes along the c-axis for the compound $[\{(PbSe)_2\}_{0.99}(WSe_2)_2]_r$. 231

B.3. The refined lattice parameter and the fractional position of atomic planes along the c-axis for the compound $[\{(PbSe)_3\}_{0.99}(WSe_2)_3]_r$. 232

B.4. The refined lattice parameter and the fractional position of atomic planes along the c-axis for the compound $[\{(PbSe)_4\}_{0.99}(WSe_2)_4]_r$. 233

B.5. The refined lattice parameter and the fractional position of atomic planes along the c-axis for the compound $[\{(PbSe)_5\}_{0.99}(WSe_2)_5]_r$. 234

CHAPTER I

INTRODUCTION

1.1. Incommensurate Crystal Systems

In the early part of the twentieth century researchers began to study naturally occurring minerals[1–4], and later synthetic crystals[2,3,5–14], composed of intergrowths of two different crystal subunits. Initially these structures were considered to be single homogeneous phases[8], but were later shown to be complex intergrowths of two substructures, each having its own sublattice related to a bulk material[8]. The geological examples of these intergrowth structures include a number of different chemistries and and crystal geometries. Of particular interest to this work are the structures based on the tochilinite, $[(Fe_{1-x}S)_2]_{1-y}((Mg,M)(OH)_2)_1$[4,8,15,16], where $0.08 \leq x \leq 0.28$, $0.58 \leq y \leq 0.75$, and M = Al or Fe, cylindrite[1,4,8], $[(PbSb)S]_{2.28}NbS_2$, or franckeite[1,4,8], $(Pb_{1+y}Sb_yS)_{1.357}[Sn_{1+x}(Cu_2)_xS_2]$, motifs shown in Figure 1.1. The tochilinite structure contains an iron-deficient tetragonal FeS structure, similar to the mineral mackinawite, and a complex metal hydroxide, isostructural with the mineral Brucite[4,15,16]. The cylindrite structure is composed of alternating subunits of rocksalt-like bilayers having square pyramidal coordination about the metal centers, and hexagonal layers which are closely isostructural with the cadmium iodide structure[1,4,8]. Synthetic analogues to the geological intergrowth structures have been produced over a wide range of chemistries. Of particular interest are the structures of the MTX_3 type[1,4,8], reported on extensively by Rouxel[7,17,18], Meerchaut[9,10,17–20], Weigers[6,8,21,22], and others[3,5–14,16,17,23].

FIGURE 1.1. Geological examples of the MLC structural motif. (a) tochilinite ($[(Fe_{1-x}S)_2]_{1-y}((Mg,M)(OH)_2)_1$, $0.08 \leq x \leq 0.28$, $0.58 \leq y \leq 0.75$, and M = Al or Fe). (b) cylindrite ($[(PbSb)S]_{2.28}NbS_2$). (c) franckeite ($((Pb_{1+y}Sb_yS)_{1.357}[Sn_{1+x}(Cu_2)_xS_2]$).)

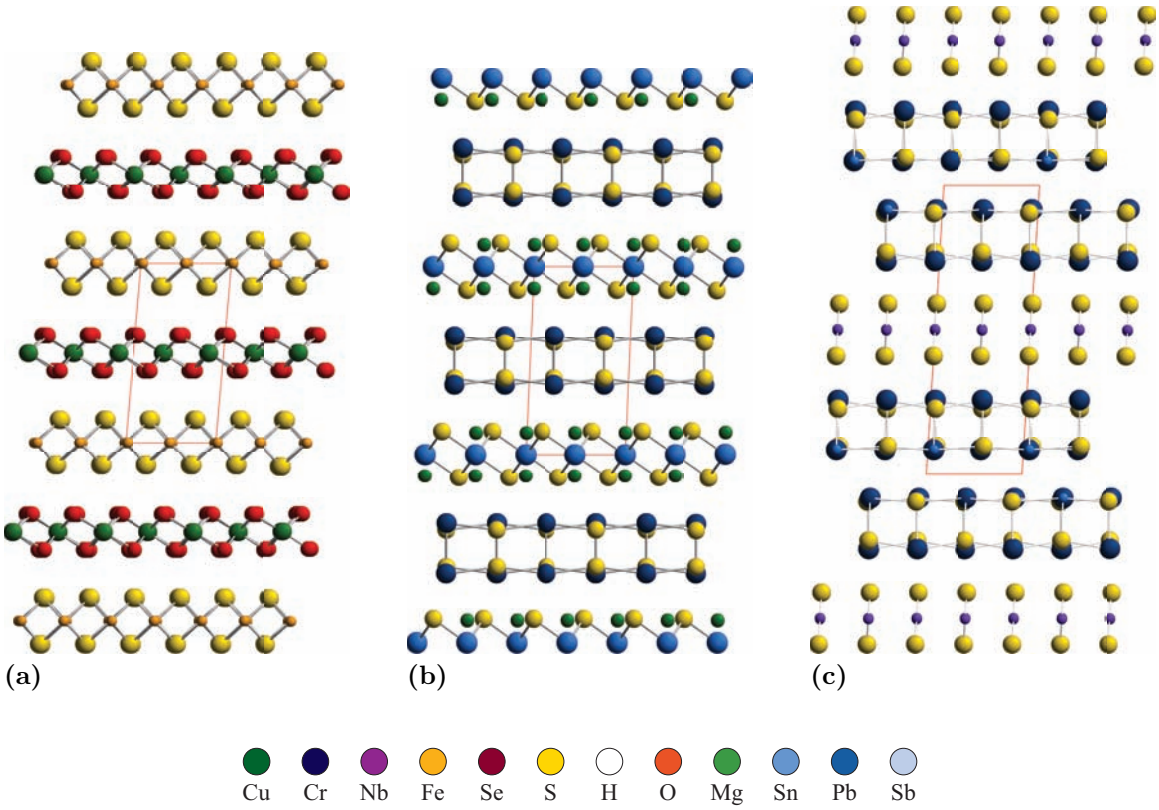

One of the most significant challenges early on for these intergrowth crystal systems was the solving of the structures from diffraction data[5,6,22,23]. Beginning in the 1990s with the work of van Smaalen[3,5,6,22,23], the crystal structures were solved for some systems which shed light on these unique crystal structures. Before van Smaalen's work, attempts to solve the structure of intergrowth compounds using standard 3D crystal theory were unsuccessful[1,3,6]. The problem arose from the mismatch, or misfit, of the incommensurate component of the crystal relative to the conventional 3D lattice. Van Smaalen's contribution was the introduction of superspace crystal theory, allowing for structures to be solved by incorporating additional dimensions into the lattice refinement to account for the mutual modulation of the two substructures[5,22]. Through the application of superspace refinements a number of different classes of incommensurate structures were described[3–5]. Of particular interest to this work are those intergrowth compounds which have been given the name MLCs. These structures are so named because the supercell consists of alternating layers of two incommensurate substructures, sharing a common axis normal to the layers, but exhibiting lattice mismatch between the lattice vectors of the substructures in the plane of the interface[3–5,8]. This work will be based in this class of intergrowth compounds. For the purposes of consistency, the common axis normal to the layered substructures will be denoted the c axis, and the axes in the plane of the incommensurate interfaces between the substructures the a and b axes.

1.2. Overview of Misfit Layer Compounds

MLCs were first identified in the literature as single-phase ternary compounds of stoichimetry, MTX_3, where M represents cations of elements tin, antimony, lead or bismuth, T cations of first- and second-row transition metals, and X anions

of a chalcogen, most commonly sulfur[3,8]. Diffraction patterns for powders of the compounds were shown to closely resemble those of an equimolar mixture of the corresponding binary compounds MX and TX_2 [2,3,8], resulting in the initial assumption that these were intimate mixtures of the two structures[3,8]. This assumption resulted in a new notation: $(MX)_mTX_2$, where the parameter m was used to capture the ratio between the cations[3,8]. The discovery of $FeCl_3$intercalated graphite, a layered compound featuring an incommensurate relationship between the layers, led to the re-examining of the MTX_3 compounds, which were determined to be the intergrowths of two distinct crystal structures[3,8]. Structures were proposed for crystal systems with closely matched a and b lattice parameters[3,8], or employed large, but finite, integer approximations of the supercell lattice vectors to attempt to capture the incommensurability of the crystal systems[3,8]. This incommensurability of the MLCs was a significant problem until it was quantified by van Smaalen, et al.[5,22,24] which allowed for the structures to be fully solved. Van Smaalen was able to refine the structure of the MLC by incorporating additional dimensions into the unit cell, resulting in a superspace refinement. During his work on the misfit structural refinement, van Smaalen proposed a series of criteria to describe a MLC: first, the structures can be approximated by a collection of translationally symmetric ordinary crystals[5], which this work refers to as subsystems or substructures; second, these substructures have voids into which the other subsystem fits. The combination of these two subsystems creates an incommensurate composite crystal that requires additional dimensionality to capture the mutual modulation of the two crystal subsystems[5]. In his exhaustive review, Wiegers outlines some interesting consequences of considering MLCs according to these criteria. First, the length ratio of the incommensurate lattice vectors determines the overall composition of the crystal

structure. Because the crystal composition is tied to the lattice vectors, it is also temperature dependent[8]. Another consequence of the solving of these and similar incommensurate structures was the need to redefine what constituted a crystal[8]. Van Smaalen pointed out that misfit structures are still crystalline, despite the short range disorder, because of the long range periodicity of the structures[5]. However, because the structures did not follow the classic definition of a crystal, the International Union of Crystallography (IUCr) definition for a crystal in aperiodic systems was changed to "any solid having an essentially discrete diffraction diagram[4]."

Naturally occurring examples of MLCs appear in the form of the previously mentioned cylindrites and franckeites[1,4,15]. The presence of geological specimens indicate that the misfit structure is kinetically stable on geological time scales, putting them in the same class of naturally occurring metastable compounds as diamond[1,4,15]. Naturally occurring misfit structures and their synthetic analogues demonstrate a number of common structural elements. First they typically incorporate a rock-salt-structured substructure[2,3,8] and a layered compound featuring van der Waals inter-layer bonding, e.g. TX_2[2,3,8]. Exceptions to this pairing of structures include the MLC $(Pb_2FeS_3)_{0.58}NbS_2$[10] and those produced by Kabbour and Cario[19,20,25–30]. Second the solved compounds tend to share a common crystal axis, by convention the a axis, in the plane of the inter-structural interface and are incommensurate with respect only to the second (conventionally the b) axis[8]. If both substructures of a MLC $(MX)_mTX_2$ are characterized by lattice vectors a_{MX}, b_{MX}, c_{MX} and $a_{TX_2}, b_{TX_2}, c_{TX_2}$[8], respectively then $a_{MX} \parallel a_{TX_2}$ but $a_{MX} \neq a_{TX_2}$, b_{MX} is equal and parallel to b_{TX_2}, as shown in Figure 1.2. The misfit in the system can then be reduced to a_{TX_2}/a_{MX}. The lattice vectors c_{MX} and c_{TX_2} do not participate in the mutual modulation of the subsystems, each being of one unit cell thickness. In the case of MLCs, the quantity

a_{TX_2}/a_{MX} is irrational and requires either the use of an average structure in the a-axis direction or the inclusion of additional dimensions to capture the misfit of the structure during refinement[8]. Were mutual modulation to exist along the b-axis, as exhibited by synthetic MLCs, additional superspace dimensions would be required for structural refinement[5,8,22].

MLCs have exhibited electrical conductivities ranging from insulating to superconducting. Compounds containing titanium, niobium, or tantalum in the TX_2 layer have been shown to be metallic[6,8], while those containing chromium have been shown to be semiconducting[6,8]. Further, compounds containing niobium or tantalum have been shown to be superconducting below $\approx 7\,\mathrm{K}$[6,8]. Compounds bearing a lanthanide in the MX layer have been shown to range from insulating[6,8] to semiconducting[6,8], depending upon the TX_2 compound in the structure. These compounds have also been show to exhibit both ferro- and ferrimagnetism[6,8], while the compound $(SmS)_mTaS_2$ has been shown to be antiferromagnetic[6,8]. A number of structurally related compounds in the tungsten and molybdenum families have also been shown to exhibit exceptionally low thermal conductivities for condensed matter, approaching that of air[13,14,31], and have been the subject of research in thermoelectric applications. A particular hallmark of these compounds is anisotropy in the observed properties. For example, in general, the electrical conductivity parallel to the c-axis is significantly enhanced when compared to the values perpendicular to the c-axis[6,8]. Likewise, the phonon scattering and thermal conductivity values are much lower and higher along the c-axis direction[6,8] respectively.

A number of the electrical properties, especially those tied to the lanthanide-bearing systems, have been shown through calculation to be dependent on the interlayer communication between substructures[6,9]. This communication mechanism

is also tied to the mechanisms for structural stabilization in the MLCs. The exact mechanism for the structural stability of these compounds is still an open question with significant debate in the literature. There are currently two competing theories as to the stabilizing mechanisms for these structures[2,6]. In the case of compounds incorporating lanthanide cations, Abramov proposes that the structures are stabilized via formal charge transfer between the two substructures[7,26,32,33]. This particular model also proposes that stabilization in non-lanthanide bearing systems is accomplished through lone pair electrons on the metal centers in the d_z orbitals[32,33] which the author indicates is the stabilizing force that induces metastable rock salt structures such as SnS[32,33]. There have been significant data put forth in the form of molecular dynamics and density functional theory calculations to support this theory[7,26,32,33]. The second proposed model suggests that the two subsystems are not mutually exclusive, and that stabilization of the overall structure is accomplished through cross-doping of the two substructures[12]. The cross-doping results in an electrostatic interaction and increase in entropy which work to stabilize the structure[12]. Estimates for the levels of doping in these systems range for 5% to 20%[12]. While there are those that propose one or the other of the two models discussed here, the exact mode of stabilization for a MLC is probably dependent on the chemistries of the two components and their ability to communicate via charge transfer or accept dopant atoms from the other substructure. This complication makes a general rule for the stabilizing mechanism in misfit structures difficult to determine.

FIGURE 1.2. Schematic representation of the classic MLC. Using the unit cells of the component substructures to illustrate the mismatch between the respective *a*-lattice vectors.

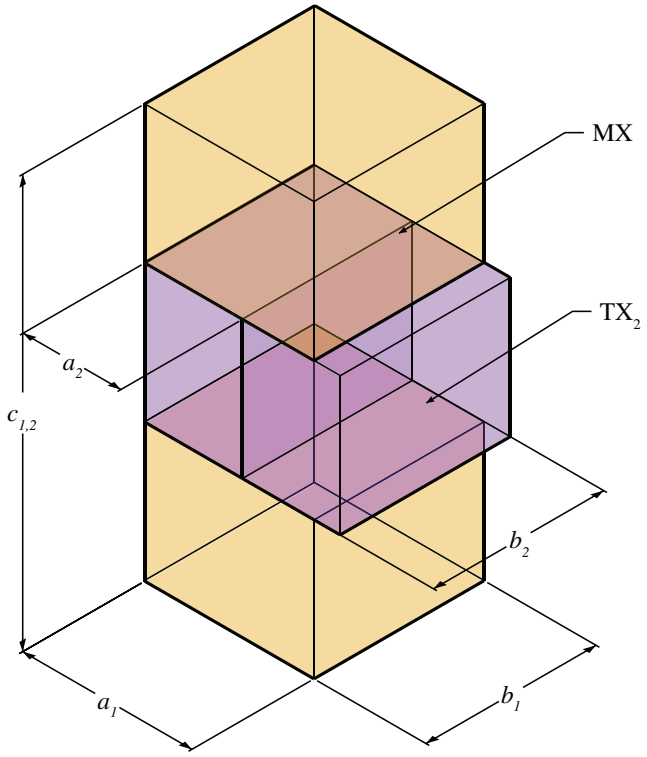

1.3. Current Misfit Layer Compounds and Composite Systems

To date there are a limited number of synthetic MLCs. The elements found in these systems are summarized in Figure 1.3. Systems made using traditional thermodynamic routes have been, not surprisingly, limited to synthetic analogues of the geological cylindrite and franckeites structures. These substructures are summarized in Table 1.1. All these structures, with the exception of the bismuth and antimony selenides, use the same transition metal dichalcogenide and rock salt structured subunits, i.e. $[\{(MX)_m\}_{1+y}(TX_2)_n]_r$ or $(m,n)^*$, that are found in the geological structures[4,6,8]. These structures are further categorized by their inability to form anything above the first order rock salt intercalates of the possible crystal combinations, i.e. $(m,n) = (1,1)$, $(1,2)$, and $(1,3)$[33]. The one apparent exception to these statements is the $(Pb_2FeS_3)_{0.58}NbS_2$ structure detailed by LaFond in 1999[10]. Closer inspection of the structure demonstrates that interface regions of the (Pb_2FeS_3) substructure are isostructural with a PbS rock salt structure. Since the structure presented to the NbS_2 substructure is no different than what would be present in a hypothetical $(PbS)_mNbS_2$ misfit, this structure could be considered a special example of the standard $[\{(MX)_m\}_{1+y}(TX_2)_1]_r$ MLCs. This case does, however, present an interesting insight into the stabilization of MLCs. It is apparent from the case of $(Pb_2FeS_3)_{0.58}NbS_2$ that it is possible to change the internal structure of a subunit for a stable MLC without effecting the stability of the overall structure, so long as the interface between the two substructures remains relatively unchanged.

Recent work on designed crystals using the same building blocks as MLCs has yielded several interesting systems that share attributes with the prototypical MLCs cylindrite and franckeite. Starting in 1996[31,34–40], designed

*See Appendix A for a detailed description of the nomenclature used in this work.

compounds using alternating layers of the same TX_2 crystal structure with different cations, i.e. $(TiSe_2)_m(NbSe_2)_n$, $(NbSe_2)_m(CrSe_2)_n$, and $(VSe_2)_m(TaSe_2)_n$, were attempted yielding new examples of incommensurate crystal structures. This designed chalcogenide misfit structure concept was later continued with the synthesis of the novel $[(Bi_xSb_{1-x})_2Te_3)]_m[(TiTe_2)_{1.36}]_n$ [41], $[PbSe)_m]_{1+y}(MoSe_2)_n$ [13] and $[PbSe)_m]_{1+y}(WSe_2)_n$ [14] misfit systems. Alternative chemistries were also explored by Kabbour and Cario who demonstrated designed mixed chacogenides incorporating rock salt, fluorite, and perovskite structural units[19,20,25–30]. In both the work at the University of Oregon and the work of Kabbour et al. the element of designed systems was employed. Nguyen goes so far as to describe the concept as crystal engineering[40]. Kabbour and Cario detail a system of rational design based on the incorporation of energy minimization calculations to chemical intuition driven design[29]. An interesting and fundamental difference in the two design processes is which mechanism for structural stabilization is chosen to drive the rational design process. Kabbour et al. designed their crystals as formal charge balanced systems with slab-like cation and anion stacking. This rationale resulted in a more formal bond between layers[29], analogous to the charge transfer seen in lanthanide MLCs. The group at the University of Oregon assumed internal charge balancing within each substructure and electrostatic interaction between the layers[40]. A common theme to both groups research however, is that the design and tailoring of MLCs provides a very rich area for research and advancement.

A second, implicit, theme of the work by the two groups is that the MLCs seem to exhibit a modularity, suggesting a more diverse and rich chemistry than is currently available. The work by LaFond on the compound $(Pb_2FeS_3)_{0.58}NbS_2$, where the substructure interfaces approximate a $(PbS)_mNbS_2$ structure, suggests that

by maintaining a stable interface, like that between the MX and TX_2 structures it is possible to create more structurally diverse MLCs. The work by Kabbour et al. and the previous work at the University of Oregon indicate that the internal structure of the compound must be itself stable, or stabilized by the incorporation into the multilayer structure, i.e. SnS in $(SnS)_m(TaS_2)_n$. Examining the naturally occurring MLCs and the previous synthetic efforts a number of potential candidates for exploring the modular nature of the misfit structure can be identified: First the compound $NbSe_2$ has already appeared in a number of previous studies[6,9,10,17,38,39]. There are also examples of structural analogues to the tetragonal α-FeSe also appearing in misfit type structures[4,15,16]. Together these present one possible new synthetic MLC, $[\{(FeSe)_m\}_{1+y}(NbSe_2)_n]_r$. Recent work by Bettinger et al.[42] suggests that the spinel-structured compound $CuCr_2Se_4$ grows with a preferred {111} texture, indicating that there is a particularly stable crystallographic orientation which might be used to stabilize a multilayer structure. This suggests that one might incorporate such a spinel structured compound into a misfit layer in place of a rock salt structured compound, i.e. $[\{(NbSe_2)_m\}_{1+y}(CuCr_2Se_4)_n]_r$, where a layered compound is used to further stabilize the interface. In the following sections, each of these materials will be reviewed to provide a context for the later discussion of the proposed MLCs.

1.4. Iron (II) Selenide

Iron (II) Selenide, FeSe, was first reported in the literature in 1933 by Hagg and Kindstrom[43] in the German journal *Zeitschrift fur physikalische Chemie*. Later work on the structure would report it as ferro- or ferrimagnetic depending on the concentration of Se in the structure. Originally the structure was researched as an interlayer between semiconductors and metallic layers, and later as a possible spin

FIGURE 1.3. The periodic table showing elements that have been incorporated into MLCs.

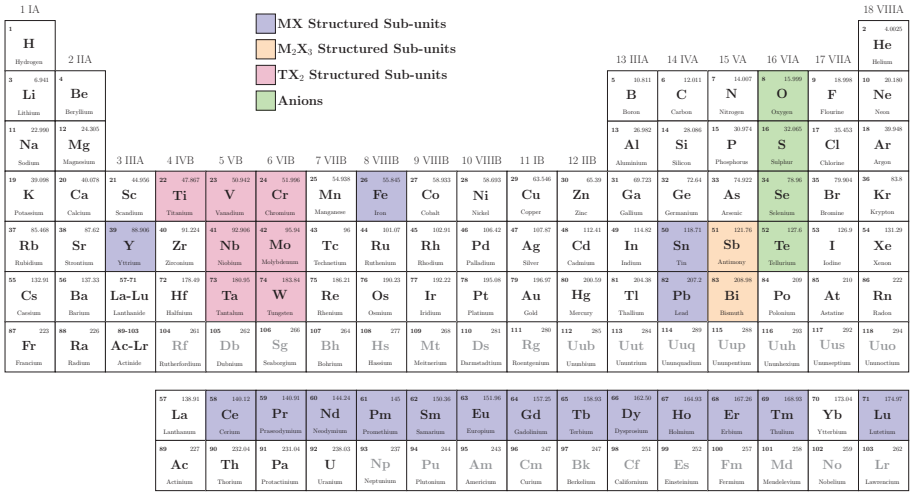

TABLE 1.1. Common substructures found in MLCs where X is a general chalogenide anion (S, Se, or Te), Ln can be a single lanthanide species (Ce,Er,Gd,La,Nd, or Sm).

Component	Prototype	Space Group	Properties
PbX	NaCl	$Fm3m$	Semiconductor
BiX	NaCl	$Fm3m$	Semiconductor
SnX	NaCl	$Fm3m$	Semiconductor
LnX	NaCl	$Fm3m$	Metallic
MoX_2	MoS_2	$P\overline{3}m1$	Semiconductor
VX_2	MoS_2	$P\overline{3}m1$	Semiconductor
WX_2	MoS_2	$P\overline{3}m1$	Semiconductor
NbX_2	MoS_2	$P\overline{3}m1$	Metallic
CrX_2	MoS_2	$P\overline{3}m1$	Metallic
Bi_2X_3	Bi_2Te_3	$R\overline{3}m$	Semiconductor
Sb_2X_3	Bi_2Te_3	$R\overline{3}m$	Semiconductor

FIGURE 1.4. The crystal structure of the $(Pb_2FeS_3)_{0.58}NbS_2$ MLC.

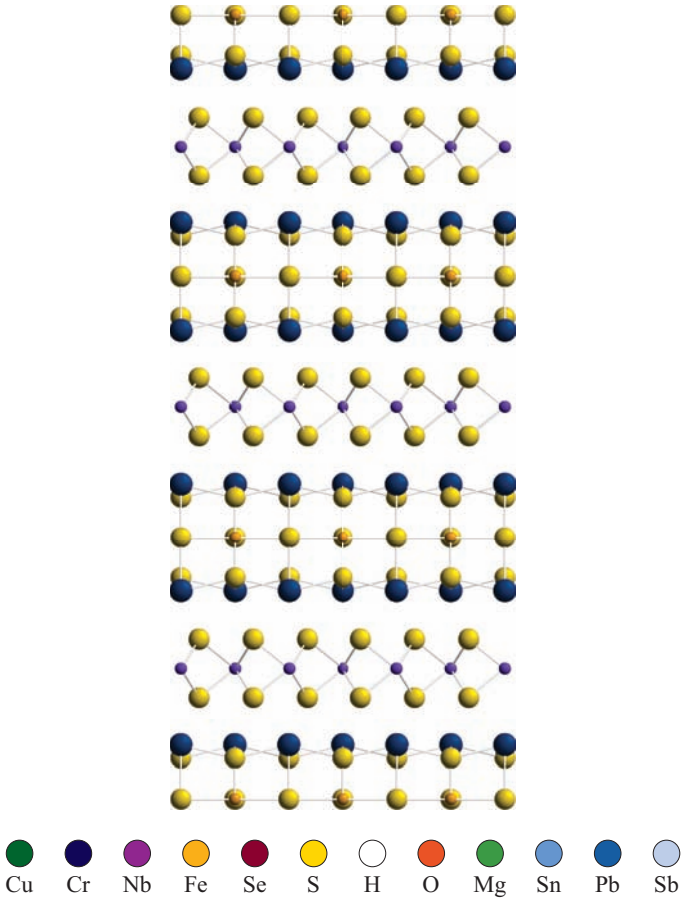

injection layer for spintronic applications. In 2008, Hsu et al. discovered that the structure would become superconducting below 8 K. The structure has to date been synthesized by a number of bulk, thin film, and nanoscale wet prep methods.

1.4.1. Structure and Polymorphism

In their 1933 work, *Rontgenuntersuchung am System Eisen-Selen*, Hagg, et al.[43] describe two polymorphs of the FeSe structure at or near the stoichiometric 1:1 ratio. The first of these is the tetragonal, PbO type ($P4/nmm$), later described more correctly as anti-PbO[44]. Indicated as α-FeSe by Jain, et al.[45], this structure has been the primary focus of the research in the system. The second compound is an orthorhombic structure based on the ($P6_3/mmc$) structure indicated as β-FeSe by Jain, et al.[45]. While the body of this work will focus on the α-FeSecompound, for comparison purposes a summary of the structures for both compounds will be included here.

The tetragonal α-FeSephase, pictured in Figure 1.5., consists of Se-Fe-Se trilayer sheets with a van der Waals type gap separating them. The structure is anti-PbO, having the Fe^{2+} cations at the center of edge sharing Se^{2-} tetrahedra. The structure shows a preferred growth orientation normal to the c-axis of the structure, forming in a sheet by sheet fashion[46]. Crystals of the structure form in hexagonal plates and thin films form with a $\{001\}$ texture. The complete crystal structure data is presented in Appendix D The α-$Fe_{1+x}Se$ structure has been formed from near stoichiometric $x = 0.01$ to Se deficient $x = 0.2$.

The β-phase, shown in Figure 1.5., is an orthorhombic crystal with the NiAs ($P6_3/mmc$) structure. β-FeSe is a continuous structure with octahedrally coordinated Fe^{2+} at the center of point sharing Se^{2-} octahedra. Literature[47] indicates that

FIGURE 1.5. The α-FeSe, (a), and β-FeSe, (a), crystal structures.

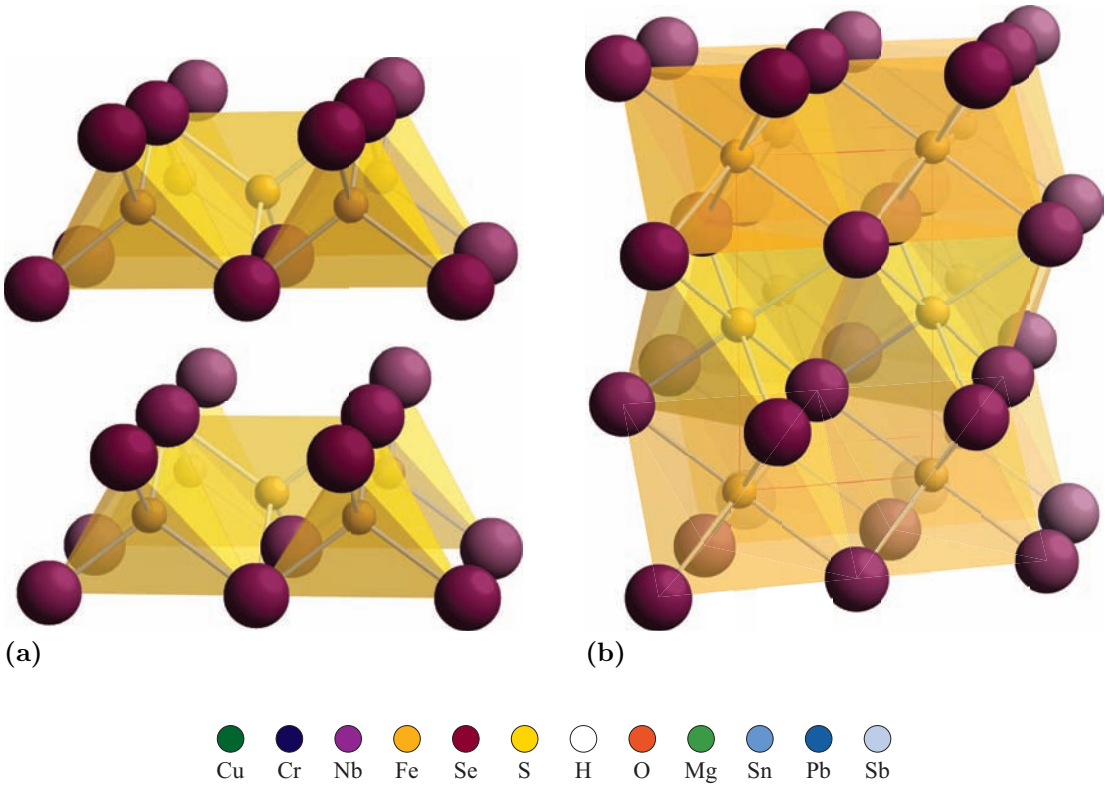

this structure is nonstoichiometric, being an Se deficient Fe_7Se_8. β-$FeSe_{1+x}$ is a high-temperature phase that can be stabilized at room temperature by making the structure slightly Se-rich.

1.4.2. Electronic Structure and Properties

The interest in the Fe-Se system to date has largely been focused on the α-FeSe structure with its recently reported superconductivity[48–54] and well documented ferromagnetism[45,46,50,55–62]. Compositionally dependent electrical and magnetic measurements conducted on FeSe have demonstrated a sensitivity between the observed properties and small fluctuations in the Fe to Se ratio[50,51,63]. This sensitivity is also complicated by the possibility for oxygen contamination during synthesis

or recrystallization[51]. These complications have, in -part, been mitigated by the use of theoretical calculations of the compounds' optimized physical and electronic structures. Given the wide range of reported values for various properties, this section will defer to the theoretical calculations for the baseline electronic properties of α-FeSe and report empirical measurements where warranted.

To date there are a number of theoretical studies on the structure of α-FeSe, this discussion uses two primarily: the work by Subdei, et. al.[64], which uses a non-spin polarized calculation and a structure derived from experimentally determined literature values, and the work by Wu, et. al.[44], that employs lattice parameters derived from an internally generated sample and spin-polarized calculations. Supplementary information will be provided by the 2009 work by Li, et al.[50], and an earlier 2007 work by Wu[65]. Comparison of the electronic structures of the spin-polarized and non-spin polarized from the two studies, reproduced in Figure 1.6., show a general agreement in the overall structure. Comparing the states contributed by the Fe and Se atoms in the non-polarized DOS histogram, selenium p states are seen predominately above and below the Fermi level, with the iron d states clustered at and just above the Fermi level[64]. The main conduction mechanism for the material is through the iron-iron interactions within the a-b planes of the crystal[64] as indicated by the states contributed by Fe to the total DOS for the system near the Fermi level. The spin polarized DOS diagram for the ideal structure demonstrates a high degree of symmetry between the spin up and spin down electrons. This would suggest that the perfect structure is in fact nonmagnetic, which has led to the working theory that the ferromagnetic properties of the crystal arise from the defect structure[44]. Work by Li, et al.[50] has demonstrated that the magnetic ordering in the structure is dependent on selenium concentration, with the magnetic ordering only appearing around selenium

vacancies, supporting the results of the other calculations. Compounds created by McQueen, et al.[51] have demonstrated that a slight selenium deficiency is required for optimum crystal structure, further supporting the hypothesis presented by Wu, et al.[44]. The calculated band structures of the stoichiometric[50] and selenium-deficient[50] structures indicate that both are metallic, but that the conduction mechanism changes as the defect density increases. The van der Pauw measurements and calculations by Wu[65], on the stoichiometric structure demonstrate a metallic two carrier mechanism with the structure exhibiting n-type conduction below 185 K and p-type conduction above this point. The selenium-deficient structure studied by Li[50] demonstrates a half metallic structure with overall ferromagnetic character, but local antiferromagnetic coupling between iron centers.

In 2008 Hsu, et al.[48], announced the discovery of superconductivity in α-FeSe. The actual superconducting properties of the material were not remarkable, a Curie temperature (T_C) in the range of 8 K and H_{c2} of 16 T, but its shared structural elements with a family of recently discovered high temperature superconductors made it an interesting target for understanding the superconductivity in this type of structure. The mechanism for superconductivity of α-FeSe, while extensively studied, is still not clear. Research to date has demonstrated that the highest, non-constrained T_C is obtained with slightly selenium-deficient samples[51]. Work by Margadonna in 2008[66] and Wu in 2009[46] have shown that the onset of superconductivity in the unconstrained structure is accompanied by a slight positive shift, on the order of 1°, in the angle away from 90°. Doping studies, also conducted by Wu in 2009[46], prohibited this shift in the γ angle of the crystal which resulted in a suppression of superconductivity in the structure. Compression studies of α-FeSe along the c-axis of the crystal demonstrated an increase in the T_C to 40 K at 8 GPa to 10 GPa[52,55,66].

Pressure dependent diffraction studies by Margadonna, et al[66], indicate that the distortion seen in the unconstrained film is stabilized at higher temperatures by the compression of the structure. It has also been demonstrated that doping can increase the onset temperature T_C of superconductivity. The structure $FeSe_{1-x}S_x$ $x = 0.02$ gives a T_C of $\approx 16\,K$[67]. $FeSe_{1-x}Te_x$ $x = 0.25$ results in a T_C of $\approx 15\,K$ for the unconstrained structures.

1.4.3. Syntheses

Compounds in the Fe-Se system have been synthesized by a number of different methods. A discussion of the relevant points of the more common methods is undertaken here. A more detailed description of solid state synthesis as it pertains to misfit structures is provided in Section 1.7.

Direct solid state reactions for powders and single crystals are conducted in evacuated quartz ampules and have been performed with and without reaction aids. Direct reaction of the powders follows the basic Formula 1.1:

$$Fe + Se \xrightarrow[1075\,^{\circ}C,72\,h]{\text{vacuum}} FeSe \qquad \text{(Formula 1.1)}$$

This reaction can be supplemented by the incorporation of a potassium bromide or potassium iodide reaction aid as a flux as in Formula 1.2[46,68]:

$$Fe + Se \xrightarrow[1075\,^{\circ}C,72\,h]{\text{vacuum, K-salt Flux}} FeSe \qquad \text{(Formula 1.2)}$$

It was noted by McQueen[51] that the powder reactions are extremely sensitive to oxygen content and will produce iron oxide and free iron impurities. Physical vapor

FIGURE 1.6. The aggregate, (a), and spin polarized, (b), density of states for α-FeSe.

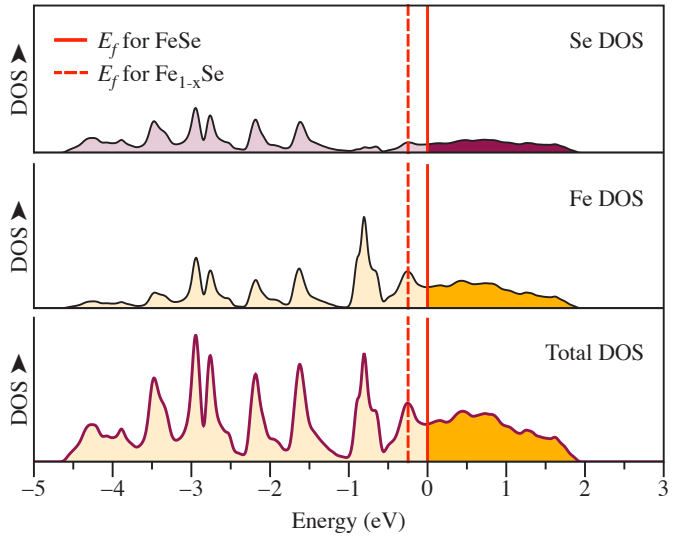

(a)

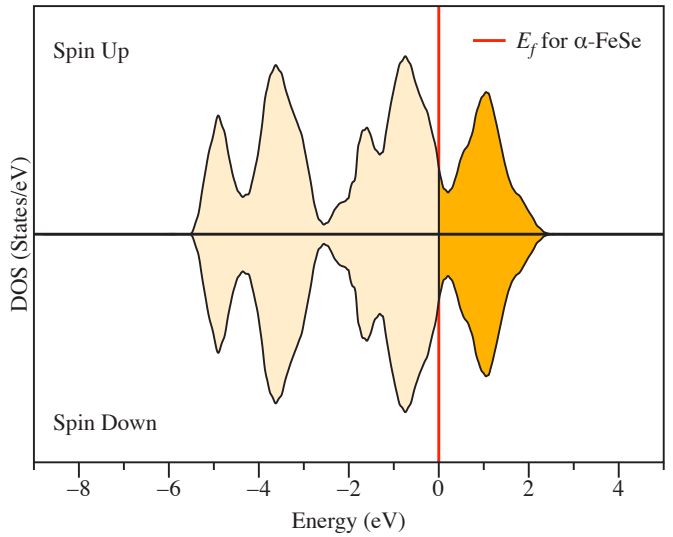

(b)

transport reactions for producing single crystal were also successful[54]:

$$\mathrm{Fe} + \mathrm{Se} \xrightleftharpoons{\mathrm{FeSe_x}\uparrow} \mathrm{FeSe} \qquad \text{(Formula 1.3)}$$

A fourth preparation method involving the mechanical alloying of iron and selenium by ball milling[69,70] has produced single phase powders via Formula 1.4.

$$\mathrm{Fe} + \mathrm{Se} \xrightarrow[\text{ball mill, } 20\,\mathrm{h}]{\mathrm{Ar}} \mathrm{FeSe} \qquad \text{(Formula 1.4)}$$

To produce thin films a number of methods were employed, the most common of which is the selenization of deposited iron films by molecular beam epitaxy (MBE). Selenium from a molecular beam is directed at an evaporated iron film heated to $\approx$670 K[56–59,62]. Films produced in this manner have been noted to be of poor quality with large impurity concentrations[58,59], which is thought to be a consequence of a concentration gradient from the surface into the film. Good quality films with low impurity concentrations have also been produced by codeposition of iron and selenium via MBE[71]. Films have also been grown by chemical vapor deposition (CVD) using iron pentacarbonyl and hydrogen selenide at 332 °C as in Formula 1.5[59]:

$$\mathrm{Fe(CO)_5}\uparrow + \mathrm{H_2Se}\uparrow \xrightarrow[\approx 7\,\mathrm{nm\,min^{-1}}]{332\,^\circ\mathrm{C}} \mathrm{FeSe} \qquad \text{(Formula 1.5)}$$

Finally films have been successfully deposited using physical vapor transport (PVT) of pressed powder pellets[46,71].

1.5. Niobium (IV) Selenide

Transition metal dichalcogenide compounds are layered structures based on hexagonal stacking of metal and chalcogen atoms in an octahedral or trigonal prismatic structure[72]. TX_2 compounds are members of a class of structures that have a van der Waals gap, in this case between double layers of chalcogen atoms[72,73]. There are additional examples in the TX_2 family that are non-layered structures based on similar stacking pattern with the exception of the van der Waals gap being filled with an additional cation layer[74]. The TX_2 compounds exhibit a broad range of electronic, mechanical, optical and thermal properties, most of which exhibit a pronounced anisotropy corresponding with the anisotropy of the structure[72,74,75]. Niobium (IV) selenide, a member of the TX_2 family, has been studied since the early part of the 20th century[72,74,75]. The compound has been found to be metallic and superconducting at temperatures below 7 K[72,74,75]. The structure has been successfully synthesized via direct reaction of elemental precursors and vapor transport methods.

1.5.1. Structure and Polytypes

Layered transition metal dichalcogenide compounds are hexagonal structures sharing the $P6_3/mmc$ space group[74]. Qualitatively the structure is formed by trilayers of hexagonally packed chalcogen atoms and transition metal atoms using a layer ordering: AbA or AbC[74]. Minor variations of the T-X bond angles for different cation species result in octahedral, trigonal prismatic, in both a formal and distorted coordination about the metal center[74]. The X-T-X trilayers are weakly bound to each other via weak van der Waals (VDW) type interactions[72–74]. Crystal growth for this structure is highly anisotropic favoring the *c*-axis, forming in plate-like crystals and growing in a sheet-by-sheet pattern[72]. Preferred rotational orientation of individual

FIGURE 1.7. Structure of the transition metal dichalcogenide $NbSe_2$.

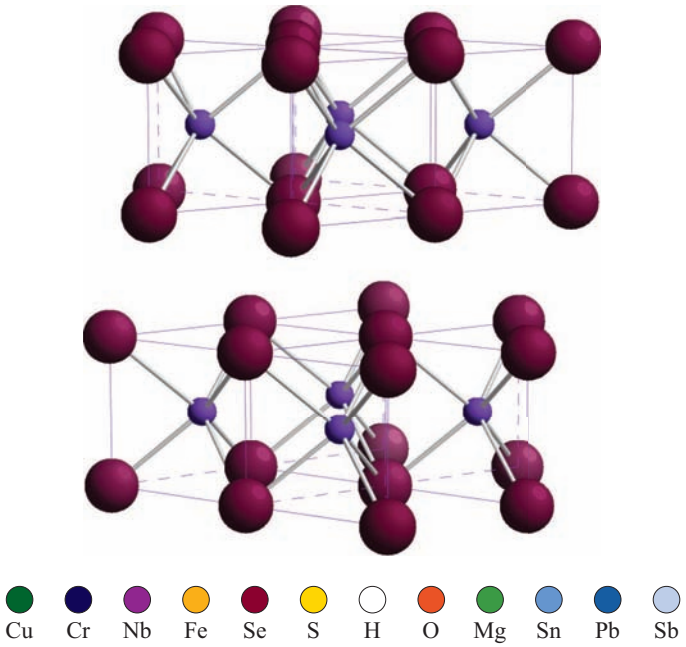

trilayers about the common *c*-axis results in a number of polymorphs within each crystal system[72–74,76]. This polymorphism dependent on small variations in the stoichiometry of the compound and has resulted in the identification of ≈ 12 different polymorphs to date[73,76]. TX_2 type structures have been shown to act as effective hosts for intercalation chemistry[77]. First row transition metals, alkalis, and alkaline earths can all intercalate into the octahedral interstices of the VDW gaps for the structure[77]. Titanium is the only exception, which will intercalate only minimally into TX_2 structures[77]. Because of the weak interaction between trilayers, TX_2 compounds can "intercalate" with secondary structures resulting in superlattices and the misfit layer type structures previously discussed[8].

1.5.2. Electronic Structure and Properties

Transition metal dichalcogenide, or TX_2, type structures have electrical properties[74,76,78,79] that range from semiconducting through to metallic and superconducting. $NbSe_2$ exhibits metallic conductivity and is superconducting below $\approx 7\,K$[74]. Most of the recent work on the material has focused on reducing the dimensionality of the $NbSe_2$ crystal structure through the creation nanotubes or other nanoscale structures[76,80], the study of the materials intercalation chemistry[75,77], and the study of charge density wave phenomenon[76,80]. Most of the general work on the electronic structure was completed prior to 2000[74,75,78,81,82], which will be the focus of this section.

The electronic structure of the material is dominated by the anisotropy of the $NbSe_2$ unit cell. This is apparent in the density of states histogram, Figure 1.8.. The density of states below the Fermi level consist mostly of the selenium $4p$-states, while at and above the Fermi level the states are dominated by the $4d$-states of niobium[80]. The high density of states at the Fermi level, which are dominated by the d_{z^2} orbitals of niobium, indicates that the material is metallic[80]. Because of the position of the Fermi level in the d_{z^2} orbital alterations to the electronic structure by intercalation or by pressure result in a decrease of the critical temperature[80]. This decrease in T_C occurs because in the un-intercalated state the Fermi level is located at the maximum of the d_{z^2} band. Intercalation induced charge transfer causes the Fermi level to shift away from this maximum, reducing the number of states at the Fermi level, $N(E_F)$[77]. Likewise, calculations have shown that constraining the unit cell along the c-direction results in a shift of the Fermi level and narrowing of the d_{z^2} band, resulting in a similar decrease in $N(E_F)$[77]. It is the decrease in $N(E_F)$ that results in the suppression of T_C, as predicted by BCS theory[83,84].

FIGURE 1.8. Density of states for $NbSe_2$.

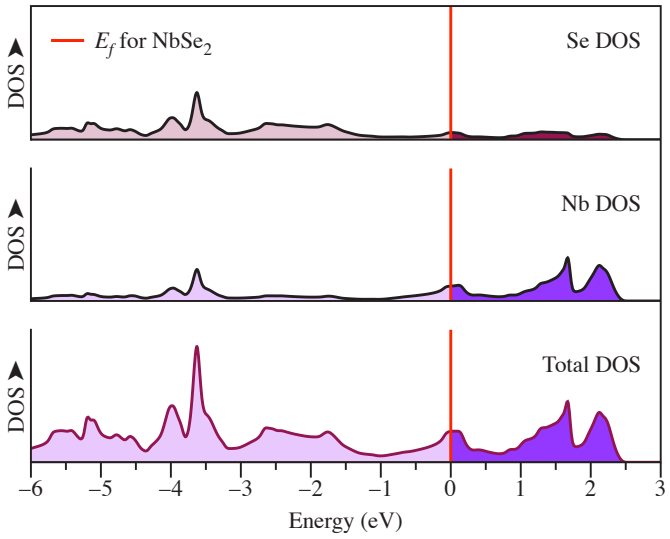

1.5.3. Syntheses

TX_2 structures, including $NbSe_2$, have been synthesized via standard reaction of powders of the elemental constituents, as well as chemical vapor transport (CVT) and PVT methods[72,74,85]. Powders of the compound are produced by direct elemental reaction at high temperatures for times on the order of 10s of hours[72], as indicated in Formula 1.6.

$$\mathrm{Nb} + 2\,\mathrm{Se} \xrightarrow[1000\,^{\circ}\mathrm{C},30\,\mathrm{h}]{\text{vacuum}} \mathrm{NbSe_2} \qquad \text{(Formula 1.6)}$$

Single crystals are typically grown by CVT using bromine and iodine as transport agents[72,80,85].

$$\mathrm{NbSe_2} + \mathrm{I}\uparrow \underset{12\,\mathrm{h}}{\overset{\approx 900\,^{\circ}\mathrm{C},\approx 700\,^{\circ}\mathrm{C}}{\rightleftharpoons}} \mathrm{NbI_x}\uparrow + 2\,\mathrm{Se}\uparrow \qquad \text{(Formula 1.7)}$$

This technique has also been used to refine previously grown raw crystals to remove defects[72,80,85]. Thin films have been made by pulsed laser deposition (PLD) and

evaporative deposition[86] from elemental reagents[86]. PVT deposited films were made from pressed powder pellets and typically resulted in chalcogen-deficient compounds[86]. These films required post-deposition annealing in a selenium-rich atmosphere to rebalance the stoichiometry[86]. Evaporative deposition and diffusion of elemental reagents resulted in single-phase films with no additional annealing beyond the initial reaction[86].

1.6. Copper Selenochromite

Spinels are a class of crystal structure with a diverse chemistry. Von Philpsborn[87,88], in 1970, indicated over 300 known examples in the literature of a spinel-structured phase incorporating a chalcogenide anion. Throughout the literature, compounds with properties ranging from insulating to metallic and including semiconducting, superconducting, ferromagnetic, ferroelectric and magneto-optical activity have been reported[87]. The spinel-structured copper selenochromite phase, $CuCr_2Se_4$, was first documented by Hahn in 1956[89]. The compound has been studied extensively over the years and is noteworthy for its high T_C of $\approx 430\,\mathrm{K}$[42,87,90,91] and magneto-optical activity[92]. It was originally investigated only as a member of the ACr_2X_4 family of compounds, where A is generally* a divalent transition metal cation and X is a chalcogen anion, which contained a number of magnetic semiconductor compounds[90,91,93–96]. $CuCr_2Se_4$ was later adopted in and of itself as a material of interest for spintronic applications due to its half-metallic structure and magneto-optical characteristics. To date the compound has been synthesized via direct elemental reaction, direct reaction of halide salts, vapor transport, and in nanoparticle form through precipitation.

*See Section 1.6.2. for a discussion around the issue of the valence of copper in $CuCr_2Se_4$.

FIGURE 1.9. A cross section of known compounds AB_2X_4, featuring divalent cations A^{2+}, trivalent cations B^{3+}, and divalent anions X^{2-}, that adopt the spinel structure.

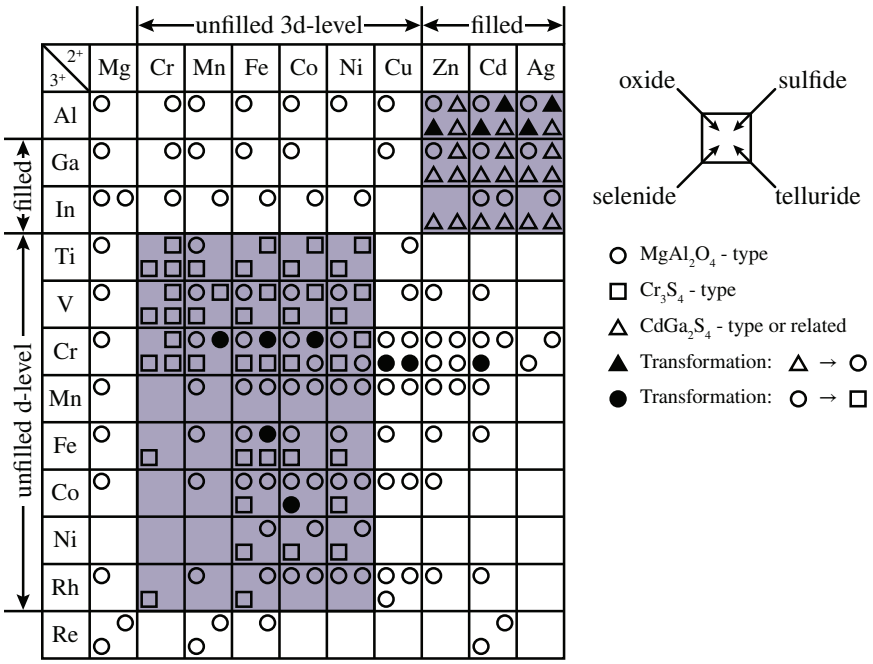

1.6.1. Structure

Copper selenochromite was initially described by Hahn[89] as being a spinel-structured compound, with the $Fd\bar{3}m$ space group. To first order, spinels can be visualized as a face-centered cubic (f.c.c.) selenium lattice where trivalent cations, Cr^{3+}, occupies a fourth of the available octahedral interstices and divalent cations, Cu^{2+}, an eighth of the available tetrahedral interstices[83,84,87]. For $CuCr_2Se_4$, as for the vast majority of spinels, the positions of the anions deviate, consistent with $Fd\bar{3}m$ symmetry, from a perfect f.c.c. array ($u_\circ = 0.25$) by the amount needed to properly coordinate the tetrahedral cation species in the lattice, resulting in a value of $u_{iso} \approx 0.29$ for selenium. As is the case with many of the spinel structures, $CuCr_2Se_4$ can accept dopants on the A, B, and X sites of the structure. The A site seems to accept dopants up to 20 mol% after which the structure destabilizes and changes

symmetry[87,90,94,96]. This shift is typically from a tetrahedral coordination on the A site to an octahedral one which results in a change in space group to $Im3m$[87,94]. The B site has been successfully doped with most of the first row transition metals[87,90,94,96]. With the exception of titanium[87,94], the structure can be fully substituted with other cations from this row without structural destabilization allowing for the formation of solid solutions involving the B-site cations[87,94]. The X site has been successfully doped with the other chalcogenide species and two component solid solutions using different chalcogenides have been created[87,94]. Doping of X site with halogens have also been successful and has been an area of major research in recent years[97–100]. The anion lattice will accept both chlorine and bromine substitutions[97–100] but no iodine substitutions have been reported to date. This may be due to the size mismatch between the selenide and iodide anions[101,102], which has apparently been leveraged for metal halide and CVT syntheses of the structure as demonstrated in Subsection 1.6.3.

1.6.2. Electronic Structure and Properties

The electronic structure of $CuCr_2Se_4$ has been the subject of controversy over the years. The controversy arose over the formal valences of the cation species in the material. The initial model for the valence in $CuCr_2Se_4$ was proposed by Goodenough in a colloquium talk given at the University of Paris in 1965[103]. Goodenough's model proposed that $CuCr_2Se_4$ was best described by a $Cu^{2+}[Cr^{3+}]_2Se_4^{2-}$, with the observed metallic conduction arising from the delocalization of the 3d electrons of the tetrahedrally coordinated copper[103] and the magnetism arising from a ferrimagnetic alignment of the chromium d-electrons. Lotgering and van Stapele[91] later proposed a competing, and simpler, model that assigned copper a 1^+ valance

FIGURE 1.10. The literature structure for $CuCr_2Se_4$. The structure has an $Fd\bar{3}m$ space group, based on a nearly f.c.c. Se sublattice with Cu occupying tetrahedral sites and Cr occupying octahedral sites in the Se matrix.

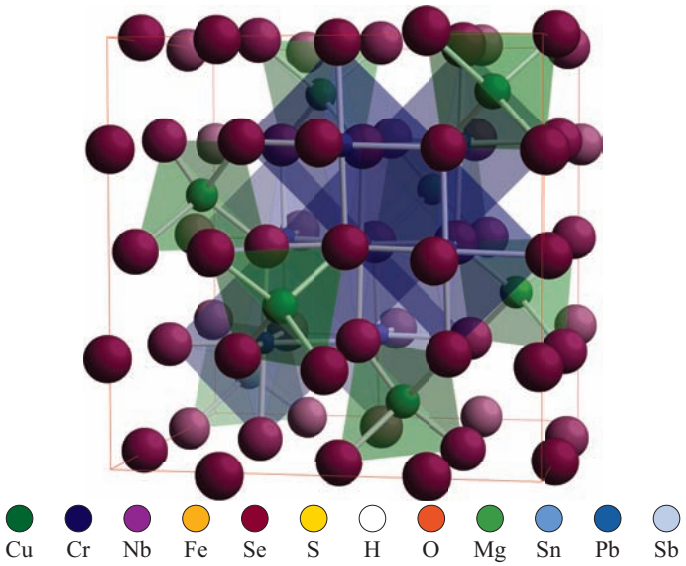

and placed chromium with an equal mixture of 3^+ and 4^+ valence centers, i.e. $Cu^{1+}[Cr^{3+}Cr^{4+}]Se_4^{2-}$, which makes the system a formal ferromagnet. This debate has gone back and forth over the years until recent work with X-ray photoelectron spectroscopy (XPS)[104] and soft X-ray absorption[105] led to the general consensus among the community around a modification of the original Goodenough model. The model was actually originally proposed by Lotgering and van Stapele[106] after their first model[106], but is recently attributed to Kimura[105]. This model assigns a 3^+ valence to the chromium cations, a 1^+ valence to the Cu cations, the charge balance in the system comes from a hole introduced into the selenium $4p$-states[105]: $Cu^{1+}[Cr^{3+}]_2\square^{+1}Se_4^{2-}$. Recent band structure calculations have shown this model to provide the best agreement with the various measurements to date[42,92,97,107–109].

Most of the literature related to electronic structure has focused on spin polarized calculations. These studies have focused on the elucidation of the valences of the

cations, with the more recent work being instrumental in the building consensus around the Kimura model. These recent calculations have also provided insights into the structure and conduction mechanisms in the material. Figure 1.11. shows the spin-polarized density of states for $CuCr_2Se_4$ as calculated by Bettinger, et al.[42] In the majority carriers copper $3d$-states can be seen to be mixed with the selenium $4p$-states. Hybridization between the selenium $4p$ and chromium $3d$ result in an octahedral crystal field splitting with the t_{2g} and e_g states on each side of the Fermi level, roughly equidistant. A small number of selenium $4p$-states are found between the chromium t_{2g} and e_g roughly straddling the Fermi level. The minority carriers have similar features with the exceptions that the minority chromium t_{2g} and e_g states reside significantly above the Fermi level, and the minority selenium $4p$-states reside in one continuous band which reaches to slightly over the Fermi level. As a consequence of the DOS structure around the Fermi level, the structure is best described as a half-metal, though as Wang, et al.[107], point out the presence of a small finite number of minority carriers about the Fermi level precludes it from being formally classified as half-metallic.

Much of the interest around $CuCr_2Se_4$ has been because of its exceptional magnetic properties. The material has been shown to demonstrate the highest T_C recorded for the chalcochromite spinels and also demonstrates a magneto-optical Kerr effect with respect to infrared light. The T_C for $CuCr_2Se_4$ is typically quoted as $460\,\mathrm{K}$[109], but work with powders and nanoparticles of various sizes[42,109–111] has indicated that there is a size dependence to the strength of magnetic ordering in the film, which can also act to suppress the T_C. A summary of the available size dependent data for various properties is provided in Table 1.2. In the bulk, the overall magnetization has been quoted in the range of $5\,\mu_B$. Within the Kimura model, this

FIGURE 1.11. The spin polarized density of states for $CuCr_2Se_4$.

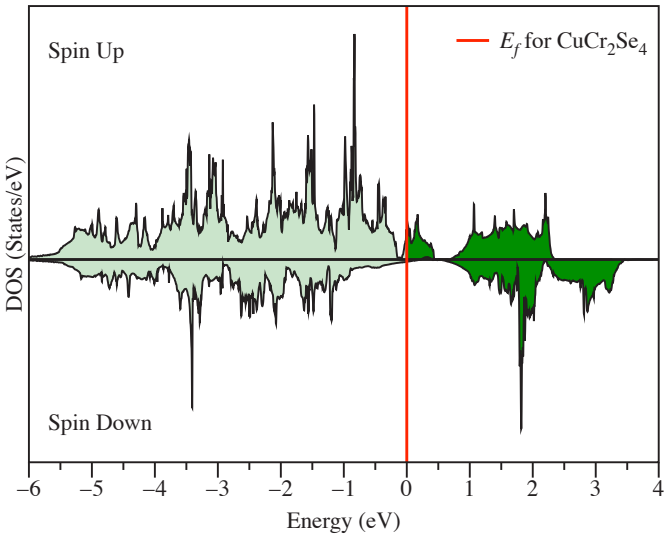

TABLE 1.2. Properties and Data For $CuCr_2Se_4$.

Morphology	Property		Reference
Nanocrystalline	Curie Temperature	(462 ± 6) K	109–111
	Curie Constant	(4.8 ± 0.2) K	110,111
	Magnetic Moment (total)	$2.8\,\mu_B$	110,111
	Magnetic Moment (Cr)	$(4.4 \pm 0.1)\,\mu_B$	110,111
Polycrystalline	Curie Temperature	(433 ± 5) K	109
	Magnetic Moment (total)		
Thin Film	Curie Temperature	>400 K	42
	Magnetic Moment (total)	$\approx 5\,\mu_B$	42

can be explained as $3\,\mu_B$ assigned to each chromium center and a $-1\,\mu_B$ assigned to each hole, which is assumed to become fully spin polarized at low temperatures.

1.6.3. Syntheses

There have been a number of different preparations for $CuCr_2Se_4$ over the years. The first synthesis available was by reaction of prepared binary precursors under

vacuum for between 300 h and 700 h, again, by Hahn[89] (Formula 1.8).

$$Cr_2Se_x + CuSe_x \xrightarrow[600\,^\circ C to 800\,^\circ C]{\text{vacuum}} CuCr_2Se_4 \qquad \text{(Formula 1.8)}$$

Hahn's paper indicated that direct reaction of the elemental reagents was problematic, forming a heterogeneous mixture of binary phases rather than the desired ternary.

Other preparations for the compound have included direct reaction of elemental reagents[42,90,94,98,110,112]. Despite the problems indicated by Hahn, this has been the most prevalent method for the production of powders and is summarized in Formula 1.9.

$$Cu + 2\,Cr + 4\,Se \xrightarrow[600\,^\circ C to 800\,^\circ C,\ >100\,h]{\text{vacuum}} CuCr_2Se_4 \qquad \text{(Formula 1.9)}$$

CVD methods from melts using halogen transport agents (Formula 1.10) have been used extensively to create single crystal specimens and the halogen doped compounds of recent interest[94,99,100,102,113].

$$CuCr_2Se_4(poly) \xrightarrow[630\,^\circ C,\ 24\,h]{I_2,\text{ or } CuCl_3} CuCr_2Se_4(single) \qquad \text{(Formula 1.10)}$$

A related technique that has had limited use is the direct reaction of halogen and other metal salts using the formation of soluble metal halides a flux[114] (Formula 1.11).

$$Cu + 2\,Cr + 4\,Se \xrightarrow[\text{wash in } H_2O]{CuI_2,\text{ vacuum } 600\,^\circ C,\ 6\,h} CuCr_2Se_4 \qquad \text{(Formula 1.11)}$$

Nano[111,115–117]- and micro[109,118,119]-crystalline powders have been prepared by precipitation from solutions of copper and chromium salts or organometallic complexes using a number of different selenium sources and solvents. Of these the reactions employing stearate (OSt) salts in mineral oil (nujol)[118] (Formula 1.12),

halogen and acetate (OAc) salts in polyol[115] (Formula 1.13), and chloride salts in oleylamine (OLA)[117] (Formula 1.14) are the most common.

$$\mathrm{Cu(OSt)_2 + 2\,Cr(OSt)_3 + 4\,Se \xrightarrow[330\,^\circ\mathrm{C},\ 8\,\mathrm{h}]{\text{nujol}} CuCr_2Se_4} \qquad \text{(Formula 1.12)}$$

$$\mathrm{CuCl + Cr(OAc)_3 + Se \xrightarrow[\text{Ar,600}\,^\circ\mathrm{C},\ 5\,\mathrm{h}]{\text{polyol, Ar, Microwave}} CuCr_2Se_4\ (50\,nm)} \qquad \text{(Formula 1.13)}$$

$$\begin{aligned} \mathrm{CuCl + 2\,CrCl_3 + OLA(excess)} &\xrightarrow{\text{Ar, }150\,^\circ\mathrm{C}} \mathrm{CuCr(OLA)_x} \\ \mathrm{Se + OLA(excess)} &\xrightarrow{\text{Ar, }330\,^\circ\mathrm{C}} \mathrm{Se(OLA)_x} \\ \mathrm{CuCr(OLA)_x + Se(OLA)_x} &\xrightarrow[\text{(2) Ar, }200\,^\circ\mathrm{C}\text{ aging}]{\text{(1) Ar, }200\,^\circ\mathrm{C},\ 2\,\mathrm{h}} \mathrm{CuCr_2Se_4(OLA)_x} \end{aligned} \qquad \text{(Formula 1.14)}$$

To date, thin film depositions and syntheses have been conducted on single-crystal substrates of silicon, sapphire, and $MgAl_2O_4$ using two techniques. The earliest was co-deposition of the elemental sources on a heated substrate to produce an amorphous thin film[120]. This film was then annealed using the same conditions as powder synthesis to produce a thin film on the order of 2 µm thickness. The second technique is the use of a ceramic target prepared from powders made by one of the previous methods and a pulsed laser deposition system[42,112]. The film is grown on a heated substrate, but typically requires additional annealing to form $CuCr_2Se_4$[42,112,120]. This method has the additional complication of an apparent loss of copper during deposition, which requires careful calibration[42].

1.7. Solid State Synthesis and Deposition Methodologies

This section discusses various synthetic methods available to solid state chemists and their relative advantages. In general, solid state reactions are difficult to consider mechanistically[121] for a number of reasons. Bonding in solid state systems can be more labile than in the organic and organometallic systems. Also, during the reaction

process bonds are in a constant state of flux which makes constructing mechanisms like those possible for organic reactions problematic. Last, reaction conditions themselves are not conducive to elucidation of reaction mechanisms: high temperatures, long reaction times, and high pressures, all with heterogeneous mixtures and multiple simultaneous reaction pathways that make monitoring the reaction progress a non-trivial exercise[121]. Under these conditions, trying to generate a reaction mechanism for a solid state reaction is problematic at best, and more generally impractical to undertake[121].

While it is impractical to consider detailed solid-state reaction mechanisms, it is possible to consider the general thermodynamics of the reaction pathways and gain an understanding of what is happening in the reaction. Solid-state reactions have two prospective rate-limiting factors, the diffusion of the reagents through the product and the nucleation of the products for a given composition[37,122,123]. The relative contributions of these two factors has been explored through the use of diffusion couples which are large scale approximations of the interface in a solid state reaction. In bulk diffusion couples the reaction rapidly becomes limited by the time needed for new reagents to diffuse through the product layer[37,122,123]. Because of this diffusion limit, a concentration gradient of the two reactants is formed moving away from the interface[37,122,123]. Diffusion-limited reactions will generally give a heterogeneous product distribution with the major product being the most thermodynamically stable[37,122,123]. These types of reactions typically will require multiple cycles of mixing and heating to product a single phase material.

The other situation is where the reaction is limited by the nucleation energetics. In studies of thin film diffusion couples, where the thickness of the reactant layers was made sufficiently small that the reaction is not diffusion limited, the reaction

was shown to follow a completely different path[37,122,123] from the bulk reaction. These reactions were shown to pass through an amorphous intermediate of constant composition rather than producing a product layer with a composition gradient leading away from the interface[37,122,123]. In this situation the reaction is limited by the formation of a nucleus of sufficient size to overcome its surface energetics and allow growth of a product[37,122,123]. The resulting products in such cases were shown to be limited by the activation energies of the possible products for a given stoichiometry[37,122,123].

If we consider solid state reaction from the standpoint of the free energy surface and the desired product on that surface, three distinct types of situations can be considered: First, the desired product is the thermodynamically stable product, i.e., the lowest point on the free energy surface, with no intermediate phases. Second, the desired product is still the thermodynamically stable product, but there are possible intermediate phases, i.e., local free energy minima, along the reaction surface. Third, the desired product is one of the local free energy minima along the reaction path for a more complex thermodynamically stable product. If the desired product is the thermodynamically stable product with no intermediate phases, the precursor state of the system is at a higher overall free energy than the product or end state. Regions of the mixture that can overcome the nucleation energy for the system proceed directly to the final product in an overall exothermic reaction[11,34,37,122–125]. These reactions are characterized by quick reaction rates and the formation of a single product[11,34,37,122–125]. When the desired product is the thermodynamically stable product but there are possible intermediate phases along reaction path, the reaction products tend to be heterogeneous with no way to separate the products. This heterogeneity is typical of multicomponent solid state reactions[11,34,37,122–125].

These reactions progress initially in the same manner as the first type, but the initial energy input results in formation of high energy reaction intermediate. The path from this high energy state to the thermodynamic minimum passes through a number of local energy minima, each corresponding to a metastable intermediate product[11,34,37,122–125]. These secondary products must decompose to produce the desired final product, which can be a rate limiting step in the reaction depending on the stability of the intermediate phases[11,34,37,122–125]. The last case is where the desired product is one of the intermediate phases along the reaction path for a more complex thermodynamic product. This case is common in designed systems where the precursor is designed at a high energy condition near the desired local minima[11,34,37,122–125]. A small energy input into such systems results in the reaction becoming trapped in the local minimum, which results in the formation of the desired metastable product[11,34,37,122–125]. In cases such as these careful control over the energy input into the system so as not to not provide sufficient energy to overcome the activation energy of the desired product, which will result in the reaction progressing to the thermodynamic minimum.

The balance of this section will contain an examination of the common synthesis methods employed to produce MLCs and the individual compounds of interest for this study. Where applicable or possible, this examination will relate back to the overall thermodynamic themes presented here.

1.7.1. Direct Reactions

Direct reactions represent the most common method for solid state syntheses. Reactions of this type use powders, compacts or films which are reacted at high temperatures for long times to produce the desired product(s)[126]. These reactions

FIGURE 1.12. The general reaction pathways possible with solid state synthetic methods. (a) The reactants move directly to the products without any stable intermediate phases. (b) The products move through a local energy minima, resulting in a metastable intermediate product which must be decomposed to react the thermodynamic product. (c) The desired product is the metastable product, requiring the reaction to be halted before it can proceed to the thermodynamic product(s).

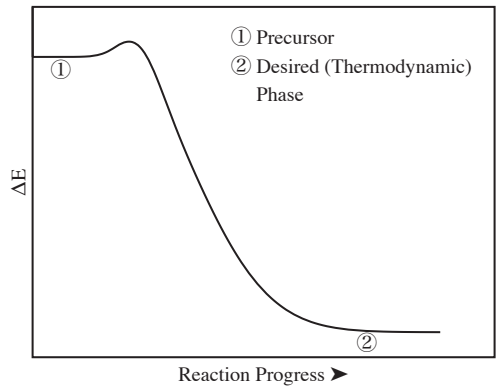

(a)

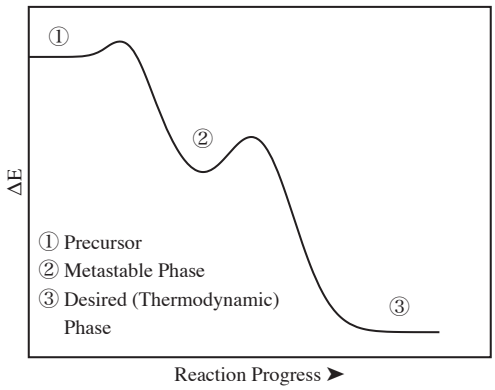

(b)

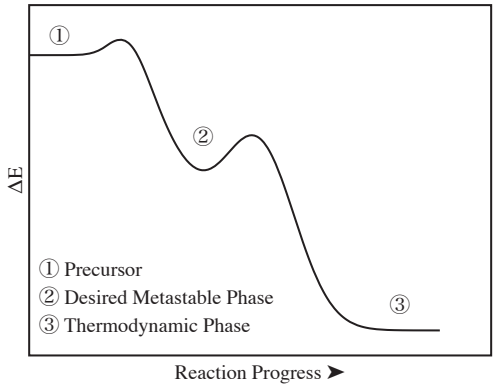

(c)

progress via interdiffusion of reagents or the formation of a melt, representing diffusion-limited reactions where fluxes or other reaction aids are used to overcome the diffusion limit[121]. In most cases these reactions tend to require multiple heat-mixing cycles to complete the reaction of the reagents and produce only thermodynamically stable products[121,126]. For this work the discussion of this topic will be limited to two different cases for this type of reaction: the two component (binary) system, and the case of three or more components (e.g., ternary or quaternary systems).

Binary reactions are solid state reactions of A and B to form desired product AB. The possible products from this reaction are a distribution of stable phase of the form AB_x, where x is limited by charge balance. In these reactions the reaction rate is limited either by diffusion or nucleation[121,122]. The diffusion rate is limited by time and temperature, and also by surface area[121–123,125]. It is the interplay of these three factors that result in the diffusion limited reaction kinetics normally ascribed to solid state synthesis for powders or thick films. The exact nucleation rate dependence for a particular product is complex and depends on the crystal structures and orientations of the precursors relative to the structure of the desired product. An additional concern is the energetic favorability of formation of nuclei of sufficient size to allow the formation of the product on a measurable scale[121–123,125]. As indicated previously, diffusion results in concentration gradients on both sides of the reaction interface. These gradients produce all stable products on the phase diagram during the course of the reaction[121–123,125]. Work by Fister[122] indicates that for a given temperature, it is possible to remove the diffusion imposed reaction rate limit by changing the length scales of the precursors, the result being faster reactions or lower reaction temperatures[122,123,125]. This change in dimensionality can be accomplished either through smaller particle sizes for powders, which increase the surface area of the

reactants, or through the shrinking of film thicknesses in multilayer precursors to remove diffusion rates as a limiting factor[122,123,125].

Ternary systems, i.e. solid state reactions of A, B, and C to form desired product ABC, represent a significantly more complex set of problems than those found in binary reactions. It can be easily seen that for ternary systems the number of possible products is significantly increased. The possible product distribution for these systems are all stable products of $A_xB_yC_z$ where x, y, z are again only limited by charge balance. For ternary and larger systems the reaction rate is limited again by diffusion of reactants and nucleation, as is the case with binary systems, but also by the added complexity introduced by the relative stability of any binary intermediate phases. The formation and decomposition of metastable binary phases can be a rate limiting step in the course of a reaction[34–37,122,123,127]. Binary products may have high activation energies which require high temperatures to overcome[34–37,122,123,127]. In direct reactions, the temperature and time required to decompose the metastable binary intermediates results in only thermodynamically stable ternary products being produced[34–37,122,123,127].

Reaction aids are a common method for enhancing basic reactivity in direct reactions[114,121,126]. The premise of their use is to incorporate an extra element or compound into the reaction system that enhances the reactivity of the reactants or produces unstable intermediate phases[114,121,126]. The aid and product must be easily separated and the aid must not appreciably dope or contaminate the system[114,121,126]. For chalcogenide systems, metal halides and halogens are common reaction aids[114,126]. Chalcogenide salts are commonly soluble in metal halide fluxes[114,126], which effectively increase the surface area for the formation of the product and allows the reaction to progress at a lower temperature and in less time[114,126]. Washing the product mixture

in a carefully chosen solvent removes metal halide flux, leaving a pure powder[114,126]. The widespread use of this technique for chalcogenide salts has lead to a number of different reviews summarizing the more widespread synthetic protocols, providing the appropriate halides and solvents for the formation of the more common chalcogenide salts[114,126].

Based in the literature to date there are a few general statements about direct reactions that can be made. First, more elements in a given reaction results in more complexity, which means it is less likely to produce a single-phase product via a single direct reaction. Second, the production of single phase products for ternary or higher systems requires high temperatures and long reaction times if stable binaries exist within the possible products for that ternary system. Third, reaction times and temperatures can be reduced by increasing the surface area of the precursor interfaces or introduction of a reaction aid. Last, because of the increased complexity introduced by the previous statements, accessing metastable or engineered products involving more than three elements by direct reaction is problematic if not impossible.

1.7.2. Chemical Vapor Techniques

For the purposes of this work, chemical vapor techniques are considered to include either CVT or PVT, CVD or atomic layer deposition (ALD). CVT/PVT has been used for many years for the growth or purification of single crystals and the growth of thin films[128–130]. The technique uses the formation of a volatile intermediate to transport precursor components to a different location in the reaction vessel where they are deposited[128–130]. CVD and ALD are used for the deposition of thin films and employs volatile organometallic precursors and gasses which decompose or react to produce a coating on the desired surface[128–130]. ALD, in some ways a subset of

CVD, is also used for deposition of thin films. The technique also uses organometallic precursors and gasses to deposit a film on the desired surface, but with the major difference being the introduction of the reactants is sequential, rather then concurrent, to prevent uncontrolled reactions of the reagent gasses. This sequential deposition results in a monolayer-by-monolayer growth mechanism unique to ALD[128–130].

For this work, CVT and PVT will be considered here in more detail. For these techniques, the reaction charge is placed at one end of a long quartz tube, which is then evacuated and sealed at both ends[130]. For CVT, the reaction charge consists of a transport agent (halogens, halides, oxides, etc.) and the reagents or raw crystal to be refined[130]. The transport agent for the reaction is selected to form volatile intermediates with the components of the desired product in the charge. These unstable intermediate phases are then decomposed at the far end of the reaction vessel to deposit the final product[130]. For PVT, the needed volatile intermediates are formed directly from the precursor material itself[130]. The reaction employs a multi-zone furnace, where the precursor mixture and growth regions are kept at different temperatures. In the resulting thermal gradient, the volatile phases act as phase transport agents, transporting desired components from the region of the vessel containing the reaction charge to the growth region where they are deposited as the desired product[130]. A side effect of this method is that the resulting crystals commonly have very high concentrations of structural defects, i.e. crystal twinning[128–130]. Both methods can employ seed crystals in the growth region to prevent these high concentrations of defects[128–130].

1.7.3. Physical Vapor Deposition Techniques

physical vapor deposition (PVD) techniques are considered here to be thermal evaporation and pulsed laser deposition. There are a number of other techniques not

discussed directly in this work that could be included in this category: sputtering, molecular beam epitaxy, and cathodic arc deposition being some of the more common[128,129,131]. MBE is here considered to be a subset of general thermal evaporation. PVD techniques share two commonalities: the deposition is conducted through the creation of a plume from the source material by some energetic process which then condenses on a substrate[128,129,131], and are limited to depositing thin films, but can produce single crystal, polycrystalline, and amorphous product phases[128,129,131]. Of the various synthetic and deposition techniques discussed in this work, PVD is probably the most versatile with a large number of source materials and deposition geometries available[128,129,131].

Pulsed laser deposition uses pressed targets of precursor material, which are ablated via a high energy laser such as a gas excimer or Nd:YAG[128,129,131]. The precursor material is synthesized using conventional solid state reaction methods and pressed into a pellet or target. The pressed pellet and substrate are placed in a high vacuum chamber where the pellet is bombarded by pulses from the laser[42,86,128,129]. The laser bombardment creates a plasma from the target, which condenses on the heated substrate. This technique is regarded as a laboratory-scale technique, and to date there are no industrial-scale PVT systems available[128,129,131]. Studies indicate that not all elements ablated from the target are transported to the substrate uniformly[42,86?]. Depositions of $CuCr_2Se_4$ from a stoichiometric ceramic pellet appeared to be slightly copper-deficient after PVT deposition[42]; $NbSe_2$ deposited by PVT was shown to be selenium deficient[86]. These studies indicate that the stoichiometry of the target may need to be adjusted in order to compensate for any such losses.

Thermal evaporation involves heating precursors with electron beams or in effusion cells. The technique has been shown to be extremely versatile and most solids can be deposited using some variation on the technique[128,129,131]. By increasing the number of sources in a given deposition system, it is possible to create compounds in situ via co-deposition of precursor materials[127]. MBE systems are a special case of these configurations[128,129,131]. It is also possible to create complex layering sequences in the deposited films using multiple sources and a shutter system to deposit sequential layers[34,39,128,129,131,132]. Syntheses incorporating thermal evaporation typically require heated substrates or ex-situ annealing of the deposited film to complete the reactions. Deposited films tend to be on the order of hundreds of nanometers, which results in the kinetics of subsequent reactions being diffusion limited[128,129]. A great advantage of this technique over PVT and other PVD techniques is that syntheses are generally capable of being scaled to industrial levels, making rapid technology transfer and adoption possible.

1.7.4. Compositionally Modulated Kinetic Trapping

The technique that will be used in this work is a variation on PVD by thermal evaporation. This technique has been given a number of names, most recently the Modulated Elemental Reactant (MER) method[11,41,127,132–134]. This particular name does not accurately capture the salient points of the technique and so will not be used here. Specifically MER neglects the use of thin multilayers to promote rapid intermixing, and the resulting product being nucleation, rather than diffusion limited. Recently the term compositionally modulated kinetic trapping (CMKT) was coined for the technique, where compositional modulation describes the multilayer precursors used for the technique and kinetic trapping describing the engineering of the precursor

to introduce a potential well in the energy surface to trap the desired product. CMKT accurately captures what sets this synthetic method apart from general thermal evaporation and other related techniques and will be used throughout this work.

CMKT employs techniques from general thermal evaporation and MBE, the result being a solid state synthetic technique with a high degree of control over the reaction pathway and therefore the product distribution of that reaction. The technique involves the deposition of a repeating series of thin layers, on the order of one to two atomic layers thick, of elemental precursors. These compositionally modulated multilayers (CMMs)[123–125] can be thought of as having modulation wavelength (λ_c)[123–125] equal to the repeat thickness of the series and a compositional waveform (ϖ_c) which captures the elemental profile of the series. The large surface area and short distances in the CMM result in rapid interdiffusion of the elemental layers[37,122–125], which causes the reaction kinetics to be nucleation rather than diffusion limited[37,122–125]. Gentle annealing results in formation of amorphous intermediate phases from which the first products to nucleate out are stabilized or trapped[37,122–125]. Multiple nucleation sites are possible based on the compositional waveform and modulation wavelength of the CMM, which can be used to generate self-assembling multilayers such as the MLCs[11,34,37–39]. Because the kinetics of the reaction can be controlled by CMKT, it is possible to stop the progress of a reaction and to stabilize a desired metastable or engineered structure[31,40,133,134].

1.7.5. Synthetic Considerations Relevant to the MLC Structural Motif

MLCs have two main synthetic routes in the literature to date, those produced as the thermodynamically stable product[8] and those produced as a metastable product[133–135]. Traditionally, MLCs have been synthesized by diffusion-limited

FIGURE 1.13. Schematic representation of the CMKT method.

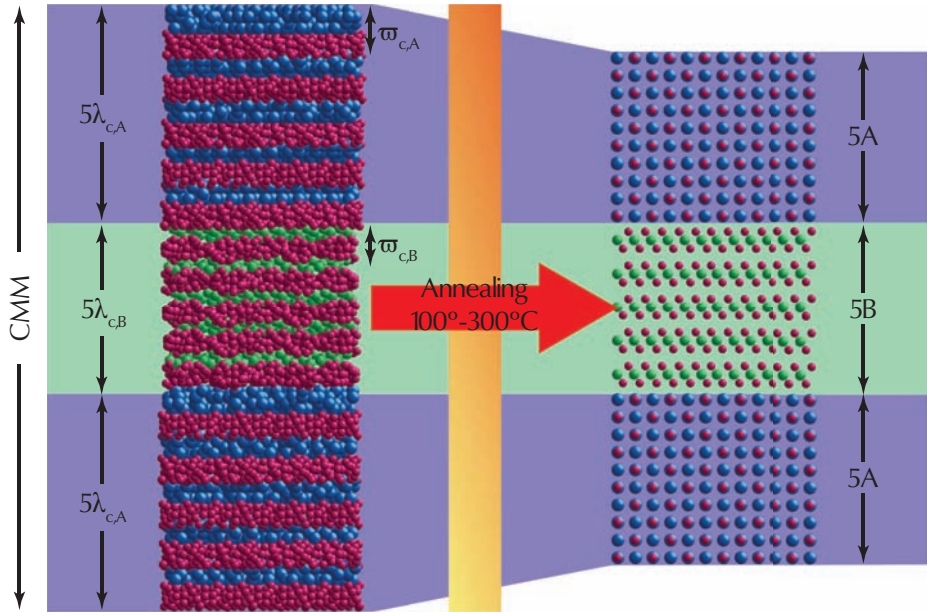

methods such as CVT / PVT or directly using a halide flux, and are therefore the most thermodynamically stable products for the given reaction conditions[8]. The advantage of these traditional methods lies in the ability to grow high-quality single crystals suitable for crystallographic studies to elucidate the complex structures of MLCs. A drawback of the thermodynamic methods is that they require long reaction and growth times and can only produce a small number of the possible compounds for a limited number of systems.

Structures generated via CMKT are not limited to thermodynamically stable phases. Rather, it is possible to access a variety of metastable products for a particular MLC system[133–135], which provides a distinct advantage over traditional thermodynamic routes. To date, it has been possible to generate arbitrary layering sequences, $[\{(MX)_m\}_{1+y}(TX_2)_n]_r$, of binary constituents (MX and TX_2), including structural isomers, i.e. (m, n) where $m = n = 2, 3, 4, 5$, which are not found in nature[133–135]. The method can produce specimens using short deposition and reaction

times and both bulk and thin films. The primary disadvantage of CMKT is that only thin films can be easily produced, which makes structural determination more complex[136].

1.8. Statement of Problem and Project Overview

In 1996 review Wiegers[8] lists five questions that needed to be addressed about misfit structures: Why do they form? What stabilizes them? Is there charge transfer between structural units? What determines composition? What is the effect of incommensurate character on observed properties? To some degree these questions have been explored, but not definitively answered. Significant work exploring the charge transfer in the lanthanide bearing incommensurate structures[6,33], as well as recent work exhibiting the stabilization of the $CrSe_2$ structure through charge transfer from metallic substructures[39], has been performed. Little evidence exists of charge transfer in substructures that do not contain lanthanides or otherwise exhibit metallic band structures[6,33]. Recent work[41,133–135] performed on the systems pairing a rock-salt- and dichalcogenide-structured units suggest that the thickness of individual structural units does not limit the formation of a stable structure, as long as the structural units are comprised of an integer number, i.e. (m, n), of unit cells. In contrast, structural variations as a function of m and n, including atomic relaxation, are poorly understood. Work by Mortensen[41] indicated that the energetic favorability of segregated systems over intermixing are quite important. For instance, if alloys are more energetically favorable than discrete segregated phases, as is the case with Bi_2Te_3 and Sb_2Te_3, the result will be intermixing, i.e. $(Bi_xSb_{1-x})_2Te_3)$, rather than the formation of the multilayer $[(Bi_2Te_3)_m(Sb_2Te_3)_n$. Additionally, the incommensurate structures of naturally occurring and synthetic structures created to date suggest that

the substructures for an incommensurate multilayer may not need to be confined to the MX and TX_2 structural types. Taking all this into consideration, the five questions posed by Wiegers can be simplified to two, of which the others can be thought of as a subset: Why do the structures form? and What stabilizes them? If these two questions were answered, it might be possible to generate misfit structures that are outside of the traditional $[\{(MX)_m\}_{1+y}(TX_2)_n]_r$ type. MLCs would then potentially comprise a broader class of materials with greater diversity of chemistry, properties, and potential applications.

1.8.1. Generality of MLC Type Structures

The examination of the literature in Section 1.1. suggests that only two criteria may need to be met to form a misfit structure. The first of these is that the substructures used to generate the crystal must satisfy the local bonding requirements for the structure being formed. In other words the substructures must be stable. This does not preclude metastable structures such as $CrSe_2$, but indicates that the other substructures present must provide a stabilizing force in order for the incommensurate crystal to form. The second criterion is that subunits must be able to create kinetically stable interfaces. The simplest examples of this are the geological MLCs which incorporate the TX_2 structure where the other substructures in the system may be thought of as intercalates of the TX_2 occupying the van der Waal's gap in the dichalcogenide structure. If these two criteria are all that need to be satisfied, a much wider array of MLCs than those currently reported in the literature may be stabilized.

Assume that the only requirements to form a MLC are the satisfaction of the two discussed criteria. Why then have only systems featuring MX, M_2X_3, and TX_2 structural units been synthesized? A possible explanation is that relatively few

such compounds can be synthesized by macroscopic thermodynamic routes, which comprise the majority of the published literature. Work by Thompson[127], as well as earlier work by Schneidmiller[137], Jensen[132], and others[34–38] have demonstrated that it is difficult to access more complex structures because of the preferential nucleation of stable binary intermediate structures. In order to produce a more complex misfit structures, alternate synthetic routes are needed which bypass undesirable intermediates. Any study of the generality of the MLCs must include the control of the reaction pathway to produce the desired structures.

1.8.2. Course of Research and Organization

This work proposes that MLCs potentially comprise a much broader class of materials than that represented by the literature to date. Further, this work proposes that the formation of MLCs is limited only by the satisfaction of the two previously mentioned criteria. This hypothesis will be tested by generating MLCs using new material combinations. The research project and this document are subdivided into three phases. First, the development of characterization methodologies and work flows that can be applied to the materials of interest will be outlined. These methodologies must be optimized to provide structural and chemical information about the sample quickly and without ambiguity. Second, a proof-of-principle MLC will be synthesized. This material should satisfy two criteria for forming a stable MLC structure, while still being composed of readily formed binary compounds. Last, the synthesis of a novel MLC will be performed. This novel compound will incorporate a combination of structural units other than the MX and TX_2 structures .

The preliminary work for this study will be the generation of a new characterization work flow to study MLCs. This new work flow will include scanning

transmission electron microscopy for structural analysis and will be tested through the characterization of $CuCr_2Se_4$ and a number of known MLCs. The work on the new characterization work flow will support a study of strategies to avoid the formation of intermediate phases in ternary systems targeted towards controlling reaction pathways through precursor layer order and the direct synthesis of $CuCr_2Se_4$, which is a necessary step for the inclusion of this structure in a self assembling multilayer structure.

After the development of the characterization scheme, the project will proceed to the generation of a MLC incorporating α-FeSe and $NbSe_2$. The material $[\{(FeSe)_m\}_{1+y}(NbSe_2)_n]_r$ is an example of a novel MLC that nevertheless exhibits the traditional attributes of binary structural units, van der Waals gaps, and thermodynamically stable component structures. This system will address the question of whether it is possible to form a stable interface in a MLC outside of the $[\{(MX)_m\}_{1+y}(TX_2)_n]_r$ family.

The last component of the study will be the generation of a MLC using $NbSe_2$ and $CuCr_2Se_4$ structural units, thus demonstrating the generality of MLCs. This compound represents a significant departure from MLCs synthesized to date, incorporating a complex ternary structure in place of the traditional binary rock-salt-structured unit.

In this document Chapters III through IX, with Appendix B being a supplement to Chapter VI, contain co-authored material. Chapters III through V contain the work related to the structural characterization schemes and the study of the direct synthesis of $CuCr_2Se_4$. These chapters are accepted or submitted at the time of this writing to *The Journal of Alloys and Compounds* (Chapter III), *The Journal of The American Chemical Society* (Chapter IV), and *The Journal of Magnetism*

and Magnetic Materials (Chapter V). Chapters VI and VII contain a study of the structure of CMKT synthesized misfit layer submitted to *Nature Materials*. Chapter VIII details the synthesis and characterization of the $[\{(FeSe)_m\}_{1+y}(NbSe_2)_n]_r$ system and is being prepared for submission to *The Journal of The American Chemical Society*. Lastly, Chapter IX contains the synthesis and characterization of $[\{(NbSe_2)_m\}_{1+y}(CuCr_2Se_4)_n]_r$ and is being prepared for submission to *The Journal of Alloys and Compounds*.

CHAPTER II

EXPERIMENTAL THEORY AND PROCEDURES*

2.1. Synthesis and Compositionally Modulated Kinetic Trapping

A number of works have treated, in great depth, the theory behind using sequences of thin elemental layers to circumvent the rate limiting diffusion found in traditional solid state reactions[11,39,41,132–135,137]. However, for the sake of continuity and context, a brief discussion of the theory of compositionally modulated kinetic trapping (CMKT) will be undertaken here. The unique strength of CMKT is the controlled intermixing of atoms in the solid state to allow the formation of a desired reaction product. CMKT based syntheses are performed by depositing thin layers, on the order of 0.1 nm to 1 nm, of elemental reactants onto a substrate, followed by heating to moderate temperatures that allow for rapid interdiffusion of the precursor, as depicted graphically in Figure 2.1.

CMKT permits the formation of a kinetically stabilized product distribution through design of the CMM in a way that favors the formation of the desired reaction products. This design process is intended to produce a CMM having precisely the needed elemental compositions in a spatial arrangement that is very close to the desired product, which forms upon gentle annealing via a self-assembly process. From the standpoint of thermodynamics, this can be thought of qualitatively in terms of the conditions required for nucleation. For nucleation to occur the correct elements in the correct ratio must be present with sufficient energy in the system to effect

*Certain commercial equipment, instruments, or materials are identified in the document. Such identification does not imply recommendation or endorsement by the National Institute of Standards and Technology, nor does it imply that the products are necessarily the best available for the purpose.

FIGURE 2.1. Schematic representation of CMKT used for generating a kinetically stable ternary structure in thin film form. In the CMM precursor the modulation wavelength (λ_c) is the distance over which one iteration of the compositional waveform (ϖ_c) is mapped. Proper calibration of the deposition parameters for the CMM results in one iteration of λ_c generating one unit cell in the final structure, denoted by C in the schematic.

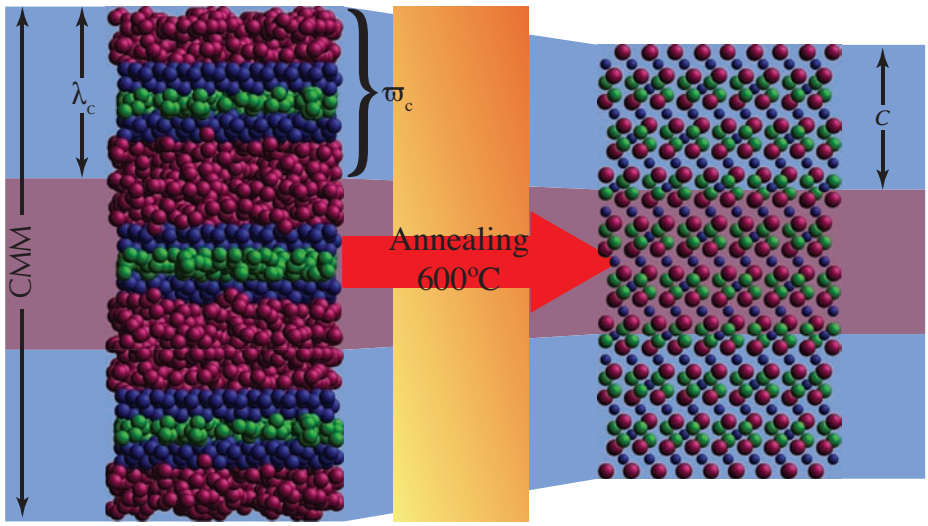

FIGURE 2.2. Annealing and nucleation in the CMM precursor. On annealing the waveform of the CMM, shown as the periodic curve, attenuates towards the average composition of the film. If the lowest energy compound for the A-B system is AB, then the first areas of the CMM to satisfy the spatial and energetic requirements to nucleate AB are shown in blue.

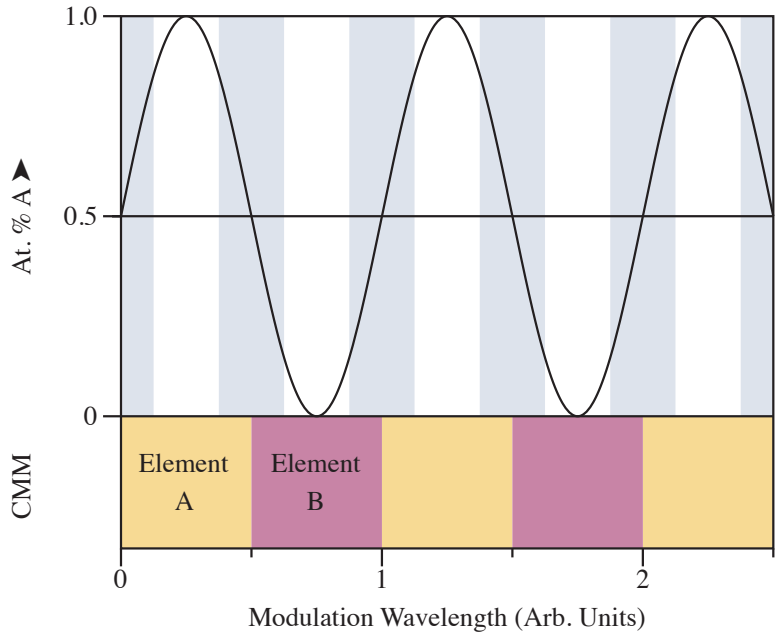

nucleation of the desired product. There are also geometric considerations when one considers nucleation in terms of bulk diffusion couples or interfaces between mesoscale crystalline solids, but as was indicated by Jensen, et al.[123,125], this particular requirement is mitigated by the rapid interdiffusion of the thin layers used for the CMM. Therefore, for a synthesis to successfully use CMKT, it must satisfy both the energetic and chemical requirements for the desired product without satisfying those of any other potential product. Since CMKT uses a CMM precursor with a ϖ_c, the chemical requirement, i.e. where the composition of the interdiffused multilayer satisfies the stoichiometry of the desired product, can be thought of in terms of the attenuation of ϖ_c.

As the CMM precursor is annealed the semi-segregated layering pattern gives way to a more homogeneous one as the layers interdiffuse. This in turn results in the profile of ϖ_c being attenuated towards the average composition of the film. When this diffusion process causes some portion of ϖ_c to match the composition of a stable product a nucleation event is possible. If the annealing temperature is sufficient to satisfy the energetic requirements for nucleation then this product will be the most likely to form and will crystallize out of the amorphous precursor. When the CMM precursor is designed so that there is a long wavelength periodicity, i.e. layering of two different waveform in a repeating pattern with the intent of creating a multilayer structure, this interdiffusion-nucleation process results in multiple nucleation sites through the thickness of the film, allowing the crystallization of the film by self-assembly.

In theory, CMKT should allow for a library of materials and crystal structures to be created, mixing various structural subunits to create new materials with novel properties. In practice, as was indicated in Section 1.7. the process is more complicated given that the design of the CMM precursor for a desired structure must avoid the creation of all possible products except the one desired. In the case of binary systems, e.g. PbSe or $NbSe_2$, the design of the CMM precursor is relatively simple, requiring only the layering of the properly calibrated binary waveforms in the desired order. However, when one considers ternary or higher-order systems, the problem becomes more complex. In a theoretical system composed of elements A, B, and C, where one desires a product composed exclusively of a product ABC, the CMM precursor must be designed such that alternative binary products AC, BC, and AB are prevented from forming or do not otherwise impede the formation of the desired ternary product. This combinatorial problem becomes increasingly complex

the more degrees of freedom, i.e. elements and elemental concentrations, present in the system. This complexity can be mitigated by two factors, the first of which is careful engineering of the CMM precursor considering not just the layering and interactions within the waveform for each subunit, but the interactions between the two waveforms. Candidate sequences of elemental reactants that avoid the formation of unwanted phases can be devised based on available phase diagrams and related literature. Second, the deposition and calibration of the CMM precursor must also be considered. These processes are the subject of the next portion of this chapter.

2.1.1. Calibration of Deposition Parameters

The calibration process for creating the CMM precursors is iterative comprising two steps, repeated until ϖ_c gives the appropriate compositional ratio and λ_c is equal to a single unit cell after annealing. First a series of binary samples are created where the composition ratio was adjusted by varying the shutter time while holding one of the components, usually the chalogen, constant. These samples are analyzed by electron probe microanalysis (EPMA), using the method described in Section 2.3., to determine the concentrations of the elements deposited. The ratio of components is then plotted against the thickness of the variable component, as derived from the source exposure time and source fluence, to create a gross calibration curve, as can shown for Nb-Se in Figure 2.3. From the calibration plot the appropriate exposure time for the desired composition ratio is chosen.

In order to calibrate λ_c to give a single unit cell per wavelength for the calibrated ϖ_c, the initial binary samples were analyzed via X-ray reflectivity (XRR) to determine the value of λ_c for each sample. A linear plot of the derived thickness of the varied component versus modulation wavelength, also shown in Figure 2.3., coupled with

FIGURE 2.3. Example Calibration Curve for Nb-Se CMM precursor aggregating two separate calibration sets. The marker indicates the experimentally verified exposure time for the Nb source to produce a single $NbSe_2$ unit cell per iteration of the CMM precursor.

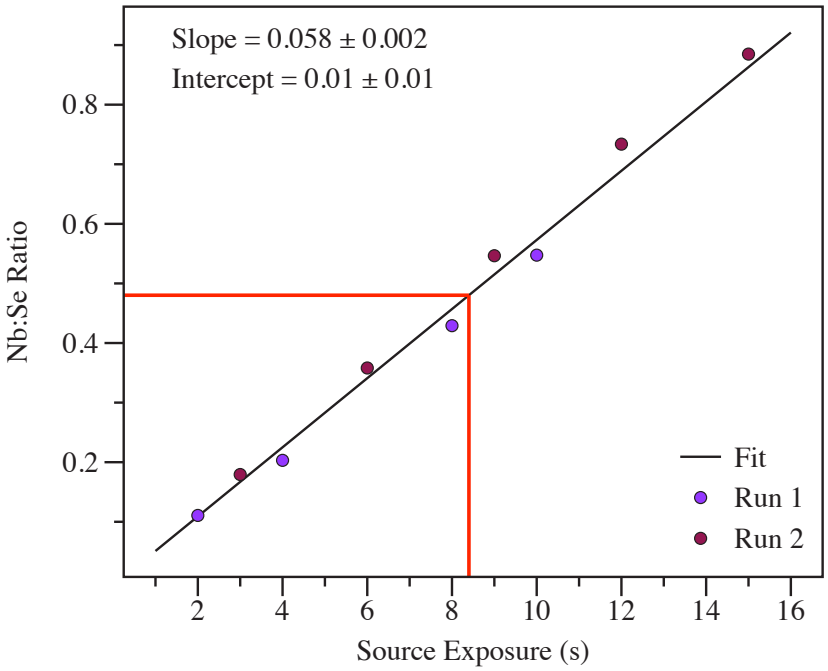

the correct elemental ratio determined by EPMA allowed for the determination of a binary thickness ratio. This ratio was then linearly scaled to give a value slightly greater than that of the desired structures unit cell parameter normal to the substrate. This gross calibration for λ_c was then refined as part of the optimization process for multilayer CMM precursors.

To calibrate the CMM precursors for a multilayer system a series of two component films incorporating grossly calibrated binary CMMs, i.e. $[\{(FeSe)_m\}_{1+y}(NbSe_2)_n]_r$, were prepared. The number of wavelengths of each binary component deposited in these films were varied separately, i.e, $(1, n)$ where $n = 1, 2, 3, 4, 5$ and vice versa. A sample of the $(1, 1)$ film was annealed at increasing temperature and analyzed via XRR and XRR to determine an initial annealing temperature for the calibration analysis. The remaining films were annealed at the determined temperature and analyzed using XRR and XRR along with their as-deposited counterparts. The c-lattice parameter, corresponding to the supercell modulation wavelength for each film was extracted using the methods indicated in Section 2.2. Plots of the extracted supercell wavelength versus the number of component wavelengths in the variable subunit were constructed, as shown in Figure 2.4., and a linear regression of the data conducted. Analysis of the fit of the data provided a number of important metrics from regarding the calibration, deposition, and the degree of control over the deposition. The slope of the fit lines provide the contribution to λ_c by the varied component. The intercepts provide an estimate for the contribution of the component held constant. The values determined from the intercepts can only be regarded as approximate do to the increasing uncertainty of the absolute value of their contribution to λ_c as λ_c becomes larger. Lastly, analysis of the residuals of the fit provide a metric for the quality of the deposition. A standard

FIGURE 2.4. Example of a plot of the supercell c-parameter versus the number of layers of the variable subunit. From such plots it is possible to extract the thickness of the variable subunit from the slope. An estimate of the constant subunit thicknesses can also be extracted from the intercept of the fitted line.

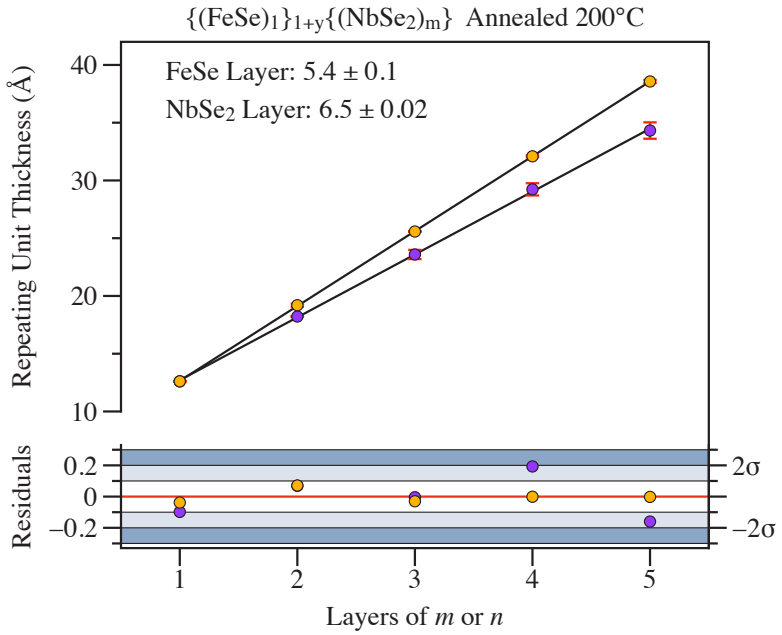

deviation of $1\sigma > 0.01\,\text{nm}$ for a crystalline or annealed film was considered outside random error and indicative of errors in the deposition process. For as-deposited samples the parameter was relaxed to $1\sigma > 0.05\,\text{nm}$ to account for roughness in the CMM and layer intermixing in the as-deposited films.

Annealed and as-deposited samples from the calibration sample set were also analyzed via EPMA, to determine the total composition for each film. A series of equations based on the compositional waveform for the CMM precursor and the number of wavelengths of each component were generated for each calibrations series. For the reaction:

$$[\mathrm{m(M \cdot X) + n(T \cdot 2\,X)]_r} \xrightarrow{\Delta T} [\{\mathrm{(MX)_m}\}_{1+y}\mathrm{(TX_2)_n}]_r \qquad \text{(Formula 2.1)}$$

with a stoichiometric equation for the final total film composition:

$$\mathrm{M_m T_n X_{m+2n}} \qquad \text{(Formula 2.2)}$$

the equations for the final annealed composition would be as follows.

$$\frac{\mathrm{M}}{\mathrm{X}} = \frac{a(m)}{c(m+2n)} \qquad \text{(Equation 2.1.)}$$

$$\frac{\mathrm{T}}{\mathrm{X}} = \frac{b(n)}{c(m+2n)} \qquad \text{(Equation 2.2.)}$$

Plots of these ratios, where a, b, and c are fitting constants, provide multiple equations with multiple unknowns allowing for linear regression and statistical analysis of the EPMA data to determine any needed fine adjustments to ϖ_c. Examples of this analysis are provided in Figure 2.5. This data set, coupled with the thickness data provided by X-ray structural analysis, were used to adjust ϖ_c and λ_c for the components of the CMM precursor such that $\lambda_c = 1c$, where c is the lattice parameter for the lattice vector normal to the substrate, of the desired crystal compound on annealing.

2.1.2. Deposition Experimental Conditions

Samples were deposited using a custom evaporative metal deposition system similar to those used in deposition of x-ray mirrors. This system is illustrated schematically as well as in operation in Figure 2.7. The system consists of commercial three 3 kW electron beam guns and a custom fabricated Knudzen style effusion cell. Elemental precursors were matched to a deposition source based on the literature values for the melting and evaporation points of the metals. Table 2.1. shows relevant

FIGURE 2.5. Example of analysis for compositional ratios as determined by EPMA. Analysis of the EPMA data by this method provides multiple equations and multiple unknowns for a give compositional series.

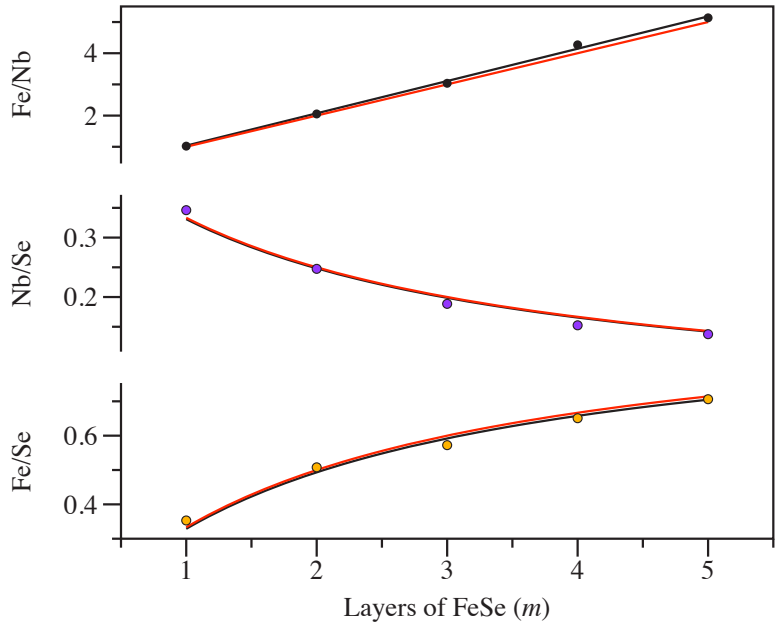

information about the materials and deposition sources used. Chromium, copper, niobium, and iron were deposited using an electron beam gun while selenium was deposited using the effusion cell. These sources are arranged around the radius of the sample chamber with a computer controlled shutter system separating the sources from the samples and quartz crystal balances over each source monitoring the source fluence. The sample substrates are suspended from a computer controlled carousel that rotates the substrate to the sources based on a deposition sequence entered into the control computer.

Samples were deposited under a vacuum of $< 1.33 \times 10^{-4}$ Pa, generally on (100) oriented commercial silicon single-crystal substrates to a minimum film thickness of ≈ 50 nm. Samples for electrical measurements and certain transmission electron microscopy (TEM) measurements employed different substrates and film thicknesses

TABLE 2.1. Relevant physical data for evaporative deposition of the elements in this work.

Elements	Melting Point (101 kPa)	Deposition Temp. (1.33×10^{-4} Pa)	Deposition Mechanism	Deposition Source
Cr	1890 °C	977 °C	Sublimation	E-beam Gun
Cu	1083 °C	857 °C	Evaporation	E-beam Gun
Fe	1535 °C	988 °C	Evaporation	E-beam Gun
Nb	2468 °C	1977 °C	Evaporation	E-beam Gun
Se	217 °C	125 °C	Evaporation	Effusion Cell

and are indicated where appropriate elsewhere in this work. Samples were annealed with an custom-fabricated hot plate in a glove box under a nitrogen atmosphere with an oxygen concentration of no greater than $\approx 500\,\mathrm{nL\,L^{-1}}$ O_2. The hot plate was allowed to equilibrate at temperature for 15 min before each annealing.

2.2. Structural Characterization and Diffraction Theory

Structural characterization was performed by a combination of X-ray diffraction (XRD), XRR and electron diffraction. Diffraction employs an incident beam of monochromatic radiation, e.g., Cu-K_α X-rays or 300 kV electrons, which is directed onto a sample. The beam interacts with the sample and, depending on its structure, beams of the radiation will occur at specific angles relative to the incident beam. A number of models and analogies have been used over the years to explain the angular location and intensities of these reflections, the most famous of which is Bragg's Law. A second model, more salient to a discussion of general kinematical diffraction, can be taken from the optical theory of constructive and destructive wave interference.

Consider a situation where a plane wave of monochromatic radiation interacts with a row of atoms, as shown schematically in Figure 2.8. The interaction between the plane wave and the atoms will produce secondary wavelets radiating out from the atomic centers. These wavelets will interfere creating resultant waves propagating

FIGURE 2.6. Image of the deposition system interior during operation, various components of the apparatus can be seen. From top to bottom: The substrate carousel with a substrate attached, cryo-diffusion pump (background), quartz crystal balance, shutter assembly, and metal evaporation source.

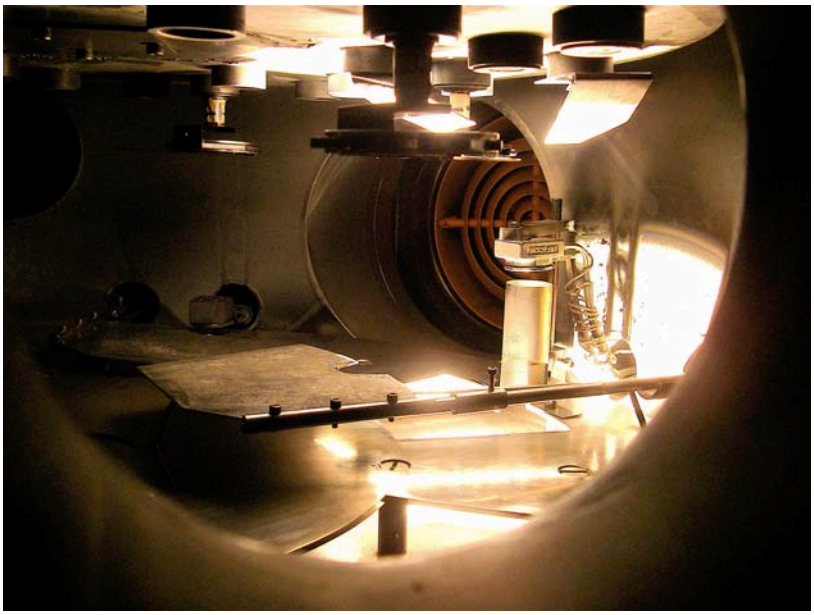

FIGURE 2.7. Scale schematic diagram of the evaporative deposition chamber in perspective, (a), and cross section, (b) views.

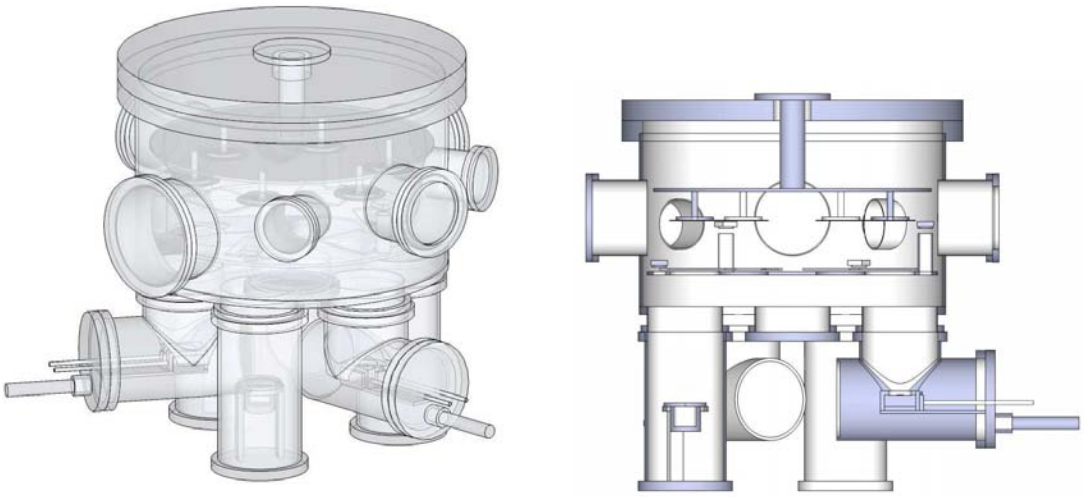

(a) **(b)**

FIGURE 2.8. Interference model of crystal diffraction. A plane wave interacts with a regularly spaced array of scattering centers to reproduce the incident wave in addition to secondary waves of the same wavelength through constructive and destructive interference.

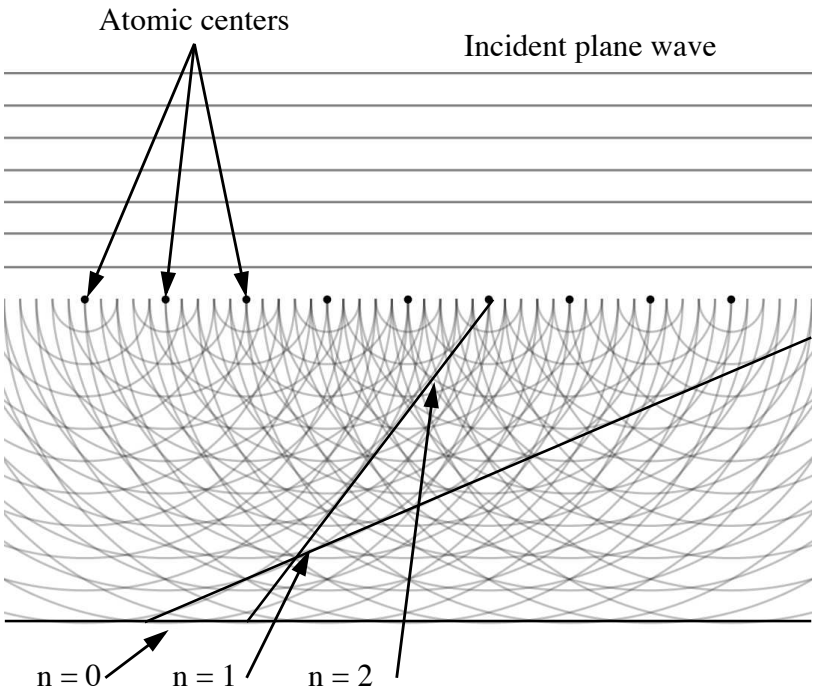

out from the specimen at specific angles relative to the incident plane wave. The strength of these diffracted waves is dependent on the type of atoms and the number of electrons that make up the diffracting array.

Consideration of the crystal in the above manner allows for the treatment of diffraction in terms of wave mechanics. A crystal by definition is a periodic array of atoms; or more specifically, a three dimensional periodic electron density function. This function can be described by a discrete series of coefficients:

$$F_{hkl} = \sum_j f_j e^{-2\pi i(hx_j + ky_j + lz_j)} \qquad \text{(Equation 2.3.)}$$

where the structure factor, $F_{hkl}$for a given sequence of integers h, k, l is determined by the coordinates x_j, y_j, z_j and elemental scattering factors f_j of all atoms composing the basis within the primitive unit cell. The dependence of the structure factor on atomic number, Z, the wavelength of the incident radiation λ, and the incident angle of the radiation, θ are captured by the quantity f_j called the atomic form factor, which provides the amplitude of the diffracted wave. The diffracted intensity for a given reflection, hkl, is the magnitude squared of its respective structure factor,

$$I_{hkl} \propto |F_{hkl}|^2. \qquad \text{(Equation 2.4.)}$$

There are also a number of instrumental parameters that can affect the intensity and shape of the peak which are well described in diffraction specific works[138–140], however these parameters in general have no appreciable effect on the positions of peaks. Shifts in the measurement of peak positions may arise because of instrument misalignment. For this work these effects are considered to be operator error and were accounted for by careful alignment of the instruments used, see Subsection 2.2.4., and inclusion of standards where possible, as indicated in Section 2.4.

The rigorous treatment of diffraction described above, while probably the most accurate, can be cumbersome for hand calculations. During the early work on XRD a simple empirical equation called Bragg's Law was found to accurately predict the possible peak positions of diffracted beams from a crystal. Bragg's Law treats diffraction as analogous to reflection and refraction by a series of semitransparent mirrors. The relationship states that for a given set of regularly repeating atomic planes, a diffracted beam may be present where the experimental geometry satisfies the relationship:

$$n\lambda = 2d \sin\theta \qquad \text{(Equation 2.5.)}$$

where n is an integer denoted the order of the reflection, λ is again the wavelength of the incident radiation, d is the spacing of the diffracting lattice planes, and θ is the angle between the incident beam and the diffracting planes*. There are a number of drawbacks and caveats to the use of Bragg's Law, foremost of which is the inability of Bragg's Law to predict the systematic peak absences found in highly symmetrical crystal systems[83,84,139,140]. Additionally, for smooth films the errors associated with calculations of the lattice spacing from experimental data increase dramatically as θ approaches zero due to the increasing influence of the sample's refractive index[140–144] relative to X-ray radiation. This effect is especially pronounced in the case of thin films in the low angle regime ($2\theta \lesssim 10^\circ$), resulting in the need for a modification† to Equation 2.5. to account for the refractive index of the sample:

$$n\lambda = 2d\sqrt{\sin^2\theta - \sin^2\theta_c} \qquad \text{(Equation 2.6.)}$$

θ_c[140–144] is called the critical angle and is dependent on the index of refraction for the material which, for a given interface, is defined as:

$$n = 1 - \delta - i\beta, \qquad \text{(Equation 2.7.)}$$

where δ accounts for the elastic scattering and is defined as

$$\delta = \frac{r_e}{2\pi}\lambda^2\rho_e \qquad \text{(Equation 2.8.)}$$

*A geometric derivation of Bragg's Law is provided in Appendix E

†A geometric derivation this modification is also provided in Appendix E

where r_e is the classical electron radius and ρ_e the mean electron density of the film. β is the absorption of the incident wave by the material[140–144]. The values for δ and β are on the order of 1×10^{-5} and 1×10^{-7} respectively. The effects of β on n for x-rays are considered to be small and negligible. The critical angle, θ_c, is the angle below which there is a total external reflection of the incident wave by the material. This condition is described by the Snell-Descartes' law such that Equation 2.7. becomes:

$$\cos\theta_c = n = 1 - \delta. \qquad \text{(Equation 2.9.)}$$

Because the values of δ are on the order of 1×10^{-5} a small angle approximation can be made such that $\cos\theta_c \approx 1 - \theta_c^2/2$ making Equation 2.9.

$$\theta_c^2 = 2\delta \qquad \text{(Equation 2.10.)}$$

In cases where the mean electron density of the film is known, either experimentally or theoretically, the critical angle for the film can be calculated using this equation. In cases where this parameter is not known, it can be used as a fitting parameter, or can be determined via modeling methods. In this work Equation 2.5. is used for simple calculations and analyses of data sets where $10^\circ \leq 2\theta \leq 180^\circ$ where $\sin^2\theta_c \approx 0$ relative to $\sin^2\theta$. In the case of analysis of XRR data the critical angle is a significant contributing factor to the observed reflections and Equation 2.6. was used.

2.2.1. Treatment of X-ray Reflectivity Data

A typical XRR data set is shown in Figure 2.9. A number of different interactions are common in XRR analysis, many of which are seen here. These interactions

are separated out in Figure 2.10. The high frequency oscillations, called Kiessig fringes, seen in Figure 2.9. and Figure 2.9.b are caused by, using the Bragg's Law approximation, the interference between reflections from the front air-film interface and the back film-substrate interface. The attenuation of the Kiessig fringes towards higher angles is caused by the roughness of the film, creating destructive interference at the Bragg condition for the Kiessig fringes. In simple terms, this destructive interference can be thought of as continually varying d from Equation 2.6. by δd in a random manner over the sampling volume of the beam. At higher angles the sensitivity to these small variations increases, decreasing the intensity of the diffracted beam proportionally to the roughness of the film. Last, superimposed over the Kiessig fringes are Bragg peaks coming from the internal repeating structure of the multilayer film.

It is possible to extract the total thickness and roughness of the film from the Kiessig Fringes using the method detailed by Phung, et al.[142,144]; rearranging Equation 2.6.

$$\sin^2\theta = (\frac{n\lambda}{2d})^2 + \sin^2\theta_c \qquad \text{(Equation 2.11.)}$$

and plotting $\sin^2\theta$ as a function of the square of the fringe index, n^2. A linear fit of the data is then taken using the index of the peaks and the critical angle as fitting parameters. The film thickness can then be extracted from the slope and other useful parameters, e.g. the mean electron density, ρ_e, or the bulk film density, ρ, from the critical angle using Equation 2.10. The roughness in the film, ΔT_r can be estimated using the angular position where the Kiessig fringes can no longer be resolved from the noise, $\theta_{n,max}$, and the relationship:

$$\Delta T_r = \frac{\lambda}{4\sqrt{\theta_{n,max} - \theta_c}} \qquad \text{(Equation 2.12.)}$$

FIGURE 2.9. Example of experimental XRR data from a multilayer thin film.

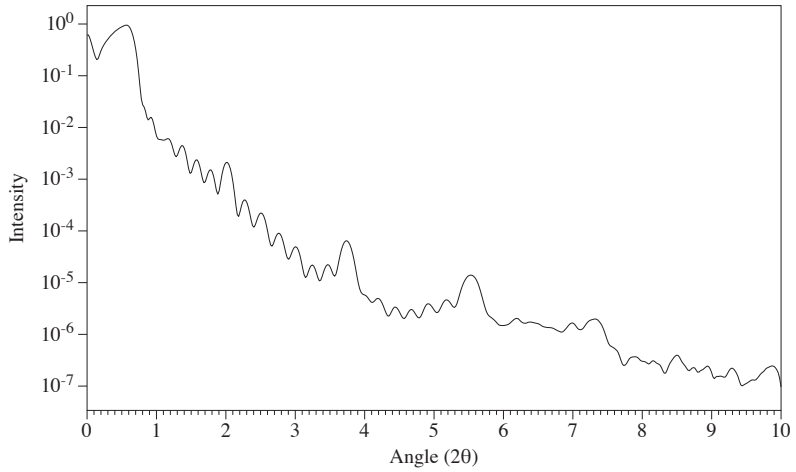

as put forth by Wainfan and Parratt[143]. In general this work employed this technique for initial analysis of film quality, but deferred to more sophisticated methods for more detailed analysis of the XRR data.

Where a more complete analysis of the XRR data was desired the REFS reflectivity modeling software was used to model the data set and extract the film and layer thicknesses, film roughness, and density as well as the associated uncertainties in these quantities. This software uses a differential evolution algorithm to programatically fit measured specular XRR curves to a calculation based on a structural model of the sample being analyzed. The measured and calculated curves are objectively compared using a goodness-of-fit function, whose value decreases towards zero as the agreement between the two curves improves and the model more closely represents the sample's structure.

2.2.2. Treatment of High Angle X-ray Diffraction Data

Analysis of XRR data was conducted by first extracting the positions of each peak and the background shape using a Voigt peak profile and an exponential decay

FIGURE 2.10. Simulations of XRR data showing the effects of various sample structures on the XRR pattern: (a) the baseline curve of absorption caused by the substrate; (b) the XRR profile for a monolithic layer of a material with a different electron density from the substrate; (c) the profile for a multilayer structure of two dissimilar materials with the same total thickness as the monolithic layer; (d) the attenuation caused by film and substrate roughness.

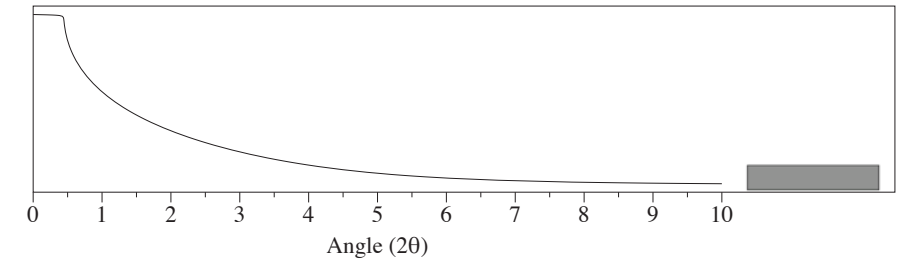

(a)

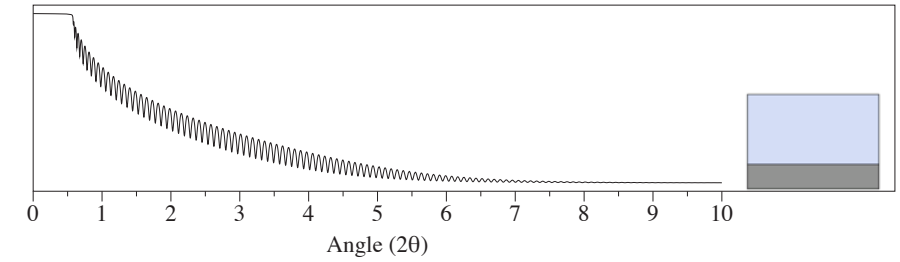

(b)

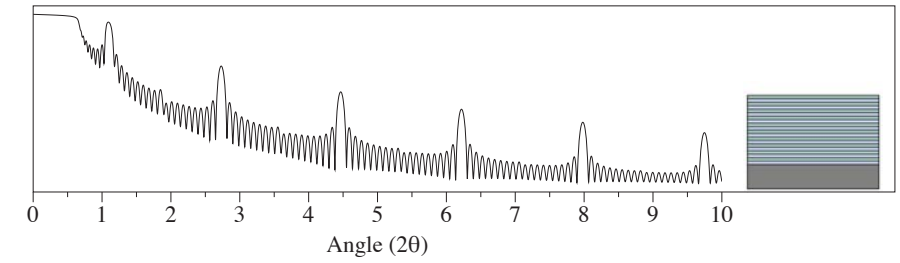

(c)

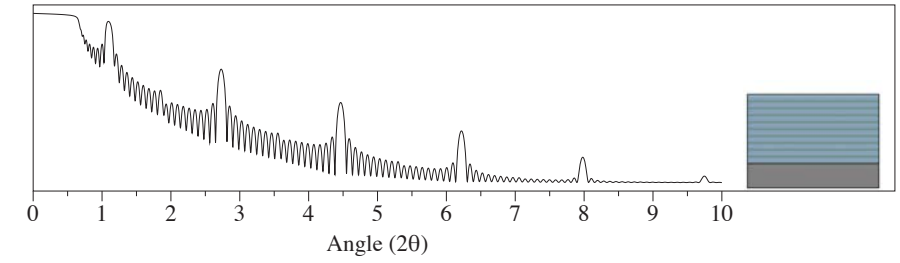

(d)

function respectively. Peak positions were then analyzed using the method first detailed by Cohen,et al.[145,146]. For measurements normal to the the substrate, corresponding to the c-lattice parameter of the superlattice, the reflections were indexed to an a priori value starting from the low angle region. The values for d were then calculated using Equation 2.6. The use of an extrapolation function, rather than a more simple determination of d directly from Bragg's Law, was chosen to account for inherent experimental errors in diffraction measurements.

In 1945 Nelson and Ridley[147] performed a detailed analysis of the errors inherent in a diffraction experiment. They determined that precise determination of lattice constants are especially sensitive to slight misalignments in the height of the sample relative to the circle of the goniometer even in well aligned instruments. In their work they proposed a linear regression using the relationship:

$$\frac{\cos^2\theta}{\sin\theta} + \frac{\cos\theta}{\theta}. \qquad \text{(Equation 2.13.)}$$

as the best method for accounting for the small variations in sample height that are present even in properly aligned specimens. For this analysis the d values calculated from Bragg's Law were plotted against the value of Equation 2.13. for each peak and a first order linear regression of the data was conducted. The y-axis intercept of the resulting line provided the value of d for the unit cell. The uncertainty in d was taken to be $\pm 1\sigma$ from the regression. The initial indexes were then adjusted as needed to correct the fit and minimize the regression uncertainty. It should be noted that this method for determining lattice parameters is usually reserved for very high angle data and there is an enhanced sensitivity to misalignment of the instrument when employing this method. As is detailed in Subsection 2.2.4., special care was

consistently taken to assure that the instrument was properly aligned before data was treated in this manner.

2.2.3. Rocking Curves

X-ray rocking curves are used to analyze the texture of a film and, in a qualitative manner, its degree of crystallinity. The source is aligned to a Bragg condition for sample being analyzed, and the detector is swept from below to above the Bragg angle. The shape of the peak is indicative of the portion of the sample that shares the same alignment. In the case of powder samples or collections of randomly oriented crystallites rocking curves will produce a broad peak, as there is always some portion of the sample at the appropriate geometry to satisfy Bragg's Law. As a sample tends more towards a single crystal condition the rocking curve will result in a sharper peak because of the smaller distribution of crystallites about the Bragg angle that will satisfy the diffraction condition.

2.2.4. X-ray Experimental Conditions

XRR and XRR data were collected on two Bruker-AXS D8 Discover X-ray Diffractometers using either a $\theta - 2\theta$ or $\theta - \theta$ configuration, both of which are shown in Figure 2.11. No distinction will be made between the two instruments beyond the initial difference in the angular configurations, as they are in all other respects identical. The incident beam was conditioned using a divergence slit and a parabolic multilayer mirror. The exit beam was conditioned with a 0.6 mm antiscatter slit, a Soller slit assembly, and detector slit. The incident beam was Cu-K_α X-rays ($\lambda = 0.154\,18\,\text{nm}$). The alignment of the sample was checked and adjusted between every data set to correct for any movement due to variations in the sample substrates.

The general experimental geometry is found in Figure 2.11. and a summary of the optical slits used for various experiments is provided in Table 2.2.

XRR was used to gather information about the total film thickness, layer thicknesses, sample roughness, and density. Samples were analyzed using a 0.1 mm divergence slit and a 0.05 mm detector slit. XRR data were collected in the range $0° \leq 2\theta \leq 7°$ with a step size of 0.008° and an integration time of 1 s per step.

High angle XRD was used to gather information about the composite unit cell, and the degree of crystallinity of the sample in the direction normal to the sample substrate. Samples were first aligned using the 0.1 mm mm divergence slit and a 0.05 mm detector slit as in the XRR analysis and were then switched to matching 1 mm slits for the data collection. This change in acquisition parameters was done to afford both an accurate and uniform sample alignment between samples and to gather data at the maximum possible intensities. XRR data was collected from $10° \leq 2\theta \leq 65°$ with a step size of 0.08° and an integration time of 1 s per step.

Rocking curves were collected on individual peaks in the diffraction patternn to check for degree of crystallinity and preferred orientation. Samples were first aligned as in the general high angle XRD experiement discussed above. The detector angle was then set to the angle of the peak of interest, θ, and held at this position during the analysis. Rocking curve data were collected from 0° to $2\theta°$ with a step size of 0.08° and an integration time of 1 s per step.

2.3. Electron Probe Microanalysis

Compositional information from the deposited films at micrometer lateral resolution was gathered using EPMA. EPMA instruments incorporate a scanning electron column around which a number of wavelength dispersive x-ray spectrometers

FIGURE 2.11. Schematic of the X-ray crystallography experimental set-up used for structural characterization. Note that the parabolic mirror would appear between the X-ray source and the divergence slit, but is omitted for clarity. (a) is the $\theta - \theta$ geometry. In this geometry the sample is stationary and the X-ray source and detector are moved simultaneously. (b) is the $\theta - 2\theta$ geometry. In this configuration the X-ray source is held stationary. The sample is moved by θ and the detector $2\theta^c irc$ relative to the plane of the detector.

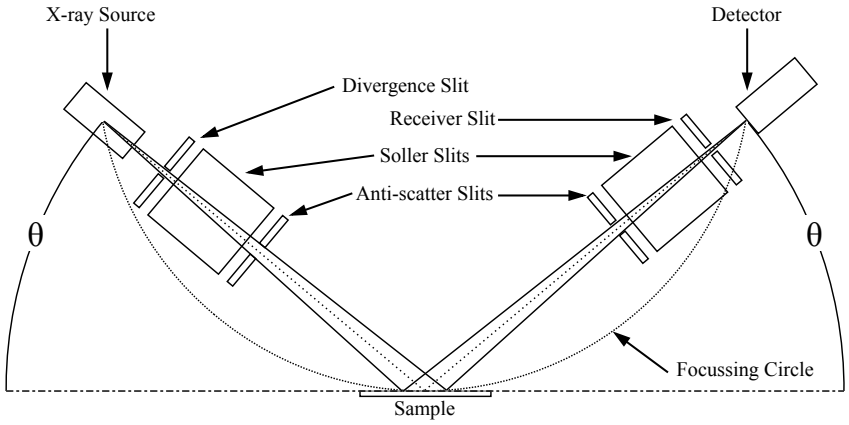

(a)

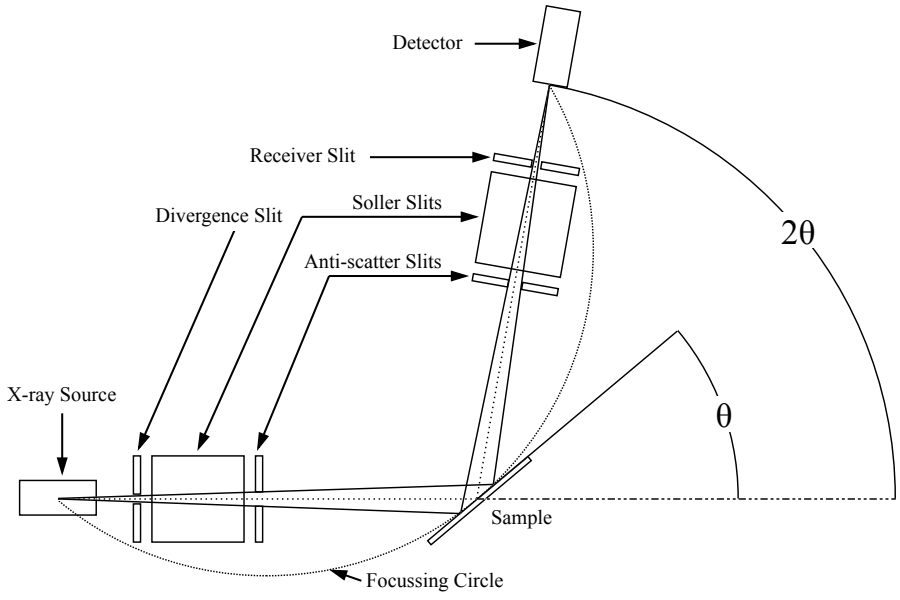

(b)

TABLE 2.2. Summary of X-ray experimental parameters. All scans used 1 s per step acquisition times.

Scan Type	Emitter Slit	Detector Slit	Scan Range	Step Size
Instrument Alignment	0.1 mm	0.05 mm	n/a	n/a
XRR (Survey)	0.1 mm	0.05 mm	0° - 10° (2θ)	0.03
XRR (Detail)	0.1 mm	0.05 mm	0° - 10° (2θ)	0.003
XRD (Collection)	1 mm	1 mm	10° - 65° (2θ)	0.03
Rocking Curve	1 mm	1 mm	0° - θ (θ)	0.03

(WDSs) are arranged[148,149]. Each spectrometer consists of a high precision x-ray diffractometer with a number of crystal mirrors of precisely known d-spacing in place of the sample. Each diffractometer is tuned by selection of an appropriate crystal mirror and adjustment of diffractometer angles to pass a narrow band of x-rays centered on a characteristic emission for a desired element to the detector[148,149].

Using a technique common in analytical chemistry it is possible to calculate, to a first order approximation, the concentration of a monitored element within the unknown sample. By measuring the response of an element of interest in a standard of known concentration it is possible to take a ratio of the measured responses in the unknown sample and the standard as representative of the ratio of concentrations of the elements in the unknown and standard[148,149]:

$$\frac{C_i^{uk}}{C_i^{std}} \approx \frac{I_i^{uk}}{I_i^{std}} = k_i \qquad \text{(Equation 2.14.)}$$

In truth, this representation of the "k-ratio" is only a simple approximation, and there are a number of secondary and tertiary effects that must be taken into account to extract the concentration in the unknown[148,149]. A detailed treatment of these effects are beyond the scope of this work, but in general are brought about by the effect of the environment on the elements ability to emit characteristic x-rays[148–152]. These so-called matrix effects are typically corrected using iterative calculations and complex

software algorithms which calculate the effects of atomic number, X-ray absorption, and X-ray fluorescence or Z_i, A_i , and F_i which are applied as a correction factor to Equation 2.14.:

$$\frac{C_i^{uk}}{C_i^{std}} = [ZAF]_i \cdot \frac{I_i^{uk}}{I_i^{std}} = [ZAF]_i \cdot k_i \qquad \text{(Equation 2.15.)}$$

Both the Probe and StrataGem software packages incorporate a number of methods for ZAF calculations. For this work, the $\phi(\rho z)$[144,148,149] and the iterative Pouchou-Pichoir methods[150–152] were used in Probe and StrataGem respectively.

2.3.1. Sample Preparation and Conditions

Samples were prepared for analysis by sectioning a $\approx 3\,\mathrm{mm}^2$ chip from the sample. These sample chips were then carefully mounted to an aluminum sample stub using quick set epoxy and allowed to dry for a minimum of 1 h . A small amount of carbon paint was applied from the surface of the sample chip to the surface of the sample stub at two corners of the chip to provide a conductive path to ground. Samples were analyzed using a Cameca SX-100 Microprobe equipped with 5 X-ray spectrometers in a range of 15 kV to 25 kV at each of 8 to 10 sites on each chip spaced at approximately 100 µm distances. Sample data sets were initially processed using Probe for Windows and then using StratGem implementation of the Pouchou and Pichoir[144,150–152] method to model the generation of x-rays as a function of accelerating voltage and determine a sample composition. Details of the experimental parameters used for each element are listed in Table 2.3.

TABLE 2.3. Summary of Electron Microprobe Analytical Parameters. Spectrometer crystals are defined as LTAP: large thallium acid phthalate, LLIF: large lithium fluoride, PET: pentaerylthritol, PC1: silicon-tungsten pseudo-crystal.

Element	Standard	X-ray Line	Energy	Crystal
Se	ZnSe (Synthetic)	Se L_α	1.379 keV	LTAP
Nb	Nb (Elemental)	Nb L_α	2.166 keV	PET
Fe	Fe (Elemental)	Fe K_α	6.400 keV	LIF
Cr	Cr (Elemental)	Cr K_α	5.414 keV	LLIF
Cu	Cu (Elemental)	Cu K_α	8.047 keV	LLIF
Si	Si (Elemental)	Si K_α	1.740 keV	PET
O	MgO (Synthetic)	O K_α	0.523 keV	PC1

2.4. Analytical Electron Microscopy

Analytical Electron Microscopy (AEM) is a broad discipline than encompasses a number of different methods and techniques. It is unreasonable to attempt to provide an exhaustive review of the field and all of the techniques in this work[153–156]. This section will touch on some general points of analytical electron microscopy (AEM) to provide context for the procedural choices made during the course of the research project. This work will then provide procedures for points specific to this work while leaving the more general aspects of the field to AEM-specific texts.

An electron beam can, because of the de Broglie relationship, be thought of in terms of its wave or particle properties. During the interaction of an electron beam with an electron-transparent specimen these two types of characteristics result in a number of possible outcomes, illustrated in Figure 2.12. The most obvious interaction is a transmission of the incident beam through the specimen with no net momentum change. This interaction is used in phase contrast imaging. The interaction of the beam with the specimen can also cause electrons to be absorbed or result in the generation of electron-hole pairs. Interaction of the beam with the specimen can also result in a number of emission electrons: Auger and secondary electrons;

FIGURE 2.12. Summary of possible outcomes of the interaction between an incident beam of electrons and a thin, electron transparent specimen.

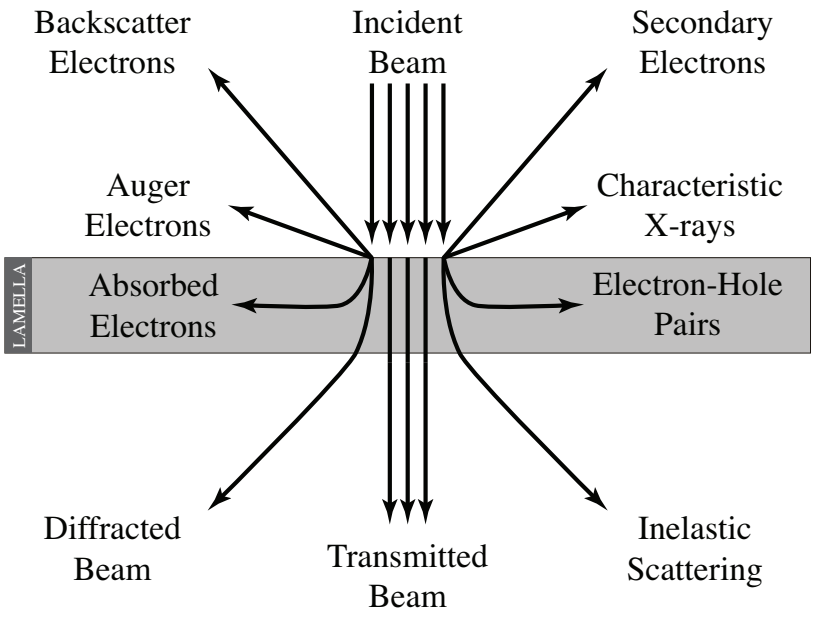

as well as emission of photons in samples with suitable electronic properties. The interaction between the sample and the electron beam also results in the generation of X-rays both characteristic of the elements present in the sample and bremsstrahlung radiation, which forms a continuous background radiation. Last, when we consider the electron beam as an incident wave of radiation the interaction with the specimen can result in scattering of the electrons in the forward and backward directions. This scattering can take the form of inelastically scattered electrons, for which some energy is lost through the interaction, and elastically scattered electrons. The research here uses predominantly the data from the transmitted beam and the elastically scattered beams.

2.4.1. Imageing Modes in the Transmission Electron Microscope

The AEM has a number of different modes or configurations that can be used to collect data. These modes can be generally grouped into three categories: imaging modes, spectroscopic modes, and hyperspectral imaging modes. Imaging modes use detectors to collect a single scalar intensity value for each point in a pixel array. The signal is created either from the transmitted or elastically scattered beam directly. The data are collected either by scanning a focused electron beam, thus collecting the intensity values serially to create an image pixel by pixel, or by uniformly illuminating the specimen with incident electrons, thus collecting the intensity values in parallel with a position-sensitive detector. Spectroscopic modes use specialized spectrometers that record the energies and intensities of the characteristic x-rays, photoemission signal, or inelastically scattered electrons. Spectroscopic modes typically employ a parallel beam, which provides the average spectroscopic signal over the whole specimen, or a convergent electron beam which gives spectroscopic data for a particular point on the specimen. When spectral data are collected in parallel with image data, the resulting data cube is a hyperspectral data set. Specifically, the instrument collects an image intensity and a full spectrum at each pixel position. A statistical analysis of this multi-dimensional data cube correlates contrast information in the image with chemical information in the spectra. This study will mostly use imaging modes. The spectroscopic modes for the study either are not well suited for the systems being studied, as is the case with electron energy loss spectroscopy (EELS), or the spatial resolution is not yet sufficient for general use, as is the case with energy dispersive X-ray spectroscopy (EDS). Hyperspectral methods are likewise not suited for analysis of the systems studied here because of the difficulties with the spectroscopic component.

2.4.2. Parallel Beam Configuration

Microscopists use "TEM" to refer to an imaging mode where the sample is illuminated by a stationary and nominally parallel beam of electrons, as shown in Figure 2.13. This illumination condition is established as electrons from a source are passed through a series of electromagnetic lenses and apertures. These lenses and apertures are used to minimize the aberrations associated with imperfections in the lenses and to collimate the electron beam. The electron beam is then formed into a nearly parallel beam by the illumination-forming lens immediately before the specimen. The parallel beam is then passed through the specimen followed by an image-forming objective lens and aperture, and finally a projection system to further magnify the image. Modern TEM systems have immersion-type objective lenses, where the objective lens is split and the specimen stage placed between them in the so-called pole-piece gap. The immersion-type lens creates a more uniform field around the specimen and minimizes resolution-limiting third-order spherical aberration, which has a coefficient of the order of the focal length of the objective lens. Under parallel illumination conditions, contrast results from phase differences in the transmitted plane wave introduced by the electron-specimen interactions. Because the contrast is dependent on optical conditions, such as the degree of defocus, this "phase contrast" is not easily interpretable without calculation and modeling. TEM images were historically recorded on film or, more recently, image plates. In the last decade charge coupled devices (CCDs), or other solid state position-sensitive detectors have become predominant.

By altering the excitation of the projection lenses in such a way that they magnify the back focal plane of the objective lens rather than the image plane, a diffraction pattern may be created. Since the diffraction pattern is formed from a selected area

FIGURE 2.13. Schematic representation of a transmission electron microscope and ray trace diagrams showing the optical paths of the beam in bright field imaging and dark field imaging or diffraction configurations.

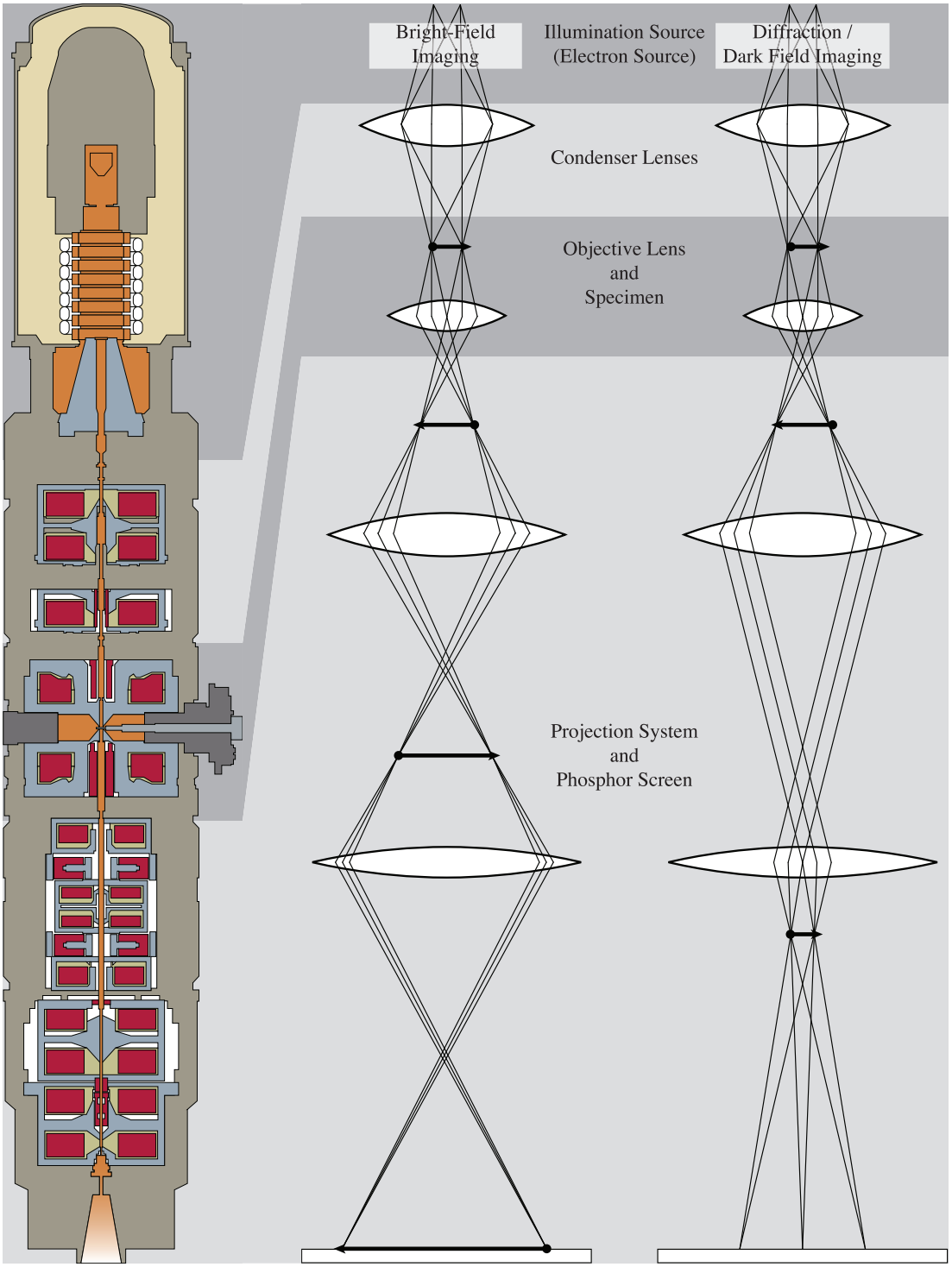

of the specimen (defined either by the illumination of the beam or the selected-area aperture), the resulting intensity distribution is called a selected area electron diffraction (SAED) pattern. An aperture in the back-focal plane of the objective lens can be used to select a specific diffracted beam (reflection) in the SAED. Returning to imaging mode results in an image created using only electrons of the selected reflection, resulting in a dark field (DF) TEM image.

2.4.3. Convergent Beam Configuration

By altering the configuration of the condenser and objective lenses, as shown in Figure 2.14., it is possible to create a focused electron probe at the plane of the specimen. The probe geometry is dependent on the diameter of the last condenser aperture, with larger apertures producing a higher current density, but at the cost of a more narrow depth of focus, greater potential for beam damage, and inaccuracy in chemical sampling. Since the beam is focused on the specimen all optical planes that would otherwise contain an image will contain an image of the convergent beam. The diffraction planes will have a disk with a radius proportional to the diameter of the probe forming aperture. By moving the cross-over points as before with the SAED pattern a convergent beam electron diffraction (CBED) pattern is formed at the image plane of the microscope. CBED patterns are generally recorded using the same methods used for TEM and SAED imaging. An important variation on the CBED pattern involves using a series of scan coils positioned before the objective lens to move the probe position on the specimen in a raster pattern. This method is referred to as scanning transmission electron microscopy (STEM). The CBED pattern for each point of the raster will reflect the local structure of the specimen directly under the probe. By placing an annular detector in an optical plane conjugate

to the back focal plane of the objective lens, it is possible to collect all diffracted electrons in a band of transverse momentum vectors $q_{min} < |\mathbf{q}| < q_{max}$ while allowing the central ($|\mathbf{q}| = 0$) transmitted beam to pass, potentially to be intercepted by other detectors on the instrument. This detector, which averages intensity variation in the azimuthal direction, is referred to as an annular dark field (ADF) detector. If the annular detector is designed to collect only electrons scattered with transverse momenta large in comparison with the characteristic reciprocal lattice vectors ($q_{min} \gg 1/d$), the detector is referred to as a high angle annular dark field (HAADF) detector. By recording the integrated intensity from the HAADF detector at each point in the raster, an image can be generated that is dependent on the incoherent elastic scattering of the atoms sampled by the probe. This incoherent elastic scattering exhibits a strong atomic number dependence ($Z^n, n > 1$), approaching that of the relativistic Rutherford cross-section ($n = 2$) at large q_{min} [153–156]. Since the major contributing factor to the number of counts recorded for a particular pixel is the mean-Z under the probe, images produced in this manner are also referred to as Z-contrast images. The use of a scanned focused probe in conjunction with a spectroscopic detector such as an EDS detector also allows the STEM to collect local chemical information that is characteristic of individual elements, and thus is more quantitative than Z-contrast imaging.

2.4.4. Methodological Choices

This work will rely primarily on STEM-HAADF imaging. Because of the complex crystal structures generated in this study phase contrast images are more difficult to interpret. This would require significant time to do the simulation series and the exit wave reconstructions to reliably interpret the resulting images. Considering the

FIGURE 2.14. Schematic representation of an aberration corrected a scanning transmission electron microscope with a ray trace diagram showing the optical path of the convergent beam and the positions of the bright field and high angle annular dark field detectors.

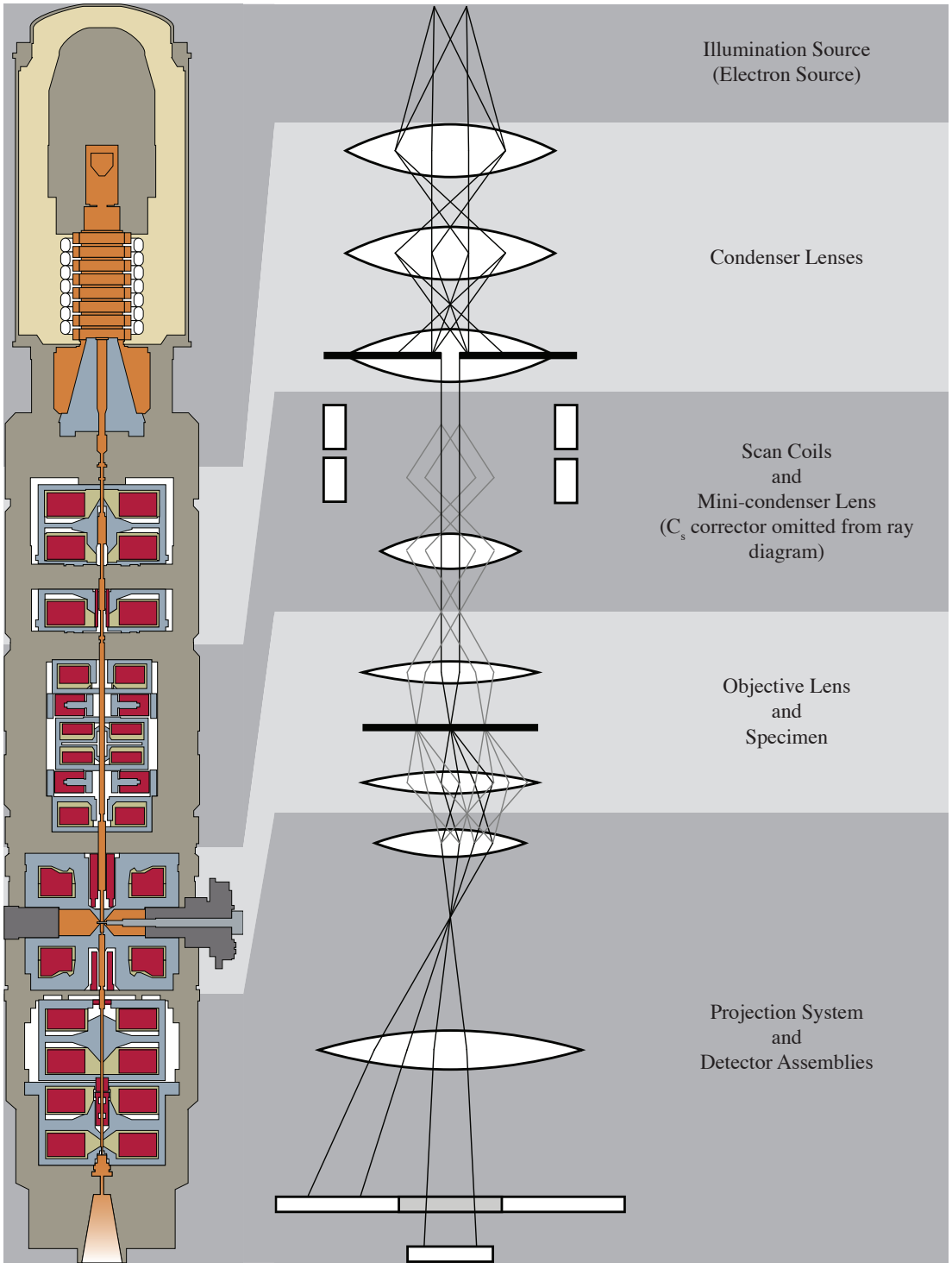

TABLE 2.4. Mean atomic number for compounds considered in this work.

Compound	Element (Z)			$\bar{Z}$
PbSe	Pb (82)	Se (34)		58
WSe_2	W (74)	Se (34)		71
$MoSe_2$	Mo (42)	Se (34)		55
FeSe	Fe (26)	Se (34)		30
$NbSe_2$	Nb (41)	Se (34)		54.5
$CuCr_2Se_4$	Cu (29)	Cr (24)	Se (34)	106.5

chemical make-up of each structure, the mean-Z values for the components, with the exception of the $[\{(FeSe)_m\}_{1+y}(NbSe_2)_n]_r$ system, are distributed over a wide range as shown in Table 2.4. The wide range of Z-values and easily interpretable image data make the STEM-HAADF an ideal choice for structural characterization in this work.

2.4.5. Sample Preparation

Samples were prepared for TEM analysis using a variation on the small angle cleavage technique (SACT) developed by McCaffrey et al.[157]. The technique itself is well documented in the literature[153,157,158] and only the modifications to the technique used in this work are detailed here. After initial thinning of the substrate, but before cleavage, the wafer was covered with a layer of protective carbon using a black permanent ink felt tip marker. The specimen was then prepared in the manner detailed in the previous references. After preliminary screening in a conventional TEM, samples were thinned for aberration corrected STEM analysis using an FEI NOVA NanoLab DualBeam™ focused ion beam (FIB) equipped with a Sidewinder™ ion column. Samples were thinned to approximately 300 nm using a 30 kV accelerating voltage, followed by polishing at 5 kV and 2 kV. Samples were plasma cleaned using

a Fischione 1020 plasma cleaner for between 1 min and 5 min prior to STEM analysis to remove residual carbon contamination.

2.4.6. STEM Configuration

Aberration corrected STEM HAADF imaging, SAED, and CBED were performed with an FEI Titan 80-300^{TM} TEM/STEM operating at an accelerating voltage of 300 kV and equipped with a double hexapole, spherical aberration corrector (CEOS GmbH), resulting in an ≈ 100 pm diameter probe of ≈ 90 pm probe current. Excepting special situations, imaging was typically conducted using a 40 µm probe forming aperture, resulting in a convergence semiangle of ≈ 12.7 mrad.

2.5. Magnetic Characterization

Magnetic measurements were carried out using a superconducting quantum interference device (SQUID) magnetometer. Both the Quantum Designs MPMS operating in DC or the Quantum Designs SVSM operating at 14 Hz were used. Significant care was taken to prevent contamination of the samples, including, but not limited to, handling of the samples only with enamel coated tweezers to prevent contact transfer of ferromagnetic atoms. Samples were mounted to silica sample rods using VGE-7031 varnish for SVSM measurements parallel to the field and to Lake Shore Kel-F perpendicular holders for MPMS measurements perpendicular to the field. After resetting the magnet to remove any trapped flux in the superconducting magnet, so that subsequent background subtractions start from a known state, hysteresis loops were measured at fixed temperatures (usually 5 K) starting from $+5.6\,\mathrm{MA\,m^{-1}}$ to $-5.6\,\mathrm{MA\,m^{-1}}$ and back to $+5.6\,\mathrm{MA\,m^{-1}}$ (a +70 kOe to −70 kOe to +70 kOe cycle of externally applied field). The data were normalized for sample mass

and background corrections for the sample mountings and Si/SiO_2 substrate. The temperature-dependent magnetization data were measured solely on the SVSM at 14 Hz. These samples were mounted, as before, to silica sample rods using VGE-7031 varnish for SVSM measurements parallel to the field. After cooling to 5 K in zero field, the field was set to $160\,kA\,m^{-1}$(2000 Oe) and the magnetization was measured in the field on warming and cooling.

CHAPTER III

NUCLEATION AND GROWTH KINETICS OF CO-DEPOSITED Cu AND Se PRECURSORS TO FORM METASTABLE COPPER SELENIDES

3.1. Co-authorship Statement

Chapter III details the analysis of the reaction kinetics of the Cu-Se system in the nucleation limited domain. The initial work for this chapter was conducted by Dr. John O. Thompson, Tim Ngai and Thomas Allen. Michael D. Anderson was responsible for the drafting of the paper from which this chapter is derived. Significant portions of the work relating to the Cu-Se diffusion and nucleation kinetics were also experimentally verified by Michael D. Anderson. Dr. David C. Johnson provided editorial support.

3.2. Introduction

In the electronics industry, circuits and display devices are fabricated by sequential layer deposition interspersed with annealing steps to arrive at a desired, often kinetically stable, structure. Since most films are deposited under conditions far from equilibrium, the structural changes and/or reactions between the films cannot be predicted solely from phase diagrams. Indeed, as early as 1958, Brewer[159] reiterated that it is very common for intermediate metastable phases to form before reaching the stable product distribution, especially when the system is far from equilibrium. Qualitatively, these metastable phases correspond to a local minimum on the free energy surface for the reaction, as indicated in Figure 3.1. Because of the high energy

condition of the amorphous precursor and the small activation energy, $E_{a,1}$, and small exothermic energy of formation, $\Delta G^{\circ}_{f,1}$, for the metastable phase relative to the thermodynamic product, it is possible to stabilize the intermediate phase by introducing a relatively small amount of energy into the system. The stabilization, or trapping, of the metastable phase is accomplished by not introducing sufficient energy into the system to overcome the large activation energy, $E_{a,2}$, required to form the thermodynamic product. In the 70s this concept was capitalized on by metallurgists seeking novel metallic glasses[160–162]. More recently the concept has been used by materials scientists employing layered precursors to produce the amorphous intermediate which was used to control the resulting product distribution of the reaction[13,14,31,122,124,125,163,164]. Still more recently this area has been studied by a number of solid state synthetic groups with a variety of new systems[165–169]. Understanding and controlling the evolution of deposited films is crucial for the successful manufacture of todays thin film electronic devices including solar cells, integrated circuits, and display technologies.

The manufacture of copper indium-gallium diselenide (CIGS) thin-film solar cells demonstrates the importance of controlling the kinetics during processing. CIGS based photovoltaics have been the subject of active research for many years due to the desirable benefit-to-cost ratio brought about by the materials exceptional optical absorption coefficient and reasonable cell efficiency, as high as 18%[170–174]. To produce the most efficient CIGS solar cells, a three-step process is employed. A molybdenum-coated glass substrate is heated and exposed to an indium-gallium-selenium flux that both grows an $(In,Ga)_2Se_3$ coating and creates a molybdenum selenide layer as an ohmic contact. The flux is then shifted to copper and selenium, which converts the $(In,Ga)_2Se_3$ layer into a copper-rich CIGS layer, the excess copper having been shown

FIGURE 3.1. Schematic diagram of the reaction path for formation of metastable intermediate phases from an amorphous precursor. The important features to note are the small activation energy, $E_{a,1}$, and small exothermic energy of formation, $\Delta G^{\circ}_{f,1}$, for the metastable phase relative to the thermodynamic product. The actual stabilization or trapping of the metastable phase is further enhanced by the larger activation energy, $E_{a,2}$, to form the thermodynamic product.

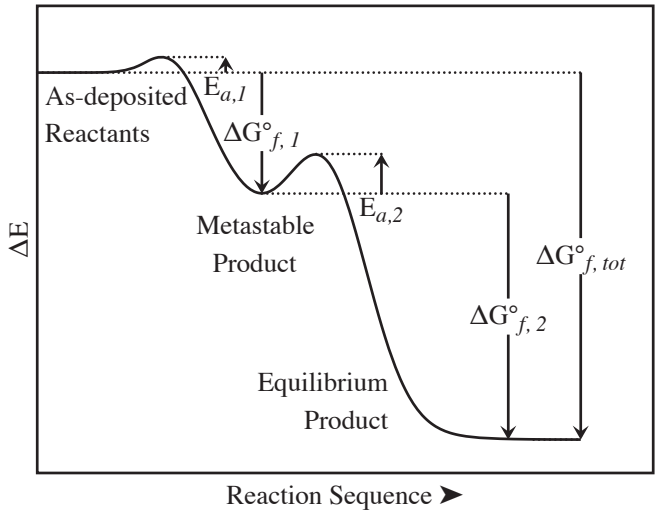

to enhance grain growth in the film[172,175]. In the final step, additional indium is added to adjust film composition, avoiding copper selenide impurity phases[170]. In this and other approaches to the synthesis of CIGS films, it is important to avoid copper selenide binary compounds in the final product as the presence of Cu-Se phases in the copper indium selenide (CIS) produce recombination sites for the minority charge carriers, reducing overall cell performance[176–178].

The use of CuSe and $CuSe_2$ as precursors in the synthesis of and their presence as secondary phases in copper indium diselenide prompted this study of the nucleation and growth kinetics of the selenium-rich portion of the copper-selenium phase diagram. Copper-selenium binary compounds have previously been investigated for their photovoltaic properties[176,179–182]. Additionally, CuSe has been used as a precursor layer for the formation of copper indium diselenide

from a selenized stacked elemental layer[183–185]. CuSe and orthorhombic $CuSe_2$ have been identified as impurity phases in copper indium diselenide grown by electrodeposition and vacuum deposition processes[186–188]. Binary copper-selenium compounds have been made by several methods including melt techniques[189–191], mechanical alloying[192], electrodeposition[193], plasma-assisted selenization[194], and at aqueous-organic interfaces[195]. This paper examines the evolution of precursors prepared by co-depositing the elements on a cold substrate. Surprisingly, we observed the nucleation and growth of the metastable cubic phase of $CuSe_2$ over a broad compositional range and are able to prepare single-phase samples of this metastable compound by controlling annealing conditions.

3.3. Experimental

The co-deposited copper-selenium films described in this study were prepared in a custom built high vacuum chamber. Copper was deposited with an electron beam gun and selenium was deposited with an effusion cell. The fluxes of each element were monitored by a quartz crystal microbalance. The deposition rates of the two elemental sources were varied between $0.01\,\mathrm{nm\,s^{-1}}$ and $0.1\,\mathrm{nm\,s^{-1}}$ to achieve the desired compositions. Copper and selenium were simultaneously deposited onto a rotating 150 mm diameter silicon wafer located approximately 56 cm above the elemental sources. The wafer was coated with poly(methylmethacrylate) (PMMA), which was later dissolved in acetone to release the deposited material for collection on filter paper and later use in differential scanning calorimetry (DSC) and X-ray diffraction (XRD) experiments. A small chip of silicon was also attached to the surface of the silicon wafer for use in compositional analysis. The target wafer was not actively heated or cooled during deposition. Film thicknesses for the as-deposited

precursors were selected to ensure sufficient quantity of sample for analysis, on the order of 200 nm.

The composition of the co-deposited copper-selenium thin films was determined by electron probe microanalysis (EPMA) using the film deposited directly on silicon. A Cameca SX-50 microprobe was used to collect the x-ray emission data from the thin film samples and standards consisting of elemental copper, selenium, and silicon. Data were collected at three different accelerating voltages in order to quantify the contributions of deposited film and underlying substrate at different electron beam depth distributions. The x-ray emission counts from the copper-selenium thin films and the silicon substrate relative to the elemental standards were modeled using the Pouchou-Pichoir method[144,149–152] as implemented in the StrataGem software package to determine the composition of the copper-selenium layer. SEM images of the films acquired during the EPMA analysis were found to be featureless, suggesting film homogeneity, and no further imaging was undertaken.

Heat flow from each copper-selenium sample was quantified using DSC. All DSC data were collected on a TA Instruments model 2920 DSC. Samples of the copper-selenium films freed from the PMMA-coated wafer were weighed and sealed in aluminum pans for analysis. Sample weights varied between 0.1 mg and 1 mg. Heat flow data were collected in a nitrogen atmosphere to prevent sample oxidation. DSC scans are plotted with exotherms in the upward direction.

A Scintag XDS 2000 θ-θ geometry diffractometer with a Cu-K_α x-ray source was used to collect XRD patterns and establish the presence and identification of crystalline phases in the as-deposited and thermally annealed powder samples. Diffraction data from the flake-like samples demonstrated significant texturing, affecting the relative intensities of the diffraction maxima in the XRD patterns.

Because of the significant texturing, Rietveld analysis of the phases in the samples was deemed impractical for the scope of this work and XRD patterns were compared to JCPDS patterns for identification purposes.

3.4. Results and Discussion

An initial suite of eleven samples was prepared by co-depositing the elements onto a cold substrate while varying the ratio of the deposition rates to prepare samples of between 51%* and 81% selenium. The EPMA data for these samples demonstrated a uniform composition across the films. The aggregate compositions as determined by EPMA are shown superimposed on the bottom axis of the phase diagram in Figure 3.2. The phase diagram contains three copper-selenium compounds with the nominal compositions Cu_2Se, CuSe, and $CuSe_2$. The copper-rich phase is cubic and exhibits an appreciable range of homogeneity at selenium-enriched compositions, and thus can be designated $Cu_{2-x}Se$. The two selenium-rich compounds are essentially line compounds, exhibiting a negligible range of homogeneity; however, these compounds each have several stable polymorphs[189–191]. The CuSe phase has three polymorphs, denoted α, β, and γ. The form of CuSe stable at room temperature is hexagonal α-CuSe, which undergoes a reversible polymorphic change to orthorhombic β-CuSe at 51 °C and a subsequent reversible polymorphic change to hexagonal γ-CuSe at 120 °C. γ-CuSe peritectically disproportionates into β-$Cu_{2-x}Se$ and a selenium-rich liquid phase at 377 °C. $CuSe_2$ has two polymorphs, only one of which is stable at ambient pressure. This thermodynamically stable phase is orthorhombic and peritectically disproportionates into γ-CuSe and a selenium-rich melt at 332 °C. The orthorhombic phase is grown through slow cooling from a melt[191]. A metastable polymorph is cubic

*All compositions in Chapter III are quoted as atomic percent.

FIGURE 3.2. Reproduction of the copper-selenium binary phase diagram[196] for compositions between 48% and 85% selenium. The red triangles located above the x-axis represent the compositions of samples prepared in this investigation as determined by EPMA. The full phase diagram is reproduced in Appendix C

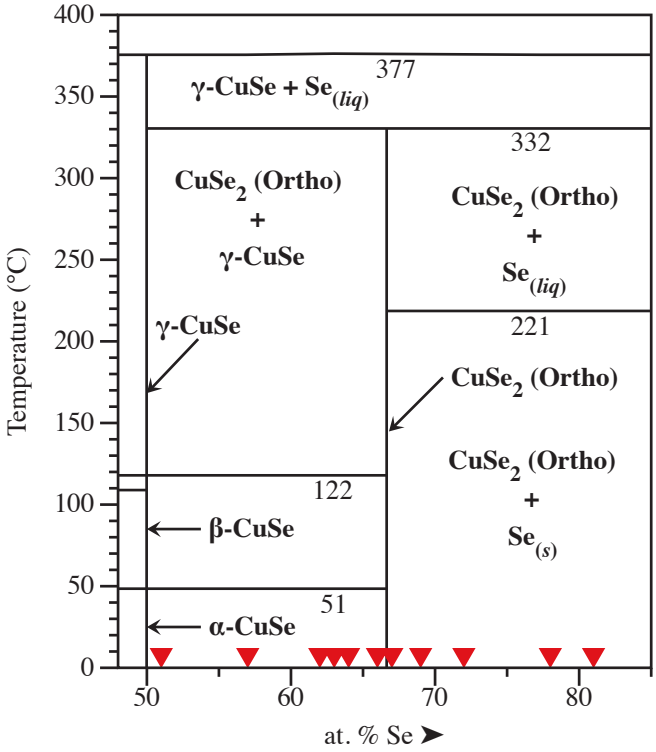

and is prepared by annealing orthorhombic $CuSe_2$ at 12 kbar and 420 °C for two hours followed by rapid cooling[191].

The phase diagram, however, does not predict the identity of compounds that will preferentially form from a co-deposited precursor with a specific composition nor does it predict the temperatures where compounds will form, which can be a function of prior annealing conditions and heating rate. Given the homogeneity of the film composition with respect to EPMA, these formation events will require an annealing induced fluctuation in the local composition. To probe the temperatures at which compounds form and the temperatures where phase transformations and decompositions occur, all of the samples prepared as part of this study were examined

using DSC. The copper rich compound, Cu_3Se_2, was not observed in the composition range and annealing conditions we investigated. Since the phase diagram is based on the formation of phases from a slowly cooling melt and the DSC scans in this study are on samples being slowly heated from a metastable precursor, the phase formation at low temperatures may not align with the phase diagram but equilibrium phases that have formed will undergo phase transitions at the temperature indicated on the phase diagram.

Figure 3.3. shows DSC scans of the as-deposited and delaminated flake samples that were heated at a rate of $4\,^{\circ}\mathrm{C\,min^{-1}}$. Consistent with the phase diagram, all scans indicate a sharp pronounced endothermic transition at 377 °C that corresponds to the peritectic decomposition of γ-CuSe to β-$Cu_{2-x}Se$ and a selenium-rich melt. The DSC behavior of the films below 377 °C divides the samples into three distinct groups. The five films containing 67% or higher selenium content exhibit sharp endothermic transitions at 221 °C and 333 °C, corresponding to the melting of the selenium solid solution and the peritectic decomposition of $CuSe_2$, respectively. Conversely, the four films with compositions between 60% and 67% selenium exhibit broad endothermic transitions with onsets below 333 °C, as well as a slight broad exothermic transition at approximately 180 °C. The two films with compositions between 50% and 60% selenium exhibit a small but sharp endothermic transition at approximately 130 °C, suggesting that α-CuSe has already formed in these films below this temperature.

To identify the compounds forming at each of the observed phase transitions, diffraction data were collected from samples that were annealed at selected temperatures and then cooled to room temperature. XRD data collected from a 51% selenium sample, which is representative of the data obtained on samples with compositions between 50% and 60% selenium, is shown at various annealing

FIGURE 3.3. DSC scans of co-deposited Cu-Se samples with compositions between 51% and 81% selenium performed at a heating rate of $4\,^{\circ}\mathrm{C\,min^{-1}}$. Exothermic transitions are indicated in the upward direction. Scans are arbitrarily offset vertically with percent of selenium, shown on the left, increasing as you move up the figure. The identities of the major endothermic transitions expected from the phase diagram in Figure 3.1. are indicated.

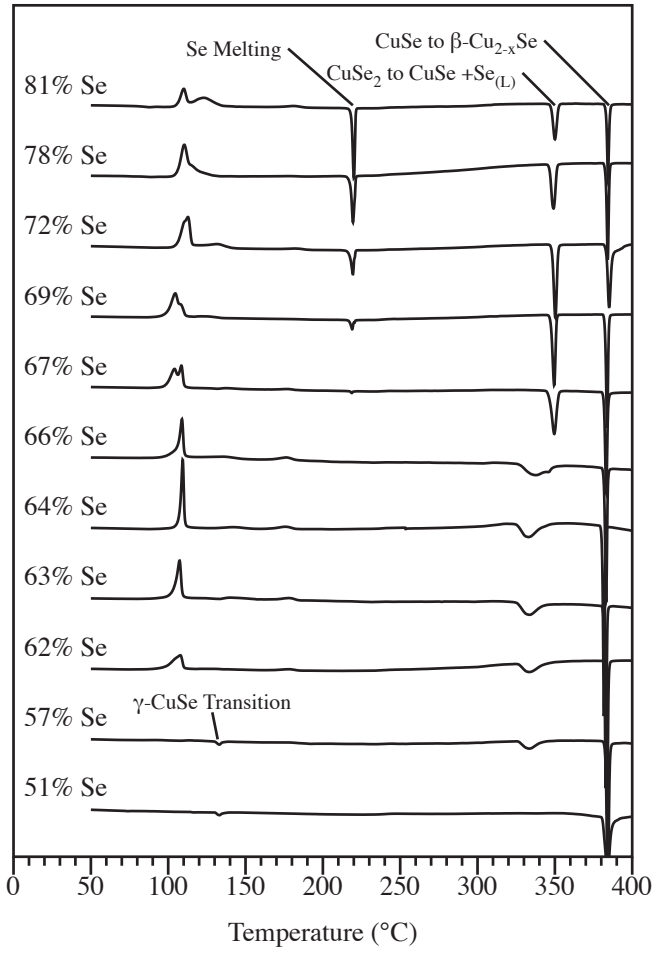

temperatures in Figure 3.4. The samples were annealed using a DSC scan to the indicated temperatures and cooled to room temperature for the diffraction scans. The two original and a second set of samples prepared with selenium composition between 50% and 60% were found to have formed α-CuSe during the deposition process; although broadened due to internal strain, all diffraction peaks could be indexed to α-CuSe. The small, reversible endothermic transition present in the DSC scan at 130 °C may result from the β-CuSe to γ-CuSe phase transition, which is expected at 120 °C; however, since we do not observe any heat signal for the α-CuSe to β-CuSe phase transition expected at 51 °C, it is possible that the 130 °C transition reflects the conversion of α-CuSe directly to γ-CuSe. The diffraction data show continued grain growth of α-CuSe with increasing temperature, as indicated by the narrowing of the diffraction peaks. After annealing at 320 °C, the size of the α-CuSe crystallites have significantly increased due to Ostwald ripening in the solid state and $CuSe_2$ appears as a minor second phase, consistent with the phase diagram. The amount of $CuSe_2$ increases in the diffraction patterns as the selenium concentration of the samples increases. The broad, reversible endothermic transition centered at 330 °C, which increases in magnitude as selenium concentration increases up to 67% selenium, has been shown by Murray[191] to denote the slow conversion of $CuSe_2$ to γ-CuSe and liquid selenium. At compositions above 66% selenium, liquid selenium is present at these temperatures, and the broad endothermic transition is replaced by a sharp, reversible endothermic transition at 332 °C. This sharp endothermic transition is also from the reversible conversion of $CuSe_2$ to γ-CuSe plus liquid selenium, as indicated in the phase diagram[191]. The temperature range and rate of this conversion is different for samples containing a selenium-rich melt versus those comprised completely of solid phases and it is surprising that the solid-state reaction starts at a lower temperature.

FIGURE 3.4. XRD data for the sample containing 51% selenium annealed to indicated temperatures in a DSC at a rate of 4 °C min^{-1} and cooled. The numbers above the red triangles are the *hkl* indices of the diffraction peaks of hexagonal α-CuSe and the numbers above the blue triangles are the indices of the diffraction peaks for orthorhombic $CuSe_2$.

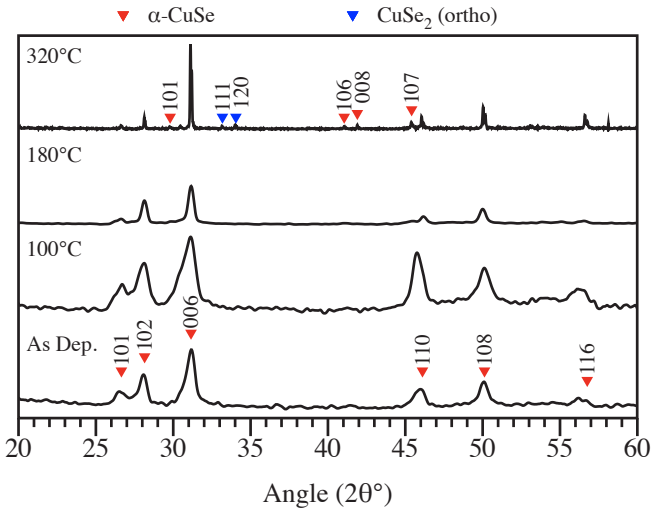

The four films with compositions between 60% and 67% selenium all have an exothermic transition that begins below 100 °C, as well as a slight exothermic transition at approximately 180 °C. Figure 3.5. shows XRD scans collected from a powder sample containing 64% selenium, which is representative of the samples with selenium compositions between 62% and 66% selenium. As deposited, the samples are x-ray amorphous, and both hexagonal CuSe and cubic $CuSe_2$ have nucleated and grown after heating to 115 °C, past the irreversible exothermic event that begins below 100 °C. Since our diffraction data are collected after cooling the film to room temperature, we do not know which polymorph of CuSe nucleates during this exotherm. We were surprised to observe the formation of the metastable, high-pressure cubic polymorph of $CuSe_2$. Diffraction scans collected on samples annealed above the 180 °C irreversible exothermic event show both grain growth of cubic $CuSe_2$ and the first appearance of the thermodynamically stable hexagonal $CuSe_2$

FIGURE 3.5. XRD data for a sample containing 64% selenium and annealed in a DSC at a rate of $4\,^{\circ}\mathrm{C\,min^{-1}}$ to the indicated temperatures and cooled to room temperature. The labels near the diffraction maxima are the indexed diffraction peaks of the observed phases.

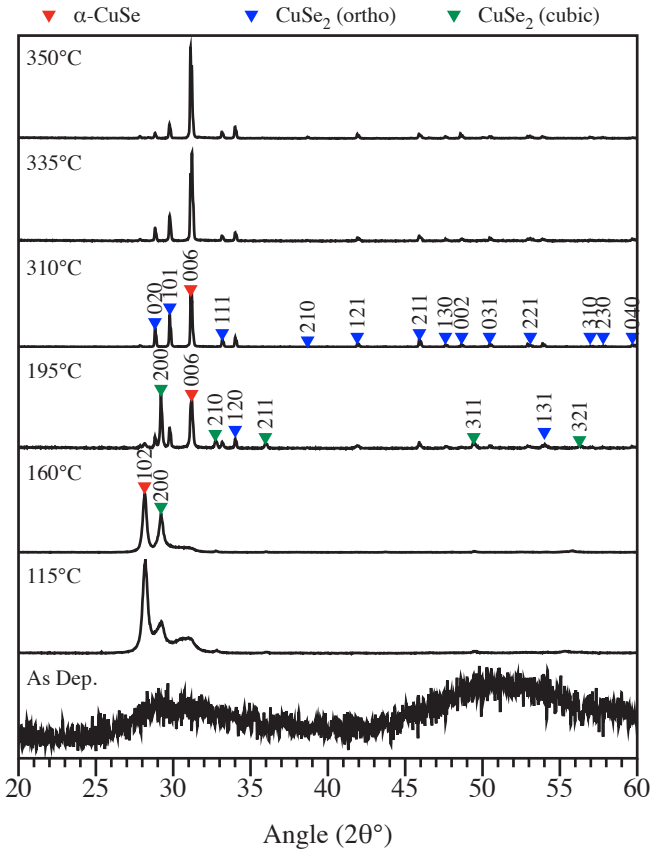

polymorph. At higher annealing temperatures, the broad, reversible endothermic transition centered at 330 °C correlates with the conversion of $CuSe_2$ to γ-CuSe and a selenium-rich melt. Only orthorhombic $CuSe_2$ is apparent in the diffraction patterns after annealing to temperatures above this endotherm, with the relative intensity of the α-CuSe diffraction peaks varying as expected from the application of the lever rule to the phase diagram. We do not observe the weak endotherm at 130 °C seen in samples with 50% to 60% selenium, presumably due to the small amounts of CuSe in these more selenium rich samples.

The DSC data of the five films containing 67% or more selenium differ from those containing between 60% and 67% selenium by having a broader exotherm with two heat flow maxima at around 100 °C, a reversible endothermic transition at 221 °C corresponding to the melting of selenium and a sharp endothermic transition at 333 °C. The slight irreversible exothermic transition at approximately 180 °C seen in the samples with 60% to 67% selenium is still observed, but only barely in some samples. Figure 3.6. presents XRD data on powdered samples containing 68% selenium, which is representative of samples that are selenium rich of stoichiometric $CuSe_2$. These samples were observed to be X-ray amorphous as deposited. After the first irreversible exotherm near 110 °C, both α-CuSe and cubic $CuSe_2$ begin to nucleate and grow. The presence of α-CuSe is surprising since it is not present at this composition in the equilibrium phase diagram, yet is observed to form even in samples with as much as 79% selenium. There is little change in the diffraction pattern until annealing past the irreversible 180 °C exotherm, after which the α-CuSe phase disappears and the orthorhombic polymorph of $CuSe_2$ is clearly present. The orthorhombic phase appears to form from the reaction of α-CuSe with the excess selenium and perhaps also from the conversion from the cubic phase. The presence of selenium in these samples is indicated by an endotherm at 221 °C, the melting point of selenium, which becomes more pronounced with increased selenium concentration, as expected from the phase diagram. The melting of selenium leads to accelerated grain growth of orthorhombic $CuSe_2$ and a large decrease in the relative amount of the cubic polymorph of $CuSe_2$, which is no longer observed after annealing to 320 °C. The reversion to the equilibrium phase of $CuSe_2$ upon melt formation may reflect the consequent relaxation of internal strain within the film.

FIGURE 3.6. XRD data for a sample containing 68% selenium and annealed to various temperatures in a DSC to the indicated temperatures and cooled to room temperature at the maximum rate experimentally accessible in the instrument. Scan rates are $4\,^{\circ}\mathrm{C\,min^{-1}}$ unless otherwise indicated. The labels near the diffraction maxima are the indexed diffraction peaks of the observed phases.

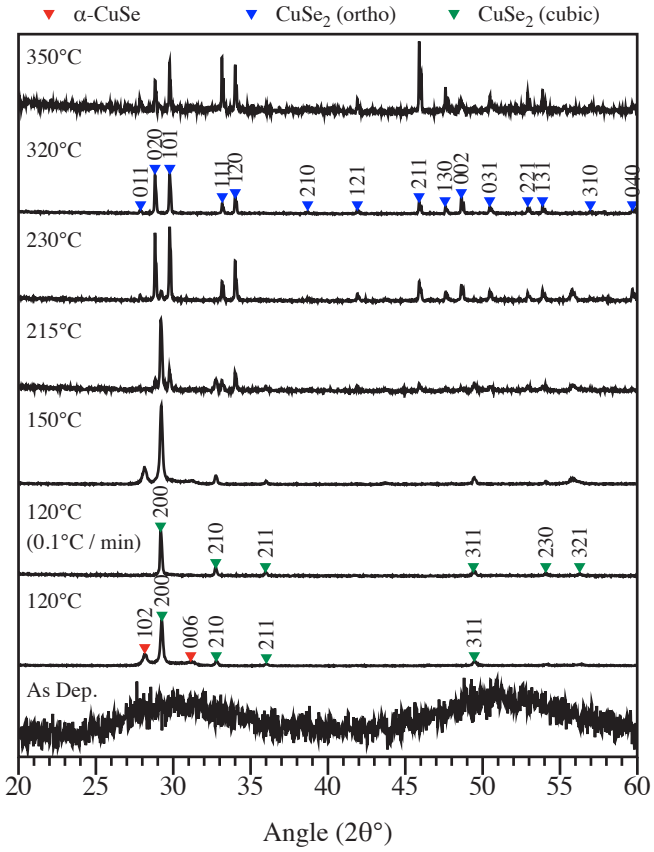

The variation of the relative amounts of α-CuSe and cubic $CuSe_2$ observed after annealing through the 100 °C exotherm leads us to further investigate the competition between the nucleation of α-CuSe and cubic $CuSe_2$ with a sample containing 67% selenium. As seen in Figure 3.3., the DSC at this composition has a distinctive double exotherm centered at 105 °C. Separate samples were heated at $4\,^{\circ}\mathrm{C\,min^{-1}}$ and $10\,^{\circ}\mathrm{C\,min^{-1}}$ to a temperature above the double exotherm with the DSC results presented in Figure 3.7. and the XRD patterns that were collected on each sample presented in Figure 3.8. The DSC results clearly indicate that a decrease in heating rate results in an increase in the magnitude of the first exotherm at the expense of the second. The XRD patterns indicate that the slower heating rate resulted in the formation of more of the metastable cubic $CuSe_2$ phase rather than the α-CuSe phase. This strongly suggests that the first DSC peak represents the nucleation of cubic $CuSe_2$ and the second is the nucleation of α-CuSe. Confirming this hypothesis, if the DSC heating rate is reduced to $0.1\,^{\circ}\mathrm{C\,min^{-1}}$ almost phase pure cubic $CuSe_2$ is produced as shown in Figure 3.6.. The metastable cubic $CuSe_2$ phase nucleates more quickly at a lower temperature than the orthorhombic $CuSe_2$ phase.

The composition near 66% selenium is unique in that only cubic $CuSe_2$ forms during the first exothermic event between 100 °C and 110 °C as shown in the diffraction patterns contained in Figure 3.9. Since only one phase forms at 110 °C, DSC data was collected at heating rates from $0.1\,^{\circ}\mathrm{C\,min^{-1}}$ to $10\,^{\circ}\mathrm{C\,min^{-1}}$ to determine the activation energy for nucleating cubic $CuSe_2$. Each sample was characterized by XRD to confirm that only the cubic $CuSe_2$ phase formed and to determine the lattice parameter ($a = (0.6116 \pm 0.0001)\,\mathrm{nm}$), which agrees with the published value[191]. Non-isothermal DSC data can be analyzed using a Kissinger analysis, for which the activation energy is obtained from the peak temperature of the DSC exotherm, T_p,

FIGURE 3.7. DSC scans for 67% selenium samples at heating rates of $4\,^{\circ}\mathrm{C\,min^{-1}}$ and $10\,^{\circ}\mathrm{C\,min^{-1}}$. The higher heating rate results in an increase in the magnitude of the second peak.

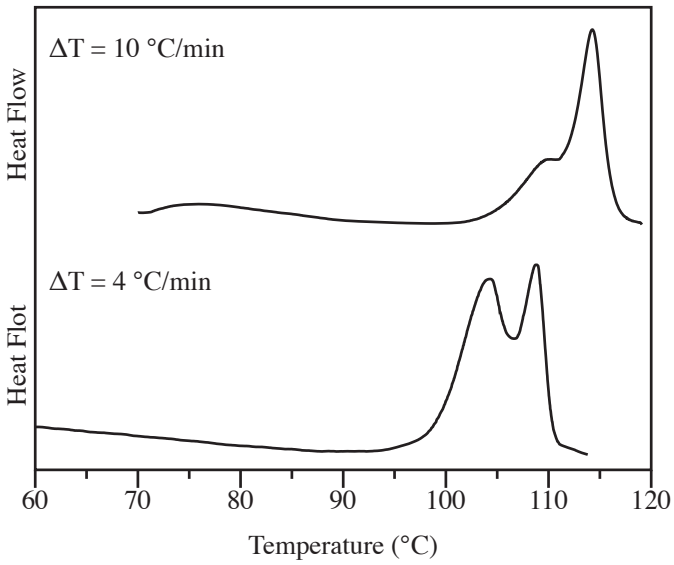

FIGURE 3.8. XRD patterns of 67% selenium samples heated at $4\,^{\circ}\mathrm{C\,min^{-1}}$ and $10\,^{\circ}\mathrm{C\,min^{-1}}$. The slower heating rate favors the formation of cubic $CuSe_2$.

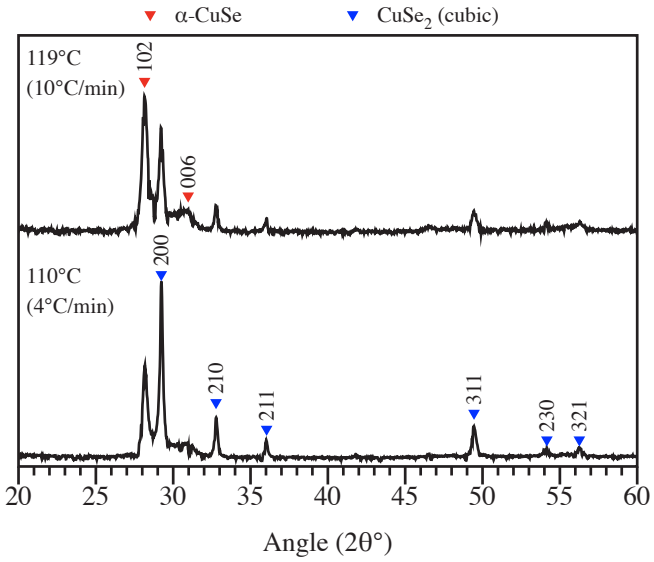

FIGURE 3.9. XRD data for a sample containing 66% selenium annealed to various temperatures at a DSC at a rate of 4 °C min^{-1}. The labels near the diffraction maxima are the indexed diffraction peaks of the observed phases.

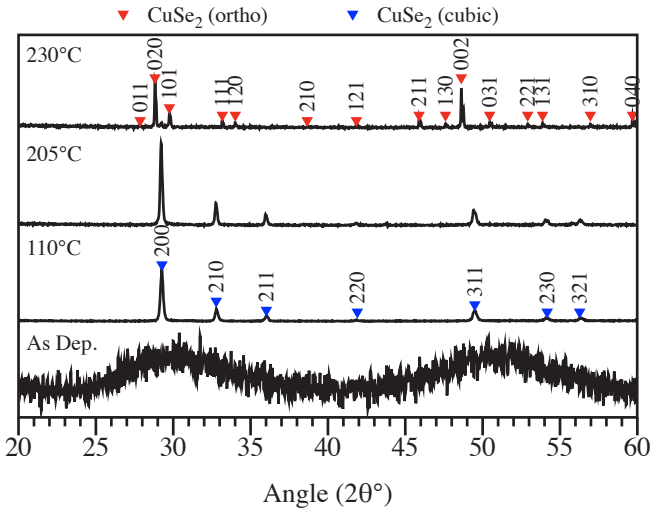

as a function of thermal scan rate Q[197]:

$$\frac{d\ln[Q/T_p^2]}{d[1/T_p]} = \frac{-E_{cryst}}{R} \qquad \text{(Equation 3.1.)}$$

where R is the gas constant. Graphing $\ln[Q/T_p^2]$ versus $1000/T_p$ gives a straight line, as shown in Figure 3.10., with a slope equaling $-E/R$ from which the activation energy for the nucleation and growth process is extracted. The activation energy for nucleation was determined to be 1.6 eV. The use of this equation requires a series of assumptions based on the nucleation mechanism, the composition of the amorphous and crystalline materials, and growth rate[198]. Specifically, the equation presented above assumes that the growth process follows a Johnson-Mehl-Avrami relationship, has a uniform composition around the nucleation and growth event, and that that the nucleation and growth are constant for a given temperature.

FIGURE 3.10. Kissinger plot used to derive the activation energy for nucleation of cubic $CuSe_2$. DSC heating rates used for the Kissinger plot were $0.1\,^{\circ}\mathrm{C\,min^{-1}}$, $1.0\,^{\circ}\mathrm{C\,min^{-1}}$, $4.0\,^{\circ}\mathrm{C\,min^{-1}}$ and $10\,^{\circ}\mathrm{C\,min^{-1}}$. The arguments of the logarithm were made unitless by dividing by the constant $T_{\circ}^2/Q_{\circ}$ where $T_{\circ}$ is 1000 K and $Q_{\circ}$ is $1\,\mathrm{K\,min^{-1}}$.

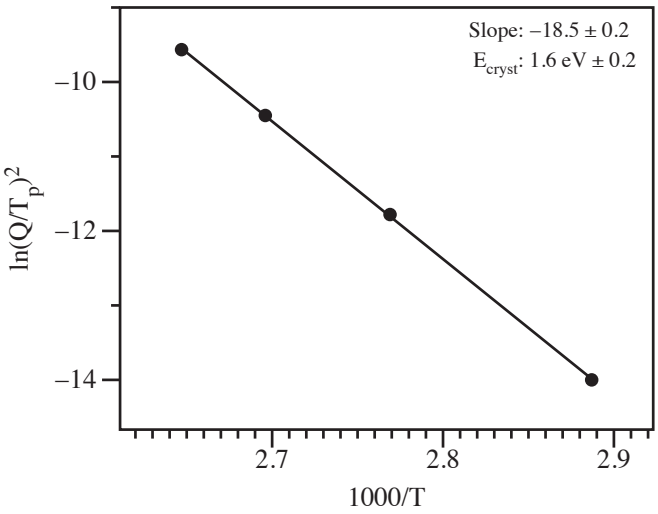

The low-temperature diffusion of copper in chalcogenides has been previously observed to lead to the formation and reordering of copper selenide over extended time periods under ambient conditions. Murray found that new XRD reflections had appeared in a seven-year-old sample of CuSe, indicating a slow ordering process[191]. More recently, Ohtani synthesized Cu_3Se_2 in an ambient temperature solid-state reaction between α-CuSe and α-Cu_2Se, the stable polymorph of this compounds at ambient temperature, over a span of several days[192]. The formation of the metastable cubic $CuSe_2$ at 100 °C and these prior reports prompted us to collect diffraction patterns on three powder samples that were stored in vials at ambient temperature for 44 months. The sample containing 72% selenium remained amorphous and the sample at 57% selenium remained unchanged with the presence of small CuSe crystallites. The sample containing 64% selenium crystallized both cubic $CuSe_2$ and α-CuSe with cubic $CuSe_2$ being the dominant phase. This further confirms that the metastable

cubic $CuSe_2$ polymorph is easier to nucleate than the more thermodynamically stable orthorhombic form at low temperatures.

3.5. Conclusions

In the phase formation of copper selenides from co-deposited precursors, non-equilibrium compounds preferentially formed, demonstrating the importance of nucleation kinetics. α-CuSe was observed to form over a broad compositional range. This range extended beyond the region of the phase diagram where the α-CuSe phase is thermodynamically stable. α-CuSe is kinetically stable in films with compositions above 67% selenium at low temperatures, but decomposes upon annealing above 140 °C by reacting with excess selenium to form orthorhombic $CuSe_2$. The low-temperature nucleation of cubic $CuSe_2$ instead of the thermodynamically stable orthorhombic polymorph was observed over a wide range of selenium-rich compositions. The composition containing 66% selenium distinguished itself by forming phase pure cubic $CuSe_2$ at heating rates up to $10\,^{\circ}\mathrm{C\,min^{-1}}$. At compositions close to stoichiometric, the cubic $CuSe_2$ phase preferentially nucleates relative to α-CuSe at slow heating rates. Cubic $CuSe_2$ is also the first phase to form at compositions above 67% selenium and its growth forces the remaining amorphous material to become further selenium enriched, providing a barrier to the nucleation of α-CuSe. The cubic $CuSe_2$ phase showed lower thermal stability than previously reported, converting to the stable orthorhombic phase near 200 °C.

3.6. Bridge

Before a synthesis of $CuCr_2Se_4$ could be undertaken it was important to develop a fundamental understanding of the diffusion and nucleation kinetics of the Cu-

Se system. Earlier work by Fister demonstrated that layer thicknesses with the compositionally modulated multilayer (CMM) are critical to avoid diffusion limited reaction conditions. This work provided the fundamental understanding for the Cu-Se system that was required to begin the design of the $CuCr_2Se_4$ CMM precursor. This work also identified an obstacle to a direct synthesis of $CuCr_2Se_4$ via compositionally modulated kinetic trapping (CMKT) in the form of the low energy of nucleation required to create copper selenide binary phases. This work specifically demonstrates that copper in close proximity to selenium will form binary copper selenides directly at relatively low temperatures, regardless of diffusion length.

CHAPTER IV

COMPOSITIONALLY MODULATED KINETIC TRAPPING: THE IMPLICATIONS OF CONTROLLED INTERMIXING ON SYNTHETIC PATHWAY CONTROL

4.1. Co-authorship Statement

Chapter IV is the result of a collaborative research project between Michael D. Anderson and Dr. John O. Thompson. The synthesis and characterization work related to the Cu-In-Se system was provided by Dr. Thompson. The balance of the work was conducted or overseen by Michael D. Anderson. Jourdain W. Roberts, Kristina Kirchgessner, and Logan LaRossa worked under Michael D. Anderson conducting data collection and preliminary analysis on the Cu-Cr-Se system. Dr. Andrew A. Herzing assisted with the scanning electon microscopy conducted on the $CuCr_2Se_4$ samples. Dr. Ian M. Anderson and Dr. David C. Johnson provided editorial support. The information contained in this chapter is being prepared for submission to *The Journal of The American Chemical Society*.

4.2. Introduction

A fundamental concept in molecular chemistry is the step-wise synthesis of complex molecules by a sequence of individual reactions or a sequenced addition of reactants that controls the reaction pathway. Protecting groups and catalysts are used either to establish or to enhance selectivity of the relative reaction rates of different sites of the reacting molecules, thus dictating intermediate and final reaction products. An understanding of the role of reactants, protecting groups and catalysts

in dictating reaction pathways can inform subsequent synthesis projects, thus enabling the design and synthesis of complex, metastable molecules using convergent reaction schemes. The increasing difficulty of such synthesis with both the number of atoms in the targeted molecule and the complexity of the molecular architecture can be somewhat mitigated by local bonding rules for metastable target molecules.

The synthesis of metastable, complex inorganic compounds is a distinctly different synthetic challenge than preparing a molecule. Preparing inorganic compounds with extended structures is similar to that of a specific crystalline polytype of a molecular crystal, in that it requires the organization of large numbers of atoms into an extended regular structure. While the development of molecular synthesis has enabled the design and synthesis of complex molecules, controlling the molecular packing of these molecules to form particular crystalline structures remains a fundamental challenge. Historically, the growth of crystals has used near-equilibrium growth techniques, with high diffusion rates (gas or liquid phases) and long times to grow crystals[126,128,129,131]. For extended inorganic structures, techniques based on epitaxy have created metastable structures consisting of intergrowths of different constituents based on controlling near-equilibrium surface and interface growth conditions[129,131].

The synthesis of extended inorganic structures traditionally involves heating powders of the reactants at high temperatures for long times to promote interdiffusion and reach thermodynamic equilibrium[8,19,20,25–30]. The use of thermodynamic equilibrium as a means to drive the reaction limits control of the reaction pathway and thus avenues for the preparation of complex structures and compounds. In particular, only the thermodynamically stable phase at the chosen reaction temperature is formed, precluding all reaction intermediates. Traditional synthesis approaches to

extended inorganic structures severely limit the number of potential new compounds in ternary and higher order systems that can be prepared.

At least two approaches have been explored to control reaction pathways in extended inorganic systems with the goal of producing metastable products. The first approach is low temperature and topochemical ("soft"), utilizing intercalation, de-intercalation and ion-exchange reactions[29,199–205]. Wiley has shown that controlling the order of a sequence of ion-exchange reactions can be used to arrive at products that cannot be obtained in a single reaction step[29,199–203]. The second approach involves the reaction of thin films of elements to control diffusion lengths. This thin-film approach was initially driven by the semiconductor industry's desire to control the formation of transition metal silicides during the reaction of deposited metal films on silicon wafers to form ohmic contacts for integrated circuits[204,205]. Researchers discovered that this approach typically results in the stepwise formation of binary compounds at the interface between the elemental reactant layers.

Subsequent research on the thin-film approach demonstrated that reducing diffusion lengths below a critical distance in a multilayered reactant film resulted in nucleation-limited reactions[35,36,122,124,125,206]. In this limit, the compositionally modulated multilayer reactants interdiffuse without the interfacial nucleation of binary compounds, forming a homogeneous amorphous reaction intermediate. The first compound to crystallize from this amorphous intermediate was found to be that with the lowest activation energy for nucleation under the reaction conditions, and not necessarily the thermodynamically most stable compound[35,36,122,124,125,206]. Given that the critical temperature for nucleation from the amorphous intermediate is typically much lower than that necessary to effect long-range diffusion during conventional powder reaction, the choice of nucleation temperature anywhere between

these two extremes provides a degree of freedom to tailor the nucleated phase and its microstructure. This approach has been successfully used to prepare new metastable binary and ternary compounds, including families of structurally related compounds with designed nanostructure, by preparing amorphous intermediates with appropriate compositions or modulated compositions, respectively[13,14,40,207,208].

The goal of the present study is to demonstrate the controlled synthesis of ternary crystalline compounds from elemental reactants in the form of a multilayer thin film, while suppressing the formation of binary compounds as reaction intermediates through careful selection of the order and thickness of the elemental reactant layers. The reaction proceeds through the formation of a homogeneous amorphous reaction intermediate. The generality of this principle is illustrated through the synthesis of two compounds with distinctly different crystal structures, $CuInSe_2$ and $CuCr_2Se_4$. To our knowledge, the juxtaposition of layers in a precursor film has not previously been either explored or exploited as a means to control reaction pathways in solid-state reactions. This paper demonstrates that the order of elemental layers in a precursor film can be selected to avoid the formation of binary compounds as reaction intermediates in the synthesis of some ternary compounds, even when individual elemental layer thicknesses are below that required to avoid interfacial nucleation and growth of binary compounds. Prior studies have demonstrated that nucleation energies increasing as composition deviates from the stoichiometry of a compound[124,125,207,209], but we show that the presence of a third element does not necessarily suppress nucleation of binary compounds. This reaction behavior can be understood based on the behavior of the relevant binary diffusion couples, and constitutes a general strategy to explore the nucleation-limited synthesis of metastable ternary and higher order compounds. The lower reaction temperatures and shorter

reaction times required to synthesize these compounds also has implications for the applications of these and other materials[131].

4.3. Experimental

Compositionally modulated multilayer (CMM) precursors were calibrated to yield a stoichiometric ratio of metal cations and a slight excess of selenium to compensate for evaporation losses during annealing. Samples were deposited using a custom evaporative metal deposition system modeled after one described previously[210]. Cr and Cu were deposited by electron beam sources. In and Se were deposited using effusion cells. Films were deposited under a vacuum of less than 1×10^{-4} Pa. Deposition of the compositionally modulated multilayer (CMM) precursors was conducted by the sequentially positioning of the substrate carousel over the desired sources and the opening of a shutter to achieve the desired layer thickness corresponding to a given shutter time or frequency shift of the quartz crystal oscillator. Samples with thickness of 50 nm or greater were deposited on commercially available (001)-oriented silicon single-crystal substrates with native oxide layers.

Samples were annealed with a custom fabricated hot plate that was equilibrated at the target temperature before each heat treatment. Annealing was conducted under a high-purity nitrogen atmosphere, with an oxygen content of less than $500\,\mathrm{nL\,L^{-1}}$, at temperatures ranging from 100 °C to 600 °C. The thin films were analyzed using electron probe microanalysis (EPMA), X-ray diffraction (XRD) and X-ray reflectivity (XRR). Powder samples were prepared by depositing films of ≈150 nm thickness on poly(methylmethacrylate) (PMMA) coated substrates. The powder films were then delaminated by dissolving the PMMA in an acetone bath, followed by filtration

to collect the powder with nominal yields of ≈4 mg. Powders were annealed under identical conditions to the substrate-supported samples.

Specimens were prepared for EPMA by sectioning a ≈5 mm^2chip from the silicon supported samples. These sample chips were carefully mounted onto an aluminum stub using quick-set epoxy and cured at ambient temperature for 24 h. Dabs of carbon paint were applied at two corners of the chip, spanning the chip surface and the aluminum stub, to provide a conductive path to ground. Samples were analyzed using a Cameca SX-100 Microprobe equipped with five wavelength dispersive x-ray spectrometers (WDSs). Samples were analyzed using a range of operating voltages between15 kV and 25 kV at (8 to 10) sites spaced approximately 100 nm apart. The resulting EPMA data were then analyzed using the Pouchou and Pichoir method, as detailed elsewhere[144,151,152].

XRR was performed on a Bruker-AXS D8 Discover X-ray diffractometer using Cu K radiation (=0.154 18 nm). The incident beam was conditioned and collimated using a parabolic multilayer mirror with a 0.1 mm divergence slit and a 0.6 mm anti-scatter slit, a Soller slit assembly. The exit beam was conditioned using a 0.05 mm acceptance slit. Each sample was carefully aligned to be centered within the goniometer. XRR data were collected over an angular range of $0° < 2\theta < 7°$with a step increment of 0.003° and a data collection time of 1 sper point. XRD was performed using the same experimental parameters but at lower angular resolution, with a 0.025° step increment, and 1 mm divergence and detector slits. Powder samples were supported using a low background quartz substrate with small quantity of silicone vacuum grease to adhere the powder to the substrate.

4.4. Results and Discussion

To calibrate the deposition of elemental reactant layers necessary to achieve a stoichiometric ternary composition, the desired elemental ratios were first calibrated for pairs of elements by holding the thickness of one elemental reactant layer constant while varying that of a second element. The ratios of the concentrations measured by EPMA analysis were then plotted as a function of variable thickness, calculated from the product of deposition time and deposition rate as measured by the quartz crystal microbalance. The absolute thicknesses of the two sets of binary films were measured by XRR. This calibration procedure yielded the expected linear changes in both elemental ratio and modulation wavelength with thickness, as shown in Figure 4.1. Modulated films of integrated composition corresponding to the desired stoichiometry were then achieved by interpolation. By varying the absolute layer thicknesses while holding the ratios of layer thicknesses constant, the modulation wavelength, λ_c, could be systematically varied while keeping the overall composition constant.

The preparation of thin-film diffusion couples of elemental reactant layers to form ternary compounds can be informed by the corresponding binary systems. For the Cr-Se system, Berseth[39] indicated that films where λ_c is less than 2 nm interdiffuse to form amorphous intermediates upon annealing. For In-Se, Oyaleran et al. reported that amorphous intermediates were formed from films where λ_c is less than 3.6 nm at near-equimolar compositions[209]. No such data have been reported for the Cu-Se, Cu-Cr or Cu-In binary systems.

A series of modulated films were prepared to investigate the nucleation behavior of Cu-Se films as a function of composition and modulation wavelength. XRR and XRD data collected on these samples as a function of annealing temperature and time were evaluated to determine the critical thickness where the binary film interdiffuses

FIGURE 4.1. The variation of the composition ratio and modulation wavelength of Cr-Se, and Cu-Cr binary films as the a function of layer thickness of the first-indicated elemental reactant, that of the second-indicated reactant being held constant.

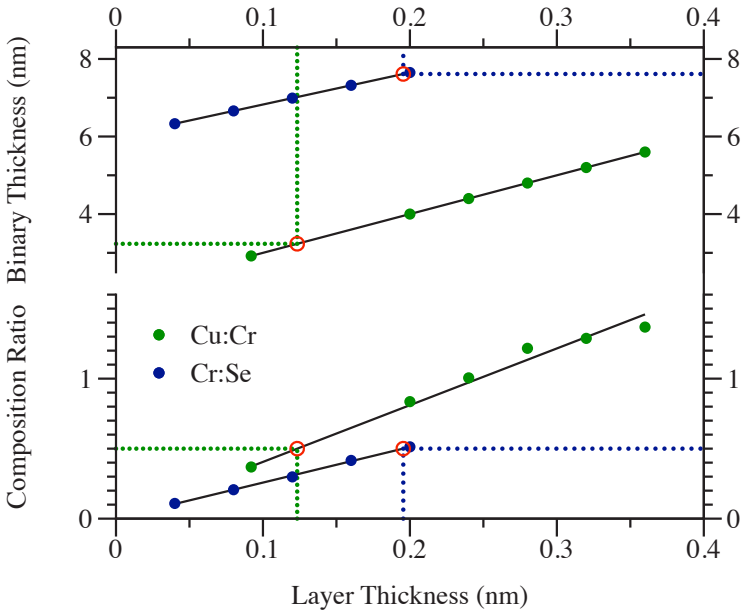

before binary compounds form via nucleation at the interfaces between the deposited reactant layers. XRD data for representative films are shown in Figure 4.2. For films with compositions less than 62 at.%* Se, hexagonal CuSe formed during the precursor deposition. For films with compositions greater than 65%, the samples were x-ray amorphous. Figure 4.3. provides a graphical summary of the diffraction data, indicating whether the samples were found to form homogeneous amorphous or crystalline phases upon low-temperature annealing of the as-deposited films, as a function of both composition and modulation wavelength. Binary films with greater than 63% or 64% Se interdiffuse to amorphous intermediates if λ_c is less than approximately 3 nm. This critical thickness increases as the films become richer in Se.

*All compositions are quoted as atomic percent.

FIGURE 4.2. XRD data collected from Cu-Se films of various composition and modulation wavelength, as indicated. The thickness of the deposited bilayers were determined from XRR thickness fringes, and the composition by EPMA. The labeled indices are for hexagonal α-CuSe.

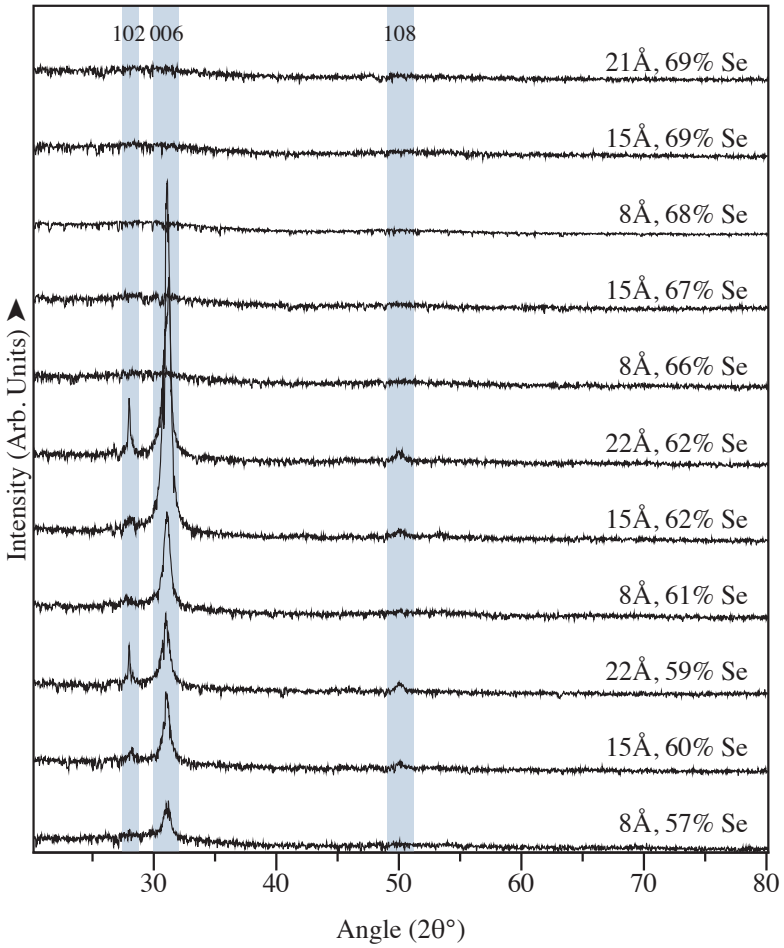

FIGURE 4.3. A summary of diffraction data on Cu-Se binary compositionally modulated multilayers, indicating whether crystalline or amorphous films were obtained, graphing modulation wavelength versus the atomic percent selenium. Data for composition and modulation wavelengths for the regions presented in white were unavailable.

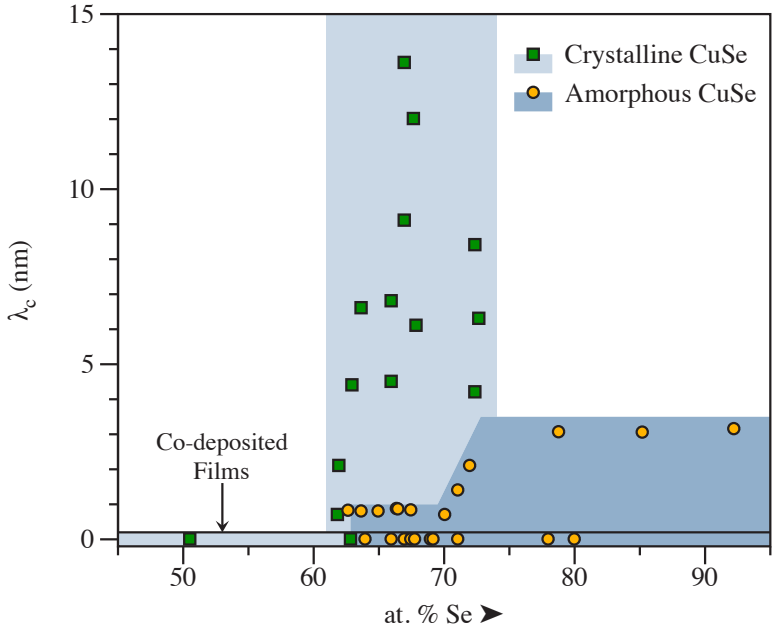

Copper and selenium interdiffusion was found to occur at temperatures below 100 °C. Accordingly, corresponding modulated binary films for the Cu-In and Cu-Cr systems were not prepared, according to the hypothesis that the selenium interdiffusion with the two metal layers would significantly precede the interdiffusion between the metal layers themselves.

Using the information about the binary diffusion couples, a series of Cu-In-Se CMM precursors was created to study the sequence of phase formation as a function of precursor structure. Our goal was to devise a precursor structure that forms the ternary compound CuInSe2 via a homogeneous amorphous intermediate, avoiding the crystallization of binary compounds as reaction intermediates. The structure of the precursor films are described by compositional waveforms, denoted by ϖ_c and shown schematically in Figure 4.4., which capture the spatial distribution of the component elements within a single iteration of λ_c. As expected from our studies of the binary couples, waveforms containing pairings of elements above the previously determined limit for nucleation-limited reactions, such as $\varpi_{c,1}$ in Figure 4.4., resulted in the formation of binary compounds such as CuSe. By reducing λ_c so the Cu-Se pairs are below the critical thickness, $\varpi_{c,2}$ in Figure 4.4., we avoid CuSe as a reaction intermediate, and the as-deposited diffraction pattern indicates that the film forms $CuInSe_2$ on deposit, as shown in Figure 5.5. This suggests that all of the elements intermix during the nominally room temperature deposition.

A third waveform, $\varpi_{c,3}$ in Figure 4.4., was designed to separate Cu and In, to delay the formation of regions containing all three elements, while also keeping the thickness of the Cu-Se pairs in the waveform below the critical length to avoid the formation of CuSe. We expected $\varpi_{c,3}$ to lead to the formation of regions of amorphous Cu-Se and In-Se. The subsequent intermixing of these layers during annealing would

FIGURE 4.4. Schematic representations of the three repeat layering schemes used to investigate the effect of layer repeat thickness and order on the reaction pathway resulting in the formation of $CuInSe_2$. Waveform 1, $\varpi_{c,1}$, has a modulation wavelength, $\lambda_{c,1}$, of $\approx$6 nm, with Cu adjacent to In. Waveform 2, $\varpi_{c,2}$, reduces the modulation wavelength such that $\lambda_{c,2} = 1/3\lambda_{c,1}$, but employs the same compositional waveform. Waveform 3, $\varpi_{c,3}$, has the same modulation wavelength as $\varpi_{c,1}$ but alters the compositional waveform to separate the Cu and In layers to delay their mixing.

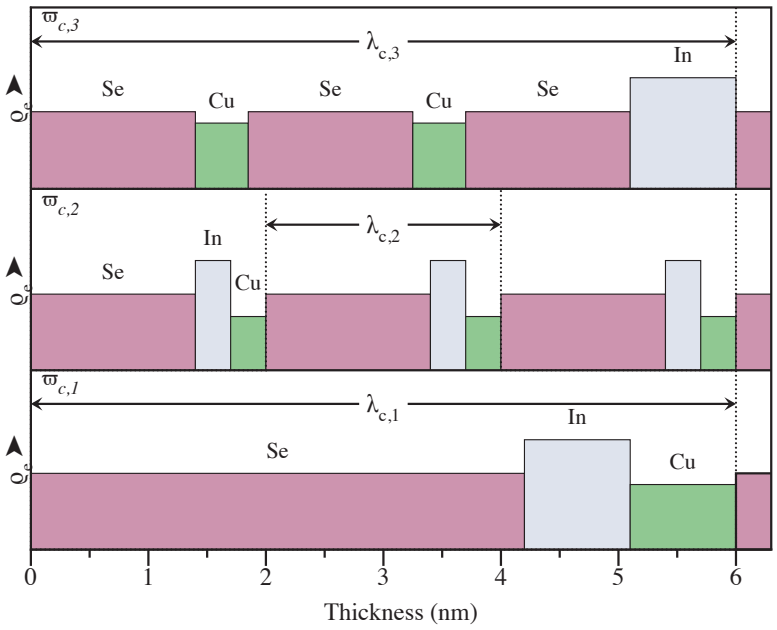

FIGURE 4.5. Representative XRD patterns for as-deposited films with waveform 3. The numbers above the scans are the relative stoichiometry of the sample relative to selenium, $Cu_xIn_ySe_2$. The bottom seven patterns represent the samples that were amorphous on deposition. The top pattern is presented as an example of a film that crystallized on deposition using waveform 2.

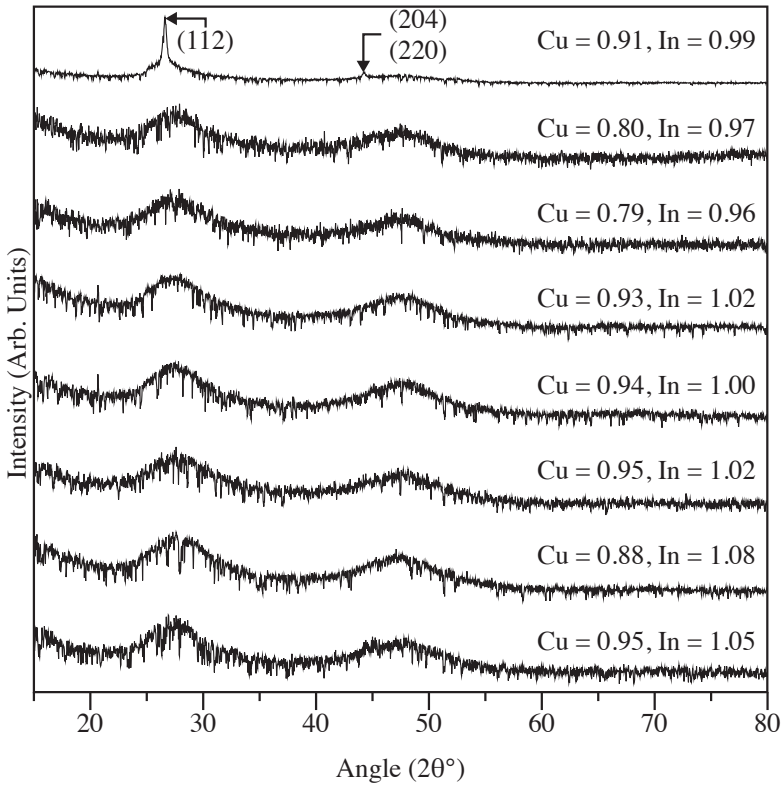

FIGURE 4.6. Representative XRD patterns collected as a function of annealing temperature for films with waveform 3. The annealing temperature is indicated above each pattern. The film is amorphous on deposition and forms $CuInSe_2$ on annealing at 100 °C. The crystallite size and the degree of preferred 112 crystallographic orientation increases as annealing temperature is increased.

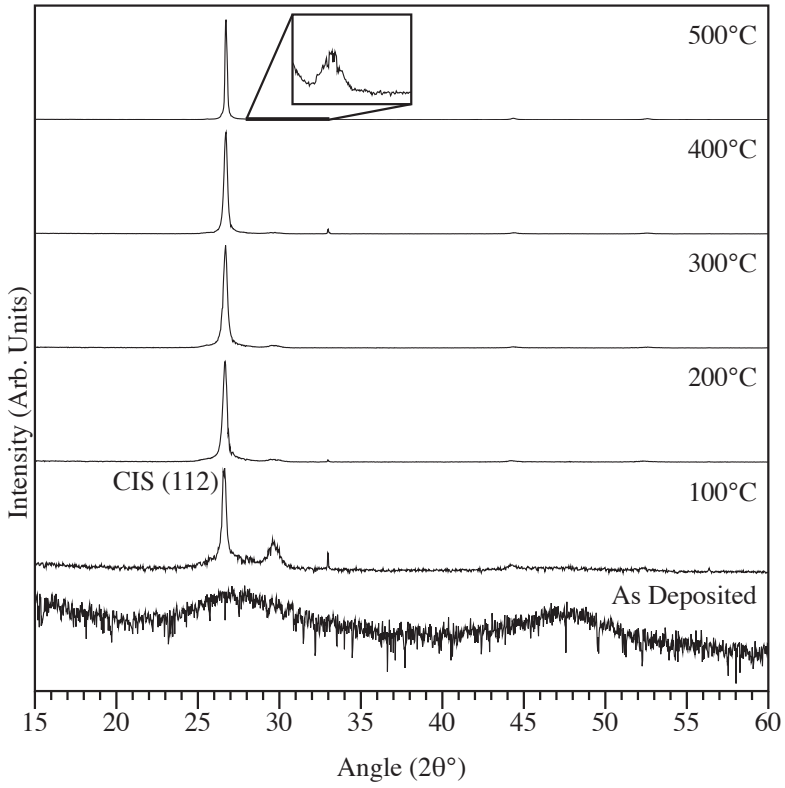

be required to form $CuInSe_2$. As can be seen in Figure 5.5., this waveform produced amorphous films on deposition for a variety of compositions around that of $CuInSe_2$, while films with waveform 2 formed crystalline $CuInSe_2$ on deposit. The amorphous, as deposited films formed $CuInSe_2$ on annealing at 100 °C as shown in Figure 4.6.

To demonstrate the generality of this design process, we targeted the ferromagnetic spinel-structured compound, $CuCr_2Se_4$, because studies indicate that heat treatments at temperatures between 500 °C and 600 °C for 8 h or longer are required to transform binary compounds, formed as reaction intermediates, into

uniform single-phase films of $CuCr_2Se_4$[39,42,120,209]. Alternatively, the formation of $CuCr_2Se_4$ from an amorphous precursor could proceed at lower reaction temperatures and times, which may be suitable for integration with silicon integrated circuit technology as a potential magnetic component[131].

Two different compositional waveforms in the Cu-Cr-Se system were explored, as shown schematically in Figure 4.7. Compositional waveforms featuring the juxtaposition of all elemental reactant layers with one another, $\varpi_{c,4}$ in Figure 4.7., universally resulted in formation of binary CuSe compounds as reaction intermediates. If the Cu-Se thickness was in excess of its characteristic critical thickness, binary Cu-Se compounds formed in the as-deposited sample. Below the critical thickness, CuSe did not form during deposition, but formed upon annealing, suggesting that greater temperatures and / or times are required to mix Cu, Cr and Se than is required to mix Cu and Se in the binary system. After additional annealing to 600 °C, $CuCr_2Se_4$, CuSe, and $Cu_{2-x}Se$ all are present as reaction intermediates, as shown in Figure 4.8. These data suggests that Cu and Se mix before Cr diffuses throughout the sample, leading to the formation of Cu-Se binary compounds; the desired $CuCr_2Se_4$ phase forms from the subsequent reaction of Cu-Se binary compounds with amorphous Cr-Se. Based on the greater interdiffusion and reactivity of Cu-Se relative to Cr-Se, a new compositional waveform, $\varpi_{c,5}$ in Figure 4.7., was designed with Cu sequestered between Cr layers to mitigate the formation of binary Cu-Se compounds upon annealing. XRD data from delaminated films deposited according to this waveform, indicate that upon annealing, $CuCr_2Se_4$ predominantly forms, with only trace amounts of binary $CuSe_x$ compounds, due to a slight excess of copper in the precursor, as shown in Figure 4.8.

FIGURE 4.7. Schematic representations of the Cu-Cr-Se compositional waveforms used to study the formation of $CuCr_2Se_4$. Both waveforms use the same modulation wavelength, but change the profile of ϖ_c. Waveform 4, $\varpi_{c,4}$, allows Cu to interact directly with Se, resulting in the formation of Cu-Se binary phases. Waveform 5, $\varpi_{c,5}$, requires that Cu intermix with Cr before interacting with Se. Electron density is used as the ordinate and the thickness of each layer, derived from the product of the source exposure and deposition rate, is plotted on the abscissa.

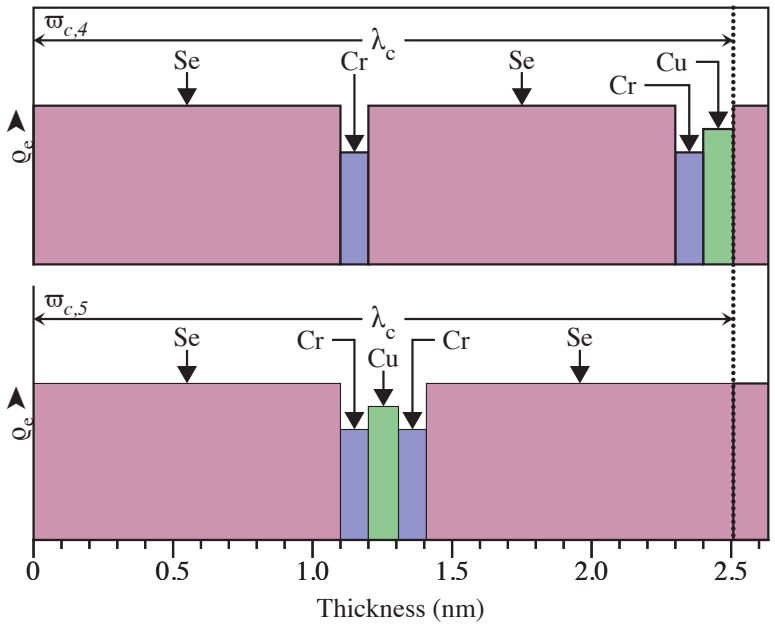

FIGURE 4.8. Powder diffraction pattern for representative Cu-Cr-Se samples using the $\varpi_{c,4}$ and $\varpi_{c,5}$ waveforms after annealing the samples at 600 °C for 1 h. There is a significant reduction in the amount of binary Cu-Se compounds in the $\varpi_{c,5}$ sample relative to the $\varpi_{c,4}$ sample. The small amount of $Cu_{2-x}Se$ secondary phase in the $\varpi_{c,5}$ scan is eliminated in samples of the correct composition.

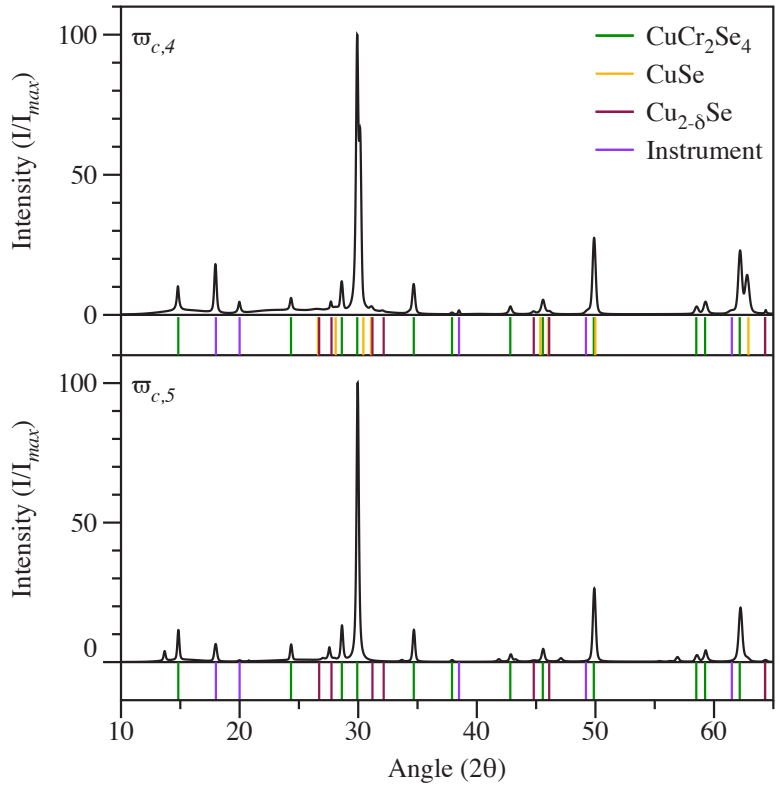

In order to determine the sequence of phase formation of a representative film with waveform 5, XRR and XRD data were collected as a function of annealing temperature, as shown in Figure 4.9. The low-angle Bragg reflection, resulting from the periodic variation of the electron density in the precursor film, shifts to higher angle upon annealing, indicating a densification of the film, while simultaneously decreasing in intensity as the elements interdiffuse. The disappearance of this low-angle reflection at annealing temperatures of 300 °C and higher indicates that the film has become uniform in composition. The absence of either low- or high-angle diffraction peaks at the intermediate annealing temperature of 300 °C suggests that, upon annealing at higher temperatures, the film crystallized from a homogeneous amorphous phase. A time dependent annealing experiment was conducted at 375 °C, just above the temperature where the CMM has completely interdiffused, for 48 h. XRD data from this experiment, shown in Figure 4.10., demonstrates that it is possible to achieve similar crystallinity as the short, intense heat treatment with a longer, lower temperature approach.

The presence of only a single family of Bragg reflections for $CuCr_2Se_4$, corresponding to the 222 and 444 reflections of the spinel structure, reflects the strong texture of the films, with a crystallographic orientation such that the planes of the close-packed anion sublattice lie parallel to the substrate surface. Rocking curve data collected about the 222 reflection at $2\theta \approx 30^\circ$ as a function of annealing temperature shows an increase of the peak intensity and narrowing of the line width with annealing temperature, as shown in Figure 4.11. scanning transmission electron microscopy (STEM)-high angle annular dark field (HAADF) analysis of the film in cross-section confirmed the highly textured nature of the film. The strong texture of the crystallized films reflects the influence of the nearby film surface and film-

FIGURE 4.9. XRD and XRR patterns a representative Cu-Cr-Se film with waveform 5 collected at different annealing temperatures. The low angle region on the left hand side of the figure contains a diffraction peak in the as deposited sample from the initial compositionally modulated multilayer precursor, which disappears with annealing as the sample progresses from an ordered multilayer film to a compositionally uniform amorphous precursor. The right hand side of the figure exhibits high-angle diffraction data over a limited range, as only the 222 (located at $2\theta = 30°$) and the 444 Bragg diffraction maxima for $CuCr_2Se_4$ are observed, consistent with prior thin film studies. The $CuCr_2Se_4$ diffraction peaks form after the Bragg diffraction peak from the precursor has disappears, suggesting that mixing of the elements precedes nucleation and crystal growth.

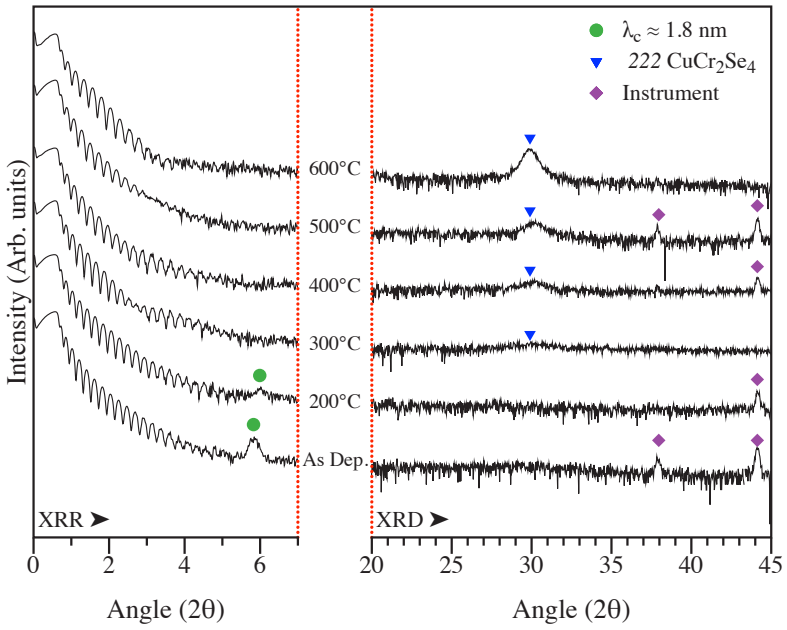

FIGURE 4.10. XRD pattern for a representative Cu-Cr-Se film with waveform 5 annealed at 375 °C for 48 h and 600 °C for 1 h. Present in the range shown are the 222 and the 444 reflections of $CuCr_2Se_4$. The film annealed at 375 °C for 48 h demonstrates a stronger reflection and narrower peak compared to that annealed at 600 °C for 1 h. This tradeoff between reaction temperature and time suggest a route for application specific optimization of the material.

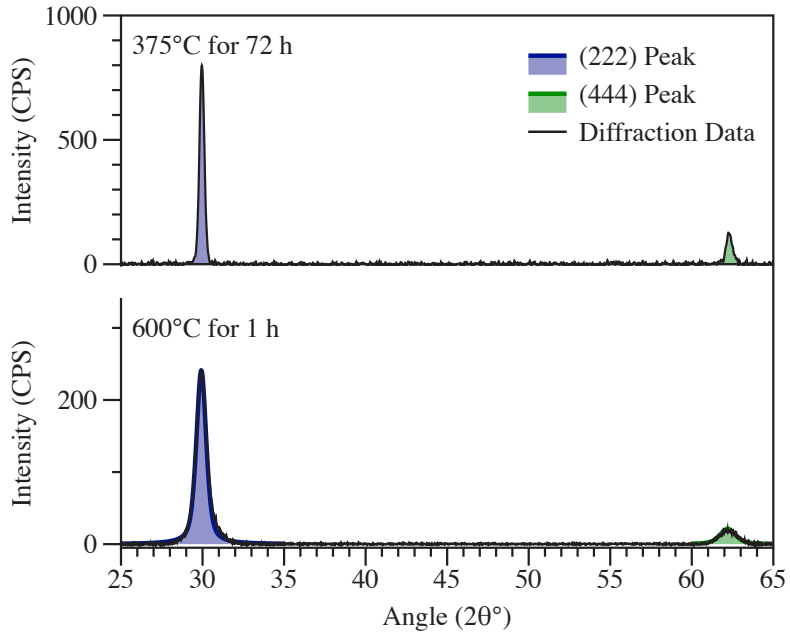

substrate interface, relative to the nominal isotropy of the amorphous bonding, for which a random distribution of grain orientation would be expected to result from homogeneous nucleation of crystallites within the film. The possibility of the texture arising from the influence of a particular substrate was investigated by repeating the deposition and annealing experiments with films deposited on a variety of crystalline and amorphous substrates. Samples deposited on silicon, sapphire, quartz and amorphous silica substrates with amorphous native oxides all produced $CuCr_2Se_4$ films with the same preferred orientation. We speculate that nucleation may occur predominantly at either the top or bottom surface of the deposited films and the preferred alignment results from the low surface energy of the 111 surface of the spinel structure. This preferred orientation was also observed in other studies of the growth of $CuCr_2Se_4$ films[39,42,120,209].

The results presented herein suggest that it is possible to rationally design ternary and higher order compositionally modulated multilayer precursors that form compositionally uniform amorphous intermediates by using critical diffusion distances of binary systems. Prior studies have demonstrated that the first compound to form from an amorphous intermediate is the easiest to nucleate, not the compound or mix of compounds that is thermodynamically most stable[35,36,124,125], and that nucleation energies depend on composition[124,125,207,209]. Our results suggest that the proper sequence of layers is required to obtain ternary and higher order amorphous intermediates. These intermediates may provide a general synthesis route for the low-temperature formation of thin films of ternary compounds, provided that the ternary compound has the lowest nucleation energy. A key remaining challenge is the development of techniques to control relative nucleation energies when the

FIGURE 4.11. Rocking curves from the 222 reflection of $CuCr_2Se_4$ collected as a function of annealing temperature. The full width at half max (FWHM) values for each peak are shown with a corresponding background color and the upper axis. The FWHM decreases and there is a significant increase in intensity between 500 °C and 600 °C.

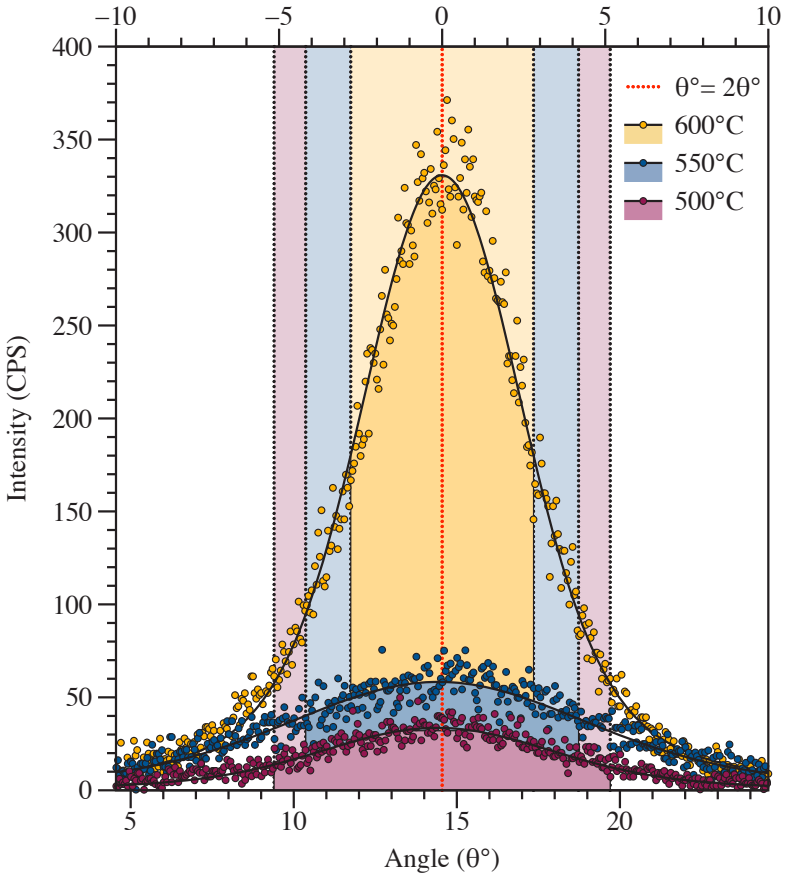

stoichiometric composition of the amorphous intermediate is not sufficient to dictate the formation of the desired target compound.

4.5. Conclusions

The sequence of phase formation of thin films consisting of different sequences and layer thicknesses of elemental Cu-In-Se and Cu-Cr-Se multilayers were investigated. Diffusion distances and the sequence of mixing of the deposited layers were controlled by manipulating the order and thickness of deposited elemental layers in multilayer precursors, We demonstrated the successful formation of an amorphous Cu-In-Se film which directly nucleated crystalline $CuInSe_2$ on annealing, avoiding the formation of binary compounds as reaction intermediates. A different layer sequence in the Cu-Cr-Se system permitted the direct formation of $CuCr_2Se_4$ from an amorphous intermediate. Controlling the reaction pathway resulted in the formation of the ternary compounds at lower temperatures and shorter times than previous methods used to form thin films of these compounds. The successful use of critical diffusion distances required to avoid formation of binary compounds in binary compositionally modulated multilayer precursors to design ternary compositionally modulated multilayer precursors suggests that this is a potential general route to the synthesis of kinetically stable ternary compounds that are thermodynamically unstable relative to a mixture of binary compounds.

4.6. Bridge

By designing the sequence and layer thicknesses of elemental Cu-In-Se and Cu-Cr-Se multilayers the ternary compounds $CuInSe_2$ and $CuCr_2Se_4$ were synthesized without the formation of intermediate binary compounds. Both layer sequence and

layer thicknesses were required to control the reaction pathway. Avoiding binary compounds as reaction intermediates lowered reaction temperatures and shortened reaction times. To design ternary compositionally modulated multilayer precursors that formed amorphous intermediates required knowledge of the diffusion distances required to avoid formation of binary compounds and form amorphous intermediates in binary compositionally modulated multilayer precursors. This suggests a rational design criteria to form ternary amorphous intermediates and a potential general route to the synthesis of kinetically stable ternary compounds that are thermodynamically unstable relative to a mixture of binary compounds.

CHAPTER V

MAGNETIC AND ELECTRICAL PROPERTIES OF THIN $CuCr_2Se_4$ FILMS SYNTHESIZED BY COMPOSITIONALLY MODULATED KINETIC TRAPPING

5.1. Co-authorship Statement

Chapter V consists of the magnetic and electrical characterization of the compositionally modulated kinetic trapping (CMKT) synthesized compound. The synthesis and characterization work was conducted or overseen by Michael D. Anderson. Jourdain W. Roberts, Kristina Kirchgessner, and Logan LaRossa worked under Michael D. Anderson collecting and analyzing structural data. Dr. Cindi L. Dennis provided the magnetic characterization and related expertise. Dr. Ian M. Anderson and Dr. David C. Johnson provided editorial support. The information contained in this chapter is being prepared for submission to *The Journal of Magnetism and Magnetic Materials*.

5.2. Introduction

The exceptional magnetic properties of $CuCr_2Se_4$ has resulted in considerable research activity over the last decade. The compound has been shown to be ferromagnetic below 460 K and has shown a tendency towards magneto-optical activity[42,90,92,94,97,102,105,111,116,119,211]. Nanoscale preparations of the compound have demonstrated a size dependence to both the magnetic susceptibility and the Curie temperature (T_C), suggesting that the properties of the material may be

tunable[109–111]. The combination of material properties and tuneability have made $CuCr_2Se_4$ a potential target for inclusion in spintronic devices[94,109,113,115,116,212].

The development of a new thin film synthesis technique is required for $CuCr_2Se_4$ that is compatible with the thermal and time constraints of semiconductor device fabrication[131]. Syntheses presented in the literature to date require long heat treatments at high temperature and may also require multiple thermal cycles to produce a single phase product[42,87,89,120,213,214]. These reaction conditions have been attributed to the formation of stable binary compounds early in the synthesis, which must react to form the desired product[42,87,89,120,213,214]. A recently presented alternative to the more traditional co-deposition or sputtering for performing complex syntheses is the CMKT[31,35,37,40,122,123,125,164,206] method. To date, CMKT has been used to generate complex intergrowth structures and metastable compounds[31,35,37,40,122,123,125,164,206]. The technique uses nucleation limited reaction kinetics and designed precursors to avoid undesirable reaction intermediates.

The CMKT method involves generation of a compositionally modulated multilayer (CMM) precursor by deposition of thin monolayers and bilayers from pure metal sources. The precursor itself is described using a compositional waveform (ϖ_c) which captures the positions and relative thicknesses of precursor layers, and a modulation wavelength (λ_c) which gives the absolute length of one iteration of ϖ_c. Creating a designed precursor such that ϖ_c matches the stoichiometry of the desired product and λ_c is sufficiently small so as to be in a nucleation limited regime allows for a specific product to be preferentially stabilized on gentle annealing. Because of the selectivity imparted by the designed precursor the method allows for engineering of the reaction pathway[34–36,122,164,209,215]. This control over the reaction pathway allows for the creation of kinetically stabilized product distributions or the avoidance of

undesirable reaction intermediates such as those found in the $CuCr_2Se_4$ system. In this document we present the CMKT parameters required to form an amorphous intermediate which evolves to form $CuCr_2Se_4$ on low temperature annealing, examine the structure of the resulting film and discuss the physical properties of CMKT generated films of $CuCr_2Se_4$.

5.3. Experimental

CMM precursors were calibrated to yield a stoichiometric ratio of metal cations and a slight excess of selenium to allow for evaporation losses during annealing. Samples were deposited using a custom evaporative metal deposition system described previously[210]. Nb, Cr and Cu were deposited by electron beam sources. Se was deposited using a Knudsen type effusion cell. Films were deposited under a vacuum of less than 1×10^{-4} Pa. Deposition of the CMM precursors was conducted by sequentially positioning the substrate carousel over the desired sources and opening the shutter to achieve the desired layer thickness corresponding to a given shutter time or frequency shift of the quartz crystal oscillator. Samples with thickness of 50 nm or greater were deposited on commercially available (001)-oriented silicon substrates with native oxide layers.

Samples were annealed on a custom fabricated hot plate that was equilibrated at the target temperature for at least 15 min before each heat treatment. Annealing was conducted under a high-purity nitrogen atmosphere (O_2 content of $\approx 500\,\mathrm{nL\,L^{-1}}$) at temperatures ranging from 100 °C to 600 °C. The thin films were analyzed using electron probe microanalysis (EPMA), X-ray diffraction (XRD) and X-ray reflectivity (XRR).

Specimens were prepared for EPMA by sectioning a $\approx 5\,\mathrm{mm}^2$chip from the silicon supported samples. These sample chips were carefully mounted onto an aluminum sample stub using quick set epoxy and cured at ambient temperature for 24 h. A dab of carbon paint was applied from the surface of the sample chip to the surface of the sample stub at two corners of the chip to provide a conductive path to ground. Samples were analyzed using a Cameca SX-100 Microprobe equipped with five X-ray wavelength-dispersive spectrometers. Samples were analyzed using a range of operating voltages between15 kV to 25 kV at8 to 10 sites each spaced approximately 100 µm apart. The resulting EPMA data were then analyzed using the Pouchou and Pichoir method as detailed elsewhere[144,151,152].

XRR was performed on a Bruker-AXS D8 Discover X-ray diffractometer using CuK_α radiation ($\lambda = 0.154\,18\,\mathrm{nm}$). The incident beam and exit beam were conditioned and collimated using a parabolic multilayer mirror with a 0.1 mm divergence slit and a 0.6 mm anti-scatter slit, a Soller slit assembly, and 0.05 mm detector silt, respectively. Each sample was carefully aligned to be centered in the goniometer. XRR data were collected over an angular range of $0^\circ < 2\theta < 7^\circ$with a step increment of 0.003°and a data collection time of 1 sper point. XRD was performed using the same experimental parameters but at lower angular resolution, with a 0.025° step increment, and 1 mm divergence and detector slits.

Samples were prepared for for scanning transmission electron microscopy (STEM) analysis using a variation on the small angle cleavage method developed by McCaffrey, et al[157,158]. After initial thinning of the substrate, but before cleavage, the wafer was covered with a layer of protective carbon using a black permanent ink felt tip marker. After preliminary TEM screening , the cleaved samples were thinned for STEM analysis using an FEI NOVA NanoLab DualBeam FIB equipped with a

Sidewinder ion column. Samples were thinned to approximately 300 nm using a 30 kV accelerating voltage, followed by polishing at 5 kV and a final polishing step at 2 kV. Samples were plasma cleaned using a Fischione model 1020 plasma cleaner for 5 min to remove residual carbon contamination prior to STEM analysis. In order to ensure proper orientation of the cross-sectioned film with respect to the electron probe, the specimen was tilted to the [110] zone axis of the single crystal silicon substrate for each analysis. Aberration corrected STEM-high angle annular dark field (HAADF) imaging and convergent beam electron diffraction (CBED) were performed with an FEI Titan 80-300 TEM/STEM equipped with a double hexapole, spherical aberration corrector (CEOS GmbH) and operating at an accelerating voltage of 300 kV, resulting in an ≈ 100 pm diameter probe of ≈ 100 pA probe current.

Magnetic measurements were carried out using a superconducting quantum interference device (SQUID) magnetometer. Both the Quantum Designs MPMS operating in DC or the Quantum Designs SVSM operating at 14 Hz were used. Significant care was taken to prevent contamination of the samples, including, but not limited to, handling of the samples only with enamel coated tweezers to prevent contact transfer of ferromagnetic atoms. Samples were mounted to silica sample rods using VGE-7031 varnish for SVSM measurements parallel to the field and to Lake Shore Kel-F perpendicular holders for MPMS measurements perpendicular to the field. After resetting the magnet to remove any trapped flux in the superconducting magnet, so that subsequent background subtractions start from a known state, hysteresis loops were measured at fixed temperatures (usually 5 K) starting from $+5.6\,\mathrm{MA\,m^{-1}}$ to $-5.6\,\mathrm{MA\,m^{-1}}$ and back to $+5.6\,\mathrm{MA\,m^{-1}}$ (a +70 kOe to −70 kOe to +70 kOe cycle of externally applied field). The data was normalized for sample mass and background corrections for the sample mountings and Si/SiO_2 substrate.

The temperature dependent magnetization data was measured solely on the SVSM at 14 Hz. These samples were mounted, as before, to silica sample rods using VGE-7031 varnish for SVSM measurements parallel to the field. After cooling to 5 K in zero field, the field set to 160 kA m^{-1}(2000 Oe) and the magnetization was measured in the field on warming and cooling.

5.4. Discussion

Previous studies using CMKT have demonstrated that calibration of the precursor with respect to total composition, captured by the ϖ_c, and diffusion distances, controlled by the λ_c is critical to directly forming the desired compound without other crystalline compounds as reaction intermediates. To calibrate ϖ_c a series of binary films were generated varying the Cr-Se and Cu-Cr ratios by varying the layer thickness of one component and holding the other constant. The composition data for these films, shown in Figure 5.1., was used to establish a series of layer thicknesses that would produce a Cu-Cr-Se ration of which could then be scaled to vary diffusion lengths. A simple Cu-Cr-Se order for the layers resulted in the formation of binary copper selenide compounds, regardless of the layer thicknesses, as shown in Chapter IV. After trying several different waveforms, the final compositional waveform for $CuCr_2Se_4$ used in this study is shown schematically in Figure 5.2. The preliminary mixing of Cu with Cr results in unfavorable nucleation energetics for CuSe phases, allowing the direct formation of the desired ternary compound. Structural studies[42,98,111,120,216,217] indicate $CuCr_2Se_4$ has a 111 textured growth direction and possibly forms in a twinned-spinel polymorph rather than the more traditional cubic structure. A final value of 1.8 nm was chosen for λ_c, which corresponds to 1 unit cell

FIGURE 5.1. The variation of the composition ratio and modulation wavelength (λ_c) of Cr-Se, and Cu-Cr binary films as the thickness of one of the elemental layers is increased while holding the other constant.

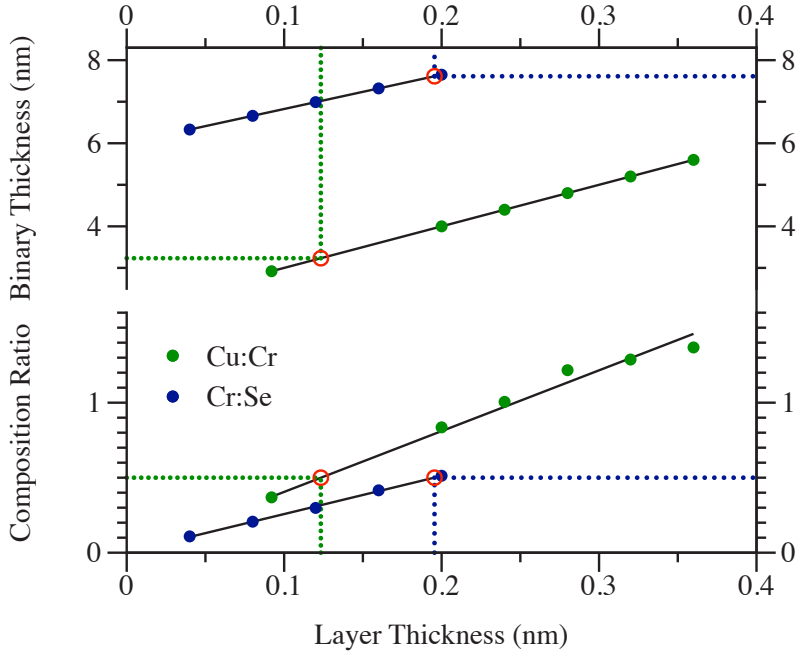

of this twinned-spinel polymorph along the c crystallographic axis, or the 111 body diagonal of the traditionally accepted spinel structure of $CuCr_2Se_4$.

Temperature dependent XRD analysis of a representative film, shown in Figure 5.3., shows the film transitioning from an ordered state through an amorphous intermediate state from which the $CuCr_2Se_4$ is formed. The structural data collected via XRR shows a single Bragg reflection at $\approx 5.8°(2\theta)$ corresponding to a periodicity of $\approx$ 1.8 nm, in the as deposited film. This reflection shifts to higher angles and decreases in intensity as the film is annealed, indicating an interdiffusion of the layered precursor. The lack of reflections in the XRD indicates that the film is forming an amorphous intermediate phase rather than nucleating a crystalline reaction intermediate. Continued increase in temperature results in the complete

FIGURE 5.2. The calibrated compositional waveform (ϖ_c) for $CuCr_2Se_4$. Layer thicknesses reported reflect the product of shutter time and deposition rates.

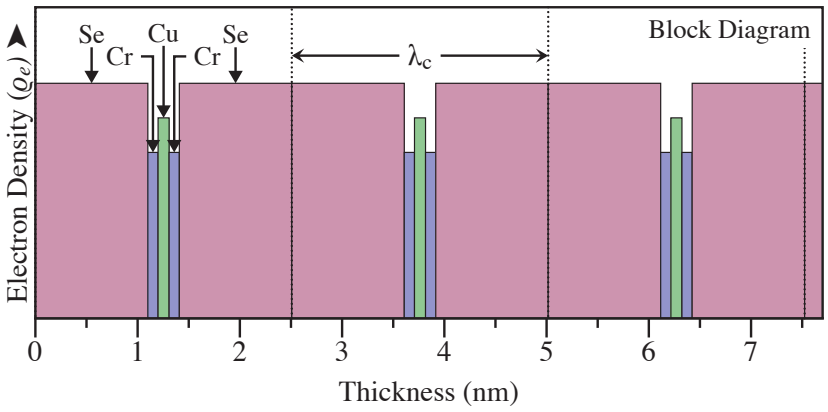

interdiffusion of the layered precursor above 200 °C. At approximately 300 °C, the 222 reflection of $CuCr_2Se_4$ begins to appear and increases in intensity with increased temperature. Other reflections for $CuCr_2Se_4$ are not observed due to the strong $\{111\}_{Fd\bar{3}m}$ texturing of the film. A powder of the 600 °C annealed compound was created from a 200 nm thick film via a lift off technique described previously[218]. XRD data from this powder, shown in Figure 5.4., can be indexed to the literature $CuCr_2Se_4$ compound yield lattice parameters of 1.034 nm. Structural refinement on the powder was not possible due to strong texture in the small powder flakes.

Currently there are two competing structural models for $CuCr_2Se_4$, the traditional $Fd\bar{3}m$[219] and a structure proposed by Neulinger with a $R\bar{3}$ space group[98]. The structures are similar in most respects, the $R\bar{3}$ structure being an orthohexagonal translation of the $Fd\bar{3}m$ structure, the major exception being the inclusion of a mirror plane at $c = 0.5$ in the $R\bar{3}$ structure. This mirror plane is consistent with a regular twinning of the spinel structure at the $\{111\}_{Fd\bar{3}m}$ planes following the Spinel Twin Law. To determine the structure of the CMKT synthesized $CuCr_2Se_4$ film, STEM-HAADF analysis of a cross-section, shown in Figure 5.4.a, was conducted. The

FIGURE 5.3. XRD and XRR data for the annealing of an $\approx 50\,\text{nm}$ film of $CuCr_2Se_4$ between 30 °C and 600 °C. The left side of the figure contains XRR data. The reflection at $\approx 5.8°(2\theta)$ corresponds to a λ_c of $\approx 1.8\,\text{nm}$. The right side of the figure shows a selected region of the high angle XRD data. The reflection at 30° is the 222 reflection for the $CuCr_2Se_4$ compound. The annealing data show the loss of the long range order of the precursor and the formation of an amorphous intermediate phase between 200 °C and 300 °C followed by the nucleation of the $CuCr_2Se_4$ compound directly from the amorphous intermediate phase.

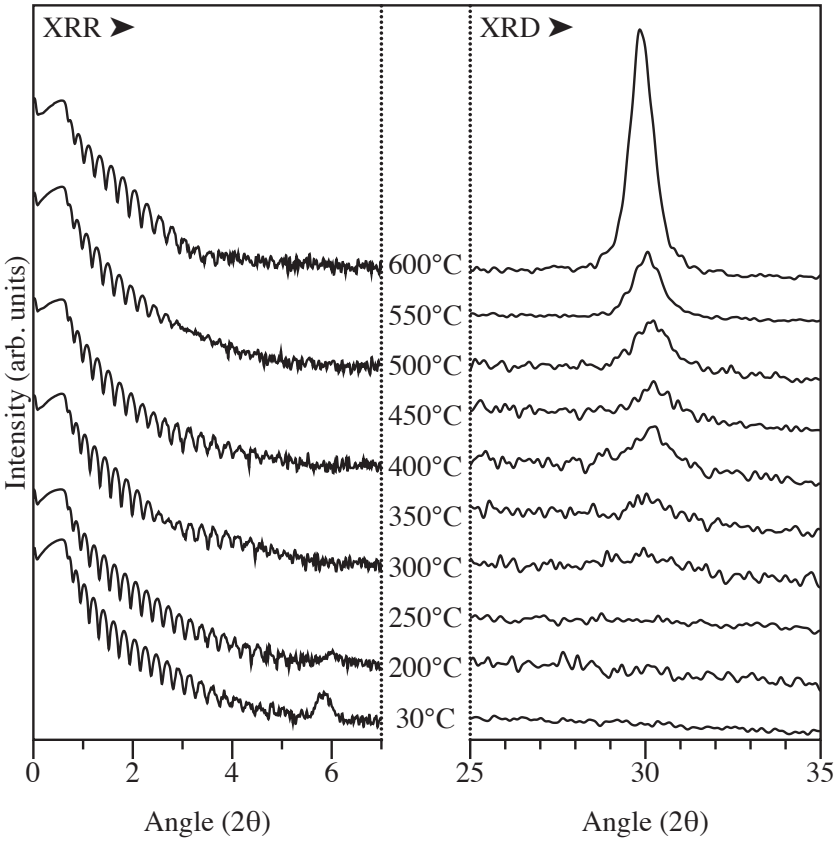

FIGURE 5.4. XRD of a powder produced from an ≈ 200 nm thick film of $CuCr_2Se_4$.

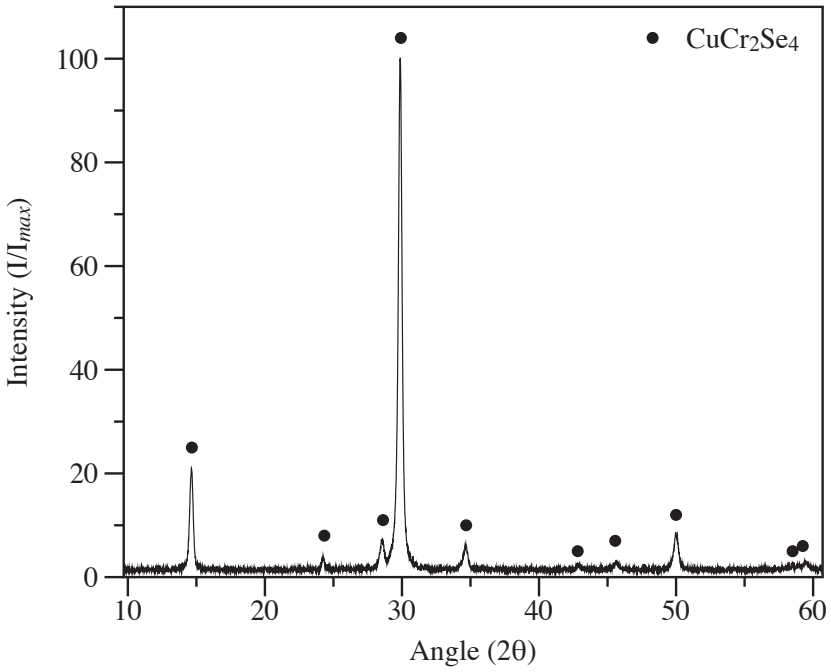

image confirms the highly textured nature of the film with a nearly undisturbed Se sublattice running parallel the substrate. A CBED pattern, collected concurrently with the STEM-HAADF analysis and presented in Figure 5.4.b, suggest the structure is more complex than the regular spinel structure generally assumed in the literature, containing an extra mirror plane along the long axis of the hexagonal spot pattern in the image. This mirror plane lies along the $111_{Fd\bar{3}m}$ systematic row, corresponding to the mirror plane in the $R\bar{3}$ polymorph candidate, giving credence to Neulingers recent claim[98].

Temperature dependent resistivity data, shown in Figure 5.6., was collected on a $CuCr_2Se_4$ film deposited on a quartz substrate using the standard van Der Pauw method with a Greek cross geometry as described previously[13,14,133]. The data shows a metallic character consistent with the powder measurements provided by previous groups[109,111,115–117,119] and prior reports on thin film samples[42]. The

FIGURE 5.5. Aberration-corrected STEM-HAADF images and CBED pattern for a CMKT generated $CuCr_2Se_4$ film. (a) Band pass filtered image showing a grain boundary. Note the continuity of the {111} planes despite rotational disorder within the plane and the layering structure within the oriented crystalline grain. (b) CBED pattern from the grain shown in (a). The diffraction pattern is inconsistent with what would be found for the spinel structure at any major zone axis, suggesting an alternate structure may be present.

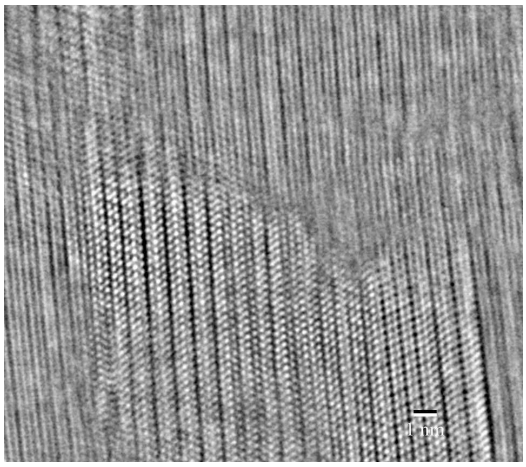

(a)

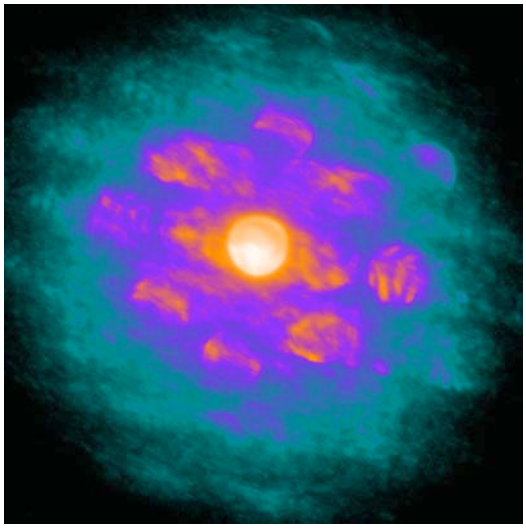

(b)

room temperature resistivity measured on the CMKT thin film ($5 \times 10^{-4}\,\Omega\,\mathrm{cm}$) is slightly higher than that reported previously ($\approx 3 \times 10^{-4}\,\Omega\,\mathrm{cm}$) for compacted powders. While the film prepared by Bettinger has a low temperature plateau in the resistivity below approximately 40 K, the CMKT films resistivity continues to decrease at low temperatures from a value of $5 \times 10^{-4}\,\Omega\,\mathrm{cm}$ at 298 K to $1.5 \times 10^{-4}\,\Omega\,\mathrm{cm}$ at 20 K. The slope in the resistivity in the CMKT samples is 1.5 times larger than that reported by Bettinger[42]. This difference in the slope is unusual as the linear temperature dependence of resistivity is usually attributed to phonon scattering[220]. These differences, supported by the structural characterization data, suggest that the CMKT samples contains fewer defects and impurities than the film produced via pulsed laser deposition (PLD) and annealing in an Se rich environment. The change in the slope at approximately 100 K, observed by Bettinger is not apparent, suggesting that this feature is a consequence of remaining Cr_3Se_4 in their $CuCr_2Se_4$ film and supporting the single phase nature of the CMKT produced film.

Measurement of the magnetic moment as a function of temperature, shown in Figure 5.7., presents two distinct regions. In the low temperature region, below ≈ 160 K, the film behaves as a ferromagnet, with the peak in the zero-field cooled data caused by the change in H_c; with temperature while the slight upturn near 0 K in the field cooled data is most likely the result of a small impurity phase. In this low temperature region the magnetization curves are not identical, but rather depend upon both the applied field and the temperature, with the bottom, blue, curve being cooled in zero field and warmed in an applied field, and the upper, red, curve being cooled in an applied field. In the high temperature region, > 160 K, the film has no measurable coercivity within instrument error and the magnetization in the high temperature region depending only on the strength of the applied field. Extrapolating

FIGURE 5.6. Temperature dependent resistivity data for a quartz supported $CuCr_2Se_4$ film. The film shows a resistivity of $5 \times 10^{-4}\,\Omega\,\mathrm{cm}$ at 298 K which reduces to $1.5 \times 10^{-4}\,\Omega\,\mathrm{cm}$ at 20 K.

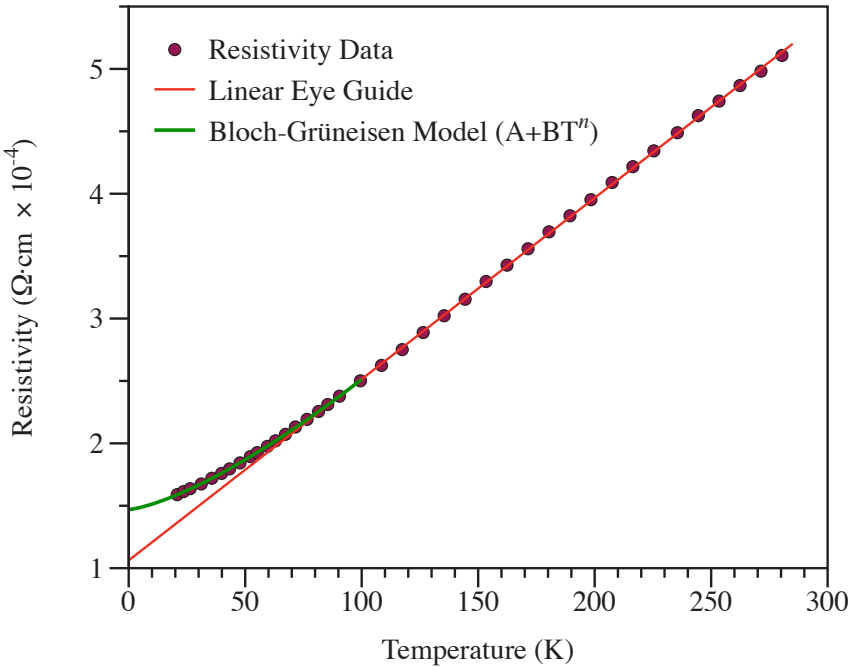

FIGURE 5.7. Temperature dependent magnetization measurements for a supported $CuCr_2Se_4$ film. Data were collected in the presence of a applied field on warming and cooling after initial cooling in zero-field. Extrapolation of the slope of the high temperature region indicates a T_C in the range of 400 K to 415 K with 415 K.

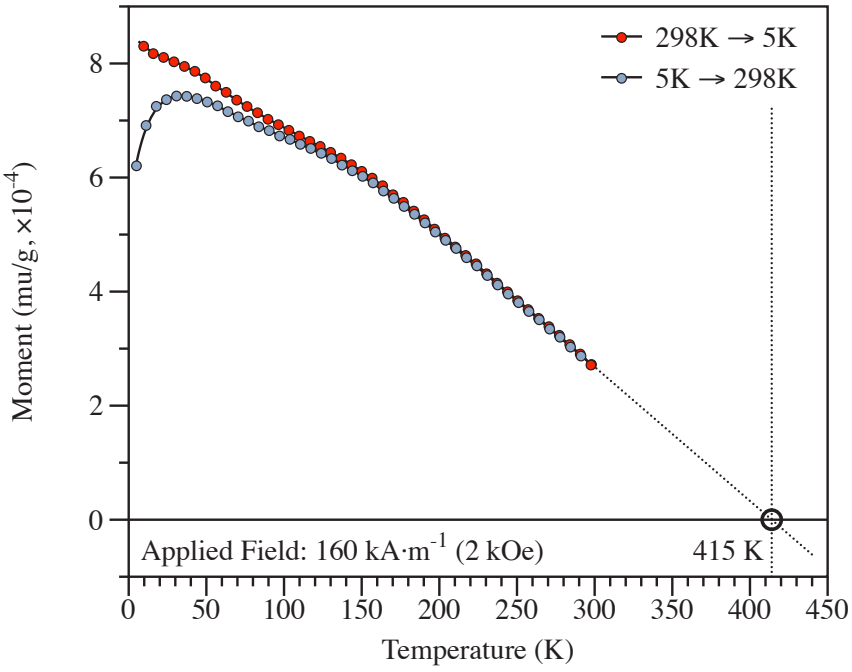

the slope of the high temperature region to a net zero magnetic moment produces an estimate for the T_C in the range of 400 K to 415 K.

Magnetization data collected as a function of applied field for various temperatures between 30 K and 300 K, shown in Figure 5.8., demonstrate a decrease in the coercivity in the film with increasing temperature. There is no coercivity apparent in the hysteresis curves above 175 K. A more quantitative analysis of the extracted coercivity and saturation magnetization, presented in Figure 5.9., demonstrate a sharp decrease in both the coercivity and saturation magnetization between 5 K and 30 K with a continued decrease in both parameters with increasing temperature. The coercivity drops below the detection limit of the instrument, 2387 A m(30 Oe), above $\approx$ 100 K and the saturation magnetization continues to decrease through the range

FIGURE 5.8. Hysteresis loops for a supported $CuCr_2Se_4$ film at 5 K, 30 K, 60 K, 125 K and 175 K.

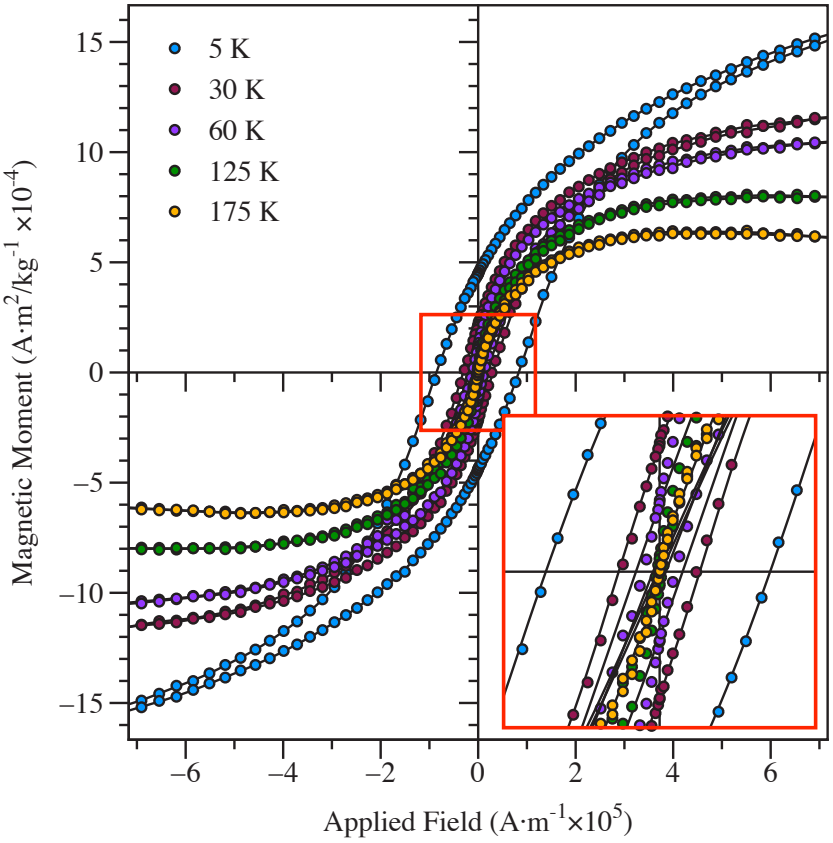

of temperature explored. Extraction of the magnetic moment per formula unit from the saturation magnetization resulted in $\approx 5\,\mu_B$/F.U. at 5 K which decreased to $\approx 1\,\mu_B$/F.U. at 175 K. The saturation magnetization at 5 K agrees with earlier single crystal studies of $CuCr_2Se_4$, and suggests that the film studied herein does not contain significant secondary (impurity) phases.

The magnetization as a function of applied field, shown in Figure 5.10., was also analyzed. Because of the texture of the $CuCr_2Se_4$ thin film, the magnetization was examined with the applied field parallel and perpendicular to the substrate, denoted as $H_{||}$ and $H_{\perp}$ respectively. This aligns the applied field parallel to the 111 planes,

FIGURE 5.9. Temperature dependent coercivity and saturation magnetization a supported $CuCr_2Se_4$ film. Both parameters show a sharp decrease between 5 K and 30 K which continues more gradually through the range of the measurement. The coercivity drops below the instrument resolution above ≈ 100 K. For convenience the appropriate conventional units for each parameter are listed next to each datum.

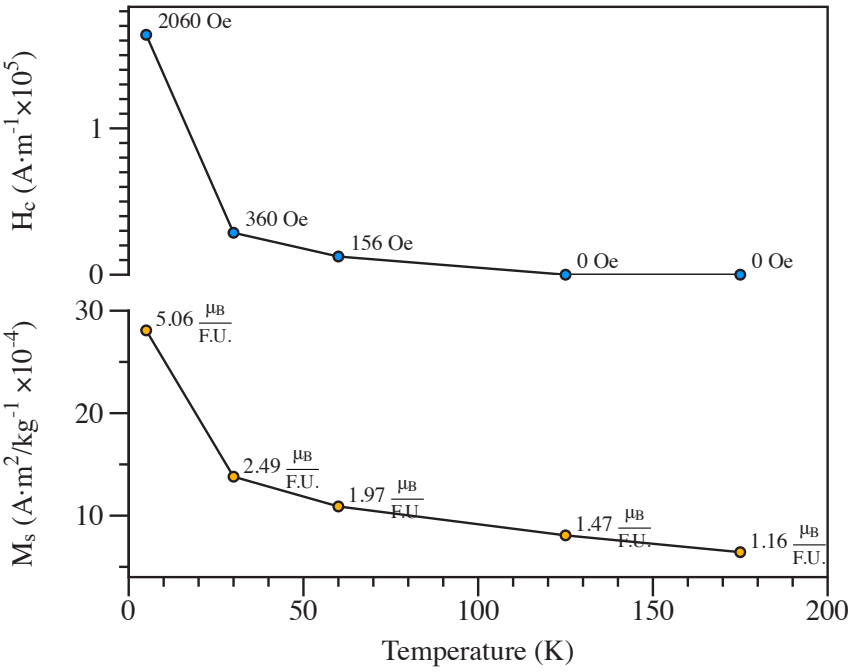

which are all equivalent, of the traditional $Fd\bar{3}m$ spinel structure. For the recently proposed $R\bar{3}$ structure[98], the geometries used place $H_{||}$ parallel to the basel plane of the hexagonal structure and $H_{\perp}$ parallel to the c-axis. As can be seen, there is a marked difference between the parallel and perpendicular field orientations. The $H_{||}$ configuration shows a soft ferromagnetic response to the applied field with an effective anisotropy field of approximately 1 T. This corresponds to an effective anisotropy constant of $3.8 \times 10^{-3}\,\mathrm{J\,g^{-1}}$. The $H_{\perp}$ data show a classic hard magnetic axis response, indicating a marked difference in anisotropy between the two orientations. The hard axis anisotropy field is approximately 5 T, which corresponds to an effective anisotropy constant of $3.5 \times 10^{-1}\,\mathrm{J\,g^{-1}}$.

The magnetic behavior of the film is, in general, consistent with that found in the literature to date. Early work by Natakani, et al.[221] performed on chemical vapor transport (CVT) grown single crystals match the results almost exactly, with the magnetization curves for the single crystal showing a similar response in the high field - high temperature range to the field cooled measurements in Figure 5.7. Magnetization analysis of thin films performed by Bettinger, et al.[42] also show a similar low temperature response to that that seen in the field cooled data. Other magnetization data on monolithic thin films of $CuCr_2Se_4$[120] were not conducted at low enough temperatures to show this region. Nanostructured $CuCr_2Se_4$ likewise shows a similar response for 18 nm nanoparticles, including an absence of measurable coercivity at higher temperatures[111]. The T_C range determined for the CMKT thin film was found to be consistent with the literature values for the single crystals of $CuCr_2Se_4$[221]. The results also agree with the T_C values reported by Tsoi, et al.[111] with a nanoscale grain structure on a similar size scale, reported as between 395 K and 414 K for 15 nm to 25 nm. Thin film measurements likewise put T_C in the same 400 K

FIGURE 5.10. Hysteresis loops for a supported $CuCr_2Se_4$ film at 5 Kcollected perpendicular and parallel the plane of the substrate. Magnetization with the field parallel to the film, $H_{||}$, shows a soft ferromagnetic response while $H_{\perp}$ shows a classic hard magnetic response. The anisotropy suggests that the structure differs from the $Fd\bar{3}m$ traditionally attributed to $CuCr_2Se_4$.

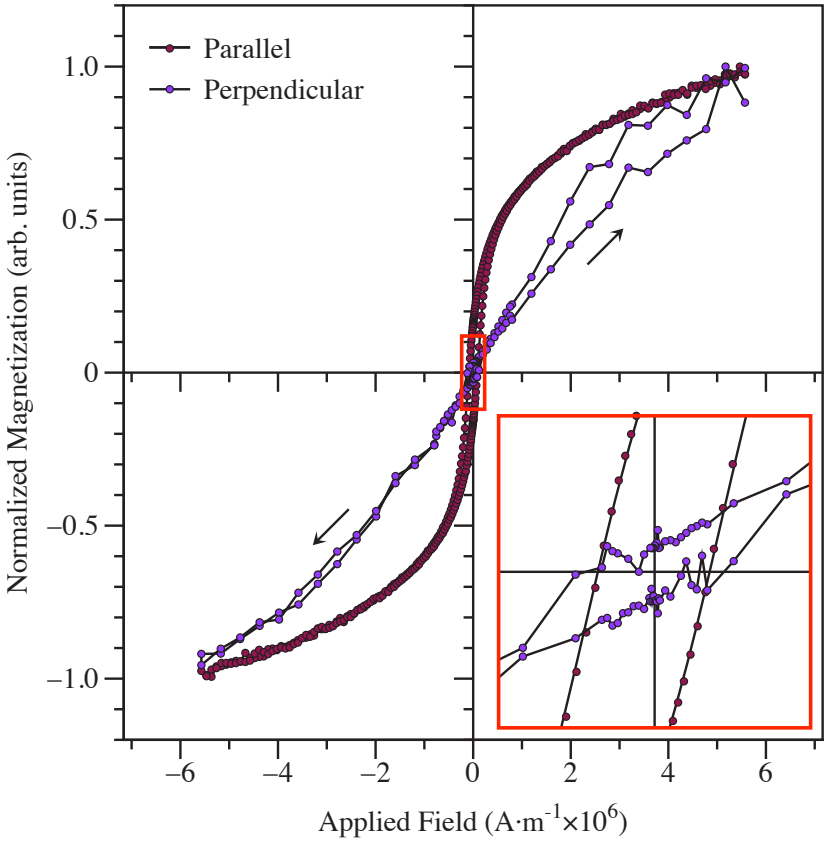

to 415 K range[42]. Values for T_C in bulk powders and single crystals are reported ranging from 300 K to 440 K depending on dopant and concentration[98,222]. The overall profile of the magnetization data presented here differs from that reported by either Bettinger[42] or Tsoi[111], having a smaller slope to the T_C than shown in either case. The cited reports of temperature dependent magnetization were conducted in fields in the range of 50 Oe to 100 Oe significantly below the 2 kOe employed here which can cause significant differences to the shape of the profile, most commonly a decrease in the concavity of the curve with increasing field strength. The work by Nakatani, et al.[221] demonstrates the breadth of this variation. The change in slope at approximately 160 K in the CMKT thin film is also mirrored in the more recent works on nanoparticle systems and is readily apparent in samples where the particle size is small[111,119]. It is reasonable to suspect that this feature arises from unbound spins on the surface of the nanoparticles or similar unmatched spins the thin film. The analysis of the saturation magnetization and coercivity for the film demonstrated trends similar those presented by Tsoi, et al.[111] with the exception of a higher saturation magnetization and coercivity at low temperatures in the thin film sample, which Tsoi reports as 3.9 μ_B/F.U. and 3.7×10^4 A m(470 Oe). The 5 μ_B/F.U. value determined here is more in keeping with the previously reported results for the undoped single crystal structure[221]. While the magnetic behavior of the film is generally consistent with what has been reported for $CuCr_2Se_4$, the combination of behaviors that coincide with nanocrystals and single crystals leads to the observation that the CMKT film is something in between but having slightly more in common with a single crystal than the free powder. It has been well documented that CMKT syntheses can produce films that behave as a highly ordered crystal normal to the substrate plane, while exhibiting a turbostratic disorder about the common

c-axis throughout the film[13,14,31,40,223]. Much of the behavior that corresponds to the nanocrystal results can be attributed to the grain sizes within the film, determined to be approximately 5 nm to 10 nm thick and 20 nm wide by low magnification STEM analysis, which is in the same range studied by Tsoi. The single crystal behavior of the film can most likely be attributed to the long range crystallographic order and texture seen in the STEM and XRD normal to the substrate.

The magnetic anisotropy observed in the thin film specimen was also observed by Nakatani in the single crystal study[90–92,106,109,111,113,211,213,221]. The anisotropy constants reported here are of the same order of magnitude as those reported by Nakatani, et al.[221], being $11.8 \times 10^{-3}\,\mathrm{J\,g^{-1}}$ and $1.5 \times 10^{-3}\,\mathrm{J\,g^{-1}}$ for the single crystal. Interestingly, Nakatani also points out diffraction and magnetic observations for significant twinning in the CVT grown crystals but continues to treat $CuCr_2Se_4$ as spinel-structured. In light of additional structural analysis shown here, the significant difference in the magnetic anisotropy in the film provides an interesting support to the argument in favor of a hexagonal polymorph of $CuCr_2Se_4$. The cubic structure that has been used historically is spinel with the $Fd\bar{3}m$ space group. As the $Fd\bar{3}m$ space group is cubic, all $\langle 111 \rangle$ orientations are equivalent. If there were a hard or easy axis for magnetization present, it would be expected that all the $\langle 111 \rangle$, or body diagonals in the cubic unit cell, would respond in the same manner. In the CMKT synthesized $CuCr_2Se_4$ this would correspond to a more complex relationship between $H_{||}$ and $H_{\perp}$ than what was observed. The proposed $R\bar{3}$ structure[98] is related to the traditional $Fd\bar{3}m$ structure through the previously mentioned orthohexagonal transformation and mirror plane at $c = 0.5(R\bar{3})$, or the 111 plane of the $Fd\bar{3}m$ structure. In such a configuration, the structure would break the symmetry of the $Fd\bar{3}m$ space group that make the $\langle 111 \rangle$ directions degenerate. Examining the magnetocrystalline anisotropy

energy for the cubic, Equation 5.1., and hexagonal, Equation 5.2., systems[224]:

$$E_{cryst,cubic} = K_1\left(\alpha_1^2\alpha_2^2 + \alpha_1^2\alpha_3^2 + \alpha_2^2\alpha_3^2\right) + K_2\alpha_1^2\alpha_2^2\alpha_3^2 \qquad \text{(Equation 5.1.)}$$

$$E_{cryst,hex} = K_1\sin^2\theta + K_2\sin^4\theta + K_3\sin^6\theta\cos 6\phi \qquad \text{(Equation 5.2.)}$$

where the K_i terms are material specific coefficients, α_i^2 is the directional cosine for the cubic geometry, and $\sin^n\theta$ and $\cos 6\phi$ are the direction cosines for the hexagonal geometry. Qualitatively when $K_1 < 0$ and $K_2 \leq 0$ the basel $\{hk0\}$ plane of the hexagonal structure contains the easy axes of magnetization and the c axis of the crystal the hard axis. For the cubic system, when $K_1 < 0$ all $\langle 111\rangle$ directions are easy axes while the $(100), (010)$ and (001) directions are hard. This is illustrated in Figure 5.11., where E_{cryst} for the hexagonal, $R\bar{3}$, and cubic, $Fd\bar{3}m$ structures was plotted on a spherical surface using the calculated anisotropy constants from the hysteresis curves. The energy surface for the $Fd\bar{3}m$ structure shows the (111) planes to contain the easy axis of magnetization, however, it also shows the hard magnetic axes are along the $\{001\}, \{010\}$, and $\{100\}$ directions. This combination of easy and hard axes orientation do not match the results of the hysteresis analysis. The energy surface for the $R\bar{3}$ structure shows a marked anisotropy, with the low energy direction being parallel to the basel plane of the structure or parallel with the $H_{||}$ structure.

5.5. Conclusion

A thin film of $CuCr_2Se_4$ generated by CMKT was characterized with respect to its magnetic and electrical properties. The film was found to have be metallic with a resistivity ranging from $5 \times 10^{-4}\,\Omega\,\text{cm}$ at 298 K to $1.5 \times 10^{-4}\,\Omega\,\text{cm}$ at 20 K. Magnetic characterization of the film indicated a T_C of 414 K consistent with a nanoscale grain

FIGURE 5.11. The E_{cryst} surfaces for the hexagonal, $R\bar{3}$, and cubic, $Fd\bar{3}m$ structures as functions of θ and ϕ using calculated anisotropy constants from the hysteresis curves. (a) The energy surface for the cubic $Fd\bar{3}m$ structure shows the (111) planes to be the easy axis of magnetization, however, it shows that the {111} directions are the easy axes and the hard magnetic axes are along the {001}, {010}, and {100} directions. (b) The energy surface for the hexagonal $R\bar{3}$ structure showing significant anisotropy between the basel, $[hk0]$, plane of the structure and the (001) direction.

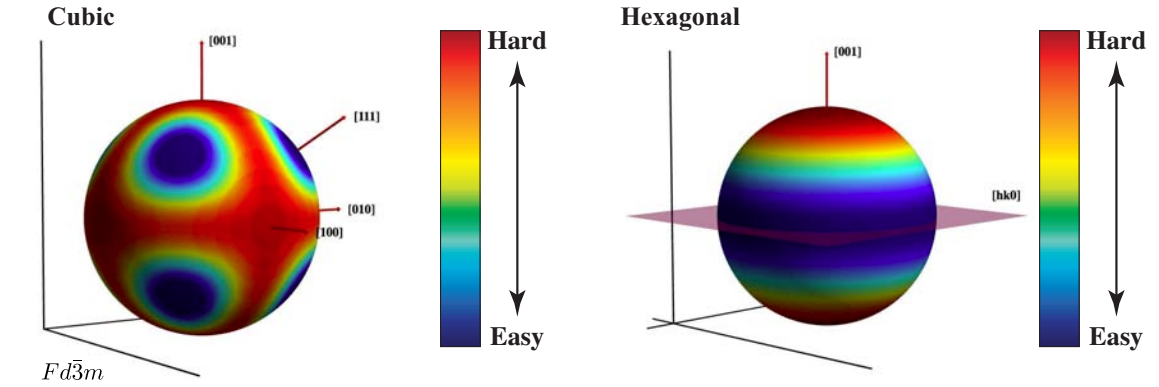

structure. The film demonstrated magnetocrystalline anisotropy which supports a previously proposed $R\bar{3}$ structural polymorph of the compound. The easy axis of magnetization for the new polymorph was found to be parallel to the 100 axis while the hard axis was found to be parallel to the *c*-axis. The magnetic anisotropy constant varies by almost two orders of magnitude between the easy and hard axes..

5.6. Bridge

In Chapter IV the general success of the synthesis of $CuCr_2Se_4$ was documented as part of a larger work on the importance of layer ordering in the CMM precursor. In this chapter the characteristics of the CMKT produced $CuCr_2Se_4$ were studied and compared to those found in the literature. The structure demonstrated an undocumented anisotropy in the magnetization of the film, but similar electrical

properties to those reported in the literature indicating the compound may represent a new polymorph of the $CuCr_2Se_4$ structure.

CHAPTER VI

STRUCTURAL ANALYSIS OF NOVEL $MoSe_2$ AND WSe_2 BASED MISFIT LAYER COMPOUNDS

6.1. Co-authorship Statement

Chapter VI is derived from the supplemental information for a paper submitted to the journal *Nature Materials* which appears as Chapter VII. Samples for this study were provided by Dr. Colby L. Heideman and Dr. Qiyin Lin. X-ray diffraction refinements were provided by Dr. Mary M. Smeller with the assistance of Dr. Paul Zschack and Dr. David C. Johnson. Density functional theory calculations were conducted by Dr. Robert Kykyneshi with the assistance of Dr. Douglas Keszler. Electron microscopy and comparative data analysis was conducted by Michael D. Anderson with the assistance of Dr. Andrew A. Herzing and Dr. David C. Johnson. Dr. Ian M. Anderson and Dr. David C. Johnson also provided editorial support.

6.2. Introduction

Misfit layer compounds (MLCs) present a number of technical challenges when attempting to solve the crystal structure from diffraction measurements. Full structural solutions via X-ray refinement require specialized multi-dimensional refinement methods to capture the incommensurability of the substructures and data collected from powder or single crystal samples[5,22,24]. The texture of thin films result in a situation where the experimentally collected data may not provide sufficient information to satisfy the degrees of freedom needed for a complete solution using these superspace refinement methods. Piecewise refinements, like those used

early in the study of misfit layer compounds, require a-priori assumptions about the structure that my not have reasonable scientific justification. Recent work by Nyugen[31,40,135], Heideman[13,133], and Lin[14,134], indicate that compounds generated through compositionally modulated kinetic trapping (CMKT) also exhibit rotational disorder between the component layers about the common *c*-axis. This added complexity makes the X-ray based structural analysis methods used by themselves impractical for structural studies of CMKT generated films.

Scanning transmission electron microscopy (STEM) is a method of imaging thin, electron transparent, specimens via a convergent beam of monochromatic electrons. In this method each atom acts as a point scatterer for the electron beam. Using detector geometry it is possible to generate images of the atomic structure in a manner that depends the Rutherford Cross-section for the atom(s) under the electron beam. This is accomplished by selectively sampling the electrons strongly scattered radially away from optical axis of the microscope using a high angle annular dark field (HAADF)detector. This Rutherford scattering is strongly dependent on the atomic number of the species involved and the intensity recorded at the HAADF detector is approximately proportional to Z^2. Sampling the HAADF intensity of the specimen by moving the beam over the specimen in a raster pattern generates a pixel array that describes the local average chemical make up of the specimen. In crystalline samples oriented such that a crystallographic zone axis is oriented parallel to the optic axis of the beam this Z^2 intensity dependance is enhanced through electron channeling . This electron channeling increases the recorded intensity above that of what would be predicted by the Rutherford cross-section. Because the image generation mechanism is related to the atomic structure directly under the beam, STEM-HAADF imaging is not hindered in the same way X-ray diffraction (XRD)

methods are by the incommensurate structure and rotational disorder of CMKT generated misfit layer compounds.

This chapter details the analysis of a series of misfit layer compounds of the form $[\{(\mathrm{MX})_\mathrm{m}\}_{1+\mathrm{y}}(\mathrm{TX}_2)_\mathrm{n}]_\mathrm{r}$, where $m = n = 1, 2, \ldots, 5$ using a combination of STEM-HAADF imaging and XRD. The structural results between the cross-section images and Rietveld refinement of the c-axis diffraction data are compared. The results of this study also the subject of the following chapter, where the structural distortions observed in STEM-HAADF images and structural refinements are discussed.

6.3. Experimental

Samples were synthesized using a custom built vacuum deposition chamber operated at a pressure of $< 10 \times 10^{-4}$ Pa. Elements Pb, Mo and W were deposited using commercially available electron beam guns, whereas Se was deposited using a custom built Knudsen type effusion cell. Quartz crystal balances used to monitor the flux of each source were connected to a computer controlled shutter and sample carousel system. Samples were deposited onto 001-oriented silicon wafers at ambient temperature, yielding amorphous precursor films. The precursors were prepared by depositing m repetitions of (Se-Pb) followed by n repetitions of (Se-T), with T = W or Mo, and repeating this sequence until a total thickness in the range of 20 nmto200 nm was obtained. Deposition parameters were determined to yield the appropriate composition and absolute number of atoms required for individual unit cells of 001-oriented PbSe (rock salt structure, composed of two equicompositional atomic layers) and TSe_2 (dichalcogenide structure, composed of three atomic layers, Se-T-Se). Samples were annealed at 400 °C for 1 h under an inert nitrogen atmosphere to crystallize the samples.

Chemical composition was determined using electron probe microanalysis (EPMA) on a Cameca SX-50 electron probe microanalyzer and the Stratagem data analysis program using a beam current of 20 nA and beam voltages of 8 kV, 12 kV and 16 kV. X-ray wavelength-dispersive spectrometry was performed using pure elements or compounds as standards. Ten independent measurements at different sample positions were averaged to determine the final composition.

The crystalline quality, orientation, and thickness of the films were evaluated by high resolution XRD and X-ray reflectivity (XRR) using a Bruker D8 Discover diffractometer with Cu-$K_{\alpha,1}$ radiation and Göbel mirror, Bragg-Brentano Optics Geometry. X-ray powder diffraction patterns were also measured in the high-resolution 33ID beam line of the Advanced Photon Source (APS) at Argonne National Laboratory. The sample was mounted on 4-circle Huber goniometer. All a- and b-axis lattice parameters of the film were calculated from grazing incidence in-plane XRD data at APS. Two dimensional (2D) k-space mapping was performed using a Marresearch GmbH MAR345 image plate detector at a grazing incidence angle of 1.0°. In the synchrotron experiments, two wavelengths of 95.78 pm and 94.29 pm were used for anomalous XRD scans and a wavelength of 92.53 pm was used for grazing incidence in-plane XRD. The diffraction data collected at different energies were refined using the General Structure Analysis System (GSAS). Several XRD patterns for samples of $[\{(PbSe)_m\}_{0.99}(WSe_2)_n]_r$ were collected for Rietveld refinement analysis in the range $12° \leq 2\theta \leq 50°$ with a step increment of 0.005° and 1s acquisition per step.

The electronic structure of $[\{(PbSe)_m\}_{1.00}(MoSe_2)_n]_r$, for $(m, n) = (1, 1)$ and $(2, 2)$ were computed with the code Wien2k[225] in the full-potential linearized augmented plane-wave formalism with the Perdew-Burke-Ernzerhof (PBE) generalized gradient approximation. The muffin-tin radii were set to 2.5 au for Pb

and 2.2 au for Se and T atoms, respectively. The potentials and charge densities were expanded on a k-mesh of 20 points in the Brillouin zone. The incommensurate structure was modeled by distorting the rock-salt lattice to tetragonal along the b-axis. Atomic positions were fully relaxed prior to electronic structure calculations.

Cross-sectioned specimens for STEM analysis were prepared using a variation on the small angle cleavage method described by McCaffrey et al.[157,158]. After initial thinning of the substrate, but before cleavage, the wafer was covered with a layer of protective carbon using a black permanent ink felt tip marker. After preliminary TEM screening, the cleaved samples were thinned for TEM analysis using an FEI NOVA NanoLab DualBeam FIB equipped with a Sidewinder ion column. Samples were thinned to approximately 300 nm using a beam of Ga ions at 30 kV accelerating voltage, followed by polishing at 5 kV and a final polishing at 2 kV. Samples were plasma cleaned using a Fischione Instruments model 1020 plasma cleaner using a 75% Ar - 25%O_2 mixture for 1 min to remove residual carbon contamination prior to TEM analysis. In order to ensure proper orientation of the cross-sectioned film with respect to the electron probe, the specimen was aligned along the [110] zone axis of the single crystal silicon substrate for each analysis.

Aberration-corrected STEM-HAADF imaging was performed with an FEI Titan 80-300 TEM/STEM equipped with a double-hexapole spherical-aberration corrector (CEOS GmbH) on the probe-forming lens. Analysis were carried out using an accelerating voltage of 300 kV, with a nominal probe current and diameter of 90 pA and 100 pm, respectively. Images were processed using the freely available package ImageJ. Final images were constructed from a series of 50 to 100 short exposures over the same area. The image series were then corrected for any drift using the StackReg algorithm in the rigid body setting[226]. The registered image sets were cropped to

the dimensions of the area common to all images in the stack, band-pass filtered to remove the high frequency noise, and then summed using the Z-projection feature of ImageJ to produce the final image. Intensity profiles were then extracted using the ImageJ line tool, averaging the intensity perpendicular to the profile direction with an integration height of nominally 300 pixels. The resulting intensity profiles were then fitted using a series of Gaussian peaks, and the centroid of each peak extracted. Figures 6.1., 6.3., 6.6., 6.8., and 6.10. contain the images for the allotropes $[\{(PbSe)_m\}_{1.00}(MoSe_2)_n]_r$, with $m = n = 1, 2, 3, 4$ and 5.

Diffraction data were refined using the Rietveld refinement method using the General Structural Analysis System (GSAS). Several starting models, using a variety of values for the distances between atom planes, were used and the refinements all converged to the endpoints reported below. Complicating the Rietveld refinements, the thin films in this study exhibit Kiessig fringes at angles up $2\theta = 30°$, as apparent in Figure B.1. Kiessig fringes arise from the interference of X-rays from the front and back surfaces of the films and indicate that these surfaces are both very smooth and parallel to one another. The GSAS program does not model this phenomenon. Therefore, LeBail fits, which refine only the unit cell size, peak profile and background parameters while automatically scaling intensites to the correct relative height of each peak, were used to define the best possible fit of each system. The peak shape, background, and unit cell size determined using the LeBail fit of each scan were used as a starting point in the subsequent Rietveld refinements of that scan. The fitted and background w_{rp} and r_p, as well as the Durban-Watson statistic and the χ^2 from the LeBail fits were compared to the error parameters of each Rietveld refinement in order to assess the relative quality of each refinement. Below we present the data,

fits and difference plots for each of the refinements, the model resulting from the refinement, and a list of refined parameters.

6.4. Results and Discussion

The cross-section of the (m, n)=$(1, 1)$ compound, shown in Figure 6.1., shows PbSe bilayers alternating with $MoSe_2$ trilayers in a regular pattern. In this particular image the structure shows layers oriented at the 100 zone axis resulting in a row of atom pairs running vertically down the image, or aligned to no particular zone axis resulting a pair of homogeneous bands of contrast running vertically through the image. Also visible in the structure are bands of the chevron-like $MoSe_2$ trilayers oriented along the 100 zone axis. The bright point at the apex of each chevron being the Nb atomic columns. The lack of layer to layer registration between the PbSe and $MoSe_2$ layers and from PbSe-$MoSe_2$ layer pair demonstrates that the structure has little long range crystallographic order between layers in the *a*-*b* plane. This is equivalent to the turbostratic disorder reported in geological circles. The results of the structural refinement for this compound, shown in Figure 6.2., show small deviations between the distance between the PbSe planes as determined by refinement and the peak to peak distance determined from the analysis of the STEM image, shown in the bottom half of Figure 6.1. However, as was previously indicated, the method of generating contrast in STEM-HAADF images is strongly dependent on the atomic number of the scattering species, meaning that the STEM analysis would have an inherent bias towards the Pb atomic centers. Accounting for this using the fine structure from the refinement brings the values within experimental error for the STEM image.

FIGURE 6.1. High resolution STEM-HAADF image of $[\{(PbSe)_1\}_{1.00}(MoSe_2)_1]_r$ with aggregate intensity plot. The distances noted are for the PbSe intra- pair distance (0.35 nm) and the distance between the last PbSe layer and the central maxima of the $MoSe_2$ region (0.48 nm).

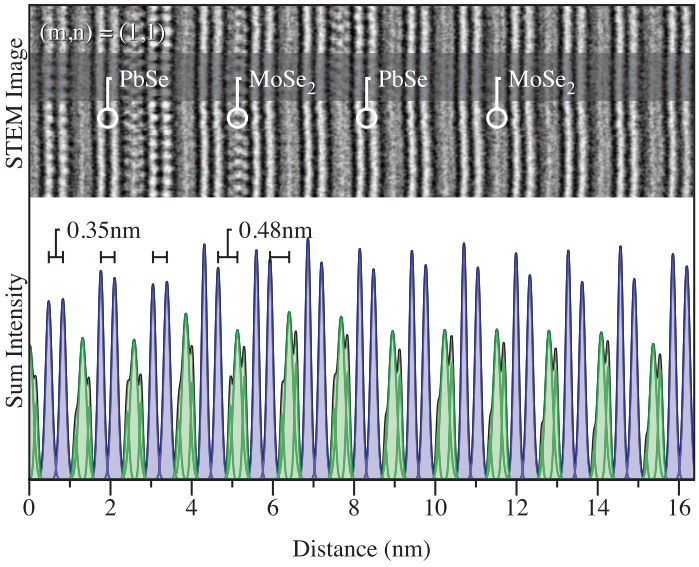

The (m, n)=$(2, 2)$ compound, shown in Figure 6.3., shows a similarly well ordered structure. In this image the PbSe layer demonstrates an example of a 110 oriented layer along with the off-axis PbSe regions. Unlike the $(1, 1)$ compound, no on-axis oriented $MoSe_2$ layers are shown in this image. This compound also shows a significant distortion of the PbSe rock-salt structure. PbSe, in the bulk is a cubic phase which has a nominally identical spacing between the atomic centers of Pb and Se. Within the *a*-*b* plane, the vertical direction in the image, the spacing between Pb centers appears regular and undistorted. Looking along the *c*-direction, the horizontal direction in the image, the PbSe planes show a pairwise contraction of the planes with the spacing in between the pairs compensating by elongating to maintain the overall unit cell vectors. The total deviation from the relaxed cubic structure caused by this distortion is $\delta =$ 0.05 nm. Examination of the spacings between the PbSe and $MoSe_2$ show no apparent distortions between the substructures. The results of the structural refinement, Figure

FIGURE 6.2. A schematic representation of the refined positions of the atomic planes along the c-axis of $[\{(PbSe)_1\}_{0.99}(WSe_2)_1]_r$.

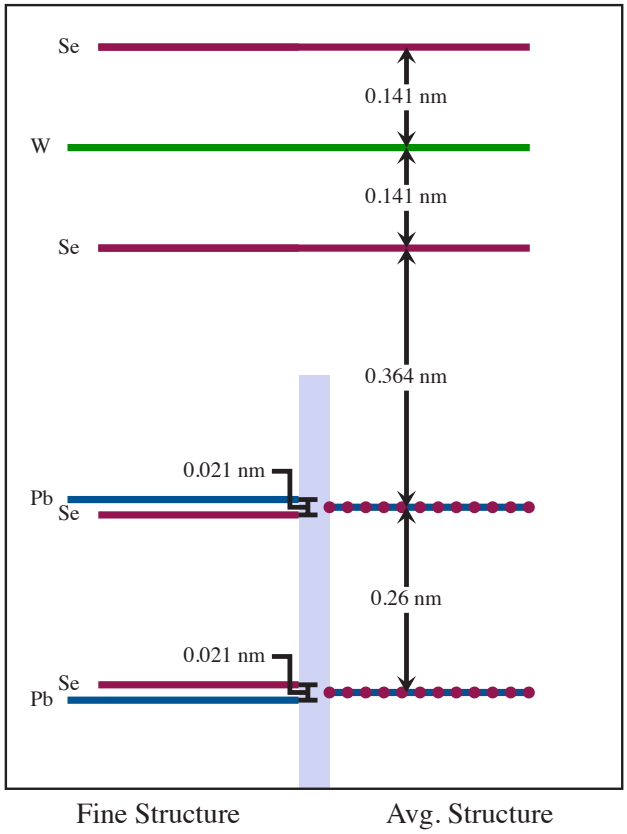

FIGURE 6.3. High resolution STEM-HAADF images of $[\{(PbSe)_2\}_{1.00}(MoSe_2)_2]_r$ with aggregate intensity plot. The distances noted are for the PbSe intra- (0.29 nm) and inter-pair distance (0.34 nm) as well as the distances between the last PbSe layer and the central maxima of the $MoSe_2$ region (0.50 nm) and the distance between consecutive $MoSe_2$ regions (0.66 nm).

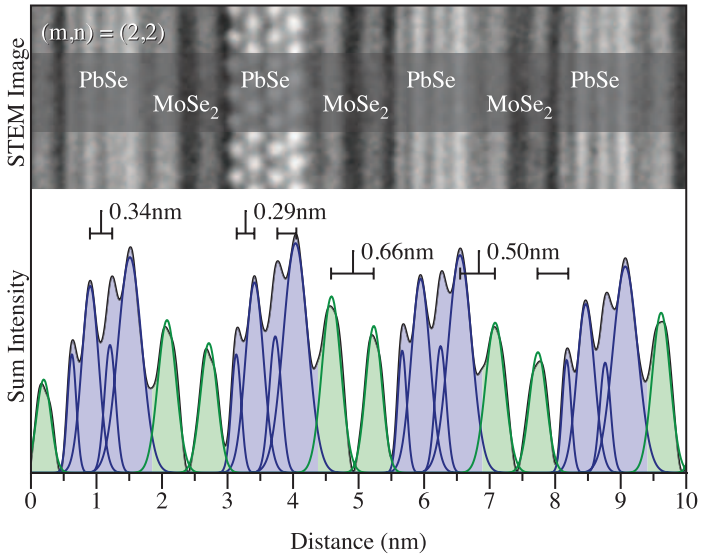

6.5., again taking into account the bias toward the Pb positions in the PbSe 100 planes, show a pairwise distortion of the same magnitude. Examination of a related film, $[\{(PbSe)_2\}_{0.99}(WSe_2)_1]_r$ shown in Figure 6.4., exhibits identical distortions in the PbSe layers to the $[\{(PbSe)_2\}_{1.00}(MoSe_2)_2]_r$ compound and no difference in the spacings between the PbSe and WSe_2 layers.

Examination of the remaining structures, (m, n)= $(3, 3)$,$(4, 4)$, and $(5, 5)$, shown in Figures 6.6. through 6.11., demonstrate a relaxation of the distortion observed in the $(2, 2)$, but otherwise the previous structural observations are consistent through the series. One of the most significant of these observations is the apparent lack of crystallographic registration between the layers or bilayers through the thickness of the film. The individual $[PbSe]_r$, where $r = 1, 2, \ldots, 5$, layers seem to act as monolithic platelets with *a*-*b* domains on the order of 20 nm, based on lower

FIGURE 6.4. High resolution STEM-HAADF images of $[\{(PbSe)_2\}_{0.99}(WSe_2)_1]_r$ with aggregate intensity plot. The distances noted are for the PbSe intra- (0.29 nm) and inter-pair distance (0.34 nm) as well as the distances between the last PbSe layer and the central maxima of the WSe_2 region (0.50 nm).

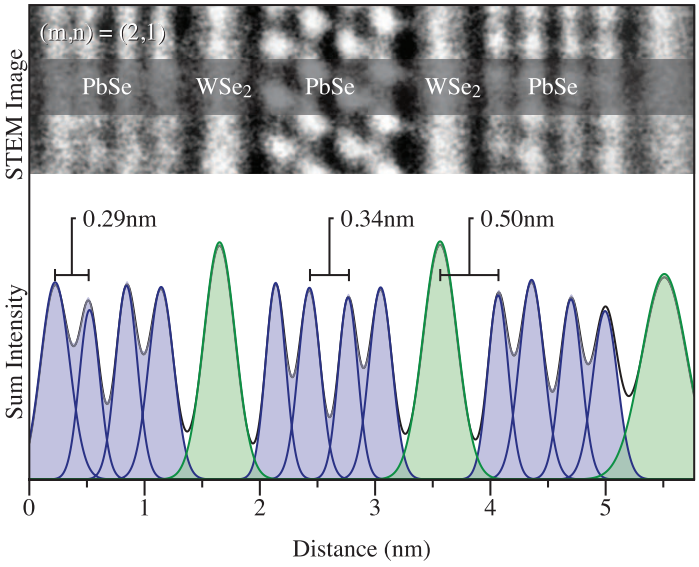

magnification observations. The $[MoSe_2]_r$ layers appear to act as buffer layers preventing communication between the individual $[PbSe]_r$ platelets. This isolation appears to work in conjunction with the random nucleation of the CMKT process to produce a highly textured solid in the *c*-lattice direction with a complete random orientation about this common axis. This is a distinct difference from the traditional misfit layer compounds in the literature to date.

6.5. Conclusions

The cross-sectional structure of $[\{(MX)_m\}_{1+y}(TX_2)_n]_r$ compounds, where MX = PbSe and TX_2 = $MoSe_2$ and WSe_2, were analyzed via STEM-HAADF imaging and synchrotron X-ray diffraction. STEM analysis documented a series of compounds with a high degree of crystallographic order along the *c*-axis of the supercell, but with significant rotational disorder about the common *c*-axis. Analysis of the distances

FIGURE 6.5. A schematic representation of the refined positions of the atomic planes along the c axis of $[\{(PbSe)_2\}_{0.99}(WSe_2)_2]_r$.

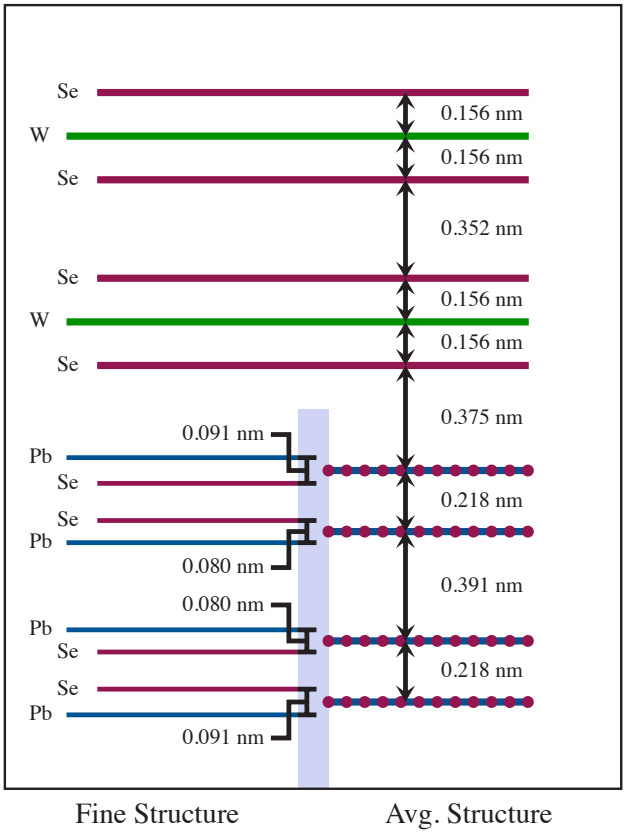

between the a-b planes along the c-axis in the cross-section images show a pair-wise distortion that decreases in magnitude with increasing m. Structural refinements of X-ray diffraction data for each compound corroborated this observed distortion. This observed distortion will be subject of Chapter VII.

The rotational disorder found in these compounds is a distinct departure from the behavior of more traditional misfit layer compounds. Members of the classic misfit layer compounds, like those discussed in the introduction, have a common c-axis between the substructures and have a common a or b axis as well, making the compound incommensurate in only one direction. Further, these compounds, possibly because of the long times at high temperature employed in the majority of the literature preparations, demonstrate a much higher degree of long range crystallographic order between the a-b planes. TEM analyses of single crystals of misfit layer compounds have shown that large portions of the sample have the same crystallographic orientation through out, i.e. when one layer of the rock-salt component is at the 100 zone axis all others are as well. The combination of these factors suggest that the compounds created by CMKT may not be best described by the term misfit layer compound. Given that the structures are crystallographically ordered along the c-direction of the supercell, but are essentially random in the a or b directions with respect to the whole structure, it seems inappropriate to call the CMKT synthesized structures crystals. It seems more reasonable that these structures be given a new designation that captures both the crystalline order of the structure as well as its disorder. The term ferecrystal, derived from the latin *fere* meaning almost, is proposed for this purpose and will be used for the balance of this work.

FIGURE 6.6. High resolution STEM-HAADF images of $[\{(PbSe)_3\}_{1.00}(MoSe_2)_3]_r$ with aggregate intensity plot. The distances noted are for the PbSe intra- (0.30 nm) and inter-pair distance (0.33 nm) as well as the distances between the last PbSe layer and the central maxima of the $MoSe_2$ region (0.50 nm) and the distance between consecutive $MoSe_2$ regions (0.66 nm).

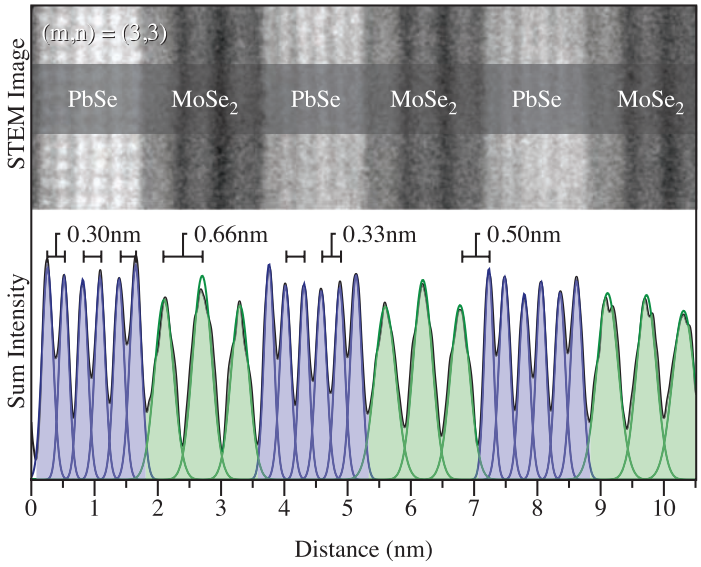

6.6. Bridge

This chapter, in conjunction with Chapter VII, demonstrate the proof of concept of the characterization scheme designed to facilitate the later structural studies. This chapter also demonstrates the utility of employing STEM based analysis for CMKT compounds before more specialized analytical methods like synchrotron based X-ray crystallography. The observed rotational anisotropy within the CMKT misfit layer compounds demonstrated sufficient differences from their geological and counterparts that a new term, ferecrystals or ferecrystalline solids, was deemed necessary.

FIGURE 6.7. A schematic representation of the refined position of the atomic planes along the c axis of $[\{(PbSe)_3\}_{0.99}(WSe_2)_3]_r$.

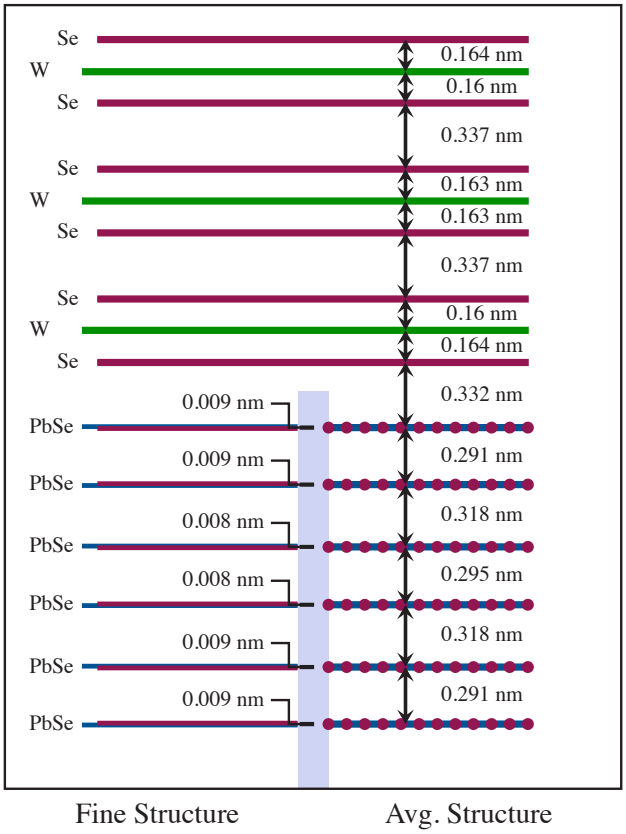

FIGURE 6.8. High resolution STEM-HAADF images of $[\{(PbSe)_4\}_{1.00}(MoSe_2)_4]_r$ with aggregate intensity plot. The distances noted are for the PbSe intra- (0.31 nm) and inter-pair distance (0.32 nm) as well as the distances between the last PbSe layer and the central maxima of the $MoSe_2$ region (0.50 nm) and the distance between consecutive $MoSe_2$ regions (0.66 nm).

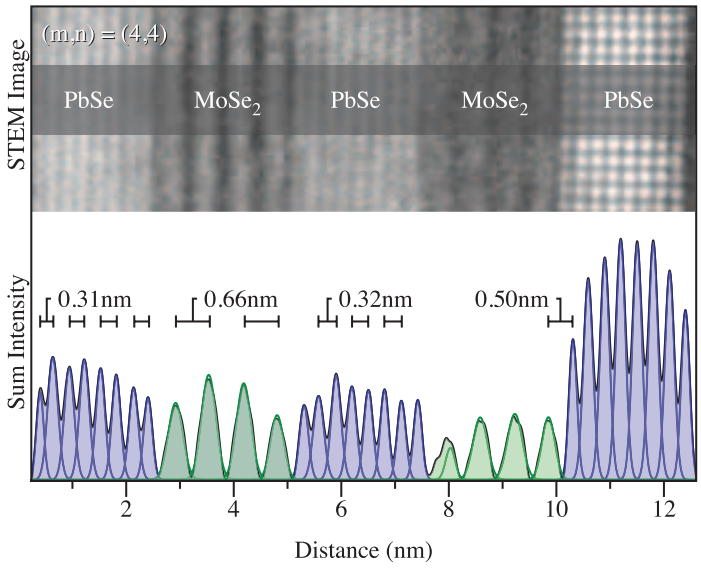

FIGURE 6.9. A schematic representation of the refined position of the atomic planes along the c axis of $[\{(PbSe)_4\}_{0.99}(WSe_2)_4]_r$.

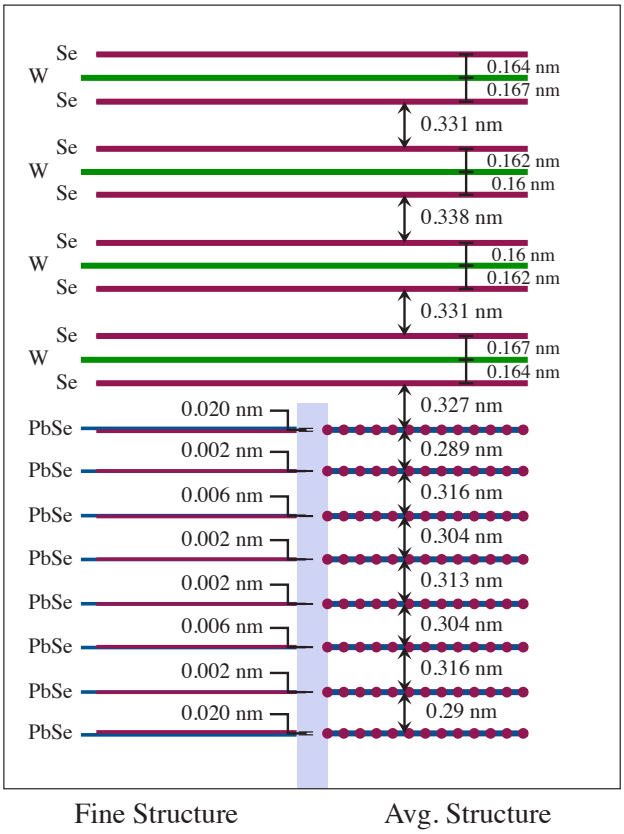

FIGURE 6.10. High resolution STEM-HAADF images of $[\{(PbSe)_5\}_{1.00}(MoSe_2)_5]_r$ with aggregate intensity plot. The distances noted are for the PbSe intra- (0.32 nm) and inter-pair distance (0.32 nm) as well as the distances between the last PbSe layer and the central maxima of the $MoSe_2$ region (0.50 nm) and the distance between consecutive $MoSe_2$ regions (0.66 nm).

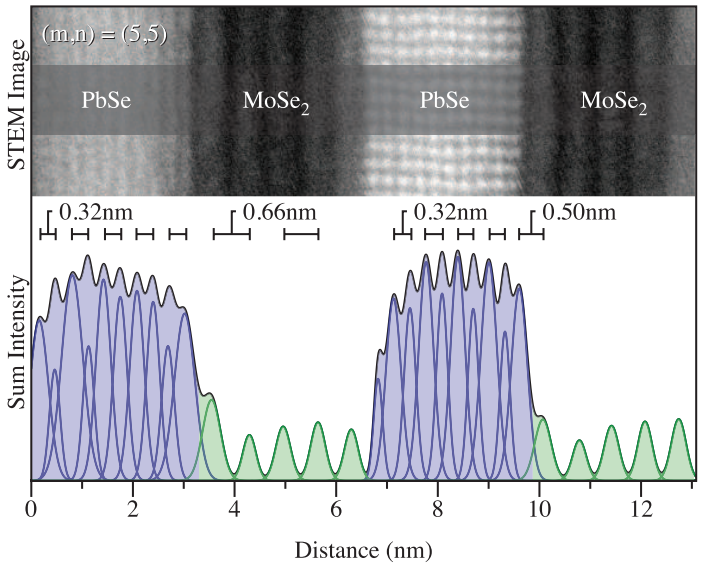

FIGURE 6.11. A schematic representation of the refined position of the atomic planes along the c axis of $[\{(PbSe)_5\}_{0.99}(WSe_2)_5]_r$.

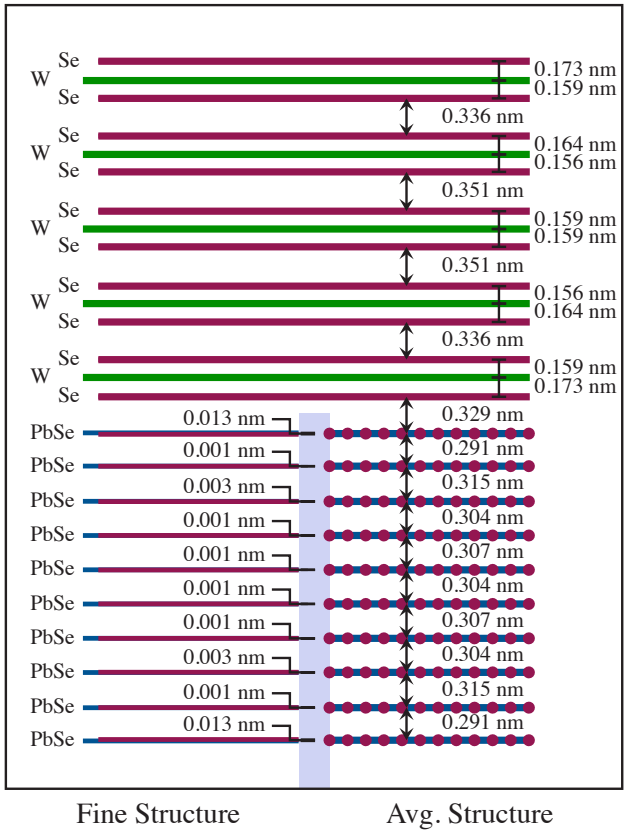

CHAPTER VII

SIZE DEPENDENT STRUCTURAL DISTORTIONS IN ONE DIMENSIONAL NANOSTRUCTURES

7.1. Co-authorship Statement

Chapter VII is derived from a paper submitted to the journal *Nature Materials*. Samples for this study were provided by Dr. Colby L. Heideman and Dr. Qiyin Lin. X-ray diffraction data found in Figure 7.3. were also provided by Dr. Heideman. X-ray diffraction refinements were provided by Dr. Mary M. Smeller with the assistance of Dr. Paul Zschack and Dr. David C. Johnson. Density functional theory calculations were conducted by Dr. Robert Kykyneshi with the assistance of Dr. Douglas Keszler. Electron microscopy and comparative data analysis was conducted by Michael D. Anderson with the assistance of Dr. Andrew A. Herzing and Dr. David C. Johnson. Dr. Ian M. Anderson and Dr. David C. Johnson also provided editorial support.

7.2. Discussion

Nanoscale materials have been intensely studied since the discovery that the optical properties of semiconductor nanoparticles are size dependent, an effect which arises due to spatial confinement of the localized wave functions of the electron-hole exciton pair by the small size of the nanoparticle[227–229]. This and subsequent research has demonstrated that a given physical property of a particle exhibits a size dependence when the size becomes comparable to its characteristic length scale. Examples of relevant length scales include the de Broglie wavelength and/or the mean free path of electrons, phonons, and elementary excitations, all of which typically

range from one to a few hundred nanometers. The ability to tune a wide variety of properties by controlling the particle size has spurred the development of novel chemistries for preparing nanostuctured elements and compounds with precise control of size, shape and ligand shell[230–234].

As the size of a nanocrystal decreases, the ratio of bulk to surface atoms decreases. This progression increases the relative contribution of the surface free energy relative to the volume free energy of the bulk structure, such that distortions from bulk equilibrium structures might be expected as nanoparticle size decreases. Unfortunately, while researchers have demonstrated the ability to prepare ordered lattices of nanoparticles[235–240], the isolation of lattices of nanoparticles with long-range atomic periodicity is rare[238,240,241] because common synthetic approaches produce a polydisperse distribution of nanoparticle sizes. Hence detailed atomic structures and, in turn, the size-structure-property relationships of most nanoparticle systems cannot readily be determined[241–243].

We recently reported the preparation of families of new compounds with the general formula $[\{(MX)_m\}_{1+y}(TX_2)_n]_r$, with M= (Pb, Bi Ce) and T= (W, Nb, Ta)[13,14]. The values of m and n represent, respectively, the number of MX and TX_2 structural units of the unit cell of the superstructure. The misfit parameter, y, describes the difference between the densities of metal cations in the two structural units. Each TSe_2 structural unit consists of a hexagonal layer of metal cations, T, sandwiched between hexagonal close-packed planes of selenium anions, with the cations located in either the octahedral (stacking sequence AcB) or trigonal prismatic (AbA) interstices of the anion sublattice. Each MSe structural unit contains two distorted $00l$ planes of the rock salt structure. The rock salt structured layers are incommensurate with the close-packed anion planes of the TSe_2 structural

unit. As reported herein, the long range structural order along the modulation direction permits us to determine the atomic structure of these precisely defined one-dimensional (1D) nanolaminate structures as a function of layer thickness using a combination of scanning transmission electron microscopy (STEM) high angle annular dark field (HAADF) imaging and X-ray diffraction (XRD) with Rietveld refinement.

STEM-HAADF images of the first five $[\{(PbSe)_m\}_{1.00}(MoSe_2)_n]_r$ compounds in the family $m = n$ are shown in Figure 7.1. All have a regular periodic structure along the modulated axis with well-defined layers of PbSe and $MoSe_2$. The STEM images show ordered domains of PbSe with characteristic dimensions of a single structural unit along the layering direction and tens of nanometers perpendicular to the layering direction, with random in-plane rotational variants both within a layer and between layers. The orientations of the $MoSe_2$ domains are more difficult to discern from the STEM images, but rotational variants have been observed between individual $MoSe_2$ structural units. The STEM-HAADF images reveal a distortion of the PbSe layers, with the atomic planes grouped into pairs rather than being evenly spaced as expected for the equilibrium (bulk) rock salt structure. The distortion is most evident in the structural variant $(m, n) = (2, 2)$ (Figure 7.2.) and decreases in magnitude until it can no longer be observed for $(5, 5)$. STEM-HAADF images of structural variants $(2, 2)$, $(3, 3)$, and $(3, 1)$ are shown in Figure 7.2., with aggregate intensity plots used to quantify the PbSe intra- and inter-pair distances. The inter-pair distances are 0.03 nm longer than the intra-pair distances in both $(3, 3)$ and $(3, 1)$, suggesting that the distortion is independent of the number of structural units in the $MoSe_2$ layer.

The extended registry of the atomic planes along the modulation axis results in X-ray diffraction patterns (Figure 7.3.a.) containing numerous $00l$ diffraction maxima, which can be used to determine the position of atomic planes along the c axis and

FIGURE 7.1. High resolution STEM-HAADF images of $[\{(PbSe)_m\}_{1.00}(MoSe_2)_n]_r$ compounds in the family $m = n$ showing the change in the pairing distortion in the PbSe layers as a function of the number of $00l$ PbSe planes. The rock-salt-structured domains exhibit numerous rotational variants within the (001)-oriented growth plane, with selected grains aligned along the $\langle 100 \rangle$- and $\langle 110 \rangle$-type zone axes.

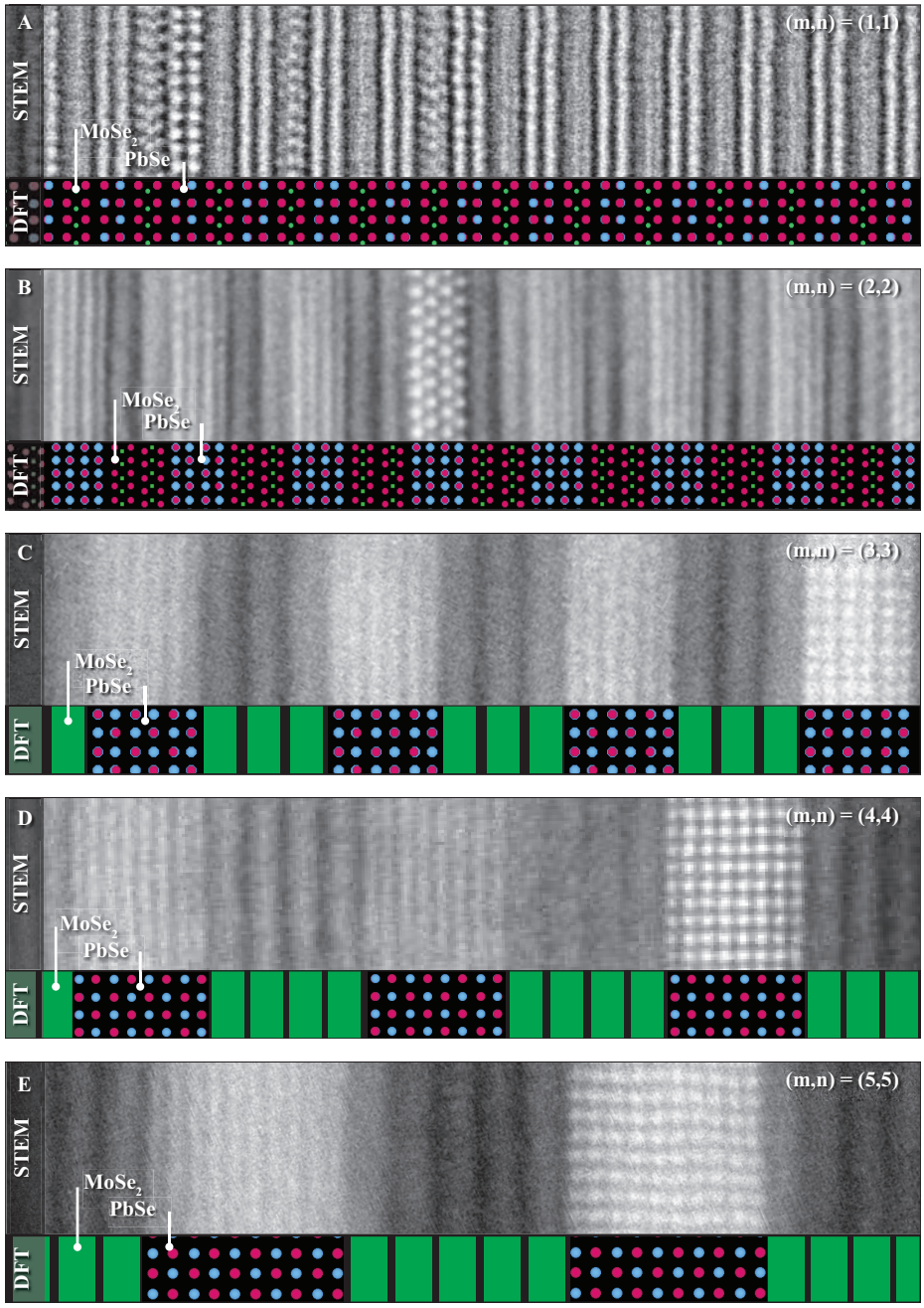

FIGURE 7.2. High resolution STEM-HAADF images of structural variants $(m, n) = (2, 2)$, $(3, 3)$, and $(3, 1)$ of $[\{(PbSe)_m\}_{1.00}(MoSe_2)_n]_r$, with aggregate intensity plots. The distances noted are for the PbSe intra- and inter-pair distances as well as the distances between the last PbSe layer and the central maxima of the $MoSe_2$ region and the distance between consecutive $MoSe_2$ regions.

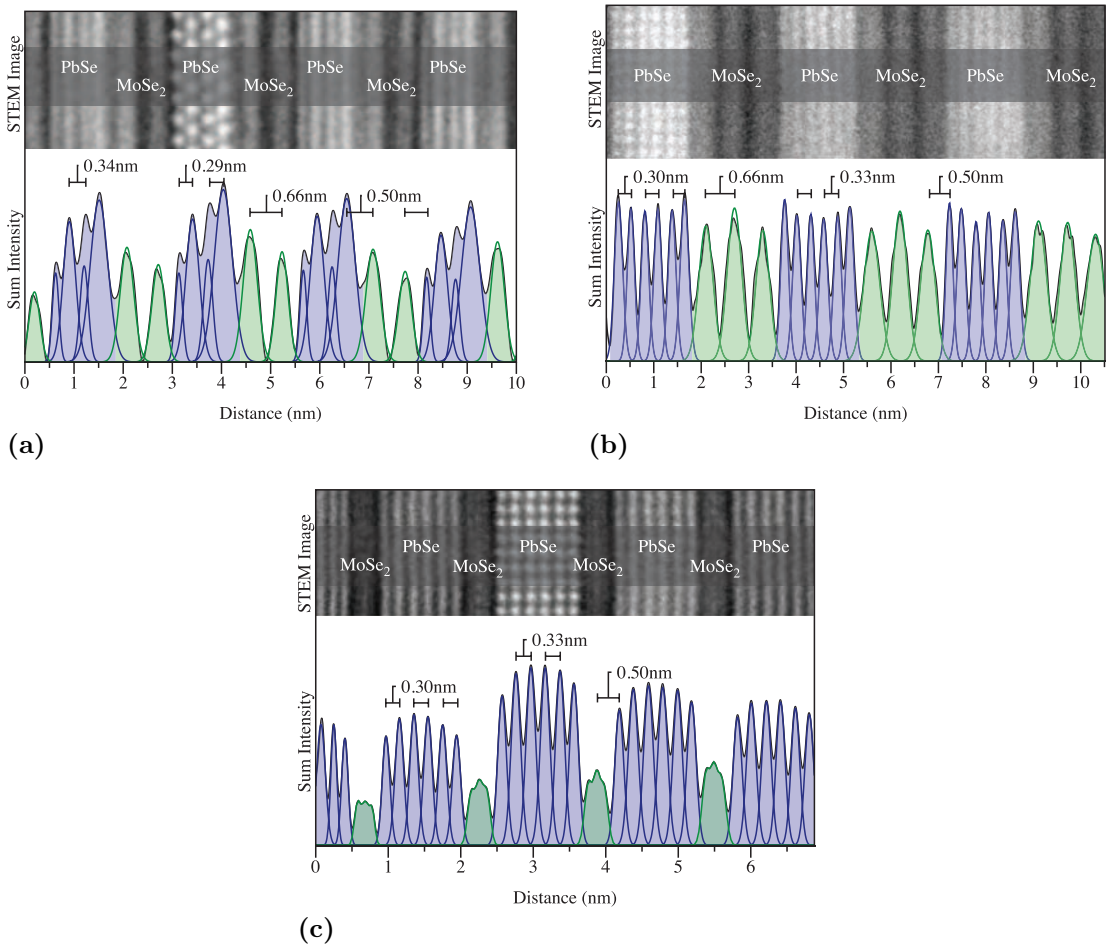

hence independently determine the magnitude of the structural distortions. The lattice parameters of the superstructure along the c-axis direction exhibit discrete changes of $\Delta c_m = (0.607 \pm 0.007)\,\mathrm{nm}$ and $\Delta c_n = (0.657 \pm 0.005)\,\mathrm{nm}$ as the number m or n of the PbSe or $MoSe_2$ structural units, respectively, is incremented. In-plane X-ray diffraction scans (Figure 7.3.b.) contain Bragg diffraction maxima that can all be indexed based on independent crystal structures for the PbSe ($a = b = 0.617\,\mathrm{nm}$) and $MoSe_2$($a = 0.332\,\mathrm{nm}$) layers. The line widths of the reflections $hk0$ of the PbSe and $MoSe_2$ structural units differ, reflecting different in-plane domain sizes of $(9 \pm 1)\,\mathrm{nm}$ for PbSe and $(4 \pm 1)\,\mathrm{nm}$ for $MoSe_2$. There is no change in the lattice parameters or in-plane domain sizes as m and n increase and the films remain flat when removed from the sample substrate, suggesting that there is little residual strain despite the significant lattice mismatch between the layers. The random rotational variants observed in the PbSe between layers precludes the observation of coherent diffraction between layers along mixed-index hkl ($h, k \neq 0; l \neq 0$) directions. As shown in Figure 7.3.b. however, weak subsidiary maxima, denoted by white arrows, are observed along mixed-index reflections of the PbSe constituent. These maxima result from the finite size of the crystallites in these directions, as can be observed by the identical patterns observed for both $(3, 1)$ and $(3, 3)$ variants. The diffraction data strongly suggest that the lattices of PbSe and $MoSe_2$ are not constrained by epitaxy at their interfaces, that the rock salt structured layers are crystallographically decoupled from one another, and that the layer thickness of one component does not affect the structure of the other.

Rietveld refinements of the $00l$ diffraction pattern of a different system, $[\{(PbSe)_m\}_{0.99}(WSe_2)_n]_r$ with (m, n)=$(1, 1)$, are consistent with that previously reported for similar $(1, 1)$ compounds[8]. The refinements reveal that Pb and Se planes

FIGURE 7.3. XRD patterns acquired from structural variants $(m, n) = (3, 3)$, and $(3, 1)$ of $[\{(\mathrm{PbSe})_{\mathrm{m}}\}_{1.00}(\mathrm{MoSe_2})_{\mathrm{n}}]_{\mathrm{r}}$. (a) Bragg-Brentano patterns acquired using Cu-K_α radiation ($\lambda = 154\,\mathrm{pm}$) with the upper and lower pairs of patterns collected parallel and perpendicular to the plane of the films, respectively. (b) Two-dimensional in-plane patterns acquired using synchrotron radiation ($\lambda = 92.53\,\mathrm{pm}$). All peaks occur near reflections expected from the bulk crystal structures for PbSe and $MoSe_2$. The four weak reflections in each pattern, indicated with arrows, correspond to non-integer indices of PbSe of type $20l$, as discussed in the text.

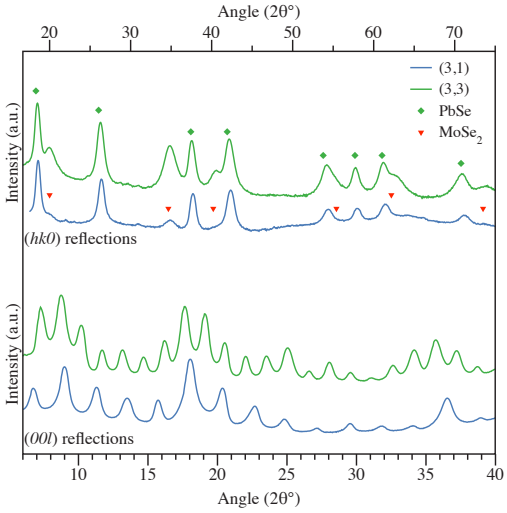

(a)

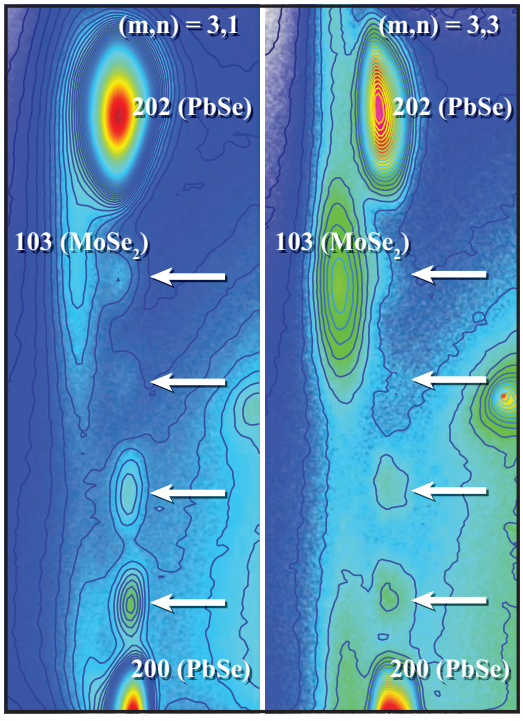

(b)

are separated by 21 pm, with the Pb in each of the distorted 001 planes of the rock salt structure displaced closer to the selenium of the dichalcogenide. This interfacial distortion or layer puckering is within the range (20 pm*to*60 pm) previously reported[8]. Refinements of other (m, n) family members in this system yield distances consistent with those shown in Figure 7.2. and show that the puckering of the surface Pb-Se layer decreases as the number of structural units, m, in the PbSe layer increases. The refinements also reveal that the PbSe planes are paired, as observed in STEM-HAADF data, and the difference between the intra-pair and inter-pair distances decreases with increasing m and with greater distance from the PbSe-WSe_2 interface.

To model the observed distortions density functional theory (DFT) simulations were performed for isolated sheets of rock salt structured PbSe with layer thickness along the c-axis ranging from 1 to 5 unit cells. Idealized PbSe structures of thickness $m \times c$ ($m = 1$ to $5; c = 0.306$ nm) were allowed to relax to minimum-energy configurations. In the case of a single unit cell ($m = 1$), a strong reduction to $c = 0.283$ nm is observed, while the a-axis lattice parameter remains unchanged. The experimentally observed pairing distortion for $m > 1$ is also observed; as m increases, the average c-axis lattice parameter approaches the bulk value. In the case of $m = 5$, the bulk PbSe structure is largely restored with only small distortions in the terminal units. These results provide additional evidence that the distortions are size dependent and decoupled from the dichalcogenide layers. Only a slight puckering (≈ 6 pm for $m < 5$; ≈ 3 pm for $m = 5$) is observed for the surfaces of the relaxed PbSe layers. This distortion is significantly smaller than the experimentally observed value of 22 pm. The puckering, however, increases to 15 pm in the presence of the dichalcogenide layer in a model $[\{(PbSe)_1\}_{0.99}(WSe_2)_1]_r$ structure, likely resulting

from Pb completing its coordination through bonding with the Se of WSe_2 and charge transfer from the WSe_2 to PbSe structural units.

Figure 7.4. contains a graph of the magnitude of the pairing distortion as a function of the number of PbSe structural units as calculated from the DFT simulations and as measured from the STEM images and the XRD pattern refinement. The magnitude of the distortion decreases as the number of structural units, m, of PbSe increases. Conceptually, the distortion of the rock salt structure arises from two distinct contributions: a distortion of the interface plane to optimize the interaction between the PbSe and $MoSe_2$ regions; and a volume distortion of the structure to minimize the total free energy. The systematic structural distortions observed in PbSe as the number of structural units decreases has significant implications, perhaps explaining the synthetic difficulties in isolating very small cluster sizes of extended structures. Our observations also suggest that structural distortions offer a possible root cause for the size dependency of physical properties at the nanoscale, and that discontinuities in physical properties with size should be expected for nanostructures as a consequence of these structural distortions.

7.3. Bridge

This chapter, along with Chapter VI, complete the first phase of the project. This final study represents a statement about the underlying need to expand and understand ferecrystalline solids. The ability to create crystallographically aligned systems that provide analogs for free nanocrystalline systems allow for a more thorough investigation of the structure-property relationship that is the cornerstone of nanotechnology. The example presented here of the structure-size dependance can be

FIGURE 7.4. The change in the magnitude of the PbSe lattice distortion with increasing layer thickness. STEM and DFT data were collected using the $[\{(PbSe)_m\}_{1.00}(MoSe_2)_n]_r$ system while the XRD data was collected using $[\{(PbSe)_m\}_{0.99}(WSe_2)_n]_r$. See text for details.

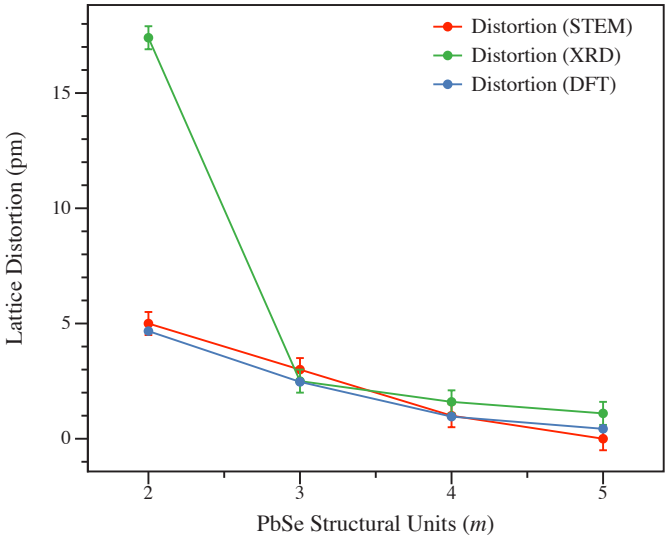

considered an example of the type of insight that would have otherwise been difficult to gain via analysis of free nanoparticles.

CHAPTER VIII

DEVELOPMENT OF $[\{(FeSe)_M\}_{1+Y}(NbSe_2)_N]_R$: AN ARTIFICIAL TOCHILINITE ANALOG

8.1. Co-authorship Statement

Chapter VIII is derived from a paper prepared for submission to *The Journal of The American Chemistry Society.* Synthesis and characterization work was conducted by Michael D. Anderson. Logan LaRosa worked under Michael D. Anderson on data collection, analysis and the annealing studies. Dr. Andrew A. Herzing assisted with the STEM and STEM-EELS analysis. Dr. Ian M. Anderson and Dr. David C. Johnson provided editorial support.

8.2. Introduction

Scientists often look to nature for inspiration. In the case of solid state chemistry this means looking at minerals and their structures. Minerals are typically defined by a common basic crystal structure, which can range from the simple, such as diamond or rock salt, to very complex, like cylindrite or franckeite. Recent work on the cylindrite and tochilinite structures shown that these minerals may be described as intergrowths of two differing substructures[5,6,10,12–14,22]. Because of this complexity, complete crystallographic descriptions of these minerals has required superspace crystallography to accurately describe the structure[5,6,22]. Examination of the literature indicates approximately 15-20 compounds based on this motif and the variation employing the bismuth telluride structure in place of the rock-salt structure[5,6,10,12,22]. Examination of component compounds sharing the same crystal

structure, i.e. rock-salt, transition metal dichalcogenide, or bismuth tellurides, demonstrate a more diverse field of possibilities than what is indicated by current literature. Looking at the sulfide misfit layer compounds[6], a combinatorial analysis of the currently known substructures indicate over 60 possible compounds. There is no apparent reason for not being able to incorporate other compounds into misfit type structures beyond not being able to avoid stable intermediate phases formed during traditional preparative methods.

Compositionally modulated kinetic trapping (CMKT), a solid state synthetic which relies on kinetic rather than thermodynamic reaction pathways, has proved successful with cylindrite-like $[\{(MX)_m\}_{1+y}(TX_2)_n]_r$ compounds, generating several hundred novel compounds within a number of different families of MX-TX_2 combinations[13,14,38,40]. The degree of control imparted by CMKT allows m and n to be chosen arbitrarily by building length scale information into the precursor[13,14,38,40,123,125]. Recent work with these cylindrite-like compounds has demonstrated CMKT also produces ferecrystalline solids which may be thought of as rotationally disordered polymorphs of the cylindrite structure[13,14,31,133–135]. The ability of this approach to independently vary m and n over a wide range of a values opens up systematic studies of structural and physical properties as a function of designed nanoarchitecture.

To date this approach for synthesis of complex intergrowths has only been applied to the previously mentioned cylindrite-like structures. Looking to other geological systems for inspiration, we attempted to extend this approach to a system related to the tochilinite structure[15,16], with a potentially interesting mix of physical properties: $[\{(FeSe)_m\}_{1+y}(NbSe_2)_n]_r$, which is shown in Figure 8.1. The proposed $[\{(FeSe)_m\}_{1+y}(NbSe_2)_n]_r$ structure was designed to be isostructural to tochilinite,

FIGURE 8.1. The proposed $[\{(FeSe)_1\}_{1+y}(NbSe_2)_1]_r$ structure. On the right the bulk structures are shown with their relevant crystallographic data. On the left is shown the incommensurability of the FeSe and $NbSe_2$ structures oriented at the major zone axes and the results of free rotation of the components about the common c-axis of the crystal. The $a_1 : a_2$ and $a_1 : b_2$ ratios are irrational meaning that no direct crystallographic alignment exists between the two in the $\{hk0\}$ plane of the crystal. Ferecrystalline compounds have been shown to exhibit a free rotation, or turbostratic disorder, about the common c - axis of the crystal.

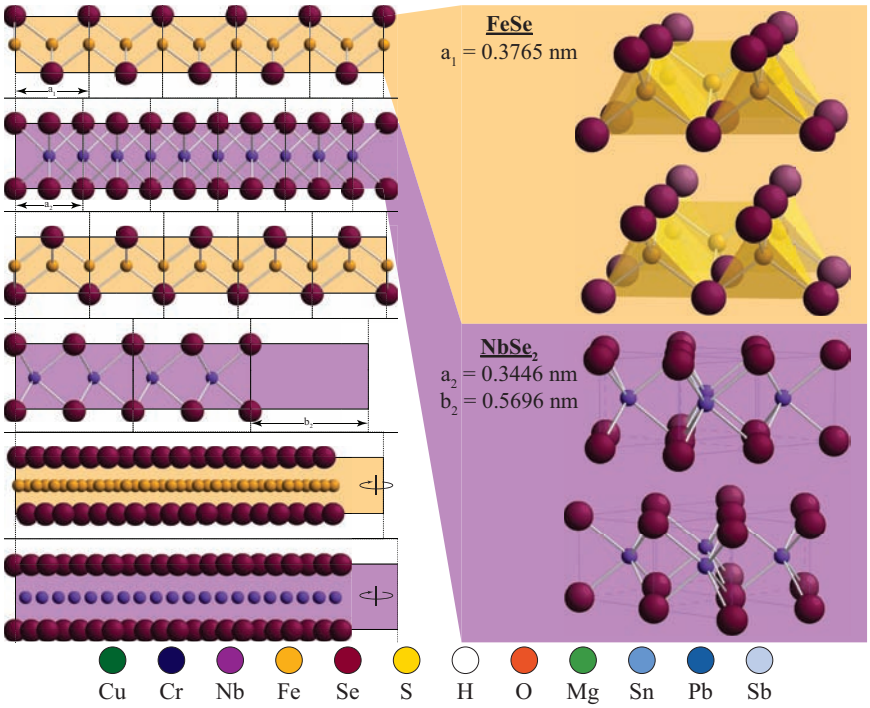

$[\{(FeS)_m\}_{1+y}(Fe, Mg(OH)_2)_n]_r$. FeSe and FeS have a similar tetragonal structure with Se-Fe-Se trilayers seperated by van Der Waals gaps, based off of the anti-PbO crystal motif. $NbSe_2$ has a hexagonal structure with Se-Nb-Se trilayers seperated by van Der Waals gaps which can be seen in the complex hydroxide portion of tochilinite. Previous literature has shown both the FeSe and $NbSe_2$ compounds to be superconductors in the range of 7 K to 9 K[9,48,51,54,74,76]. The FeSe structure has also been shown to have ferromagnetic behavior tied to the Se concentration[50,51,57,68]. This work demonstrates the CMKT based synthesis of this family of compounds.

8.3. Experimental

Compositionally modulated multilayer (CMM) precursors were calibrated to yield a stoichiometric ratio of metal cations and a slight excess of selenium to allow for evaporation losses during annealing. Samples were deposited using a custom evaporative metal deposition system described previously[210]. Fe and Nb were deposited by electron beam sources. Se was deposited using a Knudzen type effusion cells. Films were deposited under a vacuum of less than 1×10^{-4} Pa. Deposition of the CMM precursors was conducted by sequentially positioning the substrate carousel over the desired sources and opening the shutter to achieve the desired layer thickness corresponding to a given shutter time or frequency shift of the quartz crystal oscillator. Samples with thickness of 50 nm or greater were deposited on commercially available (001)-oriented silicon substrates with native oxide layers.

Samples were annealed on a custom fabricated hot plate that was equilibrated at the target temperature for at least 15 min before each heat treatment. Annealing was conducted under a high-purity nitrogen atmosphere (O_2 content of $\approx 500\,\mathrm{nL\,L^{-1}}$) at temperatures ranging from 100 °C to 600 °C. The thin films were analyzed using electron probe microanalysis (EPMA), X-ray diffraction (XRD) and X-ray reflectivity (XRR).

Specimens were prepared for EPMA by sectioning a $\approx 5\,\mathrm{mm}^2$chip from the silicon supported samples. These sample chips were carefully mounted onto an aluminum sample stub using quick set epoxy and cured at ambient temperature for 24 h. A dab of carbon paint was applied from the surface of the sample chip to the surface of the sample stub at two corners of the chip to provide a conductive path to ground. Samples were analyzed using a Cameca SX-100 Microprobe equipped with five X-ray wavelength-dispersive spectrometers. Samples were analyzed using a range of

operating voltages between15 kV to 25 kV at8 to 10 sites each spaced approximately 100 µm apart. The resulting EPMA data were then analyzed using the Pouchou and Pichoir method as detailed elsewhere[144,151,152].

XRR was performed on a Bruker-AXS D8 Discover X-ray diffractometer using CuK_α radiation ($\lambda = 0.154\,18$ nm). The incident beam and exit beam were conditioned and collimated using a parabolic multilayer mirror with a 0.1 mm divergence slit and a 0.6 mm anti-scatter slit, a Soller slit assembly, and 0.05 mm detector silt, respectively. Each sample was carefully aligned to be centered in the goiniometer. XRR data were collected over an angular range of $0° < 2\theta < 7°$with a step increment of 0.003°and a data collection time of 1 s er point. XRD was performed using the same experimental parameters but at lower angular resolution, with a 0.025° step increment, and 1 mm divergence and detector slits. In plane XRD patterns were measured in the high-resolution 33ID beam line of the Advanced Photon Source at Argonne National Laboratory using an incident beam with a wavelength of 99.19 pm.

Samples were prepared for for scanning transmission electron microscopy (STEM) analysis using a variation on the small angle cleavage method developed by McCaffrey, et al[157,158]. After initial thinning of the substrate, but before cleavage, the wafer was covered with a layer of protective carbon using a black permanent ink felt tip marker. After preliminary transmission electron microscopy (TEM) screening , the cleaved samples were thinned for STEM analysis using an FEI NOVA NanoLab DualBeam FIB equipped with a Sidewinder ion column. Samples were thinned to approximately 300 nm using a 30 kV accelerating voltage, followed by polishing at 5 kV and a final polishing step at 2 kV. Samples were plasma cleaned using a Fischione model 1020 plasma cleaner for 5 min to remove residual carbon contamination prior to STEM analysis. In order to ensure proper orientation of the cross-sectioned film

with respect to the electron probe, the specimen was tilted to the [110] zone axis of the single crystal silicon substrate for each analysis. Aberration corrected STEM-high angle annular dark field (HAADF) imaging was performed with an FEI Titan 80-300 TEM/STEM equipped with a double hexapole, spherical aberration corrector (CEOS GmbH) and operating at an accelerating voltage of 300 kV, resulting in an ≈ 100 pm diameter probe of ≈ 100 pA probe current.

8.4. Results and Discussion

Calibration of CMM precursor was first conducted on films with a desired structure of 1 unit cell each of FeSe and $NbSe_2$, ie. $[\{(FeSe)_1\}_{1+y}(NbSe_2)_1]_r$. Elemental ratios and ordering, collectively referred to as the compositional waveform (ϖ_c), and the period of the precursor, or modulation wavelength (λ_c), were adjusted to produce a film with a composition profile that closely matched that of the desired final structure. This film was subjected to an annealing study, shown in Figure 8.2. The as deposited data show a crystalline structure consistent with a layered superlattice as evidenced by the presence of the 001 reflection absent in the more symmetric $NbSe_2$ and FeSe bulk phases. This crystallinity in an as deposited film is a unique feature to this CMM precursor and may be a result of the crystallization of the FeSe subunit on deposition, a behavior which is not without precedent in FeSe[46]. Annealing the crystalline film results in a shift of the reflections to higher angles which ends at approximately 250 °C. This is thought to be caused by a combination of a small loss of excess Se in the precursor and the crystallization of the $NbSe_2$ structure. The diffraction data show the film forming at approximately 200 °C as indicated by the presence of the both the 001 and 005 reflections. As can be seen in Figure 8.1., the structures of FeSe and $NbSe_2$ are similar, and a layering of these structures will potentially result in a crystal

FIGURE 8.2. Temperature dependent XRD study of the $[\{(FeSe)_1\}_{1+y}(NbSe_2)_1]_r$ compound. The diffraction data for the optimized structure has been substituted at the 200 celsius position. The phases marked in the 500 °C are Fe_3Se_4 (gold) and $Nb_{1+\delta}Se_2$ (purple).

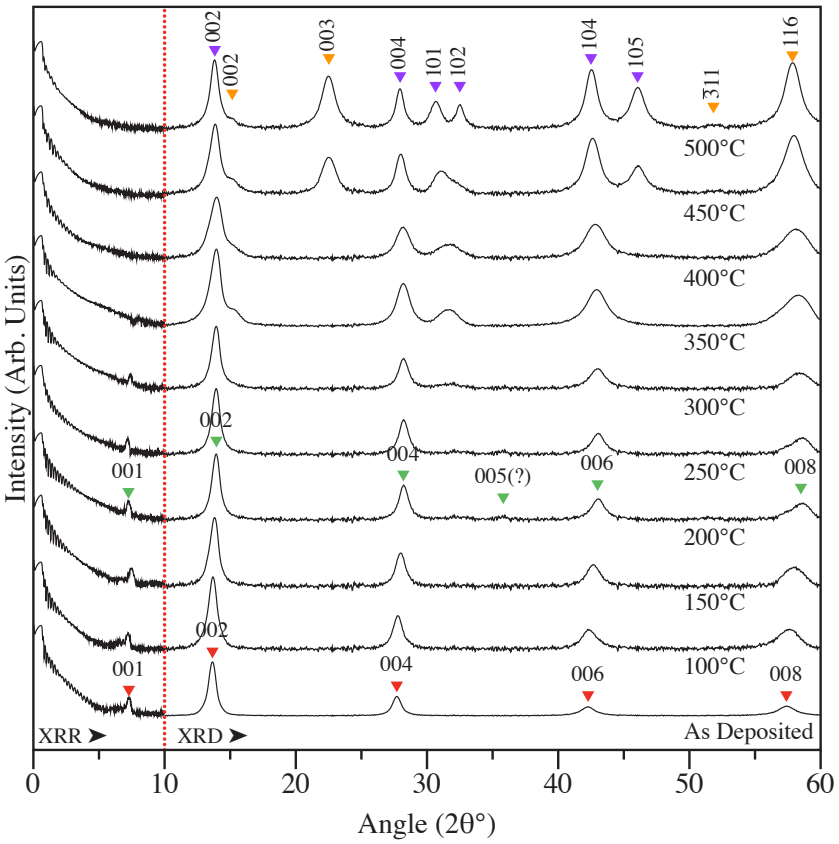

with a small variation in the overall electron density of the structure. The presence of the 001 and 005 reflections in the 200 °C would indicate the presence of a complex superstructure consistent with the desired $[\{(FeSe)_1\}_{1+y}(NbSe_2)_1]_r$ compound. All reflections in the 200 °C data can be indexed to a single 00l family with a supercell c-lattice parameter of 1.26 nm. Annealing above 500 °C results in composition of the structure into a number of $FeSe_x$ and $NbSe_x$ structures.

Next the parameter space for the $[\{(FeSe)_m\}_{1+y}(NbSe_2)_n]_r$ system was explored. Families of compounds were generated compounds varying m and n individually, and

m and n together as shown in Figure 8.3. The generation of these series demonstrate synthetic control over the system as previous experience has shown that if these multilayer compounds are stable, then all other arbitrary integer combinations of m and n within the parameter space defined by the maximum values of m and n synthesized are also stable. The generation of the $(m, 1)$ and $(1, n)$ compounds also allow for determination of the thickness of the structural subunit varied in the series. Diffraction data normal to the sample substrate for the $(m, 1)$, $(1, n)$, and $(m = n)$ series, shown in Figure 8.4., show a regular change in the patterns as a function of increasing m and n. Extraction and analysis of the c-lattice parameters for the $(m, 1)$ and $(1, n)$ families, presented in Figure 8.5., as a function of increasing m or n give a linear trend. The Δc_m and Δc_n were found to be (0.571 ± 0.048) nm and (0.653 ± 0.002) nm respectively, in good agreement with the literature value for the c-lattice parameters of FeSe and $NbSe_2$ [54,74], 0.552 nm and 0.627 nm respectively. XRD data for the $(m = n)$ series, which vary λ_c while keeping the overall composition and profile of ϖ_c constant are also shown in Figure 8.4. Diffraction data shows a regular change in the number of reflections seen, with each pattern showing only reflections indexable to a single c-lattice parameter.

A more detailed structural and chemical analysis of the $(m, n) = (5, 5)$ structure was next undertaken. The $(5, 5)$ compound was chosen for the large regions of both substructures which would simplify the chemical mapping of the structure. XRD data for the compound normal to the substrate are shown in Figure 8.6. Analysis of structure indicates a supercell of $c = 5.75$ nm. In-plane XRD data collected at the Advanced Photon Source at Argonne National Laboratory is shown in Figure 8.7. Peaks for the in-plane data can be indexed to the $hk0$ reflections of either the FeSe

FIGURE 8.3. Compositional waveforms (ϖ_c) for the (m, n)=$(1, 1)$, $(m, 1)$, $(1, n)$, and $(m = n)$ parameters of the $[\{(FeSe)_m\}_{1+y}(NbSe_2)_n]_r$ system.

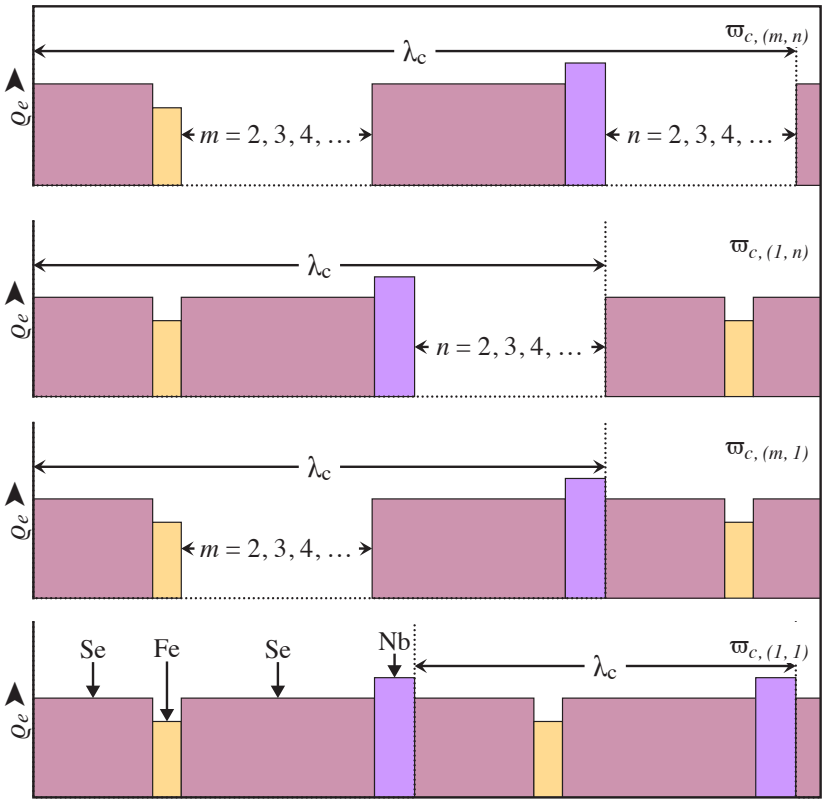

FIGURE 8.4. XRD data for the for the $(m, 1)$, $(1, n)$ and $(m = n)$ families of the $[\{(FeSe)_m\}_{1+y}(NbSe_2)_n]_r$ compounds annealed at 200 °C. For clarity, $00l$ peak indices are provided only for the major reflections, except where they are needed to support the structure determination.

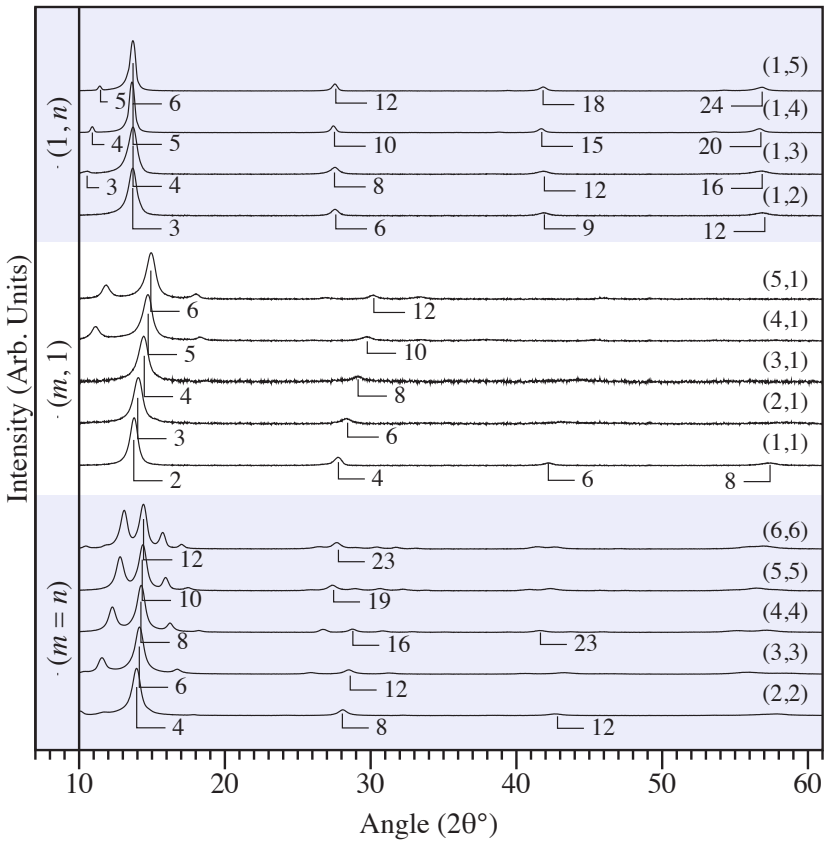

FIGURE 8.5. Analysis of the dependance of m and n on the measured c-lattice parameter for the $(m, 1)$ and $(1, n)$ families of the $[\{(FeSe)_m\}_{1+y}(NbSe_2)_n]_r$ system.

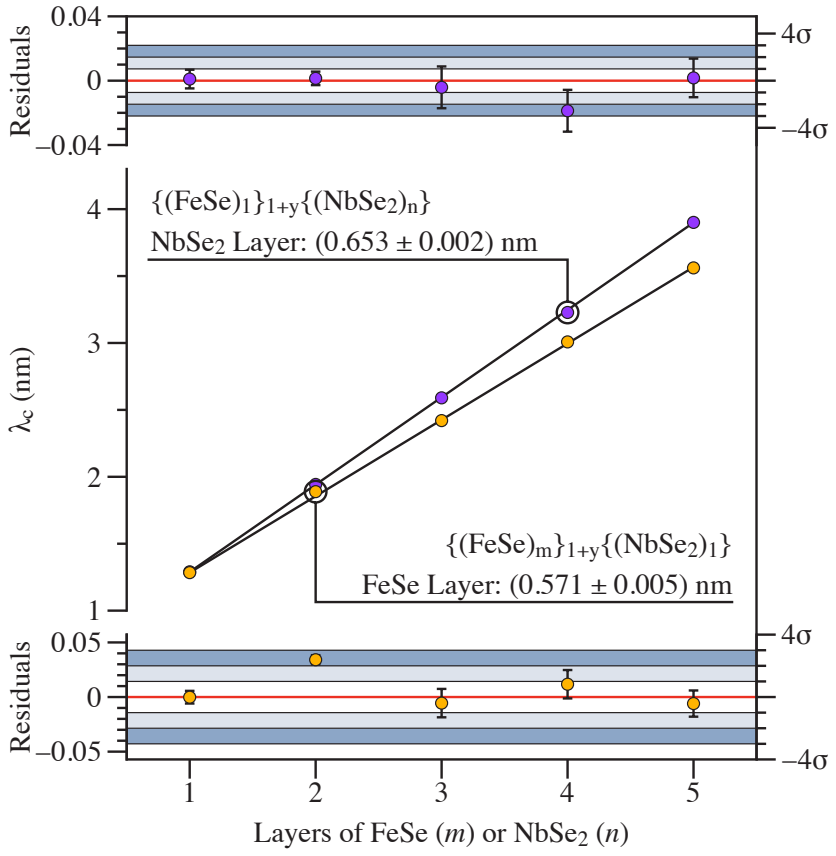

FIGURE 8.6. XRR and XRD data collected normal to the substrate for the $(5,1)$ member of the $[\{(FeSe)_m\}_{1+y}(NbSe_2)_n]_r$ family. Indices shown are for a c-lattice parameter of $c = 5.75\,\text{nm}$ for the $[\{(FeSe)_5\}_{1+y}(NbSe_2)_5]_r$ supercell.

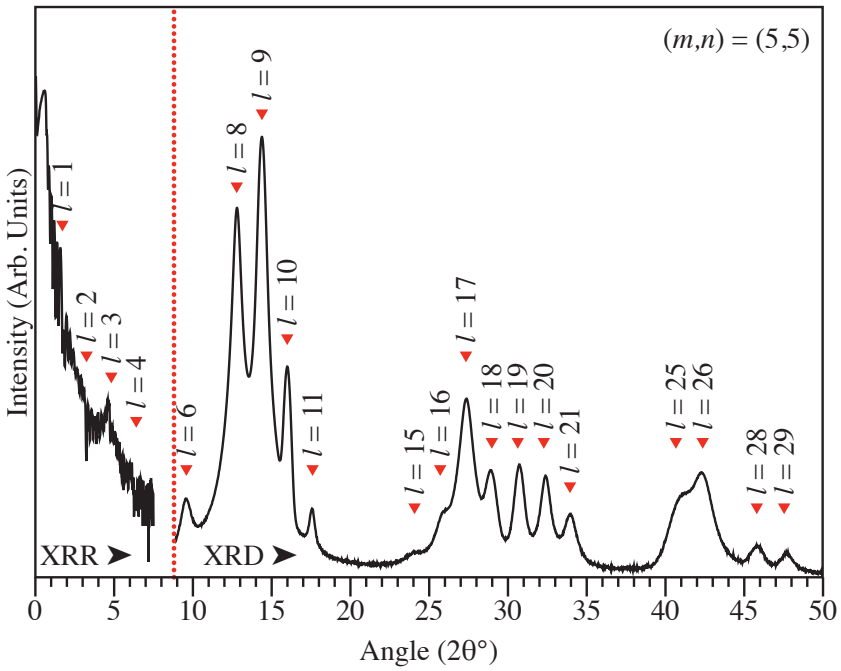

or $NbSe_2$ structure with a-lattice parameters of 0.383 nm and 0.335 nm respectively which are in agreement for the literature values for the structures.

Analysis of the $[\{(FeSe)_5\}_{1+y}(NbSe_2)_5]_r$ structure was undertaken using STEM-HAADF imaging and STEM-electron energy loss spectroscopy (EELS) chemical mapping. A STEM image of the film in cross-section, Figure 8.8., shows distinct regions of $NbSe_2$ and FeSe in a regular layering pattern. Each layer also shows an alternating pattern of lighter and darker regions corresponding to the atom bearing regions and van Der Waals gaps of the structure respectively. Examining the image from top to bottom bands of disruption in the regular layering structure are visible, these bands are attributed to grain boundaries giving an estimated grain size in the range of $\approx 20\,\text{nm}$. Chemical analysis of the film, also shown in Figure 8.9., shows little

FIGURE 8.7. In-plane XRD for the $[\{(FeSe)_5\}_{1+y}(NbSe_2)_5]_r$ compound. FeSe is weakly scattering compared to $NbSe_2$ resulting in the low intensity of the peaks.

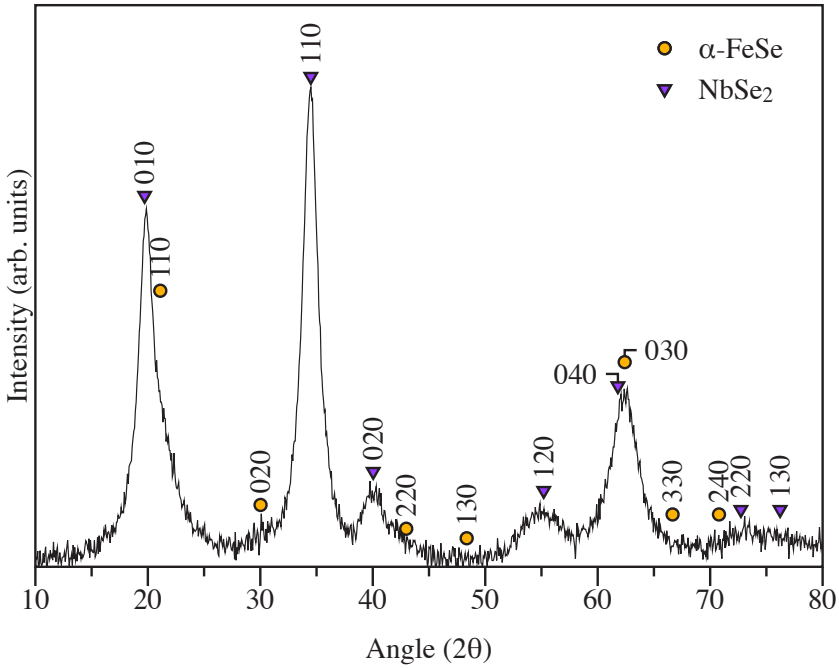

intermixing between the Nb and Fe regions further supporting the data indicating that the structure consists of two distinct substructures.

8.5. Conclusions

The ability to design and generate whole families of a compound with only a minimal relationship to a compound already found in nature suggests that the layered structure and synthetic technique are general. We may therefore take the synthesis of $[\{(FeSe)_m\}_{1+y}(NbSe_2)_n]_r$ as a representation of the potential for crystal engineering using CMKT. As shown in Figure 8.10., by designing in structural information into the compositional modulation of the multilayer precursor it is possible to engineer a local minimum in the free energy diagram for the reaction. This designed synthesis then allows a small amount of energy to be imparted into the system such that the

FIGURE 8.8. STEM-HAADF image of the $[\{(FeSe)_5\}_{1+y}(NbSe_2)_5]_r$ film showing alternating layers of FeSe and $NbSe_2$. Van der Waals gaps in the structures are also visible between the brighter atom bearing regions.

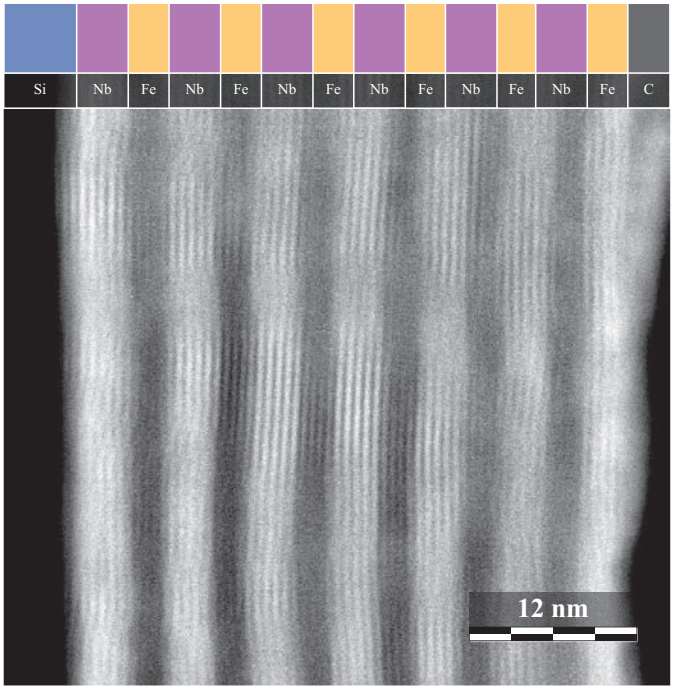

FIGURE 8.9. STEM-EELS image of the same $[\{(FeSe)_5\}_{1+y}(NbSe_2)_5]_r$ film. Chemical imaging shows segregated Fe and Nb rich regions between the Si substrate and C protective layer.

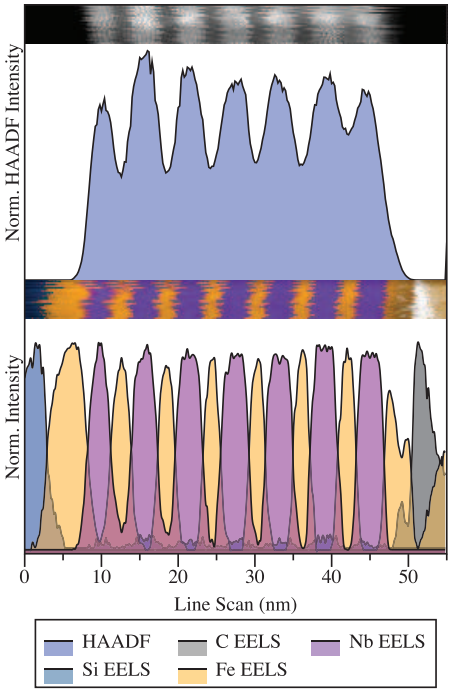

FIGURE 8.10. Schematic representation of the energy surface and reaction progress in a the precursor for a compositionally modulated kinetic trapping reaction. The reaction starts with an ordered precursor containing the layering information of the desired metastable product. Gentle annealing provides sufficient energy to overcome $E_{a,1}$ and cause diffusion and local nucleation of the component substructures, $\Delta G^{o}_{f,1}$. Continued annealing provides sufficient energy to overcome the stabilizing energetics of the metastable product, $E_{a,2}$, and destroy the intergrowth structure resulting in the nucleation of the thermodynamic mixture of products.

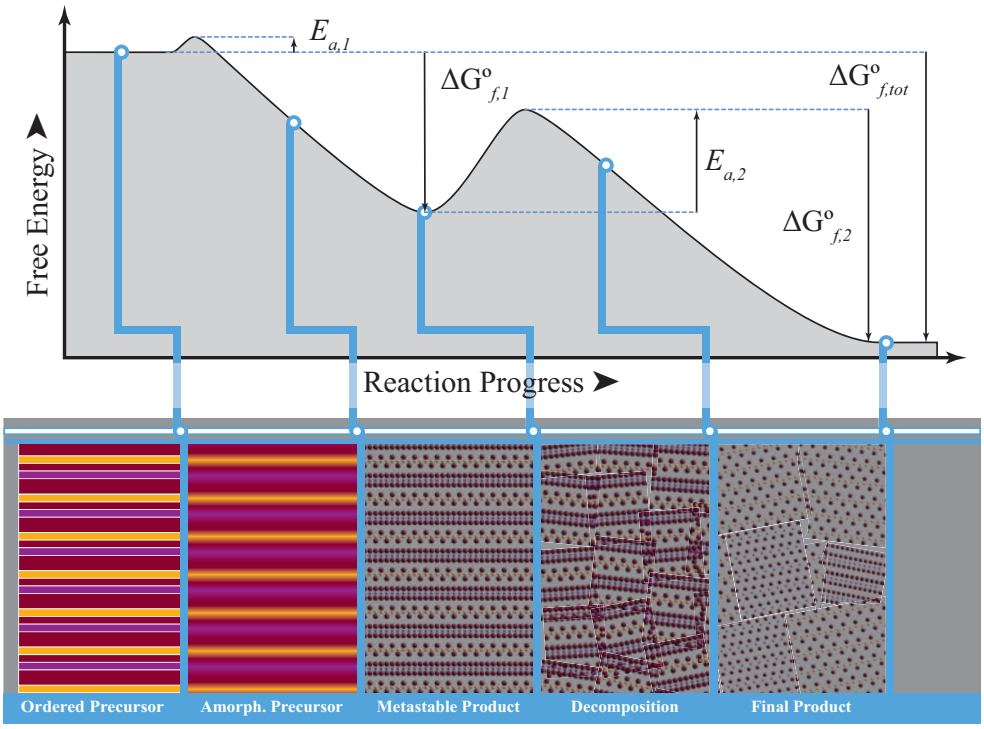

activation energy for the desired metastable product is satisfied without providing enough to cause the reaction to proceed to the thermodynamic product distribution.

8.6. Bridge

This chapter demonstrated that by designing a precursor that closely approximates the desired final product, compounds more distantly related to geological analogues may be generated using CMKT. In addition to generating a novel family of compounds, the successful synthesis of $[\{(FeSe)_m\}_{1+y}(NbSe_2)_n]_r$ provides a

proof of principle for the synthetic design rational that will be tested in the next chapter.

CHAPTER IX

SYNTHESIS OF $[\{(NbSe_2)_m\}_{1+y}(CuCr_2Se_4)_n]_r$: A DESIGNED LAYERED INTERGROWTH COMPOUND

9.1. Co-authorship Statement

Chapter IX is derived from a paper prepared for submission to *The Journal of Alloys and Compounds*. Synthesis and characterization work was conducted by Michael D. Anderson. Dr. Andrew A. Herzing assisted with the STEM analysis. Dr. Ian M. Anderson and Dr. David C. Johnson provided editorial support.

9.2. Introduction

Misfit layer compounds (MLCs) represent a unique mix of structural properties, a combination of local crystallinity within each layer and structural incommensurability between the layers[6,8] that makes them attractive for thermoelectric and other applications[13,14,31,41,133,134,223,244]. It is somewhat surprising that most of the synthetic MLCs prepared to date have a geological precedent[4,6,8]. Compounds related to the cylindrite-franckeite crystal structure, such as the recently reported $[\{(PbSe)_m\}_{0.99}(MoSe_2)_n]_r$ and $[\{(PbSe)_m\}_{0.99}(WSe_2)_n]_r$ families, have been especially prevalent[6,8,9,12–14,17,32]. These examples of the MLC structure all exhibit common rock-salt-structured, MX, and transitional metal dichalcogenide-structured, TX_2, subunits. In Chapter VIII the use of the compositionally modulated kinetic trapping (CMKT) synthetic technique allowed for design of a series of compounds related to the tochilinite structure, $[\{(FeSe)_m\}_{1+y}(NbSe_2)_n]_r$. This new structure still uses a TX_2 structured subunit but incorporates a PbO-structured tetragonal-FeSe. A

recent series of structural studies on CMKT generated compounds have demonstrated additional structural characteristics[133–136] not seen in conventional MLCs, requiring a reclassification of the CMKT generated structures as ferecrystals. Unlike the historical methods used to generate these types of layered structures, which typically yield the most thermodynamically stable product, the flexibility of CMKT that enables the synthesis of compounds with different n and m values also provides the potential to design a ferecrystal, without a geological analogue, that would still be kinetically stable.

Examination of the literature on MLCs and ferecrystals suggests that compounds that have preferred growth orientation might have a higher likelihood of success in forming a stable structure. Two such compounds are $NbSe_2$ and $CuCr_2Se_4$. $NbSe_2$, like other transition metal dichalcogenides is a hexagonal crystal structure isostructural with CdI_2 made up of Se-Nb-Se trilayer stacks in a trigonal prismatic coordination separated by a van Der Waals gap. $NbSe_2$ has a well documented preferred growth orientation, growing in plate-like Se-Nb-Se trilayers along the *c*-axis of the crystal[74,77]. Additionally, $NbSe_2$ has a literature precedent as a subunit in MLCs making it an attractive starting point for the design of a novel ferecrystal. Like $NbSe_2$, recent work presented here* and by others[42,111,120] has indicated that $CuCr_2Se_4$ has a preferred growth orientation. The majority of the literature classifies $CuCr_2Se_4$ as a spinel structured compound having f.c.c. sheets of Se with Cu occupying an eighth of the tetrahedral interstices and Cr a fourth of the octahedral interstices. Some recent work† has suggested that the compound is in fact a hexagonal polymorph of this structure with a formalized mirror plane. In the case of thin films of $CuCr_2Se_4$ the

*See Chapters IV and V.

†See Chapters IV and V.

preferred orientation results in the structure growing with the 111 planes, assuming the regular spinel structure, of the compound parallel to the growth substrate.

The combination of common structural elements with the MLCs and ferecrystals in the literature suggest that $[\{(NbSe_2)_m\}_{1+y}(CuCr_2Se_4)_n]_r$, shown schematically in Figure 9.1., may be a stable structure. Attempting a synthesis of this compound using the traditional methods for generating MLCs, such as chemical vapor transport or direct reactions of powders, would require that the product be more stable than all the possible combinations of the available elements. In the case of $[\{(NbSe_2)_m\}_{1+y}(CuCr_2Se_4)_n]_r$ this would be all possible binary, ternary and quaternary compounds of Cu, Cr, Nb, and Se. A brief search of all the possible compounds of Nb, Cu, Cr, and Se resulted in a large enough number of possible combinations to make the likelihood of the layered structure being the most favorable product remote. One of the strengths of CMKT is the ability to design the precursor to closely resemble the structure of the desired product[34,35,122,125,215,244,245]. The compositionally modulated multilayer (CMM) precursor allows for the controlled intermixing of the elements and allows for control over the reaction pathway[34,35,122,125,133–135,215,244,245] which is demonstrated in Figure 9.2. where the CMM precursors for some of the possible combinations of $NbSe_2$ and $CuCr_2Se_4$ $[\{(NbSe_2)_m\}_{1+y}(CuCr_2Se_4)_n]_r$ are illustrated. This work demonstrates that by designing an appropriate precursor it is possible to trap the $[\{(NbSe_2)_m\}_{1+y}(CuCr_2Se_4)_n]_r$ phase by engineering a situation where it is the most likely product to form, while avoiding other possible compounds.

FIGURE 9.1. Structural model of the proposed $[\{(NbSe_2)_3\}_{1+y}(CuCr_2Se_4)_1]_r$ layered intergrowth compound. The multilayer is constructed using the $R\bar{3}$ structure for $CuCr_2Se_4$, shown at top-right, and $NbSe_2$ structure shown at bottom right. Lattice parameters for the structures are also provided.

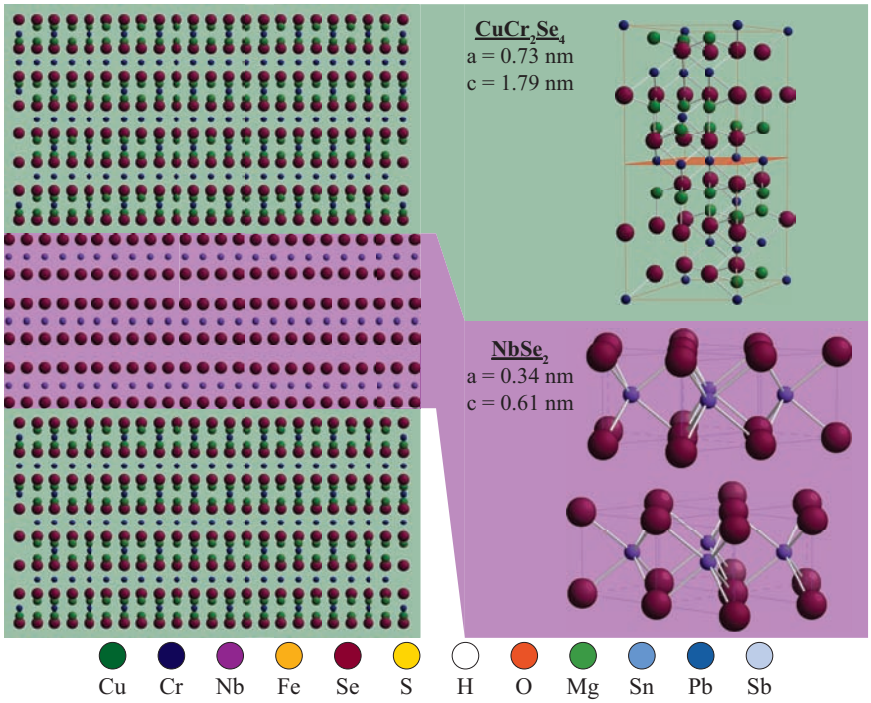

FIGURE 9.2. Possible variations to the base CMM used for the $(1,1)$ member of the $[\{(NbSe_2)_m\}_{1+y}(CuCr_2Se_4)_n]_r$ family of compounds, $\varpi_{c,(1,1)}$. $\varpi_{c,(m,1)}$ corresponds to the structures created for this study. $\varpi_{c,(1,n)}$ are hypothetical structures increasing the layer thickness of the $CuCr_2Se_4$ component. $\varpi_{c,(m,n)}$ corresponds to possible structural isomers of the $[\{(NbSe_2)_m\}_{1+y}(CuCr_2Se_4)_n]_r$ structure where the structure is varied independent of the overall film composition by making $m \equiv n = 1, 2, 3, \ldots$.

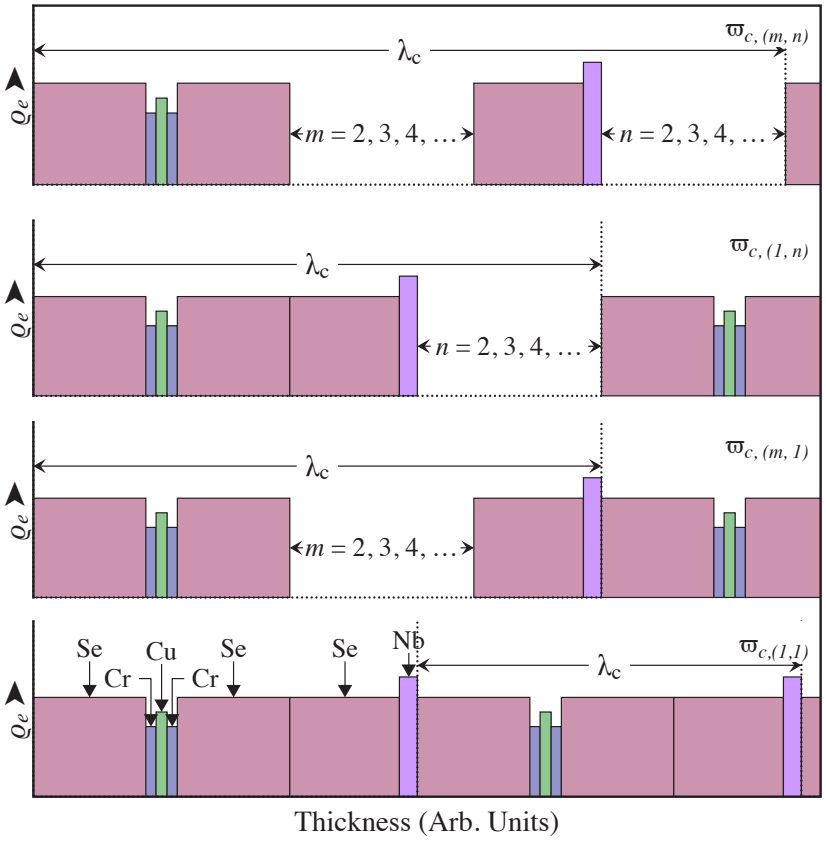

9.3. Experiemental

CMM precursors were calibrated to yield a stoichiometric ratio of metal cations and a slight excess of selenium to allow for evaporation losses during annealing. Samples were deposited using a custom evaporative metal deposition system described previously[210]. Fe and Nb were deposited by electron beam sources. Se was deposited using a Knudzen type effusion cells. Films were deposited under a vacuum of less than 1×10^{-4} Pa. Deposition of the CMM precursors was conducted by sequentially positioning the substrate carousel over the desired sources and opening the shutter to achieve the desired layer thickness corresponding to a given shutter time or frequency shift of the quartz crystal oscillator. Samples with thickness of 50 nm or greater were deposited on commercially available (001)-oriented silicon substrates with native oxide layers.

Samples were annealed on a custom fabricated hot plate that was equilibrated at the target temperature for at least 15 min before each heat treatment. Annealing was conducted under a high-purity nitrogen atmosphere (O_2 content of $\approx$ 500 nL L^{-1}) at temperatures ranging from 100 °C*to*600 °C. The thin films were analyzed using electron probe microanalysis (EPMA), X-ray diffraction (XRD) and X-ray reflectivity (XRR).

Specimens were prepared for EPMA by sectioning a $\approx 5\,mm^2$chip from the silicon supported samples. These sample chips were carefully mounted onto an aluminum sample stub using quick set epoxy and cured at ambient temperature for 24 h. Dabs of carbon paint was applied from the surface of the sample chip to the surface of the sample stub at two corners of the chip to provide a conductive path to ground. Samples were analyzed using a Cameca SX-100 Microprobe equipped with five X-ray wavelength-dispersive spectrometers. Samples were analyzed using a range of

operating voltages between15 kV*to*25 kV at8 to 10 sites each spaced approximately 100 µm apart. The resulting EPMA data were then analyzed using the Pouchou and Pichoir method method as detailed elsewhere[144,151,152].

XRR was performed on a Bruker-AXS D8 Discover X-ray diffractometer using Cu-K_α radiation ($\lambda = 0.154\,18$ nm). The incident beam and exit beam were conditioned and collimated using a parabolic multilayer mirror with a 0.1 mm divergence slit and a 0.6 mm anti-scatter slit, a Soller slit assembly, and 0.05 mm detector silt, respectively. Each sample was carefully aligned to be centered in the goniometer. XRR data were collected over an angular range of $0° < 2\theta < 7°$with a step increment of 0.003°and a data collection time of 1 s per point. XRD was performed using the same experimental parameters but at lower angular resolution, with a 0.025° step increment, and 1 mm divergence and detector slits.

Samples were prepared for for scanning transmission electron microscopy (STEM) analysis using a variation on the small angle cleavage method developed by McCaffrey, et all[157,158]. After initial thinning of the substrate, but before cleavage, the wafer was covered with a layer of protective carbon using a black permanent ink felt tip marker. After preliminary transmission electron microscopy (TEM) screening, the cleaved samples were thinned for STEM analysis using an FEI NOVA NanoLab DualBeam FIB equipped with a Sidewinder ion column. Samples were thinned to approximately 300 nm using a 30 kV accelerating voltage, followed by polishing at 5 kV and a final polishing step at 2 kV. Samples were plasma cleaned using a Fischione model 1020 plasma cleaner for 5 min to remove residual carbon contamination prior to STEM analysis. In order to ensure proper orientation of the cross-sectioned film with respect to the electron probe, the specimen was tilted to the [110] zone axis of the single crystal silicon substrate for each analysis. Aberration corrected STEM-high

angle annular dark field (HAADF) imaging was performed with an FEI Titan 80-300 TEM/STEM equipped with a double hexapole, spherical aberration corrector (CEOS GmbH) and operating at an accelerating voltage of 300 kV, resulting in an ≈ 100 pm diameter probe of ≈ 100 pA probe current.

9.4. Results and Discussion

The precursor layer order and elemental ratios, captured by the compositional waveform (ϖ_c), and the modulation wavelength (λ_c) of the precursor for $[\{(NbSe_2)_m\}_{1+y}(CuCr_2Se_4)_n]_r$ were adapted from those developed in Chapters IV and VIII. A series of films varying the thickness of the $NbSe_2$ layer by integer values of m were first generated. XRR data from these compounds, shown in Figure 9.3., show Kiessig fringes extending to between 4° and 6°(2θ) corresponding to a film roughness of ≈ 0.05 nm. Bragg reflections for a λ_c corresponding to the expected period of the CMM precursor can be seen superimposed on the Kiessig fringes. An analysis of the change in λ_c as a function of increasing m, shown in Figure 9.4., was used to evaluate the systematic changes in the CMM precursor films before annealing. The change in thickness was found to depend linearly on m, as expected from the structure of the precursors, with a $1\sigma = 0.0005$ nm reflecting the reproducibility of the deposition procedure . The thickness of the $NbSe_2$ and $CuCr_2Se_4$ components of the precursor, determined from the slope and intercept of the fit respectively, were (0.749 ± 0.003) nm and (1.87 ± 0.01) nm.

The (m, n)=$(1, 1)$ film was used in an annealing study to determine if the desired structure would form and, if successful, the optimum annealing temperature for crystallization of the desired structure. The results of the annealing study, shown in Figure 9.5., show that below 500 °C the structure appearing to form three compounds

FIGURE 9.3. XRR data for the as deposited films in the $m = 1, 2, \ldots, 5$ members of the $[\{(NbSe_2)_m\}_{1+y}(CuCr_2Se_4)_1]_r$ family of compounds. High frequency oscillations, called kiessig fringes, arising from the interference between reflections from the air-film and film-substrate interfaces are seen superimposed with Bragg reflections arising from the periodicity of the CMM precursor. These reflections move closer together and migrate to lower angles as λ_c for the CMM increases to accommodate the changes in ϖ_c.

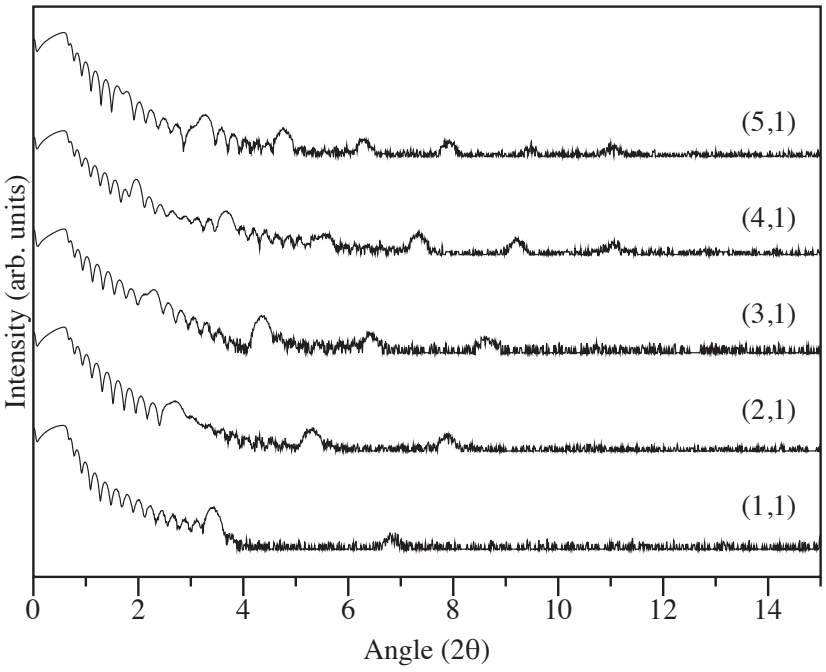

FIGURE 9.4. Regression analysis of the change in λ_c for the $m = 1, 2, \ldots, 5$ members of the $[\{(NbSe_2)_m\}_{1+y}(CuCr_2Se_4)_1]_r$ family of compounds. The thickness of the $NbSe_2$ and $CuCr_2Se_4$ precursors are (0.749 ± 0.003) nm and (1.87 ± 0.01) nm respectively.

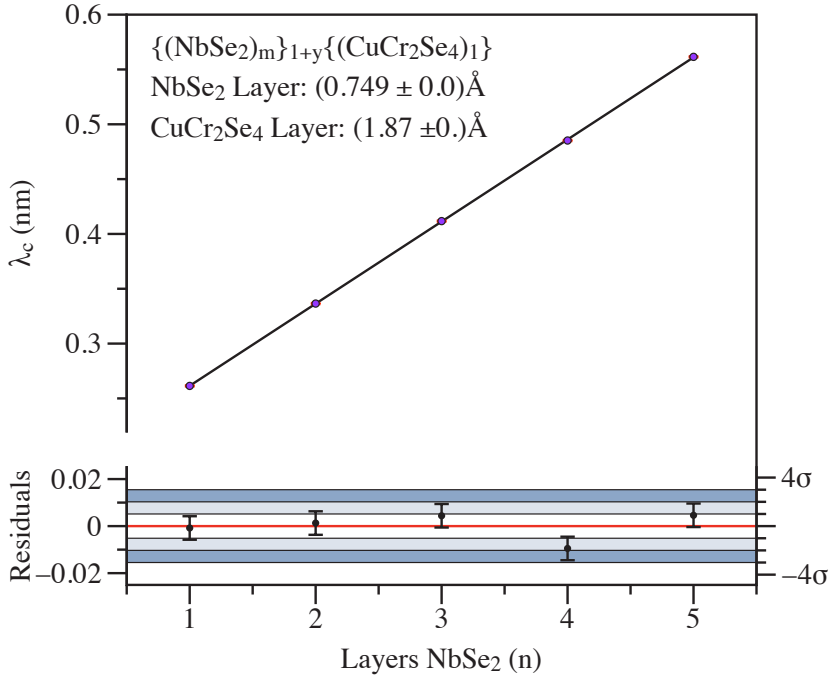

FIGURE 9.5. Temperature dependent XRD study conducted on the $(1,1)$ member of the $[\{(NbSe_2)_m\}_{1+y}(CuCr_2Se_4)_1]_r$ family of compounds. The film shows separate families of reflections corresponding to $NbSe_2$, $CuCr_2Se_4$, and $CuSe_x$ 500 °C and decomposes to $NbSe_2$, $CuSe_x$, and $CuCrSe_2$ above 500 °C.

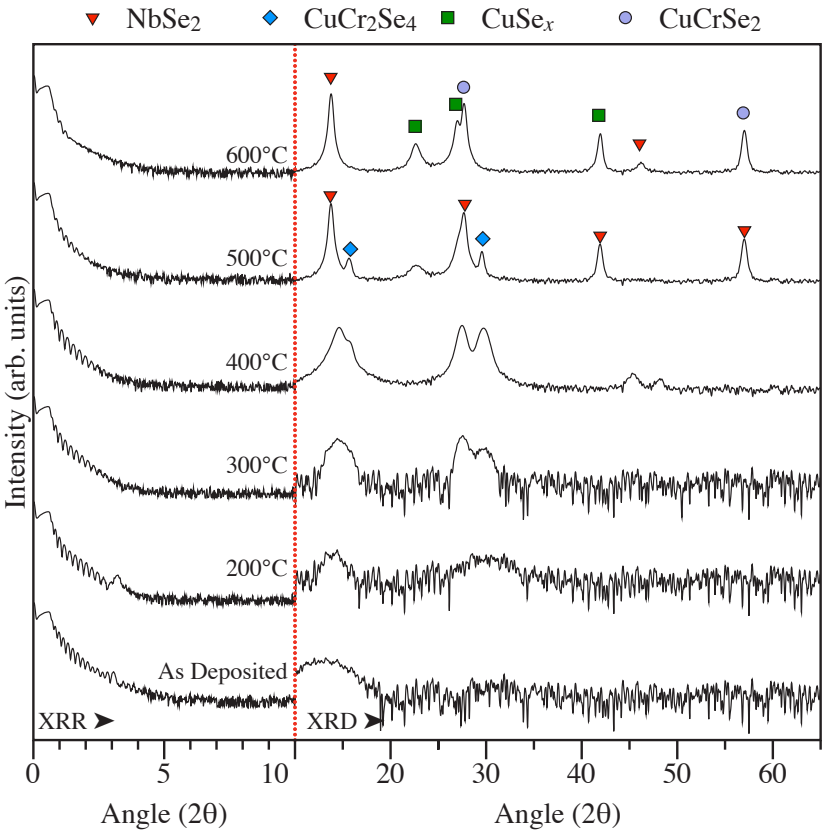

corresponding to separate $NbSe_2$, $CuCr_2Se_4$ and $CuSe_x$ phase. The presence of three independent families of reflections and absence of peaks attributable to a superlattice structure suggest annealing the film resulted in aggregation of the individual phases and not formation of the desired structure. Above 500 °C the mixture decomposes to a mixture of $NbSe_2$, $CuSe_x$ and $CuCrSe_2$ which is presumably the thermodynamic mixture for this composition.

The (m,n)=$(5,1)$ compound was then annealed at 500 °C, the last temperature where both $NbSe_2$ and $CuCr_2Se_4$ were still stable, to determine if the increased layer

thickness of $NbSe_2$, which increases the distance that atoms need to diffuse to phase segregate, could be used to stabilize the ferecrystal structure. The XRD pattern for this film, Figure 9.6., shows a single family of reflections that can be indexed to a single c-lattice parameter of 5.224 nm, close to what is expected for 5 unit cells of $NbSe_2$, with a literature value for $c = 0.627$ nm, and 1 unit cell of $CuCr_2Se_4$, $c_{111} = 1.787$ nm along the body diagonal of the cubic structure. In-plane XRD data from the film, shown in Figure 9.7., show only $hk0$ reflections indicating that the $CuCr_2Se_4$ and $NbSe_2$ phases are highly textured with the $\{111\}_{Fd\bar{3}m}$ planes parallel to the sample substrate. The $CuCr_2Se_4$ indexing used here utilizes an orthohexagonal translation of the traditional $Fd\bar{3}m$ structure into an $R\bar{3}$ translation to simplify the indexing. Lattice parameters extracted from the peak fitting are 0.347 nm and 1.040 nm for the a lattice parameters of $NbSe_2$ and $CuCr_2Se_4$ respectively. These values are in good agreement with the literature values reported for the respective structures[74,221].

The remainder of the films between the $(1, 1)$ and $(5, 1)$ compounds were annealed under the same conditions as the $(5, 1)$ film to determine the minimum thickness of $NbSe_2$ that would form a stable $[\{(NbSe_2)_m\}_{1+y}(CuCr_2Se_4)_n]_r$. The XRD and XRR patterns for all samples above the $(1, 1)$ structure, shown in Figure 9.8., demonstrate patterns consistent with multilayer structures, with diffraction patterns that can be indexed as $00l$ reflections and a low angle 001 diffraction peak expected for the superlattice unit cell. The X-ray data for the $(2, 1)$ compound shows the super cell peaks, but also show the indications of a secondary phase as seen in the $(1, 1)$ compound. The $m = 5, 4$, and 3 patterns do not contain evidence for secondary phases and can be indexed to a single supercell c-parameter. Analysis of the change in λ_c as a function of increasing m, shown in Figure 9.9., was used to determine the thickness of one $NbSe_2$ and $CuCr_2Se_4$ subunit in the multilayer film. The change

FIGURE 9.6. XRD pattern for the $(5,1)$ member of the $[\{(NbSe_2)_m\}_{1+y}(CuCr_2Se_4)_1]_r$ family of compounds. The pattern shows a single family of reflections corresponding to a c-lattice parameter of (4.99 ± 0.02) nm.

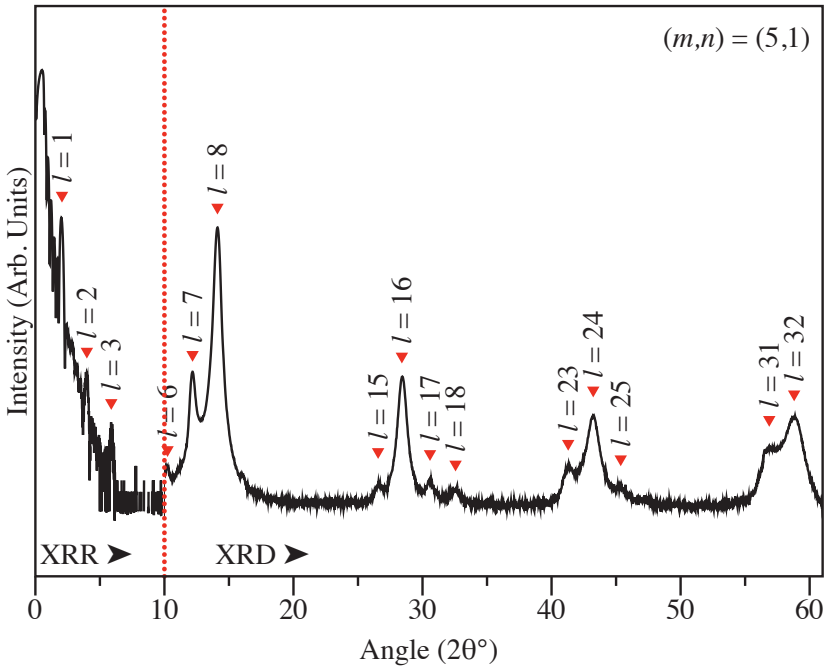

FIGURE 9.7. In-plane XRD for the $[\{(NbSe_2)_5\}_{1+y}(CuCr_2Se_4)_1]_r$ compound. The $CuCr_2Se_4$ phase here is indexed using an $R\bar{3}$ orthohexagonal translation of the traditional $Fd\bar{3}m$ structure to simplify the indexing. The $\{110\}_{R\bar{3}}$ are perpendicular to the $\{111\}_{Fd\bar{3}m}$ planes of the traditional cubic structure.

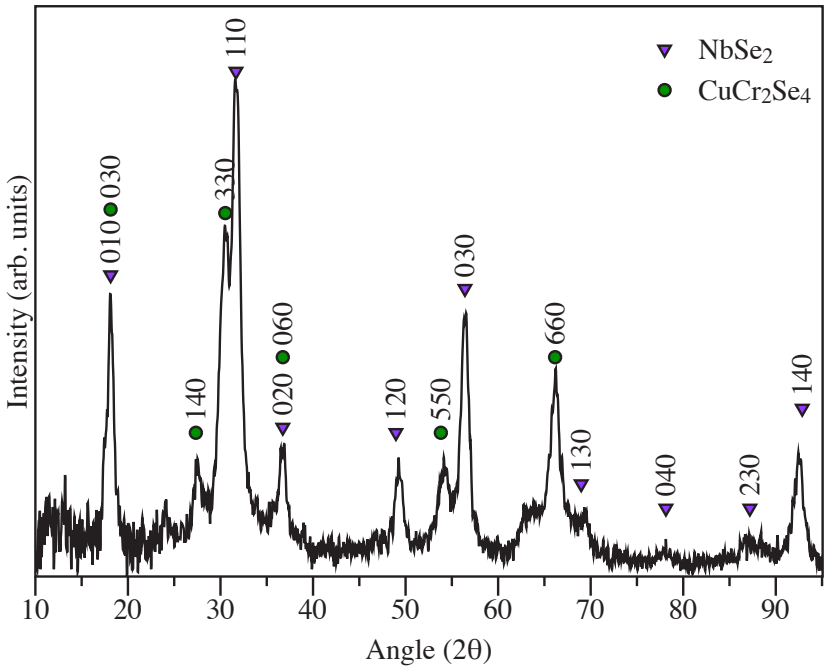

FIGURE 9.8. XRD patterns for the $m = 1, 2, \ldots, 5$ members of the optimized $[\{(NbSe_2)_m\}_{1+y}(CuCr_2Se_4)_1]_r$ system. Members below $(3, 1)$ show a secondary phase indicating instability in the multilayer.

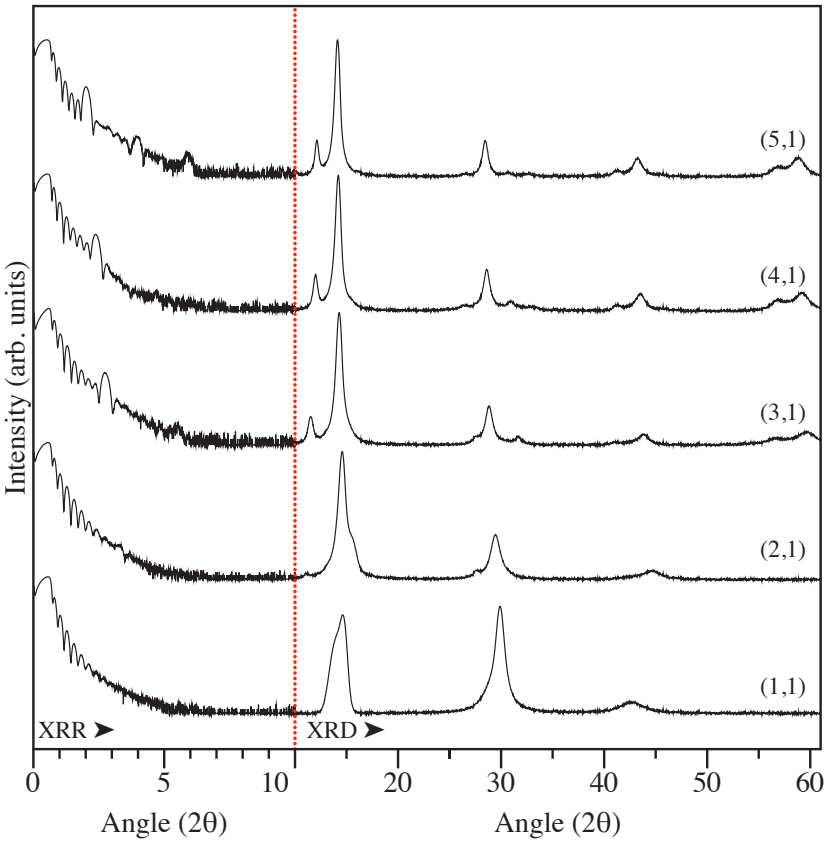

in thickness was found to depend linearly on m. The thickness of the $NbSe_2$ and $CuCr_2Se_4$ components of the precursor, determined from the slope and intercept of the fit respectively, were (0.648 ± 0.004) nm and (1.76 ± 0.01) nm.

STEM-HAADF images of cross-sections from the $(m, 1)$ series, shown in Figure 9.10., were collected to examine the local structure of the films. The $m = 1$ sample shows little local order that can be attributed to the desired $[\{(NbSe_2)_m\}_{1+y}(CuCr_2Se_4)_n]_r$ ferecrystal, appearing to be a polycrystalline mixture of $NbSe_2$ and $CuCr_2Se_4$. Specimens for $m \geq 2$ show a layered structure correlating with what was found in the XRD analysis. Together these observations suggest

FIGURE 9.9. Regression analysis of the change in c for the $m = 2, 3, 4, 5$ members of the $[\{(NbSe_2)_m\}_{1+y}(CuCr_2Se_4)_1]_r$ family of compounds. The thickness of the $NbSe_2$ and $CuCr_2Se_4$ precursors are (0.648 ± 0.004) nm and (1.76 ± 0.01) nm respectively.

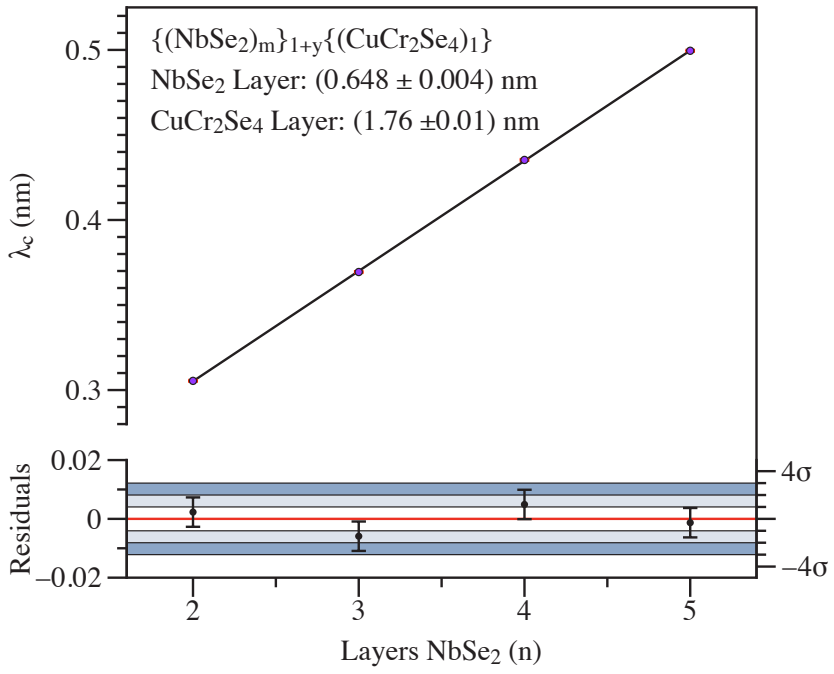

FIGURE 9.10. STEM-HAADF image of the $m = 1, 2, 3, 4$ members of the $[\{(NbSe_2)_m\}_{1+y}(CuCr_2Se_4)_1]_r$. The $(1, 1)$ film shows large grains of $NbSe_2$ and $CuCr_2Se_4$ and no structural layering. The $(2, 1)$ film shows the desired layering structure with alternating layers of $NbSe_2$ and $CuCr_2Se_4$. The $(3, 1)$ and $(4, 1)$ continue the trend of well segregated structures.

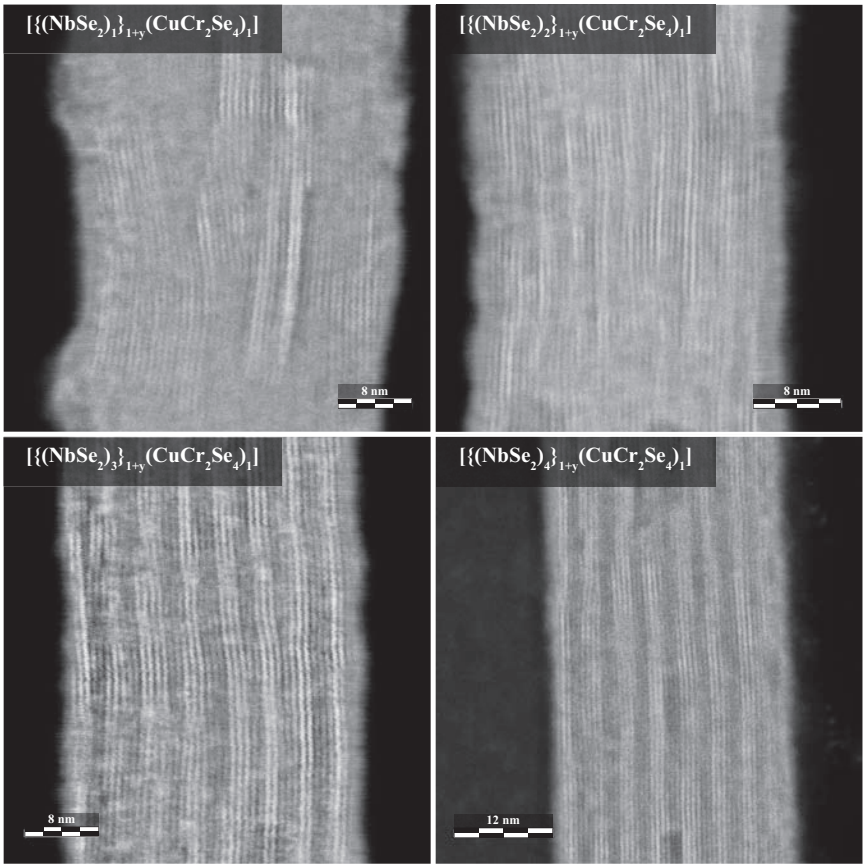

$[\{(NbSe_2)_m\}_{1+y}(CuCr_2Se_4)_n]_r$ has a minimum threshold of stability tied to the thickness of the $NbSe_2$ layer. STEM images of the $m = 5$ film cross-section, shown in Figure 9.11., demonstrate the desired structure, with strongly textured $NbSe_2$ layers separated by $CuCr_2Se_4$ regions. Also apparent in these images are a number of defects in the layering structure that indicate further optimization of the precursor structure or annealing conditions are required to improve the long range order.

A number of possible explanations exist for the lack of stability in $[\{(NbSe_2)_m\}_{1+y}(CuCr_2Se_4)_n]_r$ below the $m = 3$ compound. The $(1, 1)$, and to a lesser

FIGURE 9.11. STEM-HAADF image of the $[\{(NbSe_2)_5\}_{1+y}(CuCr_2Se_4)_1]_r$ compound showing segregated regions of $NbSe_2$ and $CuCr_2Se_4$.

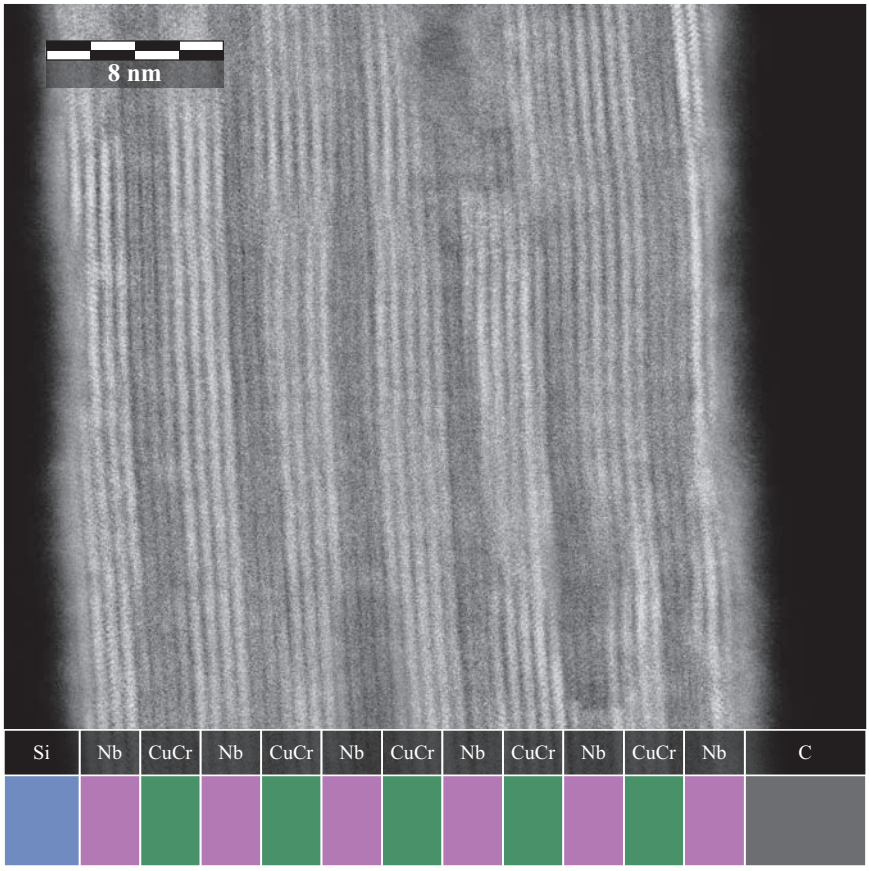

degree the $(2,1)$, structures contain many interfaces that are potentially kinetically or energetically unfavorable to the nucleation of $NbSe_2$. $NbSe_2$ and $CuCr_2Se_4$ are both thermodynamically favorable structures, so the next available energetically favorable state may be to aggregate into the grains seen in Figure 9.11.. In the $(3,1)$ structure, the center Nb-Se bilayer might nucleate first and then act as a template for the outer layers to form. Evidence presented in Chapter VII demonstrated that the size of the subunits in an MLC can result in large changes to the local structure. It would follow that there may be a minimum surface to volume ratio between subunits required to form a stable structure which is not satisfied by the $(1,1)$ compound. Last, charge transfer between $NbSe_2$ and $CuCr_2Se_4$ may destabilize the structure below $(2,1)$. Above the $(1,1)$ this charge transfer could be distributed over a larger volume of $NbSe_2$ limiting the disruption to the structure.

9.5. Conclusion

Compounds from the $[\{(NbSe_2)_m\}_{1+y}(CuCr_2Se_4)_n]_r$ family were designed and synthesized using CMKT. This family of compounds represent the first example of a ferecrystal or MLC incorporating a spinel structured subunit. Compounds where $m \geq 3$ and $n = 1$ were found to form stable superstructures, but compounds where $m \leq 2$ and $n = 1$ exhibited instability or aggregated into random regions of $NbSe_2$ and $CuCr_2Se_4$. A series of possible causes for this were proposed, and further investigation is required to determine the destabilizing force in the smaller structures as well as optimize the stable structures.

CHAPTER X

CONCLUSIONS

The stabilizing mechanisms and design consideration for generating misfit layer compounds (MLCs) with a variety of different structural motifs were explored. The importance of layer order in the precursor film on the product distribution was investigated. Control over reaction pathway was demonstrated by using the behavior of binary reaction couples as an aid in designing ternary waveforms to avoid undesirable reaction intermediates. A new classification was proposed for new compositionally modulated kinetic trapping (CMKT) generated MLC analogues.

In Chapters III and IV the importance of composition and layer order in the compositionally modulated multilayer (CMM) precursor on the product distribution was investigated. It was first noted through investigation of Cu-Se binary films that any composition containing an intimate mixture of Cu and Se would result in nucleation of Cu-Se binary phases on annealing above $\approx$ 150 °C. In the Cu-In-Se and Cu-Cr-Se systems a combination of controlled intermixing modulation wavelength calibration provided increased control over the reaction progress and product distribution for the system. The controlled intermixing of Cu with Se and In with Se allowed for controlled nucleation of copper indium selenide (CIS) from an amorphous precursor. The segregation of Cu from Se using Cr as an intermediate layer allowed the direct formation of $CuCr_2Se_4$ with one annealing step at moderate temperatures.

Analysis of the CMKT generated $CuCr_2Se_4$ compound was conducted in Chapter V. Electron diffraction patterns of the film cross-section were inconsistent with the literature spinel structure and were found to be more consistent with a hexagonal $R\bar{3}$

structure. scanning transmission electron microscopy (STEM) imaging of the crystal lattice supported these observations, suggesting the compound may represent a new polymorph of $CuCr_2Se_4$. Electrical measurements differed from those presented in the literature and were interpreted to arise from a film with fewer defects or impurities than those previously studied. The magnetic behavior of the CMKT film exhibited characteristics of both nanostructured and single crystalline compounds Magnetic susceptibility measurements parallel and perpendicular to the plane of the film show a pronounced hard and easy axis of magnetization consistent with a hexagonal crystal symmetry. This combination of nanocrystalline and magnetic behaviors is consistent with the observed c-axis order and $a-b$-plane rotational disorder seen in other CMKT systems.

The $[\{(PbSe)_m\}_{0.99}(WSe_2)_n]_r$ and $[\{(PbSe)_m\}_{1.00}(MoSe_2)_n]_r$ systems were investigated by STEM, XRD and refinement, and density functional theory (DFT) modeling in Chapters VI and VII. No crystallographic registration between MSe and TSe_2 layers was observed and the diffraction observed in the $hk0$ and hkl directions, where $h = k \neq 0$, can be described by diffraction from discrete layers of finite thickness. This structure is inconsistent with traditional MLCs, such as cylindrite and franckeite, which generally demonstrate either a commensurate a or b axis. Taking the observations of the CMKT generated compounds studied in these chapters[13,14], and previous work by Nyugen[31,40] as a whole, it became apparent that multilayer structures generated via CMKT do not fit into the classic definition of an MLC as outlined in Chapter I. The compounds exhibit strong crystallographic registration along the c-axis, but appear polycrystalline in the a-b plane with a random rotational order about the common c-axis. The presence of discrete diffraction diagrams still classifies these compounds as aperiodic crystal systems but the data as a whole

suggest a new classification is necessary. Therefore, the new terms, ferecrystal, or ferecrystalline solids, was proposed to describe these new compounds.

During the analyses conducted in Chapter VI, a novel pairwise distortion of the MSe bilayers in the $[\{(MX)_m\}_{1+y}(TX_2)_n]_r$ system was observed. The distortion in the MSe layers was found to be a contraction of MX bilayers accompanied by an corresponding expansion of the distances between the paired bilayers. This distortion was found to decrease with increasing values of m and to be independent of TX_2 composition or thickness. Analysis of the trend in relaxation of the distortion suggests an upper size limit of $m = 5$; above which the MX structures with the MLC behave as the bulk rock-salt. In the PbSe system investigated this corresponds to a layer thickness on the order of 2 nm to 3 nm which, interestingly, corresponds to the upper end of the desirable size range for rock-salt nanoparticle applications. This coincidence suggests a new route for examination of the structure property relationship in nanoparticle systems using ferecrystalline solids as 1D analogues .

A novel family of compounds, $[\{(FeSe)_m\}_{1+y}(NbSe_2)_n]_r$, were generated, which were modeled after a precedent from the geological literature. Single FeSe and $NbSe_2$ layer thicknesses were found to be (5.71 ± 0.05) nm and (6.53 ± 0.02) nm respectively, consistent with literature values for these structures. STEM high angle annular dark field (HAADF) images of the $[\{(FeSe)_5\}_{1+y}(NbSe_2)_5]_r$ structure showed a multilayer compound with two distinct structures. STEM electron energy loss spectroscopy (EELS) analysis of the film showed no intermixing between the Nb and Fe regions within the limit of the measurement. The combination of these data indicate that the compound was successfully formed, providing a proof of principle for the the design rules proposed in Chapter I.

Another family of misfit layer compounds, $[\{(NbSe_2)_m\}_{1+y}(CuCr_2Se_4)_n]_r$, designed to test requirements for a stable misfit layer compound, were successfully synthesized. STEM analysis of the $[\{(NbSe_2)_5\}_{1+y}(CuCr_2Se_4)_1]_r$ compound showed a well segregated film with two distinct subunit structures. Thicknesses for individual layers of $NbSe_2$ or $CuCr_2Se_4$ ((0.648 ± 0.004) nm and (1.76 ± 0.01) nm respectively) are consistent with prior literature reports of the individual binary compounds. Below the $m = 3$ member of the system, the ability to form a layered structure appears compromised. Further investigation is required to determine the cause of this destabilization. The successful design and synthesis of $[\{(NbSe_2)_m\}_{1+y}(CuCr_2Se_4)_n]_r$ demonstrate that careful consideration of diffusion length and intermixing in the CMM precursor are a general approach to the design of novel ferecrystalline systems that removes the synthetic barriers of more conventional synthetic routes.

APPENDIX A

NOMENCLATURE AND NOTATIONS

Since the initial synthesis of artificial superlattices in the early 1980's it has been difficult for the nomenclature and notations to keep up with the pace of the new synthetic variations appearing in the literature. Because of the ambiguity that may result from multiple notation styles, the following nomenclatures and notations are used in this work. In some cases the styles represented here may differ slightly from those used in the literature.

A.1. Nomenclature

multilayer composite An artificial material made from two chemically dissimilar materials, with distinct interfaces. General examples of composites are myriad in the materials science community over a number of length scales[246].

superlattice A composite material consisting of repeating nanometer scale layers of multiple materials. These materials have engineered long range order from the layering structure and may demonstrate an epitaxial relationship between the component layers[83,84,128,246].

misfit layer compound (MLC) A sub-set of superlattice materials, made with alternating layers of crystalline materials with a mismatch in geometries of the *a*-*b* planes as shown in Section 1.2. The periodicity of the layering in these materials is on the order of 1 nm to 2 nm.

ferecrystal(-line solid) A recent off-shoot of the MLC structure. The material class is distinct in that it demonstrates precisely layered superstructures, like the

the more general superlattices and MLCs, but little or no crystallographic registration between crystalline structural subunits, and commonly exhibits a turbostratic rotational disorder about the c-axis of the supercell. The term is derived from the Latin *fere*, meaning almost.

compositionally modulated multilayer (CMM) The precursor multilayer used in the compositionally modulated kinetic trapping (CMKT) synthesis method* containing a periodic structure that closely approximates that of the desired final structure.

modulation wavelength (λ_c) The length of the smallest repeating unit within a CMM that, when combined with the ϖ_c, contains all the chemical and spatial information required to generate the complete desired final structure. One iteration of λ_c in the CMM will correspond to one unit cell of the the desired structure in the final film.

compositional waveform (ϖ_c) The elemental profile of the smallest repeating unit within a CMM that contains all the information to generate the complete desired final structure. One iteration of ϖ_c in the CMM will correspond to one unit cell of the the desired structure in the final film.

A.2. Notation

One of the challenges for the chemist working with multilayer materials is the lack of rigorous chemical notation for both the products and reactants; as well as the reactions themselves. The CMM precursors used in CMKT rely on a heterogeneous

*See Chapter II

precursor* to control reaction pathway and product distribution which does not fit the underlying assumption of homogeneous reaction mixtures used in historical preparations requiring a new notation for CMMs. The notations for MLCs and ferecrystals are adapted from those used by Wiegers and Rouxel[6–8,33] where possible, with new elements added to clarify the salient points of the reaction. This new notation system is detailed below.

A.2.1. Compositionally Modulated Multilayer Precursors, Ferecrystalline Solids and Misfit Layer Compounds

Formula A.1 shows an example of the notation used to describe the CMM precursors used in CMKT. Layer interfaces are indicated by "$\cdot$" symbols; while compositional ratios are indicated in the usual manner. Parentheses ,(), are used to indicate the ϖ_c that will form a particular structure. Square braces, "[]", are used to indicate the overall ϖ_c of the structure, with the number of λ_cs indicated as either as a discrete numerical subscript, $[\ldots]_{10}$, or the variable r, $[\ldots]_r$. In Formula A.1 the notation indicates that the CMM precursor is a single component film consisting of a ϖ_c with Cu, Cr, and Se in the order Se-Cr-Cu-Cr-Se being $25\lambda_c$ thick. The ϖ_c has the elements arranged in a ratio of $2:1:1:1:2$ resulting in an overall composition of $CuCr_2Se_4$.

$$[(2\,\mathrm{Se}\cdot\mathrm{Cr}\cdot\mathrm{Cu}\cdot\mathrm{Cr}\cdot 2\,\mathrm{Se})]_{25} \qquad \text{(Formula A.1)}$$

Building on Formula A.1 the example of Formula A.2 shows the notation for CMM precursor for a theoretical MLC. It is interpreted to be a composite with m wavelengths of a M-X waveform with a $1:1$ M to X ratio followed by n wavelengths

*See Subsection 1.7.4. in Chapter I, Section 2.1. in Chapter II, and Chapter IV.

of a T-X waveform with a $1:2$ ratio of T to X with the overall film being $15\lambda_c$ thick.

$$[\mathrm{m(M \cdot X) + n(T \cdot 2\,X)}]_{15} \qquad \text{(Formula A.2)}$$

If $m = n = 1$, then notation for the precursor could also be written as

$$[\mathrm{(M \cdot X \cdot T \cdot 2\,X)}]_{15} \qquad \text{(Formula A.3)}$$

Note that m always applies to the first listed compound and n to the second.

When the multilayer structure is known, or a theoretical structure is being discussed, the previous notation by Wiegers and Rouxel is used, as shown in Formula A.4, with some modification.

$$[\{(\mathrm{MX})_{\mathrm{m}}\}_{1+\mathrm{y}}(\mathrm{TX_2})_{\mathrm{n}}]_{15} \qquad \text{(Formula A.4)}$$

The m and n subscripts corresponds to the number of wavelengths for each waveform in the precursor, but as subscripts represent the number of unit cells for each crystalline subunit. The subscripted quantity $1 + y$ is the crystallographic mismatch between the two substructures as defined in Chapter I.

It should be noted that Formula A.4 differs slightly from the original work by Wiegers and Rouxel. The original notation had the misfit parameter attached to the structural unit: $[(\mathrm{MX})_{1+\mathrm{y}}]_{\mathrm{m}}$. This was was a derivation of a previous notation used before the structure of the system was full understood[6–8,33], where the compound was classified by its empirical notation, as in Formula A.5, with y being some number less than one to account for the cation nonstoichiometry introduced by the misfit between the two sublattices of the supercell. For the compounds initially studied by Wiegers

and Rouxel, where m was usually 1 or 2 at most, there is no significant difference between the original notation and the one suggested here. However, when employing CMKT, m and n can be an arbitrary integer requiring a refinement in the notation to demonstrate that the component subject to the misfit parameter is the continuous substructure and that the misfit is not applied piece-wise to each individual unit cell in the subunit.

In cases where the layering structure of the material is not known, e.g. measurements of bulk composition, Formula A.5 is used. The subscripts denote mole fraction normalized to 1 mol total.

$$\mathrm{M_aT_bX_c} \qquad \text{(Formula A.5)}$$

Overuse of the full notation for for multilayer systems in texts can become tedious and detract from the more salient points of the narrative. When it is clear what the subunits of the system under consideration are, m and n and r subscripts are used as a shorthand notation. In the case of $[\{(\mathrm{MX})_1\}_{1+\mathrm{y}}(\mathrm{TX}_2)_3]_\mathrm{r}$, the shorthand would be $(1,3)_\mathrm{r}$; or more simply $(1,3)$ if the total thickness of the film were unimportant.

A.2.2. Reactions Involving Compositionally Modulated Multilayer Precursors

Combining the previous notation elements, Formula A.6 shows an example of the notation for CMKT reactions used in this text. The reaction starts with a CMM precursor similar to **??**, but including additional Se. The reaction pathway involves annealing at 600 °C and the final product forms from an amorphous intermediate. The reaction product, $\mathrm{CuCr_2Se_4}$, is shown to have a $Fd\bar{3}m$ symmetry and is indicated to

TABLE A.1. Notation for crystallographic planes and reflections in real and reciprocal space.

Real Space	Reciprocal Space	Indices
A specific direction	A specific plane	$[UVW]$
A general direction	A general plane	$\langle UVW \rangle$
A specific plane	A specific direction	(hkl)
A general plane	A general direction	$\{hkl\}$
Diffracting plane	Indexed reflection	hkl

have a $\langle 111 \rangle$ texturing $(_T)$. The parenthetical notation is optional and only used where needed to emphasize a relevant point in the narrative.

$$[((2+\delta)\mathrm{Se} \cdot \mathrm{Cr} \cdot \mathrm{Cu} \cdot \mathrm{Cr} \cdot (2+\delta)\mathrm{Se})] \xrightarrow[\text{amorphous melt}]{600\,^{\circ}\mathrm{C}}$$

$$\mathrm{CuCr_2Se_4}(Fd\bar{3}m,\, \langle 111 \rangle_T) + \mathrm{Se}\uparrow \quad \text{(Formula A.6)}$$

A.2.3. Crystallographic Notation

Table A.1. contains a summary of the standard notation[153,247] for Miller indices in real and reciprocal space used in this work.

APPENDIX B

RIETVELD REFINEMENTS FOR THE $[\{(PbSe)_M\}_{0.99}(WSe_2)_N]_R$ FAMILY OF COMPOUNDS

FIGURE B.1. Diffraction data and calculated diffraction profile for the $(1, 1)$ compound of the $[\{(PbSe)_m\}_{0.99}(WSe_2)_n]_r$ family collected at two wavelengths (0.9429 nm and 0.9578 nm - above and below the Pb-L_3 absorption edge). A representation of the refined structure is contained in Figure 6.2. and the parameters from the refinement are contained in Table B.1.

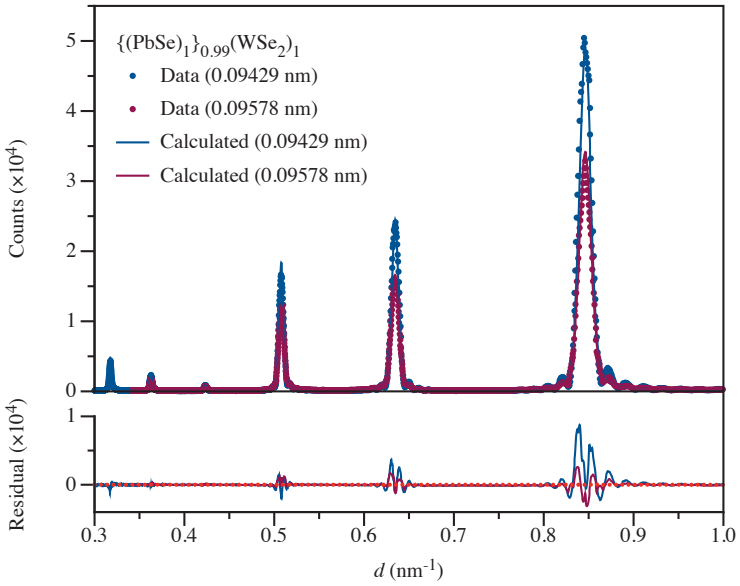

FIGURE B.2. Diffraction data and calculated diffraction profile for the $(2, 2)$ compound of the $[\{(PbSe)_m\}_{0.99}(WSe_2)_n]_r$ family collected at two wavelengths, above and below the Pb absorption edge. A representation of the refined structure is contained in Figure 6.5. and the parameters from the refinement are contained in Table B.2.

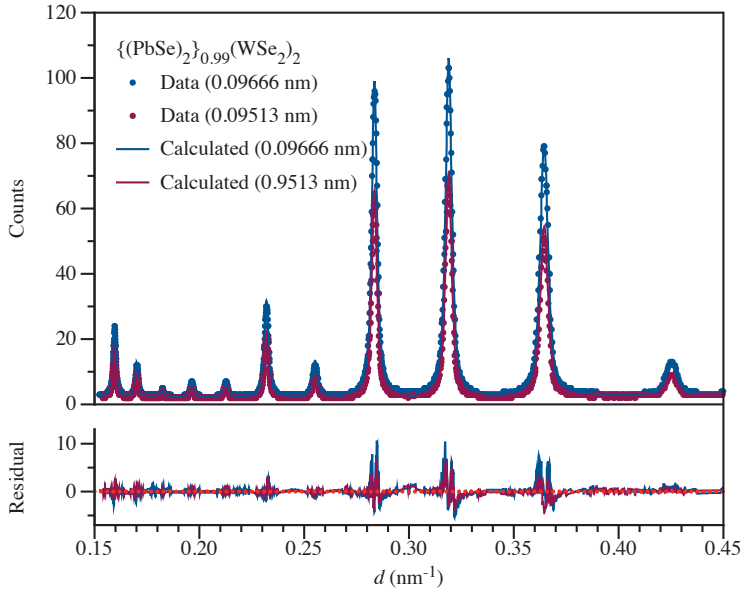

FIGURE B.3. Diffraction data and calculated diffraction profile for the $(3, 3)$ compound of the $[\{(PbSe)_m\}_{0.99}(WSe_2)_n]_r$ family collected using Cu-K_α radiation. A representation of the refined structure is contained in Figure 6.7. and the parameters from the refinement are contained in tabtab:s3

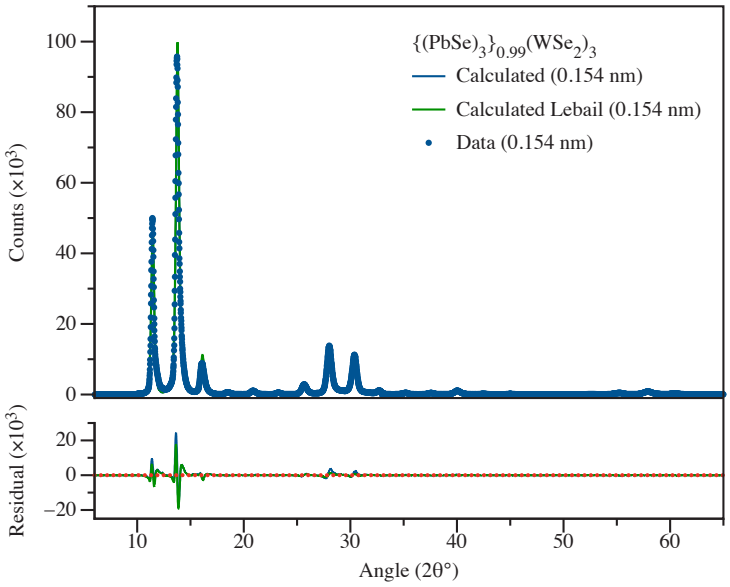

FIGURE B.4. Diffraction data and calculated diffraction profile for the $(4, 4)$ compound of the $[\{(PbSe)_m\}_{0.99}(WSe_2)_n]_r$ family collected using Cu-K_α radiation. A representation of the refined structure is contained in Figure 6.9. and the parameters from the refinement are contained in Table B.4.

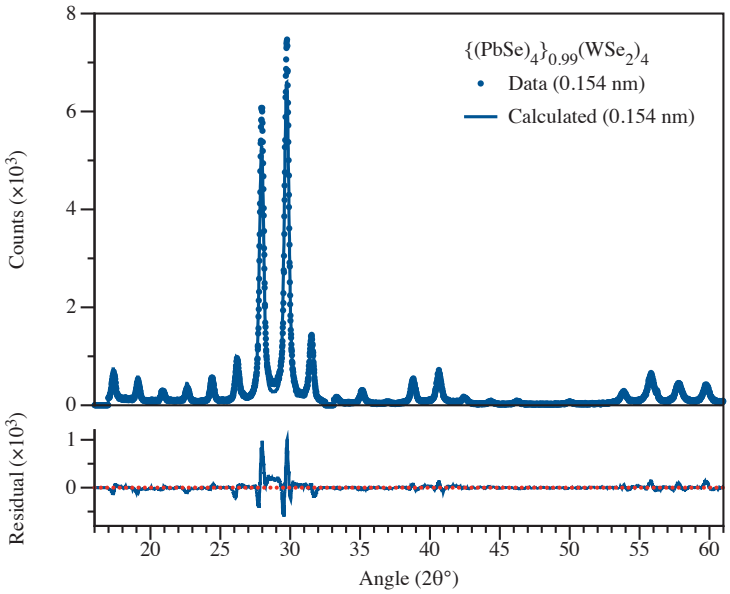

FIGURE B.5. Diffraction data and calculated diffraction profile for the $(5, 5)$ compound of the $[\{(PbSe)_m\}_{0.99}(WSe_2)_n]_r$ family collected using Cu-K_α radiation. A representation of the refined structure is contained in Figure 6.11. and the parameters from the refinement are contained in Table B.5.

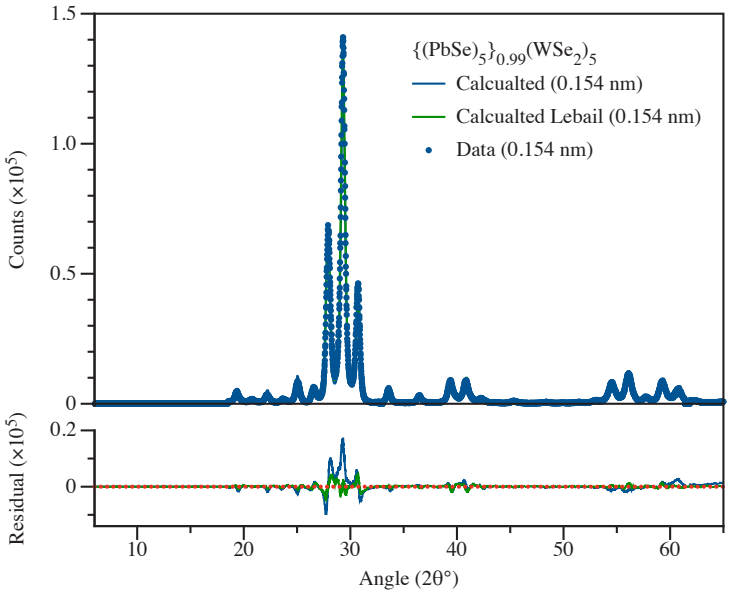

TABLE B.1. The refined lattice parameter and the fractional position of atomic planes along the c-axis for the compound $[\{(PbSe)_1\}_{0.99}(WSe_2)_1]_r$, along with information on the quality of the refinement. This data is an average of refinements from six different starting positions.

Element	c fract. position	Occupancy
W	0	1
Se1	0.111(1)	1
Pb	0.389(1)	0.5
Se2	0.406(1)	0.5
c = 1.2697(1) nm, U_{iso} (Å^2) = 0.079(1)		
Fitting Parameter	Lebail Fitting	Model Fitting
w_{rp}	0.1776	0.1788
R_p	0.1151	0.1160
Bkgroudnd w_{rp}	0.1560	0.1580
Bkground R_p	0.1058	0.1067
D_{wd}	0.089	0.085
χ^2	33.91	34.37

TABLE B.2. The refined lattice parameter and the fractional position of atomic planes along the c-axis for the compound $[\{(PbSe)_2\}_{0.99}(WSe_2)_2]_r$, along with information on the quality of the refinement. This data is an average of refinements from five different starting positions.

Element	c fract. position	Occupancy
Se1	0.06891)	1
W1	0.130(1)	1
Se2	0.191(1)	1
Pb1	0.320(1)	0.5
Se3	0.356(1)	0.5
Se4	0.408(1)	0.5
Pb2	0.439(1)	0.5
c = 2.5529(1) nm, U_{iso} (Å^2) = 0.12(1)		
Fitting Parameter	Lebail Fitting	Model Fitting
w_{rp}	0.0759	0.1051
R_p	0.0600	0.0808
Bkgroudnd w_{rp}	0.0702	0.1118
Bkground R_p	0.0577	0.0901
D_{wd}	0.240	0.141
χ^2	4.003	7.212

TABLE B.3. The refined lattice parameter and the fractional position of atomic planes along the c-axis for the compound $[\{(PbSe)_3\}_{0.99}(WSe_2)_3]_r$, along with information on the quality of the refinement. This data is an average of refinements from five different starting positions.

Element	c fract. position	Occupancy
W1	0	1
Se1	0.0425(1)	1
Se2	0.1307(1)	1
W2	0.1725(1)	1
Se3	0.2154(1)	1
Pb1	0.3010(1)	0.5
Se4	0.3035(1)	0.5
Se5	0.3771(2)	0.5
Pb2	0.3795(1)	0.5
Pb3	0.4603(4)	0.5
Se6	0.4625(1)	0.5
c =3.8263(1) nm, U_{iso} (Å^2) = 0.0538(1)		
Fitting Parameter	Lebail Fitting	Model Fitting
w_{rp}	0.112	0.240
R_p	0.073	0.172
Bkgrnd w_{rp}	0.098	0.235
Bkgrnd R_p	0.068	0.170
D_{wd}	0.521	0.111
χ^2	4.05	19.32

TABLE B.4. The refined lattice parameter and the fractional position of atomic planes along the c-axis for the compound $[\{(PbSe)_4\}_{0.99}(WSe_2)_4]_r$, along with information on the quality of the refinement.

Element	c fract. position	Occupancy
Se1	0.0332(1)	1
W1	0.0646(1)	1
Se2	0.0965(1)	1
Se3	0.1615(1)	1
W2	0.1943(1)	1
Se4	0.2266(1)	1
Pb1	0.2888(1)	0.5
Se5	0.2928(1)	0.5
Se6	0.3475(1)	0.5
Pb2	0.3478(1)	0.5
Pb3	0.4091(1)	0.5
Se7	0.4103(1)	0.5
Se8	0.4691(1)	0.5
Pb4	0.4695(1)	0.5
c =5.0922(2) nm, U_{iso} (Å^2) = 0.0468(1)		

Fitting Parameter	Lebail Fitting	Model Fitting
w_{rp}	0.174	0.199
R_p	0.134	0.151
Bkgrnd w_{rp}	0.159	0.181
Bkgrnd R_p	0.129	0.145
D_{wd}	0.052	0.043
χ^2	9.15	12.0

TABLE B.5. The refined lattice parameter and the fractional position of atomic planes along the c-axis for the compound $[\{(PbSe)_5\}_{0.99}(WSe_2)_5]_r$, along with information on the quality of the refinement.

Element	c fract. position	Occupancy
W1	0	1
Se1	0.0249(1)	1
Se2	0.0798(1)	1
W2	0.1042(1)	1
Se3	0.1299(1)	1
Se4	0.1825(1)	1
W3	0.2074(1)	1
Se5	0.2344(1)	1
Pb1	0.2848(1)	0.5
Se6	0.2868(1)	0.5
Pb2	0.3312(1)	0.5
Se7	0.3314(1)	0.5
Pb3	0.3804(1)	0.5
Se8	0.3808(1)	0.5
Se9	0.4281(1)	0.5
Pb4	0.4282(1)	0.5
Pb5	0.4761(1)	0.5
Se10	0.4763(1)	0.5
c = 6.3939(1) nm, U_{iso} (Å^2) = 0.0299(1)		
Fitting Parameter	Lebail Fitting	Model Fitting
w_{rp}	0.118	0.245
R_p	0.072	0.160
Bkgrnd w_{rp}	0.122	0.343
Bkgrnd R_p	0.072	0.170
D_{wd}	0.312	0.076
χ^2	6.7	28.4

APPENDIX C

SOLID STATE PHASE DIAGRAMS

Binary and ternary phase diagrams referenced throughout this work. Diagrams are organized by relevant substructure and are adapted from the data found in the ASM Alloy Phase Diagram Center[196].

C.1. FeSe

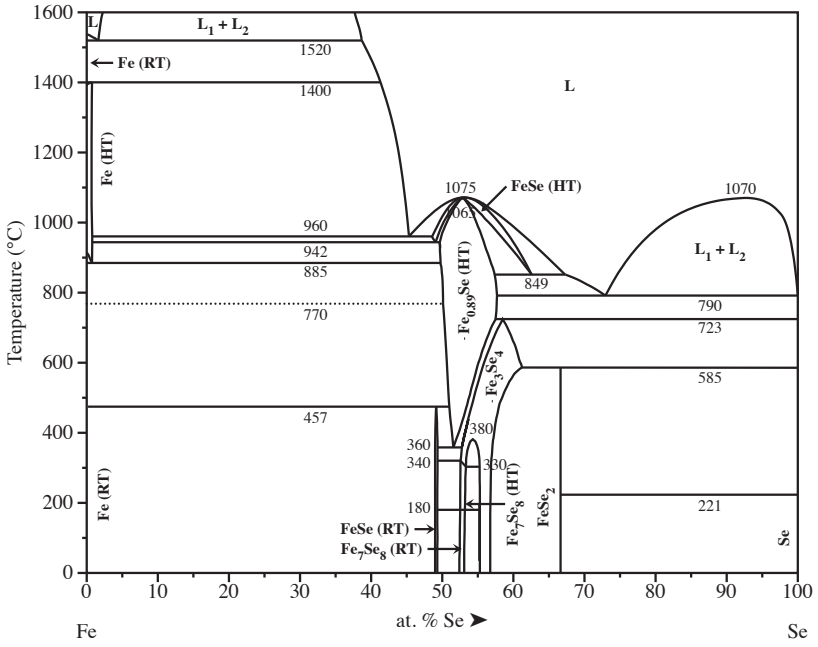

C.2. $NbSe_2$

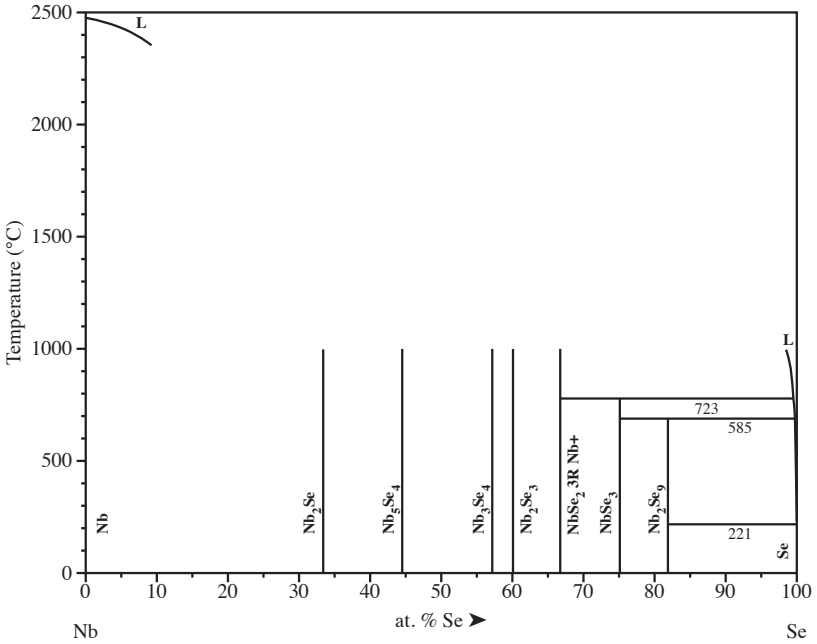

C.3. $CuCr_2Se_4$

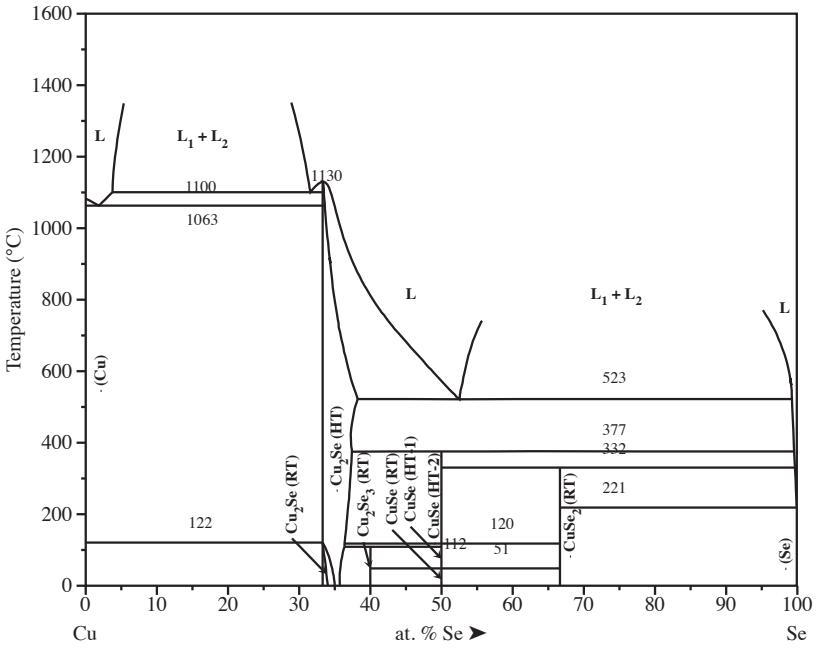

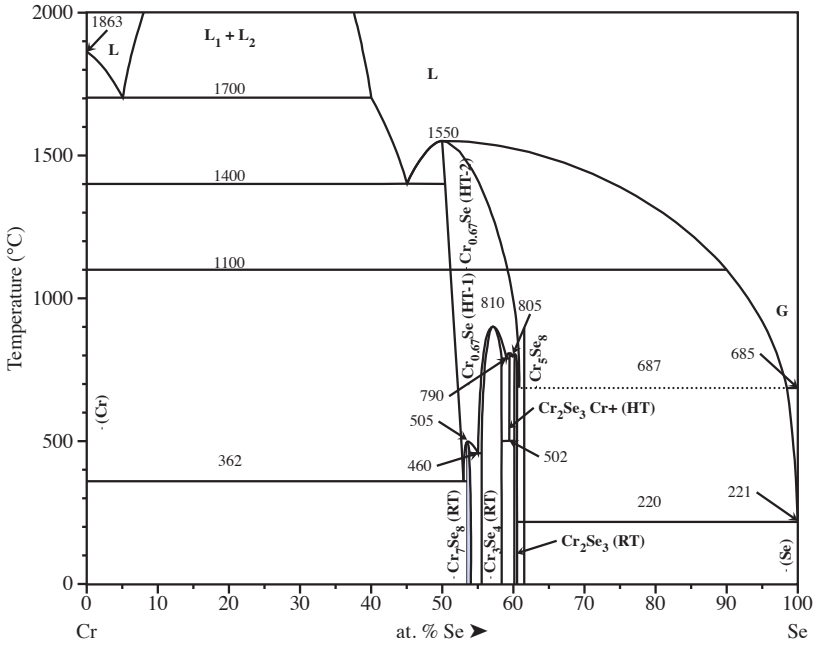
2000
1500
1000
500
0
Temperature (°C)
1863
L
L1 + L2
1700
1400
1100
L
1550
Cr0.67Se (HT-2)
Cr0.67Se (HT-1)
810
805
Cr5Se8
687
685
G
790
505
362
460
Cr2Se3 Cr+ (HT)
502
220
221
Cr2Se3 (RT)
Cr7Se8 (RT)
Cr3Se4 (RT)
(Cr)
(Se)
0
10
20
30
40
50
60
70
80
90
100
Cr
at. % Se ➤
Se

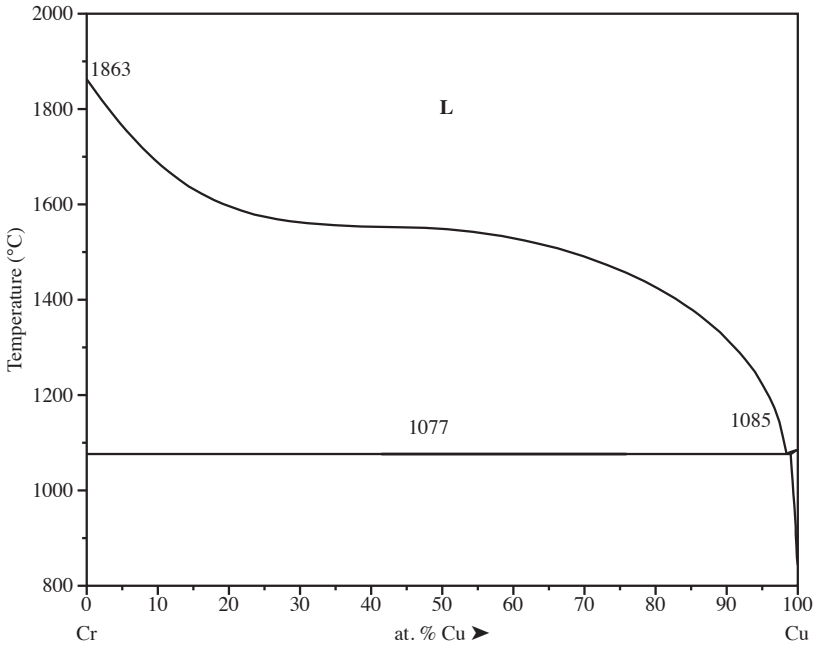
2000
1800
1600
1400
1200
1000
800
Temperature (°C)
1863
L
1077
1085
0
10
20
30
40
50
60
70
80
90
100
Cr
at. % Cu ➤
Cu

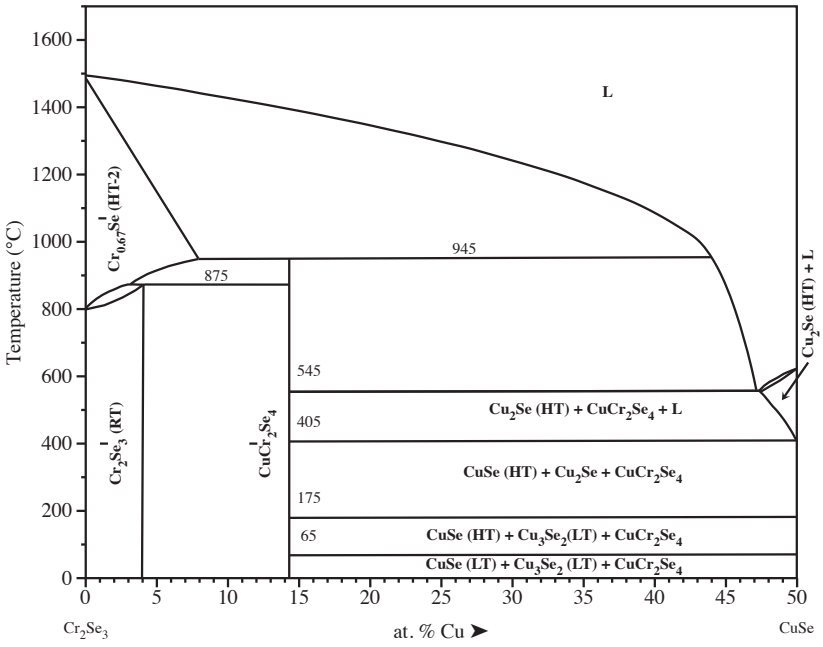
Temperature (°C)
1600
1400
1200
1000
800
600
400
200
0
0
5
10
15
20
25
30
35
40
45
50
Cr2Se3
at. % Cu ➤
CuSe
L
Cr0.67Se (HT-2)
945
875
Cu2Se (HT) + L
545
Cu2Se (HT) + CuCr2Se4 + L
405
Cr2Se3 (RT)
CuCr2Se4
CuSe (HT) + Cu2Se + CuCr2Se4
175
65
CuSe (HT) + Cu3Se2(LT) + CuCr2Se4
CuSe (LT) + Cu3Se2 (LT) + CuCr2Se4

APPENDIX D

CRYSTAL STRUCTURES

Included here are detailed descriptions and relevant data fro the crystal structures used in this work. The references for the structural data presented here are found in the relevant sections of the introduction.

D.1. FeSe

Chemical Formula:	FeSe	
Space Group:	129, Origin 1 ($P4/nmm$)	
Structure Name:	Tetragonal PbO	
Lattice Parameters:	a =0.377 nm	$\alpha = 90°$
	b =0.377 nm	$\beta = 90°$
	c =0.553 nm	$\gamma = 90°$
Element:	Fe	Se
Site:	$2c$	$2a$
Coord:	T_d	
Lattice Position:	$0, \frac{1}{2}, \frac{3}{4}$	$0, 0, 0$
Occupancy:	1	1

D.2. $NbSe_2$

Chemical Formula:	$NbSe_2$	
Space Group:	164 ($P6_3/mmc$)	
Structure Name:	Transition Metal Dichalcogenide (TX_2)	
Lattice Parameters:	a =0.348 nm	$\alpha = 90°$
	b =0.348 nm	$\beta = 90°$
	c =0.607 nm	$\gamma = 120°$
Element:	Nb	Se
Site:	$1a$	$2d$
Coord:	C_{2v}	
Lattice Position:	$0, 0, 0$	$\frac{2}{3}, \frac{1}{3}, \frac{1}{4}$
Occupancy:	1	1

D.3. $CuCr_2Se_4$(Cubic)

Chemical Formula:	$CuCr_2Se_4$		
Space Group:	227, Origin 2 ($Fd\bar{3}m$)		
Structure Name:	Spinel (AB_2X_4)		
Lattice Parameters:	$a = 1.0336$ nm	$\alpha = 90°$	$U_{iso,\mathrm{Se}} = 0.000739$
	$a = b = c$	$\alpha = \beta = \gamma$	
Element:	Cu	Cr	Se
Site:	$8a$	$16d$	$32e$
Coord:	T_d	O_h	
Lattice Position:	$\frac{1}{8}, \frac{1}{8}, \frac{1}{8}$	$\frac{1}{2}, \frac{1}{2}, \frac{1}{2}$	$\frac{1}{4}, \frac{1}{4}, \frac{1}{4}$
Occupancy:	1	1	1

D.4. $CuCr_2Se_4$(Hexagonal)

Chemical Formula:	$CuCr_2Se_4$				
Space Group:	148, Origin 1 ($R\bar{3}$)				
Structure Name:	Twinned-Spinel				
Lattice Parameters:	$a = 0.729\,590\,\text{nm}$		$\alpha = 90°$		
	$b = 0.729\,590\,\text{nm}$		$\beta = 90°$		
	$c = 1.786\,580\,\text{nm}$		$\gamma = 120°$		
Element:	Cu	Cr1	Cr2	Se1	Se2
Site:	$18f$	$3a$	$9d$	$6c$	$18f$
Coord:	T_d	O_h	O_h		
Lattice Position:	$0, \frac{1}{2}, \frac{3}{8}$	$0, 0, 0$	$\frac{1}{2}, 0, \frac{1}{2}$	$0, 0, \frac{1}{4}$	$\frac{1}{6}, \frac{1}{3}, \frac{1}{12}$
Occupancy:	1	1	1	1	1

APPENDIX E

BRAGG'S LAW

E.1. High Angle Approximation

Assume that a crystal can be considered as a series of parallel planes that interact with incident radiation in a manner similar to that of semitransparent mirrors; transmitting the majority of the incident radiation but reflecting a small portion at an angle equal to the angle of incidence, θ, as shown schematically in Figure E.1. Further, assume that absorption of the incident radiation can be neglected. If the incident radiation is monochromatic, a diffracted beam will be recorded at a detector when the reflected* beams from each plane of atoms $n\lambda$ wavelengths out of phase. This condition is satisfied when the difference in the path lengths traveled by $11'$ and $22'$, δ, is an integer number of wavelengths:

$$\delta = n\lambda \qquad \text{(Equation E.1.)}$$

By drawing perpendiculars between O and 1 and between O and 2, this phase difference can be shown to be equal to the sum of the distances between AB and BC.

$$\delta = \mathrm{AB} + \mathrm{BC} = 2\mathrm{AB} \qquad \text{(Equation E.2.)}$$

*Note that the term "reflection" is a colloquialism used in the diffraction community for a diffracted beam. It is generally understood that diffracted beams and reflected beams are fundamentally different phenomena.

FIGURE E.1. Geometric derivation of Bragg's Law.

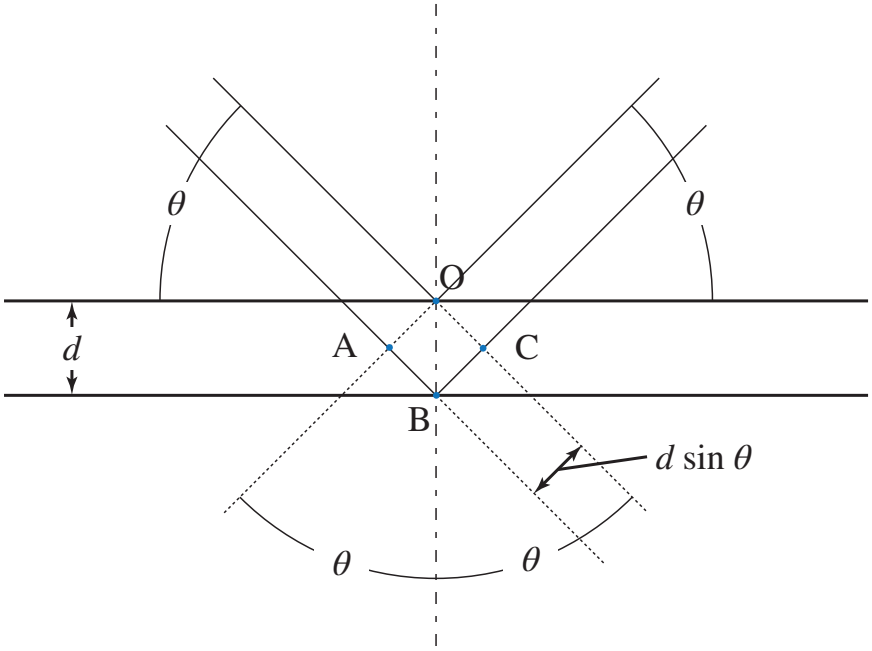

Using trigonometry, the distance AB can be shown to be related to BO, or d, by $\sin\theta$.

$$\delta = 2\mathrm{BO}\sin\theta = 2d\sin\theta \qquad \text{(Equation E.3.)}$$

So the fundamental condition required to see a diffracted beam at a given angle of incidence is that

$$n\lambda = 2d\sin\theta. \qquad \text{(Equation E.4.)}$$

E.2. Low Angle Correction

Bragg's Law, in its original derivation, does not take into account the effects of refraction in the interaction of the X-ray with the specimen. For most powder and high angle experiments, this consideration is moot as the change in path length resulting from the refractive index of a crystal with respect to X-ray wavelengths is

FIGURE E.2. Geometric derivation of Bragg's Law corrected for refraction.

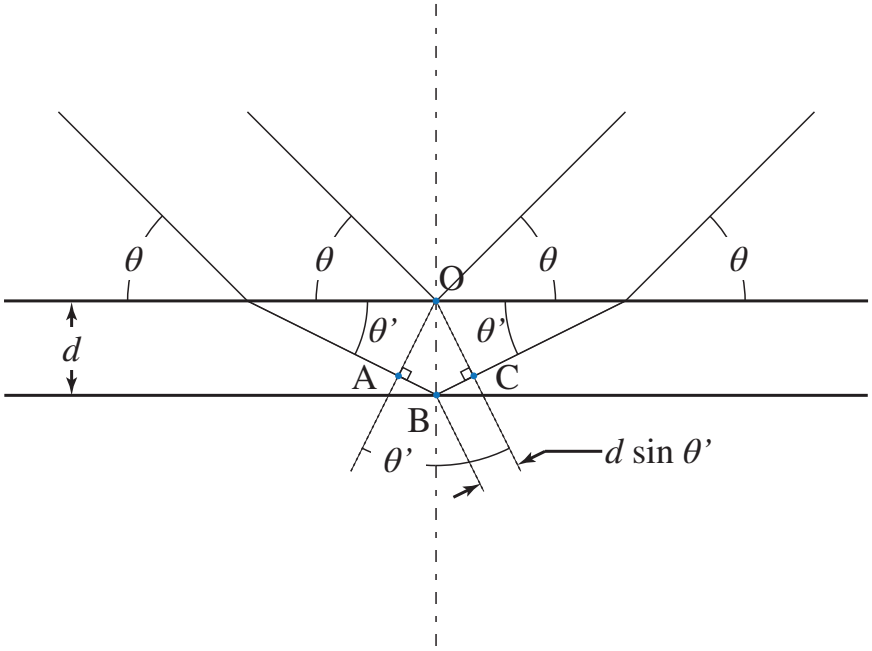

small. With smooth thin film specimens at low incidence angles this is not the case and the effects of refraction must be taken into account. Comparing Equation 2.5. and Equation 2.6. from Chapter II, it can be seen that they appear quite similar, the former appearing to be a special case of the later. On a conceptual level this modification of Bragg's Law is a correction for the refraction induced difference in path lengths from the geometry used to derive Bragg's Law, as shown in Figure E.2. At higher angles this path length difference is negligible, as $\sin^2\theta_c \lll \sin^2\theta$ for large angles, and the $\sqrt{\sin^2\theta - \sin^2\theta_c}$ term reduces to $\sin\theta$.

The derivation is most easily accomplished by noting that the path length difference is a result of the difference of the wavelength of light in air, λ, and that of the the film, λ'. The ratio of these two wavelengths, μ_r, and the resulting change in path within the film is captured by the Snell-Descartes Law:

$$\mu_r = \frac{\lambda}{\lambda'} = \frac{\cos\theta}{\cos\theta'} \qquad \text{(Equation E.5.)}$$

from which it can be shown that μ_r is related to a critical angle θ_c where $\lambda = \lambda'$:

$$\cos\theta_c = \mu_r \qquad \text{(Equation E.6.)}$$

below which the light will not penetrate the film. The path length of the x-ray within the crystal is simply Bragg's Law defined using the angle and wavelength within the medium:

$$n\lambda' = 2d\sin\theta' \qquad \text{(Equation E.7.)}$$

substitution of Equation E.7. into Equation E.5. and simplifying yields Equation E.8. Since the quantity $\mu_r \approx 1$, $n\lambda\mu_r$ may be approximated as $n\lambda$ allowing for the rearrangement and simplification shown in Equation E.9. Employing the Pythagorean trigonometric identity, Equation E.10., Equation E.9. can be further simplified to the equation provided in Chapter II.

$$\mu_r = \frac{\lambda}{\lambda'} = \frac{\lambda}{2(d/n)sin\theta'} = \frac{n\lambda}{2d[1-(\cos^2\theta)/\mu_r^2]^{\frac{1}{2}}} \qquad \text{(Equation E.8.)}$$

$$n\lambda = 2d\sqrt{\mu_r^2 - \cos^2\theta} = 2d\sqrt{\cos^2\theta_c - \cos^2\theta} \qquad \text{(Equation E.9.)}$$

$$n\lambda = 2d\sqrt{(1-\sin^2\theta_c) - (1-\sin^2\theta)} \qquad \text{(Equation E.10.)}$$

$$n\lambda = 2d\sqrt{\sin^2\theta - \sin^2\theta_c} \qquad \text{(Equation E.11.)}$$

APPENDIX F

THE ISSUE OF NOMENCLATURE IN TETRAGONAL FeSe

The two phases of FeSe discussed in Section 1.4. have very different properties and structure, but only a slight variation to the overall stoichiometry. Currently, an issue has arisen over which FeSe phase should bear the α or β designation. While this is a small issue the potential for confusion is significant, especially when the small differences* in composition between the two are considered. The issue has apparently already resulted in both designations being used in the literature to describe the same† tetragonal-FeSephase[50,60]. The starting point for the confusion is most likely attributable to a 2009 paper by McQueen, et al.[51] where the tetragonal phase is first referenced as β. This appendix provides a brief history of the issue from the first paper on the FeSe system to the present work, which will show McQueen's assertion to be in error.

Hagg and Kindstrom[43] published the original work on the Fe-Se binary system. Originally the paper was published in formal German and there is no English translation currently published. However using a rough translation it is easy to see that this work does not use greek designations but lattice types, or the older, *Structurbericht* notation system to distinguish between phases. From approximately 1933 through 2009 the tetragonal phase was designated as α and the orthorhombic phase as β. Two notable examples of this distinction are from Jain, et al.[45], and Hsu, et al.[48]. In his introduction Jain writes:

*See Appendix C, Section C.1.

†See Appendix D, Section D.1.

> X ray analysis of Hagg and Kindstrom (1933) showed that iron selenide exists in two forms: (i) α-FeSe having the PbO (B10) type tetragonal structure and (ii) β-FeSe, isotypic with NiAs (B8) (Alsen 1925, Hagg and Kindstrom 1933).

In the PNAC publication announcing the discovery of superconductivity in tetragonal-FeSe Hsu makes a similar clear distinction:

> FeSe comes in several phases: (i) a tetragonal phase α-FeSe with PbO-structure, (ii) a NiAs-type β-phase with a wide range of homogeneity showing a transformation from hexagonal to monoclinic symmetry, and (iii) an $FeSe_2$ phase that has the orthorhombic marcasite structure.

Both individuals are clear in their assertion that the literature precedent for the nomenclature is to designate tetragonal-FeSe as the α phase.

In 2009 McQueen, et al.[51] indicate that the previous literature was incorrect in its use of the α designation for the tetragonal form:

> ... [β-FeSe; recent publications have referred to this, improperly, as the α form. In phase diagrams and the original literature, it is the β form that is tetragonal (cf. Refs. 8 and 9, although a few, e.g., Ref. 10, refer to tetragonal FeSe as the α form. α is used here to designate the stoichiometric NiAs-type variant.]...

The evidence used for this assertion, references 8 and 9 in the quote, are the 1978 work by Jain, et al.[45], previously quoted, and a 1952 work by Grønvold, et al.[248] respectively. However, these assertions do not seem to agree with those of the cited literature. As previously stated, Jain uses the α designation for the tetragonal, B10, type structure, which is at odds with the assertions of McQueen. The Grønvold

paper is a work dealing with synthetic and naturally occurring iron (II) sulfides and the only relevant phase discussed is is a selenium rich FeS phase which exhibits the NiAs structure, similar to those found in the FeSe system. This phase is a high temperature phase, designated with a β transition on the iron-sulfur phase diagram. The only work that does agree with the assertion of McQueen is the 1991 phase diagram by Okamoto[249], which designates tetragonal FeSe as β. This work provides no rational for labeling and provides as the only reference on the tetragonal phase the original work by Hagg, et al.[43]

Since McQueens work was published a number of papers have been released using the β designation for tetragonal FeSe, citing only the McQueen paper or the references used to support its argument for their justification. This commonality suggests that the authors of these later papers are using McQueen, and not the body of literature itself as the primary source for their shift in nomenclature. As evidenced above, the literature supports the use of α to label the tetragonal phase. Without further rational from the author of the phase diagram, it is necessary to consider the β designation in the Okamoto 1991 phase diagram to be in error, and side with the literature precedent in the use of the α designation where necessary for this work.

APPENDIX G

LIST OF ACRONYMS AND ABBREVIATIONS

λ_c modulation wavelength

ϖ_c compositional waveform

ADF annular dark field

AEM analytical electron microscopy

ALD atomic layer deposition

BF bright field

CBED convergent beam electron diffraction

CIGS copper indium-gallium diselenide

CIS copper indium selenide

CMKT compositionally modulated kinetic trapping

CMM compositionally modulated multilayer

CVD chemical vapor deposition

CVT chemical vapor transport

DF dark field

DFT density functional theory

DSC differential scanning calorimetry

EDS energy dispersive X-ray spectroscopy

EELS electron energy loss spectroscopy

EPMA electron probe microanalysis

FIB focused ion beam

HAADF high angle annular dark field

IUCr International Union of Crystallography

MER modulated elemental reactant

MBE molecular beam epitaxy

MLC misfit layer compound

nujol mineral oil

OAc acetate (CH_3COO^-)

OLA oleylamine ($CH_3(CH_2)_7CH{=}CH(CH_2)_7CH_2NH_2$)

OSt stearate ($C_{17}H_{35}COO^-$)

PLD pulsed laser deposition

PMMA poly(methylmethacrylate) ($[CH_2C(CH_3)(CO_2CH_3)]_n$)

PVD physical vapor deposition

PVT physical vapor transport

SACT small angle cleavage technique

SAED selected area electron diffraction

SQUID superconducting quantum interference device

STEM scanning transmission electron microscopy

T_C Curie temperature

TEM transmission electron microscopy

WDS wavelength dispersive x-ray spectrometer

XPS X-ray photoelectron spectroscopy

XRD X-ray diffraction

XRR X-ray reflectivity

REFERENCES CITED

[1] Wang, S.; Kuo, K. H. *Acta Crystallog., Sect. A: Found Crystallogr.* **1991**, *47*, 381–392.

[2] Cailleau, H.; Ecolivet, C. *Mater. Sci. Forum* **1992**, *100-101*, 367.

[3] Kuypers, S.; Van Landuyt, J. *Mater. Sci. Forum* **1992**, *100-101*, 223.

[4] Makovicky, E.; Hyde, B. G. *Mater. Sci. Forum* **1992**, *100-101*, 1.

[5] Van Smaalen, S. *Mater. Sci. Forum* **1992**, *100-101*, 173.

[6] Wiegers, G. A.; Meerschaut, A. *Mater. Sci. Forum* **1992**, *100-101*, 101.

[7] Rouxel, J.; Moelo, Y.; Lafond, A.; Disalvo, F. J.; Meerschaut, A.; Roesky, R. *Inorg. Chem.* **1994**, *33*, 3358–3363.

[8] G Wiegers, S. R. *Prog. Solid State Chem.* **1996**, *24*, 1–139.

[9] Nader, A.; Briggs, A.; Meerschaut, A.; LaFond, A. *Solid State Commun.* **1997**, *102*, 401–403.

[10] LaFond, A.; Deudon, C.; Meerschaut, A.; Palvadeau, P.; Moėlo, Y.; Briggs, A. *J. Solid State Chem.* **1999**, *142*, 461–469.

[11] Harris, F. R. Fundamental Investigations of Bismuth Telluride-Titanium Telluride Layered Nanostructured Materials Synthesized by Modulated Multilayer Elemental Reactants. Ph.D. thesis, University of Oregon, 2004.

[12] Kallaene, M.; Rossnagel, K.; Marczynski-Buehlow, M.; Kipp, L.; Starnberg, H. I.; Stoltz, S. E. *Phys. Rev. Lett.* **2008**, *100*, 065502.

[13] Heideman, C. L.; Rostek, R.; Anderson, M. D.; Herzing, A. A.; Anderson, I. M.; Johnson, D. C. *J. Elec. Mater.* **2010**, *39*, 1–6.

[14] Lin, Q.; Smeller, M.; Heideman, C. L.; Zschack, P.; Koyano, M.; Anderson, M. D.; Kykyneshi, R.; Keszler, D. A.; Anderson, I. M.; Johnson, D. C. *Chem. Mater.* **2010**, *22*, 1002–1009.

[15] Kakos, G. A.; Turney, T. W.; Williams, T. B. *J. Solid State Chem.* **1994**, *108*, 102–111.

[16] Peng, Y.; Xi, G.; Zhong, C.; Wang, L.; Lu, J.; Sun, X.; Zhu, L.; Han, Q.; Chen, L.; Shi, L.; Sun, M.; Li, Q.; Yu, M.; Yin, M. *Geochim. Cosmochim. Acta* **2009**, *73*, 4862–4878.

[17] Auriel, C.; Roesky, R.; Meerschaut, A.; Rouxell, J. *Mater. Res. Bull.* **1993**, *28*, 247–254.

[18] Moelo, Y.; Meerschaut, A.; Rouxel, J.; C., A. *Chem. Mater.* **1995**, *7*, 1759–1771.

[19] Cario, L.; Kabbour, H.; Meerschaut, A. *Chem. Mater.* **2005**, *17*, 234–236.

[20] Kabbour, H.; Cario, L.; Danot, M.; Meerschaut, A. *Inorg. Chem.* **2006**, *45*, 917–22.

[21] Fang, C. M.; vanBruggen, C. F.; deGroot, R. A.; Wiegers, G. A.; Haas, C. *J. Phys. Condens. Matter* **1997**, *9*, 10173–10184.

[22] Van Smaalen, S.; Meetsma, A.; Wiegers, G. A.; De Boer, J. L. *Acta Crystallog., Sect. B: Struct. Sci.* **1991**, *47*, 314–325.

[23] Evain, M.; Petricek, V.; Moelo, Y.; Maurel, C. *Acta Crystallog., Sect. B: Struct. Sci.* **2006**, *62*, 775–789.

[24] Van Smaalen, S. *Incommensurate Crystallography*; International Union of Crystallography Monographs on Crystallography 21; Oxford University Press, 2007.

[25] Cario, L.; Lafond, A.; Morvan, T.; Kabbour, H.; Andre, G. *Solid State Sci.* **2005**, *7*, 934–944.

[26] Kabbour, H.; Cario, L.; Boucher, F. *J. Mater. Chem.* **2005**, *15*, 3525–3531.

[27] Kabbour, H.; Cario, L.; Jobic, S.; Corraze, B. *J. Mater. Chem.* **2006**, *16*, 4165–4169.

[28] Kabbour, H.; Cario, L. *Inorg. Chem.* **2006**, *45*, 2713–2717.

[29] Kabbour, H.; Cario, L. *Phys. Status Solidi C* **2006**, *3*, 2867–2870.

[30] Kabbour, H.; Janod, E.; Corraze, B.; Danot, M. *J. Am. Chem. Soc* **2008**, *130*, 8261–8270.

[31] Nguyen, N. T.; Berseth, P. A.; Lin, Q.; Chiritescu, C.; Cahill, D. G.; Mavrokefalos, A.; Shi, L.; Zschack, P.; Anderson, M. D.; Anderson, I. M.; Johnson, D. C. *Chemistry of Materials* **2010**, *22*, 2750–2756.

[32] Abramov, S. *J. Alloys Compd.* **1997**, *259*, 212–218.

[33] Wiegers, G. *J. Alloys Compd.* **1995**, *219*, 152–156.

[34] Noh, M.; Thiel, J.; Johnson, D. *Science* **1995**, *270*, 1181–1184.

[35] Noh, M.; Johnson, D. C. *J. Am. Chem. Soc.* **1996**, *118*, 9117–9122.

[36] Noh, M.; Thiel, J.; Johnson, D. C. *Adv. Mater.* **1996**, *8*, 596–599.

[37] Noh, M.; Johnson, C.; Hornbostel, M.; Thiel, J.; Johson, D. C. *Chem. Mater.* **1996**, *8*, 1625–1635.

[38] Noh, M.; Johnson, D.; Elliott, G. *Chem. Mater.* **2000**, *12*, 2894–2901.

[39] Berseth, P. Sythesis and Characterization of $[(NbSe_2)_m(CrSe_2)_n]$ Superlattices. Ph.D. thesis, University of Oregon, 2004.

[40] Nguyen, N. T.; Howe, B.; Hash, J. R.; Liebrecht, N.; Zschack, P.; Johnson, D. C. *Chem. Mater.* **2007**, *19*, 1923–1930.

[41] Mortensen, C. D. The effect of grain size, alloy composition and turbostratic disorder on the thermal and electrical properties of Bi_2Te_3 based materials. Ph.D. thesis, University of Oregon, 2008.

[42] Bettinger, J.; Chopdekar, R.; Liberati, M. *J. Magn. Magn. Mater.* **2007**, *318*, 65–73.

[43] Hagg, G.; Kindstrom, A.-L. *Z. Phys. Chem* **1933**, *22*, 453–464.

[44] Wu, X.; Zhang, Z.; Zhang, J.; Li, B.; Ju, Z. *J. Appl. Phys.* **2008**, *103*, 113501.

[45] Jain, B.; Singh, A.; Chandra, K. *J. Phys. F: Met. Phys.* **1978**, *8*, 2625.

[46] Wu, M.; Hsu, F.; Yeh, K.; Huang, T.; Luo, J. *Physica C* **2009**, *469*, 340–349.

[47] Williams, A. J.; McQueen, T. M.; Cava, R. J. *Solid State Commun.* **2009**, *149*, 1507–1509.

[48] Hsu, F. C.; Luo, J. Y.; Yeh, K. W.; Chen, T. K.; Huang, T. W.; Wu, P. M.; Lee, Y. C.; Huang, Y. L.; Chu, Y. Y.; Yan, D. C. *PNAC* **2008**, *105*, 14262–14264.

[49] Kotegawa, H.; Masaki, S.; Awai, Y.; Tou, H. *J. Phys. Soc. Jpn.* **2008**, *77*, 113703.

[50] Li, Z.; Ju, J.; Tang, J.; Sato, K.; Watahiki, M. *J. Phys. Chem. Solids* **2010**, *71*, 495–498.

[51] McQueen, T. M.; Huang, Q.; Ksenofontov, V.; Felser, C.; Xu, Q.; Zandbergen, H.; Hor, Y. S.; Allred, J.; Williams, A. J.; Qu, D. *Phys. Rev. B* **2009**, *79*, 014522.

[52] Medvedev, S.; McQueen, T. M.; Troyan, I. A.; Palasyuk, T.; Eremets, M. I.; Cava, R. J.; Naghavi, S.; Casper, F.; Ksenofontov, V.; Wortmann, G. *Nat. Mater.* **2009**, *8*, 630–633.

[53] Mizuguchi, Y.; Tomioka, F.; Tsuda, S. *Appl. Phys. Lett.* **2008**, *93*, 152505–(0–3).

[54] Patel, U.; Hua, J.; Yu, S.; Avci, S.; Xiao, Z. *Appl. Phys. Lett.* **2009**, *94*, 082508–(0–3).

[55] Braithwaite, D.; Salce, B.; Lapertot, G.; Bourdarot, F.; Marin, C.; Aoki, D.; Hanfland, M. *J. Phys. Condens. Matter* **2009**, *21*, 232202.

[56] Feng, Q.; Shen, D.; Zhang, J.; Shan, C. *J. Magn. Magn. Mater.* **2004**, *279*, 435–439.

[57] Feng, Q.; Shen, D.; Zhang, J.; Li, B.; Li, B. *Appl. Phys. Lett.* **2006**, *88*, 012505–(0–3).

[58] Hamdadou, N.; Bernede, J. C.; Khelil, A. *J. Cryst. Growth* **2002**, *241*, 313–319.

[59] Liu, K.; Zhang, J.; Shen, D.; Shan, C.; Li, B. *Appl. Phys. Lett.* **2007**, *90*, 262503–(0–3).

[60] Oyler, K.; Ke, X.; Sines, I.; Schiffer, P.; Schaak, R. *Chem. Mater.* **2009**, *21*, 3655–3661.

[61] Takemura, Y.; Honda, N.; Takahashi, T.; Suto, H.; Kakuno, K. *J. Magn. Magn. Mater.* **1998**, *177-181*, 1319–1320.

[62] Wu, X.; Zhang, Z.; Zhang, J.; Ju, Z.; Shen, D. *J. Cryst. Growth* **2007**, *300*, 483–485.

[63] Margadonna, S.; Takabayashi, Y.; McDonald, M. *Chem. Commun.* **2008**, *2008*, 5607–5609.

[64] Subedi, A.; Zhang, L.; Singh, D.; Du, M. *Phys. Rev. B* **2008**, *78*, 134514.

[65] Wu, X.; Shen, D.; Zhang, Z.; Zhang, J.; Liu, K. *Appl. Phys. Lett.* **2007**, *90*, 112105–(0–3).

[66] Margadonna, S.; Takabayashi, Y.; Ohishi, Y. *Phys. Rev. B* **2009**, *80*, 1–6.

[67] Mizuguchi, Y.; Tomioka, F.; Tsuda, S.; Yamaguchi, T.; Takano, Y. *Appl. Phys. Lett.* **2009**, *94*, 012503–(0–3).

[68] Zhang, S.; Sun, Y.; Zhu, X.; Zhu, X.; Wang, B. *Supercond. Sci. Technol.* **2009**, *22*, 015020.

[69] Campos, C. E. M.; De Lima, J. C.; Grandi, T. A.; Machado, K. D.; Pizani, P. S. *Solid State Commun.* **2002**, *123*, 179–184.

[70] Campos, C.; Lima, J.; Grandi, T. *J. Phys. Condens. Matter* **2004**, *16*, 8485.

[71] Jourdan, M.; Ten Haaf, S. *J. Appl. Phys.* **2010**, *108*, 023913.

[72] Brixner, L. *J. Inorg. Nucl. Chem.* **1962**, *24*, 257–263.

[73] Huisman, R.; Jellinek, F. *J. Less-Common Met.* **1969**, *17*, 111–117.

[74] Wilson, J. A.; Yoffe, A. D. *Adv. Phys.* **1969**, *18*, 193–335.

[75] Birks, A.; Hind, S.; Lee, P. *Phys. Status Solidi B* **1976**, *76*, 599–604.

[76] Yokoya, T.; Kiss, T.; Chainani, A.; Shin, S.; Nohara, M. *Science* **2001**, *294*, 2518–2520.

[77] Voorhoeve, J.; Van Den Berg, N.; Robbins, M. *J. Solid State Chem.* **1970**, *1*, 134–137.

[78] Doran, N.; Titterington, D.; Ricco, B. *J. Phys. C: Solid State Phys.* **1978**, *11*, 685.

[79] Straub, T.; Finteis, T.; Claessen, R.; Steiner, P. *Phys. Rev. Lett.* **1999**, *82*, 4504–4507.

[80] Corcoran, R.; Meeson, P.; Onuki, Y. *J. Phys. Condens. Matter* **1994**, *6*, 4479.

[81] Mattheiss, L. *Phys. Rev. B* **1973**, *8*, 3719–3740.

[82] Hind, S. P.; Lee, P. M. *J. Phys. C: Solid State Phys.* **1980**, *13*, 349.

[83] Smart, L. E.; Moore, E. A. *Solid state chemistry: An introduction*, 3rd ed.; CRC Press, 2005.

[84] West, A. R. *Solid state chemistry and its applications*; John Wiley & Sons, Ltd., 1987.

[85] Oglesby, C.; Bucher, E.; Kloc, C.; Hohl, H. *J. Cryst. Growth* **1994**, *137*, 289–294.

[86] Day, A.; Zabinski, J. *Thin Solid Films* **1994**, *238*, 207–212.

[87] von Philipsborn, H. *Z. Kristallogr.* **1971**, *133*, 464–472.

[88] Snyder, G. J.; Caillat, T.; Fleurial, J. P. *Mater. Res. Innovations* **2001**, *5*, 67–73.

[89] Hahn, H.; de Lorent, C.; Harder, B. *Z. Anorg. Allg. Chem.* **1956**, *283*, 138–42.

[90] Lotgering, F. K. *Proc. Int. Conf. Magn.* **1964**, 533–537.

[91] Lotgering, F.; Stapele, R. V. *Solid State Commun.* **1967**, *5*, 143–146.

[92] Bordács, S.; Kézsmárki, I.; Ohgushi, K.; Tokura, Y. *New J. Phys.* **2010**, *12*, 053039.

[93] Goodenough, J. B. *Solid State Commun.* **1967**, *5*, 577–580.

[94] Wojtowicz, P. *IEEE T. Magn.* **1969**, *5*, 840–848.

[95] Amith, A.; Friedman, L. *Phys. Rev. B* **1970**, *2*, 434–445.

[96] Haas, C. *Crit. Rev. Solid State Sci.* **1970**, *5*, 487–494.

[97] Liberati, M.; Neulinger, J. R.; Chopdekar, R. V.; Bettinger, J. S.; Arenholz, E.; Butler, W. H.; Stacy, A. M.; Idzerda, Y. I.; Suzuki, Y. *J. Appl. Phys.* **2008**, *103*, 07D711.

[98] Neulinger, J. Synthesis, structure and magnetism in copper chalcochromite spinels. Ph.D. thesis, Uniersity of California at Berkley, 2006.

[99] Ametani, K. *Bull. Chem. Soc. Jpn.* **1976**, *49*, 450–456.

[100] Ametani, K. *Bull. Chem. Soc. Jpn.* **1974**, *47*, 242–243.

[101] Krok-Kowalski, J.; Warczewski, J.; Nikiforov, K. *J. Alloys Compd.* **2001**, *315*, 62–67.

[102] Ogasawara, T.; Ohgushi, K.; Tomioka, Y.; Takahashi, K. S.; Okamoto, H.; Kawasaki, M.; Tokura, Y. *Phys. Rev. Lett.* **2005**, *94*, 87202.

[103] Goodenough, J. B. Description of transition-metal compounds: application to several sulfides. 1967.

[104] Hollander, J. C. T.; Sawatzky, G.; Haas, C. *Solid State Commun.* **1974**, *15*, 747–751.

[105] Kimura, A.; Matsuno, J.; Okabayashi, J.; Fujimori, A.; Shishidou, T.; Kulatov, E.; Kanomata, T. *Phys. Rev. B* **2001**, *63*, 224420.

[106] Lotgering, F. K. *J. Phys., Colloque* **1971**, Cl–34–Cl–38.

[107] Wang, Y. H. A.; Gupta, A.; Chshiev, M.; Butler, W. H. *Appl. Phys. Lett.* **2008**, *92*, 062507–(0–3).

[108] Saha-Dasgupta, T.; De Raychaudhury, M.; Sarma, D. D. *Phys. Rev. B* **2007**, *76*, 54441.

[109] Rusnak, A. N.; Kim, D.; Parameswaran, S.; Patra, C. R.; Trofimov, V. B.; Harpness, R.; Gedanken, A.; Tver'yanovich, Y. S. *J. Non-Cryst. Solids* **2006**, *352*, 2885–2891.

[110] Rodic, D.; Antic, B.; Tellgren, R.; Rundlof, H.; Blanusa, J. *J. Magn. Magn. Mater.* **1998**, *187*, 88–92.

[111] Tsoi, G. M.; Wenger, L. E.; Wang, Y. H. A.; Gupta, A. *J. Magn. Magn. Mater.* **2010**, *322*, 142–147.

[112] Kim, D. S.; Rusnak, A. N.; Tver'yanovich, Y. S.; Volobueva, O.; Kim, M.; Kwon, S. *Glass Phys. Chem.* **2008**, *34*, 146–149.

[113] Pinch, H. L.; Ekstrom, L. *RCA Rev.* **1970**, *31*, 692–701.

[114] Kwestroo, W. In *Preparative methods in solid state chemistry*; Hagenmuller, P., Ed.; Prep. Methods Solid State Chem., 1972; pp 563–574.

[115] Kim, D.; Gedanken, A.; Tver'yanovich, Y.; Lee, D. W.; Kim, B. K. *Mater. Lett.* **2006**, *60*, 2807–2809.

[116] Kim, D.; Rusnak, A. N.; Parameswaran, S.; Patra, C. R.; Trofimov, V. B.; Harpness, R.; Gedanken, A.; Tver'yanovich, Y. S. *Glass Phys. Chem.* **2006**, *32*, 330–336.

[117] Lin, C. R.; Yeh, C. L.; Lu, S. Z.; Lyubutin, I. S.; Wang, S. C.; Suzdalev, I. P. *Nanotechnology* **2010**, *21*, 235603.

[118] Mitchell, P. W. D.; Morgan, P. E. D. *J. Am. Ceram. Soc.* **1974**, *57*, 278.

[119] Ramesha, K.; Seshadri, R. *Solid State Sci.* **2004**, *6*, 841–845.

[120] Berzhanskii, V. N.; Krokin, N. A.; Ivanov, V. I.; Kononov, V. P.; Edel'man, I. S.; Gavrichkov, S. A.; Chernov, V. K.; Shishkov, A. G.; Pirogova, A. M. *Thin Solid Films* **1990**, *190*, 199–215.

[121] Cotton, F. A.; WIlkinson, G.; Gaus, P. L. *Basic Inorganic Chemistry*, 3rd ed.; John Wiley & Sons, Ltd., 1994.

[122] Fister, L.; Johnson, D. C. *J. Am. Chem. Soc.* **1992**, *114*, 4639–4644.

[123] Jensen, J.; Kyablue, X.; Ly, S.; Johnson, D. *J. Appl. Phys.* **2003**, *94*, 1252–7.

[124] Jensen, J. M.; Ly, S.; Johnson, D. C. *Chem. Mater.* **2003**, *15*, 4200–4204.

[125] Jensen, J.; Ly, S.; Kyablue, X.; Johnson, D. *Mater. Res. Soc. Symp. Proc.* **2003**, *775*.

[126] Hagenmuller, P. *Preparative Methods in Solid State Chemistry*; Academic Press, 1972.

[127] Thompson, J. O. The Importance of Elemental Stacking Order and Layer Thickness in Controlling the Formation Kinetics of Copper Indium Diselenide. Ph.D. thesis, University of Oregon, 2008.

[128] Ohring, M. *Materials Science of Thin Films: Deposition and Structure*, 2nd ed.; Academic Press, 2002.

[129] Smith, D. *Thin Film Deposition: Principles and Practice*; McGraw Hill Professional, 1995.

[130] Isshiki, M.; Wang, J. F. In *Bulk Crystal Growth of Electronic, Optical, and Optoelectronic Materials*; Capper, P., Ed.; John Wiley & Sons, Ltd., 2005; Chapter 9, pp 269–297.

[131] Wolf, S.; Tauber, R. N. *Silicon Processing for the VLSI Era*, 2nd ed.; Lattice Press, 2000; Vol. 1.

[132] Jensen, J. M. Selective Preparation of Nickel Silicides and Nickel Gremanides form Multilayer Reactants. Ph.D. thesis, University of Oregon, 2003.

[133] Heideman, C. Families of metastable misfit layered compounds prepared by modulated elemental precursors and the resulting physical properties. Ph.D. thesis, University of Oregon, 2010.

[134] Lin, Q. Synthesis and thermoelectric properties of a new family of misfit layered compounds: lead selenide-tungsten selenide. Ph.D. thesis, University of Oregon, 2009.

[135] Nguyen, N. T. Designed superlattices: From lattice matched to lattice mismatched building blocks. Ph.D. thesis, University of Oregon, 2007.

[136] Smeller, M. M. Structural Studies of $[(PbSe)_{0.99}]_m[WSe_2]_n$, $[(PbSe)_{1.00}]_m[MoSe_2]_n$, and $[(SnSe)_{1.03}]_m[MoSe_2]_m$ Misfit Layered Compounds. Ph.D. thesis, University of Oregon, 2011.

[137] Schneidmiller, R. Synthesis of Ternary Chevrel Phases Using Elemental Modulated Reactants. Ph.D. thesis, University of Oregon, 2000.

[138] Suryanarayana, C.; Grant Norton, M. G. *X-ray diffraction: A practical approach*, 1st ed.; Springer, 1998.

[139] Cullity, B. D.; Stock, S. R. *Elements of X-ray diffraction*, 3rd ed.; Prentice Hall, 2001.

[140] Azaroff, L. V. *Elements of X-ray crystallography*; McGraw Hill, 1968.

[141] Dalliant, J., Gibaud, A., Eds. *X-ray and neutron reflectivity*, 1st ed.; Lecture notes in physics; Springer, 2009; Vol. 770.

[142] Peitsch, U.; Holy, V.; Baumbach, T. *High resolution x-ray scattering: from thin films to lateral nanostructures*, 2nd ed.; Springer tracts in modern physics; Springer, 2004; Vol. 149.

[143] Wainfan, N.; Parratt, L. G. *J. App. Phys.* **1950**, *31*, 1331–1337.

[144] Phung, T. M.; Jensen, J. M.; Johnson, D. C.; Donovan, J. J.; Mcburnett, B. G. *X-Ray Spectrom.* **2008**, *37*, 608–614.

[145] Cohen, M. *Review of Scientific Instruments* **1936**,

[146] Cohen, M. U. *Review of Scientific Instruments* **1935**, *6*, 68.

[147] Nelson, J. B.; Riley, D. P. *Proceedings of the Physical Society* **1945**, *57*, 160–177.

[148] Reed, S. J. B. *Electron Microprobe Analysis and Scanning Electron Microscopy in Geology*, 3rd ed.; Cambridge University Press, 2010.

[149] Goldstein, J.; Newbury, D. E.; Joy, D. C.; Lyman, C. E.; Echlin, P.; Lifshin, E.; Sawyer, L.; Michael, J. *Scanning electron microscopy and X-ray micronanlysis*, 3rd ed.; Springer, 2003.

[150] Pouchou, J. L. *Microchimica Acta* **2002**, *138*, 133–155.

[151] Pouchou, J. L.; Pichoir, F. *Scanning Microscopy International* **1993**, *7*, 167–190.

[152] Pouchou, J. L. *Analytica chimica acta* **1993**, *283*, 81–97.

[153] Williams, D. B.; Carter, C. B. *Transmission electron microscopy: A textbook for materials science*, 2nd ed.; Springer, 2009.

[154] Reimer, L.; Helmut, K. *Transmission electron microscopy*, 5th ed.; Springer series in optical sciences; Springer, 2008; Vol. 36.

[155] Fultz, B.; Howe, J. M. *Transmission electron microscopy and diffractiometry of materials*, 3rd ed.; Springer, 2008.

[156] Egerton, R. F. *Physicsal principles of electron microscopy: An introduction to TEM, SEM, and AEM*, 1st ed.; Springer, 2010.

[157] McCaffrey, J. P. *Microsc. Res. Tech.* **1993**, *24*, 180–184.

[158] Walck, S. D.; McCaffrey, J. P. *Mater. Res. Soc. Symp. Proc.* **1997**, *480*, 149–172.

[159] Brewer, L. *J. Chem. Educ.* **1958**, *28*, 48.

[160] Johnson, W. L.; Poon, S. J.; Duwez, P. *Phys. Rev. B* **1975**, *11*, 150–154.

[161] Johnson, W. L.; Williams, A. R. *Phys. Rev. B* **1979**, *20*, 1640–1655.

[162] Mogilatenko, A. V.; Allenstein, F.; Schubert, M. A.; Falke, M.; Beddies, G.; Neumann, W. *Mater. Sci. Forum* **2010**, *638*, 2938–2943.

[163] Fischer, D.; Jansen, M. *Angew. Chem. Int. Ed.* **2002**, *41*, 1755–1756.

[164] Novet, T.; Johnson, D. C. *J. Am. Chem. Soc.* **1991**, *113*, 3398–3403.

[165] Jansen, M. *Angew. Chem. Int. Ed.* **2002**, *41*, 3746–3766.

[166] Liebold-Ribeiro, Y.; Fischer, D.; Jansen, M. *Angew. Chem.* **2008**, *120*, 4500–4503.

[167] Risbud, A. S.; Snedeker, L. P.; Elcombe, M. M.; Cheetham, A. K.; Seshadri, R. *Chem. Mater.* **2005**, *17*, 834–838.

[168] Waniuk, T.; Schroers, J.; Johnson, W. L. *Phys. Rev. B* **2003**, *67*, 184203.

[169] Wuttig, M.; Yamada, N. *Nat. Mater.* **2007**, *6*, 824–832.

[170] Gabor, A. M.; Tuttle, J. R.; Albin, D. S.; Contreras, M. A.; R, *Appl. Phys.* **1994**, *65*, 198–200.

[171] Gosavi, S. R.; Deshpande, N. G.; Gudage, Y. G.; Sharma, R. *J. Alloys Compd.* **2008**, *448*, 344–348.

[172] Kim, M. S.; Chalapathy, R. B. V.; Yoon, K. H.; Ahn, B. T. *J. Electrochem. Soc.* **2010**, *157*, B154–B158.

[173] Kim, Y.; Lee, J.; Shin, D.; Chen, H. *Photovoltaics Specialists Conference* **2009**, 001232–001233.

[174] Xu, J.; Lee, C. S.; Tang, Y. B.; Chen, X.; Chen, Z. H.; Zhang, W. J.; Lee, S. T.; Zhang, W.; Yang, Z. *ACS nano* **2010**, *4*, 1845–1850.

[175] Contreras, M. A.; Egaas, B.; Ramanathan, K.; Hiltner, J.; Swartzlander, A.; Hasoon, F.; Noufi, R. *Prog. Photovoltaics* **1999**, *7*, 311–316.

[176] Heske, C.; Fink, R.; Umbach, E.; Riedl, W.; Karg, F. *Appl. Phys. Lett.* **1996**, *68*, 3431–3433.

[177] Nishiwaki, S.; Kohara, N.; Negami, T.; Wada, T. *Jpn. J. Appl. Phys., Part 2* **1998**, *37*, 71–73.

[178] Wei, S.-h.; Zhang, S. B.; Zunger, A. *J. App. Phys.* **1999**, *85*, 7214–7218.

[179] Kharchenko, M.; Boyko, B.; Panchekha, P.; Chernikov, A.; Novikov, V. 1998.

[180] Lakshmikumar, S.; Rastogi, a. *Sol. Energ. Mat. Sol. C.* **1994**, *32*, 7–19.

[181] Okimura, H. *Thin Solid Films* **1980**, *71*, 53–59.

[182] Schimmel, M. I.; Bottechia, O. L.; Wendt, H. *J. Appl. Electrochem.* **1998**, *28*, 299–304.

[183] Hergert, F.; Hock, R.; Weber, a.; Purwins, M.; Palm, J.; Probst, V. *J. Phys. Chem. Solids* **2005**, *66*, 1903–1907.

[184] Hergert, F.; Jost, S.; Hock, R.; Purwins, M. *J. Solid State Chem.* **2006**, *179*, 2394–2415.

[185] Kim, S.; Kim, W. K.; Kaczynski, R. M.; Acher, R. D.; Yoon, S.; Anderson, T. J.; Crisalle, O. D.; Payzant, E. a.; Li, S. S. *J. Vac. Sci. Technol. A.* **2005**, *23*, 310.

[186] Chraibi, F.; Fahoume, M.; Ennaoui, A.; Delplancke, J. L. *M. J. Condens. Matter* **2004**, *5*, 88–96.

[187] Kim, W.; Payzant, E.; Yoon, S.; Anderson, T. *J. Cryst. Growth* **2006**, *294*, 231–235.

[188] Pisarkiewicz, T.; Jankowski, H.; Schabowska, E. *Opto-Electron. Rev.* **2003**, *11*, 297–304.

[189] Heyding, R. D. *Can. J. Chem.* **1966**, *44*, 1233–1236.

[190] Murray, R. M.; Heyding, R. D. *Can. J. Chem.* **1976**, *54*, 841–848.

[191] Murray, R. M. L.; Heyding, R. D. *Can. J. Chem.* **1975**, *53*, 878–887.

[192] Ohtani, T.; Motoki, M.; Koh, K.; Ohshima, K. *Mater. Res. Bull.* **1995**, *30*, 1495–1504.

[193] Garcia, V. M.; Nair, P. K.; Nair, M. T. S. *J. Cryst. Growth* **1999**, *203*, 113–124.

[194] Lakshmikumar, S. T.; Rastogi, A. C. *J. App. Phys.* **1994**, *76*, 3068.

[195] Rao, C. N. R.; Kulkarni, G. U.; Agrawal, V. V.; Gautam, U. K.; Ghosh, M.; Tumkurkar, U. *J. Colloid. Interf. Sci.* **2005**, *289*, 305–18.

[196] Villars, P., Ed. *ASM Alloy Phase Diagrams Center*; ASM International, 2007.

[197] Kissinger, H. E. *Anal. Chem.* **1957**, *29*, 1702–1706.

[198] Johnson, C. D.; Anderson, K.; Gromko, A. D.; Johnson, D. C. *J. Am. Chem. Soc* **1998**, *120*, 5226–5232.

[199] Neiner, D.; Golub, V.; Wiley, J. B. *Mater. Res. Bull.* **2004**, *39*, 1385–1392.

[200] Viciu, L.; Kodenkandath, T. A.; Wiley, J. B. *J. Solid State Chem.* **2007**, *180*, 583–588.

[201] Sivakumar, T.; Wiley, J. B. *Mater. Res. Bull.* **2009**, *44*, 74–77.

[202] Hermann, A. T.; Wiley, J. B. *Mater. Res. Bull.* **2009**, *44*, 1046–1050.

[203] Ranmohotti, K. S.; Josepha, E.; Choi, J.; Wiley, J. B. *Adv. Mater.* **2011**, *23*, 442–60.

[204] Walser, R. M.; Bene, R. W. *Appl. Phys. Lett.* **1976**, *28*, 624–5.

[205] Theron, C.; Ndwandwe, O.; Lombaard, J.; Pretorius, R. *Mater. Chem. Phys.* **1996**, *46*, 238–247.

[206] Park, W.; Fister, L.; Johnson, D.; Cohen, J. *J. Appl. Phys.* **1994**, *75*, 2294–6.

[207] Williams, J. R.; Johnson, M. B.; Johnson, D. C. *J. Am. Chem. Soc.* **2003**, *125*, 3589–3592.

[208] Sellinschegg, H.; Stuckmeyer, S. L.; Hornbostel, M. D.; Johnson, D. C. *Chem. Mater.* **1998**, *10*, 1096–1101.

[209] Oyelaran, O.; Novet, T.; Johnson, C. D.; Johnson, D. C. *J. Am. Chem. Soc* **1996**, *118*, 2422–2426.

[210] Fister, L.; Li, X. M.; McConnell, J.; Novet, T.; Johnson, D. C. *J. Vac. Sci. Technol. A.* **1993**, *11*, 3014–3019.

[211] DiSalvo, F. J.; Waszczak, J. V. *Phys. Rev. B* **1982**, *26*, 2501–2506.

[212] Kalinnikov, V. T.; Aminov, T. G.; Novotortsev, V. M. *Inorg. Mater.* **2003**, *39*, 997–1012.

[213] Lotgering, F. *Solid State Commun.* **1964**, *2*, 55–6.

[214] Babitsyna, A. A.; Emel'yanova, T. A.; Chernitsyna, M. A.; Kalinnikov, V. T. *Zh. Neorg. Khim.* **1978**, *23*, 267–268.

[215] Johnson, D. *Curr. Opin. Solid State Mater. Sci.* **1998**, *3*, 159–167.

[216] Daneu, N.; Rečnik, A.; Yamazaki, T.; Dolenec, T. *Physics and Chemistry of Minerals* **2007**, *34*, 233–247.

[217] Rao, M.; Shamsuzzoha, M.; Gupta, A. *Journal of Crystal Growth* **2007**, *306*, 321–325.

[218] Thompson, J. O.; Anderson, M. D.; Ngai, T.; Allen, T.; Johnson, D. C. *J. Alloys Compd.* **2011 (Accepted)**,

[219] Okonska-Kozlowska, I.; Kopyczok, J.; Lutz, H.; Stingl, T. *Acta Crystallog., Sect. C: Cryst. Struct. Comm.* **1993**, *C49*, 1448–1449.

[220] Kittel, C. In *Introduction to Solid State Physics*, 8th ed.; Johnson, S., Ed.; John Wiley & Sons, Ltd., 2005.

[221] Nakatani, H.; Nosé, H.; Masumoto, K. *J. Phys. Chem. Solids* **1978**, *39*, 743–749.

[222] Miyatani, K.; Minematsu, Y.; Wada, Y.; Okamoto, F.; Kato, K.; Baltzer, P. K. *J. Phys. Chem. Solids* **1971**, *32*, 1429–1434.

[223] Beekman, M.; Heideman, C.; Anderson, M. D.; Smeller, M.; Atkins, R.; Lin, Q.; Nguyen, N.; Johnson, D. C. In *Design and realization of nanostructured inorganic intergrowths*, 2nd ed.; Rowe, D. M., Ed.; CRC Handbook of Thermoelectrics; CRC Press, 2011 (In Press).

[224] Getzlaff, M. *Fundamentals of Magnetism*; Springer, 2008.

[225] Blaha, P.; Schwarz, K.; Madsen, G. K. H.; Kvasnicka, D.; Luitz, J. WIEN2k, An Augmented Plane Wave + Local Orbitals Program for Calculating Crystal Properties. (Karlheinz Schwarz, Techn. Universität Wien, Austria), 2001.

[226] Thevenaz, P.; Ruttimann, U. E.; Unser, M. *IEEE T. Image. Process.* **1998**, *7*, 27–41.

[227] El-Sayed, M. A. *Acc. Chem. Res* **2004**, *37*, 326–333.

[228] Rao, C. N.; Kulkarni, G. U.; Thomas, P. J.; Edwards, P. P. *Chemistry* **2002**, *8*, 28–35.

[229] Sapra, S.; Nanda, J.; Sarma, D. D. In *Encyclopedia of Nanoscience and Nanotechnology*; Nalwa, H. S., Ed.; American Scientific Publishers, 2004; Vol. 3; pp 181–192.

[230] Mao, Y.; Park, T. J.; Wong, S. S. *Chem. Commun.* **2005**, *2005*, 5721–5735.

[231] Puntes, V. F.; Krishnan, K. M.; Alivisatos, A. P. *Science* **2001**, *291*, 2115–2117.

[232] Sun, Y.; Xia, Y. *Science* **2002**, *298*, 2176.

[233] Yacamán, M. J.; Ascencio, J. A.; Liu, H. B.; Gardea-Torresdey, J. *J. Vac. Sci. Technol. B.* **2001**, *19*, 1091–1103.

[234] Yu, W. W.; Wang, Y. A.; Peng, X. *Chem. Mater.* **2003**, *15*, 4300–4308.

[235] Chen, J.; Ye, X.; Murray, C. B. *ACS nano* **2010**, *4*, 2374–2381.

[236] Murray, C. B.; Kagan, C. R.; Bawendi, M. G. *Science* **1995**, *270*, 1335.

[237] Murray, C. B.; Kagan, C. R.; Bawendi, M. G. *Annu. Rev. Mater. Sci.* **2000**, *30*, 545–610.

[238] Talapin, D. V.; Schevchenko, E. V.; Bodnarchuk, M. I.; Ye, X.; Chen, J.; Murray, C. B. *Nature* **2009**, *461*, 964–967.

[239] Sun, S.; Murray, C. B.; Weller, D.; Folks, L.; Moser, A. *Science* **2000**, *287*, 1989.

[240] Talapin, D.; Kotov, N.; O'Brien, S.; Murray, C. *Nature* **2006**, *439*, 55–59.

[241] Brown, L. O.; Hutchison, J. E. *J. Phys. Chem. B* **2001**, *105*, 8911–8916.

[242] Billinge, S. J. L.; Levin, I. *Science* **2007**, *316*, 561.

[243] Rogach, A. L.; Talapin, D. V.; Shevchenko, E. V.; Kornowski, A.; Haase, M.; Weller, H. *Adv. Funct. Mater.* **2002**, *12*, 653–664.

[244] Johnson, C.; Sellinschegg, H.; Johnson, D. *Chem. Mater.* **2001**, *45*, 3876–3881.

[245] Berseth, P. A.; Hughes, T. A.; Schneidmiller, R.; Smalley, A.; Johnson, D. C. *Solid State Sci.* **2002**, *4*, 717–722.

[246] Callister, W. D. *Materials Science and Engineering*, 6th ed.; John Wiley & Sons, Ltd., 2003.

[247] Hahn, T., Ed. *Space-group Symmetry*; International Union of Crystallography, 2006; Vol. A; 1st online ed.

[248] Gronvold, F.; Haraldsen, H. *Acta Chem. Scand.* **1952**, *6*, 1452–1469.

[249] Okamoto, H. *J. Phase Equilib.* **1991**, *12*, 383–389.